THE EVALUATION OF POSITRON EMISSION TOMOGRAPHY TO ASSESS PHARMACODYNAMICS AND PHARMACOKINETICS OF ANTI CANCER DRUGS

Submitted for the degree of Doctor of Medicine

Imperial College

University of London

By

Nishi Gupta

MBBS MRCP FRCR

2008

Abstract

Positron emission tomography (PET) is a non-invasive imaging technique that is emerging as a useful tool in the field of cancer medicine particularly in drug development. The purpose of this thesis has been to perform clinical studies using two different radiotracers, 5-[^{18}F]fluorouracil (5-[^{18}F]FU) and 2-[^{11}C]thymidine, to assess pharmacokinetic and pharmacodynamic parameters respectively, which were derived from PET imaging and to establish the contribution that PET can add to drug development, *in vivo*, in man.

Aims: 1) Quantify the pharmacodynamic effects of cytotoxic agents in tumour and normal tissue using 2-[^{11}C]thymidine 2) Measure changes in tumour and normal tissue pharmacokinetics of 5-Fluorouracil in response to the modulating agents carbogen and nicotinamide or interferon 3) Assessment of blood flow change in tumour and normal tissue to carbogen and nicotinamide or interferon 4) Interpretation of PET data using novel analysis methods with modified Patlak and spectral analysis

Methods: In the 5-[^{18}]FU study, patients with metastatic gastrointestinal cancer underwent PET scanning at the start of 2 separate chemotherapy cycles. The 2nd scan was performed after the administration of carbogen and nicotinamide or interferon. In the 2-[^{11}C]thymidine study patients receiving chemotherapy were scanned before commencing chemotherapy, and 1 week after the 3rd cycle of chemotherapy. Patients also had conventional imaging before the start of and after 3 cycles of treatment.

Findings: After carbogen and nicotinamide administration, 5-[^{18}]FU uptake was increased in tumour, but not in normal tissue. Regional perfusion was elevated in tumours but decreased in kidneys after carbogen and nicotinamide. After interferon administration, there was an increase in 5-[^{18}]FU retention in tumours, but no increase in uptake. Regional perfusion in tumour and normal tissue was unaltered by interferon. Retention of 2-[^{11}C]thymidine decreased in tumour in keeping with the results of conventional radiology, suggesting a pathological response, assessed *in vivo*, to chemotherapy.

Table of Contents

Abstract 2
Table of Contents 3
List of Figures 7
Declaration 11
Acknowledgments 12
Abbreviations 13
Chapter 1 Introduction 14
1.1 Positron Emission Tomography 14
1.2 Outline of Thesis 16
Chapter 2 Principles of PET Scanning and Data Modelling 17
2.1 Introduction 17
2.2 PET Image Acquisition 17
2.2.1 Basic Physics 17
2.2.2. PET Scan Detectors 20
2.2.3 Image Data Correction 22
2.2.4 Three-Dimensional PET 30
2.2.5 PET Image Reconstruction 30
2.2.6 PET Performance Characteristics 31
2.3 PET Calibration 35
2.4 Radioisotope Production 36
2.5 Radiochemistry of Radioactive Tracers 36
2.6 PET Modelling Techniques 38
2.6.1 Semi-Quantitative Modelling Methods 40
2.6.2 Quantitative Modelling Methods 42
2.7 Summary 52
Chapter 3 Molecular Imaging in Oncology 53
3.1 Introduction 53
3.2 Angiogenesis 54
3.2.1 Antiangiogenesis 55
3.2.2 Antivascular 56
3.3 Gene Expression 56
3.3.1 Direct Imaging 57
3.3.2 Indirect Imaging 57
3.4 Markers of Hypoxia 60
3.5 Receptor Detection and Drug Interactions 63
3.5.1 Oestrogen 63
3.5.2 Androgen 64
3.5.3 Neuroendocrine 65
3.5.4 Epidermal Growth Factor 65
3.5.5 Antibodies 66
3.6 Apoptosis 66

3.7 Other Applications of PET Imaging 67
3.7.1 Choline 67
3.7.2 Multi-Drug Resistance 68
3.8 Summary 69
Chapter 4 Methodology 70
4.1 Introduction 70
4.2 Ethics and ARSAC Approval 70
4.3 Production of Radionuclides 71
4.4 Radiopharmaceutical Production 72
4.4.1 5-[^{18}F]Fluorouracil 72
4.4.2 $H_2[^{15}O]$ and $C[^{15}O]_2$ 73
4.4.3 2-[^{11}C]thymidine 73
4.4.4 [^{11}C]HCO_3 74
4.5 Quality Control 74
4.6 Quality Assurance 74
4.7 Patient Recruitment and Preparation 75
4.8 PET scanners 76
4.8.1 ECAT 931 Scanner 76
4.8.2 ECAT HR$^+$ 962 Scanner 76
4.9 Tissue Acquisition Protocols 77
4.9.1 Carbogen and Nicotinamide Modulation Study 77
4.9.2 Interferon-α Modulation Study 78
4.9.3 2-[^{11}C]thymidine Study 80
4.10 Tissue Data Calibration and Reconstruction 81
4.10.1 ECAT 931 PET scanner 81
4.10.2 ECAT HR+ 962 PET scanner 82
4.11 Blood Data Acquisition 82
4.11.1 Metabolite Analysis of Discrete Blood Samples 85
4.11.2 5-[^{18}F]FU analysis 85
4.11.3 2-[^{11}C]thymidine metabolite analysis 85
4.11.4 Processing Blood Data 86
4.12 Analysis of PET Tissue Data 87
4.12.1 Tissue sampling and analysis 87
4.12.2 ROIs 88
4.13 Modelling Of Tissue Data 88
4.14 Modelling of Tissue and Blood Data 89
4.14.1 Tissue Perfusion 89
4.14.2 5-[^{18}F]FU Studies 89
4.14.3 2-[^{11}C]thymidine Study 90
4.15 Statistical Analysis 91
Chapter 5 PET Pharmacokinetics and 5-[^{18}F]fluorouracil 92
5.1 Introduction 92

5.2 5-Fluorouracil 92
5.2.1 Mechanism of Action 92
5.2.2 Plasma Pharmacokinetics 95
5.2.3 Catabolism and Excretion 95
5.2.4 5-FU and Use in Oncology 96
5.3 [^{18}F] Radiolabelled 5-FU and PET Imaging 97

Chapter 6 Carbogen and Nicotinamide Modulation of 5-FU 101
6.1 Introduction 101
6.2 Study Aims 103
6.3 Methods 103
6.3.1 Patient Selection 104
6.3.2 Study Design 104
6.3.3 Procedures 106
6.4 Data Analysis and Statistics 106
6.5 Results 107
6.5.1 Patient characteristics 107
6.5.2 Scan Details 109
6.5.3 Localisation of H_2[^{15}O] and 5-[^{18}F]FU in Tumour and Normal Tissue 110
6.5.4 Physiological results 111
6.5.5 Perfusion and Volume of Distribution (V_d) 113
6.5.6 Semi-quantitative Analysis 120
6.5.7 Spectral Analysis 129
6.5.8 Patlak Analysis 140
6.6 Discussion 142
6.7 Summary 150

Chapter 7 5-FU and Interferon 151
7.1 Introduction 151
7.2 Study Aims 152
7.2.1 Primary Aim 152
7.2.2 Secondary Aims 152
7.3 Methods 153
7.3.1 Patient Selection 153
7.3.2 Study Design 153
7.4 Procedures 154
7.5 Data Analysis and Statistics 154
7.6 Results 155
7.6.1 Patient Characteristics 155
7.6.2 Scan Details 157
7.6.3 5-[F^{18}]FU Pharmacokinetic Results 158
7.6.4 Semi-Quantitative Analysis 159
7.6.5 Spectral Analysis Results 163
7.6.6 Patlak Results 169

7.6.7 Tissue Perfusion and Volume of Distribution 170
7.7 Discussion 175
7.8 Summary 179
Chapter 8 2-[^{11}C]thymidine To Measure the Pharmacodynamic Endpoint of Anti-cancer Drugs 180
8.1 Introduction 180
8.2 Thymidine Background 181
8.3 Development of Thymidine in PET 182
8.4 Pre-Clinical Studies 184
8.5 Clinical Studies 186
8.6 Analysis of [^{11}C]thymidine images 187
8.7 2-[^{11}C]thymidine to Assess Pharmacodynamic End-Points 189
8.8 Study Aims 190
8.9 Methods 190
8.9.1 Patient Selection 190
8.9.2 Study Design 191
8.10 Procedures 191
8.11 Data Analysis 192
8.12 Results 194
8.12.1 Patient Characteristics 194
8.12.2 PET Scan Details 194
8.12.3 Conventional Radiology 195
8.12.4 Haematological Results 195
8.13 2-[^{11}C]thymidine Analysis 195
8.13.1 Semi-Quantitative Analysis 196
8.13.2 Spectral Analysis 199
8.14 Discussion 203
8.15 Summary 208
Appendix A 210
Appendix B 211
Awards and Publications 215
References 217

List of Figures

Figure 1: An example of radioactive decay using Carbon-11 19

Figure 2: Coincidence Event Detection and Sinogram Formation Coincidence Event Detection and Sinogram Formation. 22

Figure 3: Coincidence Events Detected During PET Scanning 26

Figure 4: Diagram Showing Attenuation Probabilities used in PET Scanning a) Attenuation for an internal source b) Attenuation for an external source 29

Figure 5: Parameters of Transverse Resolution 32

Figure 6: One-tissue compartment blood flow model 45

Figure 7: Graphical Representation of Radiotracer Transfer and Typical Patlak Plot 48

Figure 8: Diagram illustrating the paradigm of imaging gene expression with the PET reporter gene, HSV1-tk 59

Figure 9: (a): [^{18}F]MISO; (b): [^{18}F]FETA 61

Figure 10 (a): Oestrogen (b): 16α-[^{18}F] fluoro-17β-oestradiol (FES) ... 64

Figure 11: Radiosynthesis of 5-[^{18}F] fluorouracil 73

Figure 12: Anabolism of 5-FU 94

Figure 13: Study Design 105

Figure 14: CT and PET Images 110

Figure 15: Arterial pO_2 before and after Carbogen and Nicotinamide 111

Figure 16: Tumour Perfusion Before and After Carbogen and Nicotinamide 113

Figure 17: Tumour V_d Before and After Carbogen and Nicotinamide 114

Figure 18: Spleen Perfusion Before and After Carbogen and Nicotinamide 115

Figure 19: Spleen V_d Before and After Carbogen 116

Figure 20: Kidney Perfusion Before and After Carbogen and Nicotinamide 117

Figure 21: Kidney V_d Before and After Carbogen and Nicotinamide 117

Figure 22: Liver Perfusion Index Before and After Carbogen and Nicotinamide 118

Figure 23: Liver V_d Index Before and After Carbogen and Nicotinamide 118

Figure 24: Representative Tissue Activity Curves for (i) liver (ii) metastasis (iii) kidney and (iv) spleen 121

Figure 25: Tumour $SUV_{3.75mins}$ Before and After Carbogen and Nicotinamide.. 122

Figure 26: Spleen $SUV_{3.75mins}$ Before and After Carbogen and Nicotinamide.... 123

Figure 27: Kidney $SUV_{3.75mins}$ Before and After Nicotinamide 123

Figure 28: Liver $SUV_{3.75mins}$ Before and After Carbogen and Nicotinamide..... 124

Figure 29: Tumour AUC_{90mins} Before and After Carbogen and Nicotinamide ... 125

Figure 30: Spleen AUC_{90mins} Before and After Carbogen and Nicotinamide 125

Figure 31: Kidney AUC_{90mins} Before and After Carbogen and Nicotinamide.... 126

Figure 32: Liver AUC_{90mins} Before and After Carbogen and Nicotinamide 126

Figure 33: Correlation between perfusion and $SUV_{3.75min}$ in liver metastases (a) before and (b) after carbogen and nicotinamide 128

Figure 34: Correlation between perfusion and AUC_{90mins} in liver metastases (a) before and (b) after carbogen and nicotinamide 128

Figure 35: Results for Spectral Analysis Using Total Arterial Plasma Input 131

Figure 36: Tumour K_1 Before and After Carbogen and Nicotinamide Using Total Plasma Input..... 132

Figure 37: Tumour K_1 Before and After Carbogen and Nicotinamide Using Parent Plasma Input Function 132

Figure 38: Spleen K_1 Before and After Carbogen and Nicotinamide Using Total Plasma Input Function 133

Figure 39: Spleen K_I Before and After Carbogen and Nicotinamide Using Parent Plasma 133

Figure 40: Tumour FRF Before and After Carbogen and Nicotinamide Using Total Plasma Input Function 135

Figure 41: Tumour FRF Before and After Carbogen and Nicotinamide Using Parent Plasma Input Function 135

Figure 42: Spleen FRF Before and After Carbogen and Nicotinamide Using Total Parent Input Function 136

Figure 43: Spleen FRF Before and After Carbogen and Nicotinamide Using Parent Plasma Input Function 136

Figure 44: Tumour PS Before and After Carbogen and Nicotinamide Using Total Plasma Input Function 138

Figure 45: Tumour PS Before and After Carbogen and Nicotinamide Using Parent Plasma Input Function 138

Figure 46: Spleen PS Before and After Carbogen and Nicotinamide Using Total Plasma Input Function 139

Figure 47: Spleen PS Before and After Carbogen and Nicotinamide Using Parent Plasma Input Function 139

Figure 48: Tumour K_I Before and After Carbogen and Nicotinamide 141

Figure 49: Spleen K_I Before and After Carbogen and Nicotinamide 142

Figure 50: Typical Tissue Activity Curves for 5-[^{18}F]FU in (i) Tracer Dose and (ii) Full Dose Studies 159

Figure 51: Tracer Dose: Tumour AUC_{60mins} before and after Interferon 160

Figure 52: Full Dose: Tumour AUC_{60mins} Before and After Interferon 161

Figure 53: Tracer Dose: Tumour $SUV_{3.75mins}$ before and after Interferon 162

Figure 54: Full Dose: Tumour $SUV_{3.75mins}$ Before and After Interferon 162

Figure 55: Parent Plasma and Total Plasma Input Functions for (i) Tracer Dose and (ii) Full Dose Tracer Dose 5-[^{18}F]FU Studies 164

Figure 56: Tumour K_1 Before and After Interferon 170

Figure 57: Tumour Blood Flow Before and After Interferon 170

Figure 58: Tumour V_d Before and After Interferon 171

Figure 59: Spleen Perfusion Before and After Interferon-α 172

Figure 60: Spleen V_d Before and After Interferon-α 172

Figure 61: Liver Perfusion Index Before and After Interferon 173

Figure 62: Liver V_d Index Before and After Interferon 173

Figure 63: Kidney Perfusion Before and After Interferon 174

Figure 64: Kidney V_d Before and After Interferon 174

Figure 65: Diagram Showing Incorporation of Thymidine into DNA via Exogenous and Endogenous Pathways 182

Figure 66: Diagram showing catabolism of [^{11}C]thymidine Labelled in 5-Methyl- and 2- Carbonyl Positions, to Show Different Metabolite Profile 183

Figure 67: Coronal View of Thorax Using 2-[^{11}C]thymidine Imaging 196

Figure 68: Tissue Radioactivity Versus Time Curves for (a) Tumour, (b) Normal Lung and (c) Bone Marrow 197

Figure 69: Spectral Analysis Curve for 2-[^{11}C]thymidine 200

Declaration

I declare that this submission is my own work. It contains no material written, submitted or published by any other person except where due acknowledgement is made.

Nishi Gupta

Acknowledgments

The work undertaken for this thesis was performed in the MRC Cyclotron Building (Hammersmith Imanet Limited) based at the Hammersmith Hospital, between 2000 and 2004. I would like to express my gratitude to members of staff here who have assisted me during this period.

In particular I would like to thank my two supervisors, Professor Pat Price and Professor Eric Aboagye. Professor Price has always provided constructive comments and insight and has been enthusiastic even in times of seeming adversity. Professor Aboagye has been an inspirational teacher displaying great patience whilst guiding me through my years of research. I am indebted to Cancer Research UK and the Medical Research Council who provided funding for this research project.

PET is a multi-disciplinary speciality involving many individuals whom I would like to thank directly for contributing to this thesis. Professor Vincent Cunningham, has written much of the software used in this thesis; Dr Rainer Heinz for help with data modelling; Dr Terry Spinks and his team for data acquisition, reconstruction and archiving; Dr S Luthra and her team for the synthesis of radiotracers and particularly Hanna Wilson for her perseverance with 2-[^{11}C]thymidine; the late Keith Poole and his team for quality control of the radiotracers; Dr Safiye Osman and her team for blood data analysis; Andy Blythe and his team of radiographers, Hope McDevitt, Stella Ahier and Jo Holmes and Lynn Maslen for her organisational skills. I would like to extend my thanks to the staff and participating patients from the Clinical Oncology Departments at Charing Cross and Hammersmith hospitals, especially Sister Cathy Purnell for her skills in patient care and recruitment.

Dr Paula Wells performed the preliminary studies with 2-[^{11}C]thymidine respectively and Dr Robert Harte was responsible for the acquisition of some of the data analysed in the 5-[^{18}F]fluorouracil studies and I would like to acknowledge their contribution. I would also like to thank my other colleagues, Drs Saleem Azeem, Laura Kenny and George Laking who all helped make research such a rewarding and enjoyable experience.

Finally I would like to thank my family: my parents, Krishan and Shashi for their constant support; my husband Hugh, for his tolerance, technical ability and humour; and Sarika, for her arrival in the middle, and who has provided unlimited joy and laughter since.

Abbreviations

5-FU; 5-Fluorouracil
5-[^{18}F]FU; 5-[^{18}F]fluorouracil
AUC; Area under curve
BAIB; β- aminoisobutyrate
BUIB; β-ureiodoisobutyric acid
CH_2-THF; 5,10-methyltetrahydrofolate
C/N; carbogen and nicotinamide
dATP; deoxyadenosine triphosphate
dGTP; deoxyguanidine triphosphate
dTMP; deoxythymidine monophosphate
dTTP; deoxyuridine triphosphate
dUMP; deoxyuridine monophosphate
DD; dihydrothymine dehydrogenase;
DPD; dihydropyrimidine dehydrogenase
FBAL; α-fluoro-β-alanine
F-DHU; 5-fluorodihydrouracil
FRF; fractional retention of 2-[^{11}C]thymidine
FRT; fractional retention of 5-[^{18}F]fluorouracil
FUTP; 5-fluorouridine-5'-triphosphate
HPLC; high performance liquid chromatography
IFN-α; Interferon- α
PS: Permeability surface area product
SUV; Standardised uptake value
TP: thymidine phosphorylase
TMP; thymidine monophosphate
TS; thymidylate synthase
V_d; Volume of distribution

Chapter 1 Introduction

The widespread nature of cancer represents a major worldwide issue responsible for a third of all deaths in the developed world with an increasing number in the developing world, despite a massive investment of time and money by governments, charities, scientists, healthcare professionals and drug industries.

Recent advances in molecular science have led to an increase in the understanding and elucidation of tumour biology, particularly with regard to the molecular basis of cell cycle control and proliferation, with cancer now viewed as a series of biological processes rather than a single disease entity. New insights into the genetic and molecular basis of cancer development have resulted in a fundamental re-ordering of drug development and therapeutic approaches from empirical drug observations, towards rational drug discovery based on molecular sites of action. Treatment strategies have therefore altered to assimilate the evolving identification of abnormal pathways in cancer biology. This has required a paradigm shift in the demands on imaging, moving from solely providing rigid structural and anatomical details, to providing *in vivo* methods to detect and characterise cellular and biochemical changes in the cancer cell itself.

Just as molecular science has advanced, simultaneous progress has been made in nuclear imaging technology, particularly in positron emission tomography and magnetic resonance imaging and spectroscopy. This has been based upon improved electronics, greater computing powers, better sensitivity resolution and new tracers for key molecules that facilitate cancer growth and development. These imaging technologies now allow real-time, non-invasive assessment of physiological, biochemical, biological, pathological and pharmacological processes *in vivo*, in man, which was not previously available.

1.1 Positron Emission Tomography

Positron emission tomography (PET) is a quantitative and dynamic imaging technique with high spatial (clinical scanners of 4-7mm; animal scanners of 1mm)

and temporal (5-10 s) resolution. PET has unrivalled sensitivity and is able to provide information down the sub-picomolar level and it is therefore possible to measure the distribution of tracer amounts of a radiolabelled compound in a subject, without perturbing the biological or physiological process under examination. Furthermore, there are many naturally occurring positron emitting isotopes for elements which are found in a large number of compounds, so there are an infinite number of radiolabelled tracers that are potentially available providing radiochemical synthesis and the other pre-requisites for a clinical PET radiotracer are achievable. Developments in instrumentation, analysis and methodology have enabled PET to be used increasingly for quantitative measurements.

PET encompasses complex technology and requires an expert multi-disciplinary approach involving experts from the fields of chemistry, pharmacology, physics, computer science, radiology, oncology and molecular biology to operate successfully. However, for the reasons described above, PET provides an ideal imaging technique in oncology.

A major area that can benefit from PET imaging is that of drug development. At the present time this is an extremely slow process taking many years to progress from drug conception to clinical trials and costing several millions of pounds. In addition, of the thousands of promising new drugs discovered, only a few eventually enter routine clinical practice. PET can facilitate drug development by identification of relevant avenues for targeted drug treatment in conjunction with molecular and genetic findings. PET can also aid the elucidation of the pharmacokinetic profile of a novel or modulated therapy using not only plasma samples, but by direct tissue analysis and with PET animal studies to facilitate this process. Finally, the pharmacodynamic endpoint to assess drug effect can potentially be measured in tumour and also normal tissue and at an earlier time point than with conventional practices.

Apart from FDG-PET, the use of other radiotracers in PET has predominantly been as research tools. The purpose of this thesis has been to perform clinical studies using two different radiotracers, 5-[^{18}F]fluorouracil and 2-[^{11}C]thymidine,

to assess PET derived pharmacokinetic and pharmacodynamic parameters respectively, and to establish the contribution that PET can add to drug development.

1.2 Outline of Thesis

In this thesis, the pharmacokinetics of the commonly used anti-metabolite drug, 5-Fluororacil, will be studied alone and in combination with biomodulating agents. The pharmacodynamic endpoint of anti-cancer drugs will be examined using 2-[^{11}C]thymidine, in tumour and normal tissue.

The thesis begins with a chapter (Chapter 2) outlining PET and looks in detail at image acquisition and processing and the methods of semi-quantitative and quantitative analysis of data. The next chapter (Chapter 3) reviews the potential role of PET in molecular imaging in oncology with particular emphasis on the use of newer, investigational, radiotracers in preliminary studies in man and animals.

Subsequent chapters (Chapters 4, 5 and 8) provide information on the methodology of the studies undertaken in this thesis and on the current methods and limitations of pharmacokinetic and pharmacodynamic assessment in man, with the potential of radiolabelled 5-FU (5-[^{18}F]FU) and radiolabelled thymidine (2-[^{11}C]thymidine) explored in each field respectively.

In Chapters 6 and 7 the effect of modulation of 5-[^{18}F]FU with carbogen and nicotinamide, and interferon, will be reported respectively, and in Chapter 8 the use of 2-[^{11}C]thymidine in PET scanning to measure disease response to chemotherapy in comparison to conventional imaging will be assessed.

Chapter 2 Principles of PET Scanning and Data Modelling

2.1 Introduction

PET scanning falls within a specialised category of nuclear imaging. Nuclear imaging methods are based on the external detection of nuclear radiation emitted from a radiolabelled compound introduced into the body either intravenously or via inhalation. The isotopes used to label these compounds are unstable and decay by emitting radiation to achieve a stable non-radioactive state. The radiolabelled compound is an analogue of a biochemical of interest that behaves identically *in vivo* to its counterpart without perturbing the pharmaceutical, biological or physiological properties of the system under observation, allowing imaging of the underlying process. It is the type of radiation emission that characterises PET imaging namely, positrons, and this is dependent on the configuration of the nucleus of the radiotracer used in PET scanning, which must disintegrate by the production of positrons.

PET imaging is a complex, multidisciplinary technique. In this chapter the fundamental requirements of PET scanning, radiotracer production, image acquisition and processing will be discussed. The derivation of quantitative data to describe the fate of radiolabelled compounds in tissue is one of the most important aspects of PET and the models utilised in this process will be fully outlined as well.

2.2 PET Image Acquisition

2.2.1 Basic Physics

P.Dirac, a theoretical physicist, first postulated the existence of positive electrons (positrons) on the basis of the equations of quantum mechanics and Einstein's theory of relativity (Dirac, 1930). CD Anderson, a couple of years later, proved their existence by observing experimentally that cosmic rays include particles with the mass of electrons but which move along a magnetic path indicating that

they have a positive charge (Anderson, 1932). He called these particles positrons, or positive electrons.

The PET scanner does not detect positrons directly, but uses the important feature of positron annihilation to determine their spatial location. Proton rich isotopes reduce the excessive positive charge of their nucleus by either electron capture, or positron emission. In positron emission, the extra proton (p) is converted to a neutron (n), with the release of a positron (p+) and neutrino (v), leaving a stable daughter nuclide that has the same atomic number as the parent (A) but with a reduction in proton number (Z) by one.

The emitted positron has an initial kinetic energy characteristic of the radioisotope, with the remaining energy removed by the neutrino. The positron travels a few mms in tissue before losing its kinetic energy through collisions with neighbouring electrons in surrounding tissue (see Table 2.1).

Table 2.1: Characteristics of Positron Emitters Used in this MD

Positron Emitter	Maximum positron energy (MeV)	Half-life (min)	Maximum range in soft tissue (mm)	Mean range in soft tissue (mm)
^{18}F	0.63	109.8	2.6	0.6
^{11}C	0.96	20.3	4.2	1.2
^{15}O	1.74	2.04	8.4	2.9

When the positron loses all or most of its energy it combines with an electron to form a positronium. A positronium has a short half-life, resulting in the annihilation of the positron/electron pair, with all the mass being converted into electromagnetic radiation. In order to conserve energy and linear momentum, the electromagnetic radiation appears in the form of two photons of equal energy of 511 keV (equal to the resting energy of the electron and positron) and which are always in opposite directions at 180° (see Figure 1). The emitted photons can be recorded by two opposing coincidence detectors, which transmit a signal if, within a narrow time frame of nanoseconds, both are stimulated simultaneously. Such

detection of photons enables localisation of the source of radiation without the need for physical collimation, and is called 'electronic collimation'. Electronic collimation is more efficient than absorption collimation used for gamma ray photons in single photon emission computerised tomography (SPECT), another form of nuclear imaging, as the latter relies on exclusion, with many photons emitted by the patient absorbed and not contributing to the final image. Electronic collimation can utilize potentially all of the photons emitted by the radiotracer provided that the source of the photons is completely surrounded by detectors. This forms the basis of PET imaging and confers one advantage of it over other forms of nuclear imaging. Furthermore, the sensitivity of the coincidence counting system within the volume subtended by the two detectors varies only slightly, with a region between the two detectors where the sensitivity is almost uniform. In contrast, absorption collimators exhibit greatly varying sensitivity.

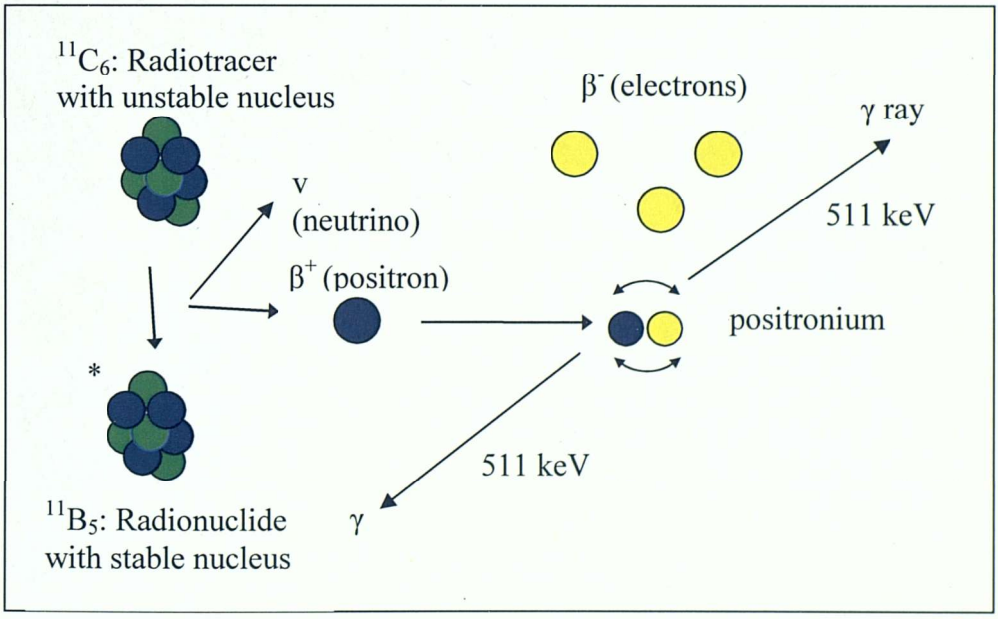


Figure 1: An example of radioactive decay using Carbon-11

Carbon-11 ($[^{11}C]_6$ has an unstable nucleus with an excess of protons (green) of which there are 6 in total. The unstable nucleus decays naturally by emitting a positron (blue) and neutrino (ν), which has negligible energy and mass, to leave the stable nucleus, boron ($^{11}B_5$). The asterix *, denotes the proton which has changed into a neutron. The positron travels a short distance in tissue before colliding with a surrounding electron (yellow) and forms a positronium. Almost instantaneously, the positronium disintegrates, forming two gamma rays (γ) that are simultaneously emitted at approximately 180^0 to one another.

2.2.2. PET Scan Detectors

The detection apparatus in a typical PET scanner consists of multiple rings of scintillation detector blocks that are composed of inorganic crystals such as bismuth germinate ($Bi_4Ge_3O_{12}$ or BGO) which are arranged around the area to be imaged in the patient. Each block is divided into arrays of detector elements (usually 8 x 8 or 8 x 4) with detector elements having a specific size according to the PET scanner type. The detector blocks are in contact with a number of photomultiplier tubes (PMT), typically four per detector. Measurement of annihilation radiation is based on the fact that the photon to be detected transfers its energy by accelerating electrons within the BGO detector block. As BGO has a high density and atomic number, this ensures with a high probability that such an exchange of energy takes place. The photons thus absorbed by the BGO crystal converts the energy into flashes of light or scintillations, which, after amplification are then converted into a measurable electrical signal by the PMT, and are then processed by the computer system. BGO generates approximately 2 500 light photons per 511 keV, and has a short decay time of around 300 nanoseconds so that high counting rates can be counted. The detector block is fabricated in such a way that the amount of light collected by each PMT varies uniquely depending on the crystal in which the scintillation occurred (Dahlbom *et al.*, 1988). Identification of the detector element where the photon interacted is achieved by decoding integrals of the PMT outputs to yield the exact position of every scintillation. The sum of the integrated PMT outputs is proportional to the energy deposited in the crystal.

The signals from the individual detectors on opposite sides of a ring are fed into separate amplifier and energy discrimination circuits. If both these circuits produce a signal within a very short (around 10 nanoseconds) timing window (the coincidence timing window) a 'coincidence event' is recorded. As the annihilation photons are propagated in opposite directions, the origin of the annihilation event is assumed to have occurred along the line between detectors known as the line of response (LOR). The intersecting coincidence lines formed between the detectors facilitate electronic collimation by dual photon coincidence counting.

During a PET scan several million coincidence events are recorded. Each detector is in a circular array and can form a fan of coincidences with any number of detectors. The location and direction of any given coincidence event is unique and all the coincidence lines form the data set for the final PET image. Acquired coincidences are stored as two-dimensional matrices, in which the horizontal direction describes the offset (p) from the centre of the field of view (FOV), and the vertical direction describes the projection angle. This two dimensional matrix is called a sinogram, and is a convenient way of storing the data prior to reconstruction (see Fig 2).

Before reconstruction of the image can occur, corrections must be made for detector inefficiency of response and attenuation of the photons in the body. Not all coincidence events are true or valid such as random coincidences, and not all coincidences are detected due to scatter and must be taken into consideration. This is outlined in the next section.

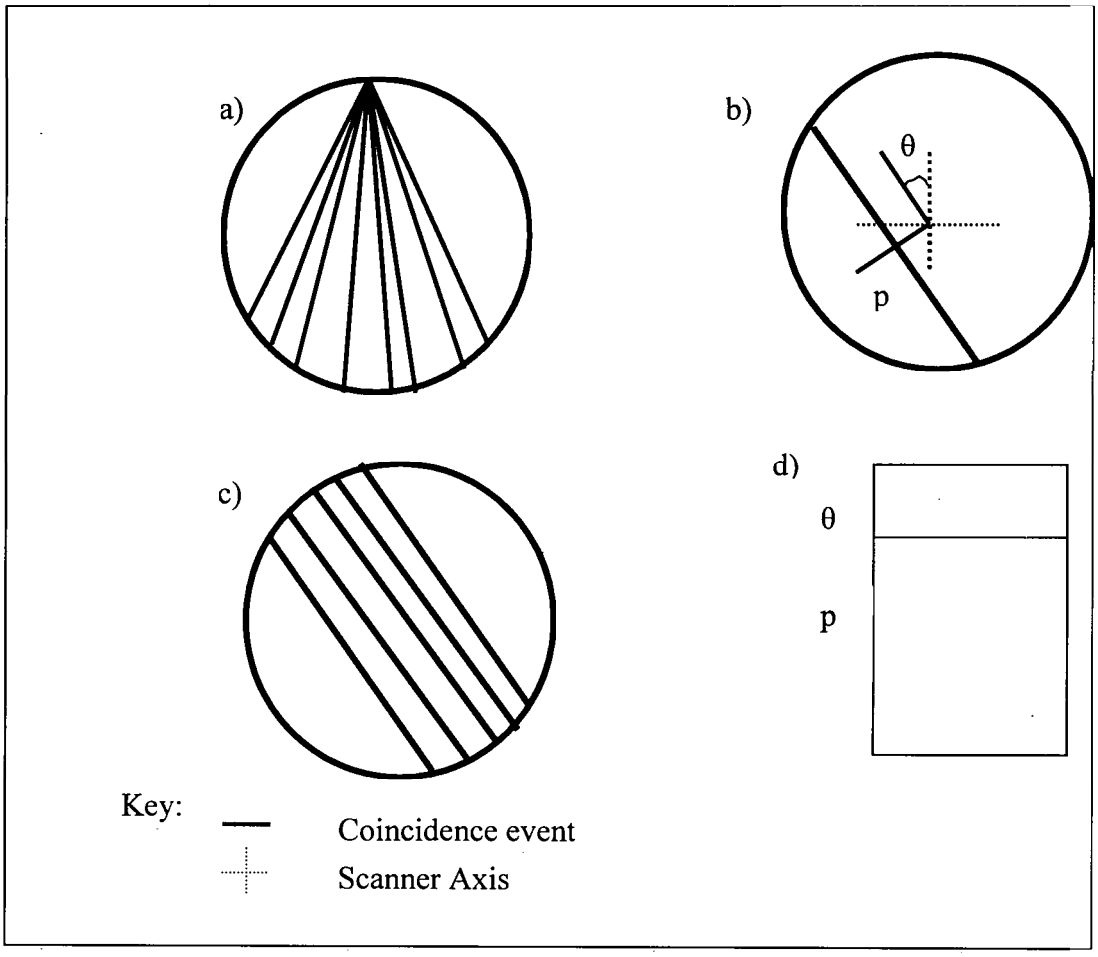


Figure 2: Coincidence Event Detection and Sinogram Formation Coincidence Event Detection and Sinogram Formation.

a) A detector can be in coincidence with any number of opposing detectors, each of which has (b) a unique offset p, and angle θ, from the centre of the scanner. c) Parallel coincidence lines can be separated into a set, (d) and re-arranged into a 2-dimensional sinogram.

2.2.3 Image Data Correction

2.2.3.1 Normalisation

Numerous coincidence events are detected during the course of a PET scan. However, due to geometrical arrangements of the detectors and differences in energy discrimination there may be significant variation in the efficiency of detector elements in the system, for example, the detectors at the edge of the BGO block may be less effective than those at the centre. If this is not corrected for, artefacts may be present in the final image. A correction factor is therefore applied

to normalise the data. This is achieved by exposing all detectors to a uniform flux of photons to measure the inherent variations. The data is subsequently adjusted to account for this.

2.2.3.2 Dead Time Correction

The time required to process a single event limits the counting rate of a PET scanner. Dead time refers to the period of time in which the detector or electronic circuitry are unable to recognize an incoming event as the apparatus is still processing the previous one, and is therefore proportional to the incoming photons approaching the detector. Dead time is the dominant effect that limits the dose of injected activity (Ollinger *et al.*, 1997). For scanners in which the number of photomultiplier tubes is greater than one, electronic circuitry is needed to determine which crystal detected the photon, and this processing circuitry can contribute a major source of dead time. With high count rates, mispositioning of individual events can occur with more events assigned to detector elements near the centre of the crystal array rather than at the periphery. This can result in loss of in-plane resolution by 1 – 2 mm.

Quantification of the PET image without correction for dead time would underestimate actual activity. Correction of dead time can be obtained by scanning a phantom containing short-lived positron emitter e.g. [^{11}C] at serial times as the activity decays. Dead time loss is extrapolated from low activity measurements to estimate the true *plus* scatter (see next section) that would have been obtained without the losses. The activity level where the percent dead time loss is 50% is calculated from the extrapolated and measured counts. Most commercial scanners provide automatic dead time correction.

2.2.3.3 Non-Valid Coincidence Correction

A true coincidence event is one where the detectors record an event from a unique positron annihilation that occurred along the line between two activated detectors. However, PET scanners also detect other types of coincidences that arise from unrelated annihilation photons, which degrade the quality of the 'true' image

(Figure 3a). Non-valid coincidences fall into three categories and require different correction strategies:

(i) Multiple coincidences

This occurs if two or more photons are recorded during the coincidence window resulting from more than one positron annihilation. It therefore becomes ambiguous where the line of response should be positioned (Figure 3b). Multiple coincidences, which are easily distinguished from unique coincidences, are usually discarded even though two may have represented a valid coincidence.

(ii) Random coincidences

As there are a large number of scattered photons and a relatively small angle subtended by the detector ring, it is apparent that only one photon will be detected for some annihilation events, which are known as singles. Random or accidental coincidences arise when two, unrelated single events from separate annihilations are detected within the same coincidence timing window and registered as a coincidence (Figure 3c). A coincidence window is necessary because even though two detectors should be stimulated simultaneously by a true annihilation event, limitations of the scintillation detectors and processing circuitry requires that coincidence events have to be accepted within a certain finite time interval, as mentioned. Random coincidences do not contain any spatial information about activity distribution and contribute to a smooth 'background' in the image, and therefore need to be corrected for.

Random coincidences can be corrected for by two methods. In the first way, direct measurement is made by delayed coincidence. This employs a second coincidence circuit where one circuit is delayed by several times the length of the coincidence window so that only random coincidences are measured. The second method makes use of the relationship that exists between the random coincidence rate (R) and is expressed by:

$$R = 2\pi \times (S_1 \times S_2)$$

where S_1 and S_2 are the single counting rates for each detector, and π is the coincidence window. In both methods, the random counting is subtracted from the measured coincidence data prior to image reconstruction.

As can be seen from the equation, random coincidences can be reduced by decreasing the coincidence window interval if faster detectors and electronics are used, though this still results in a sufficient number of random counts to warrant correction. However, BGO detectors require at least a 10-15 ns timing window due to variations in the rise-time of the crystal light output.

As the incident counting rate for singles is proportional to the amount of injected isotope, the random coincidence rate increases as the square of the amount of isotope in the field of view (when the detectors are not saturated). This, and detector dead time, imposes an upper limit on injected dose activity in some studies.

(iii) Scattered Coincidence Events

Compton interaction describes the predominant exchange between photons and matter. If an annihilation photon interacts with an electron in the surrounding tissue, the photon will not only incur some energy loss, but will also be deflected from their original path. When both photons are eventually detected, the LOR assigned to it will not represent the true LOR that would have occurred if the photon had not been diverted, and the coincidence event is said to be 'mispositioned'. Scatter coincidences originate from activity both inside and outside the coincidence FOV and contributes around 15% to the measured coincidences. The inclusion of scattered events in the projection data does not significantly affect the spatial resolution of the reconstructed image but lessens the contrast by adding a structureless background to the image and causes inaccuracies in quantification. Theoretically, as these scattered photons lose energy after their collisions, they should be distinct from unscattered photons by energy discrimination. However, the PET detectors actually have poor energy resolution and can only distinguish photons having undergone appreciable energy loss after large-angle scatter events.

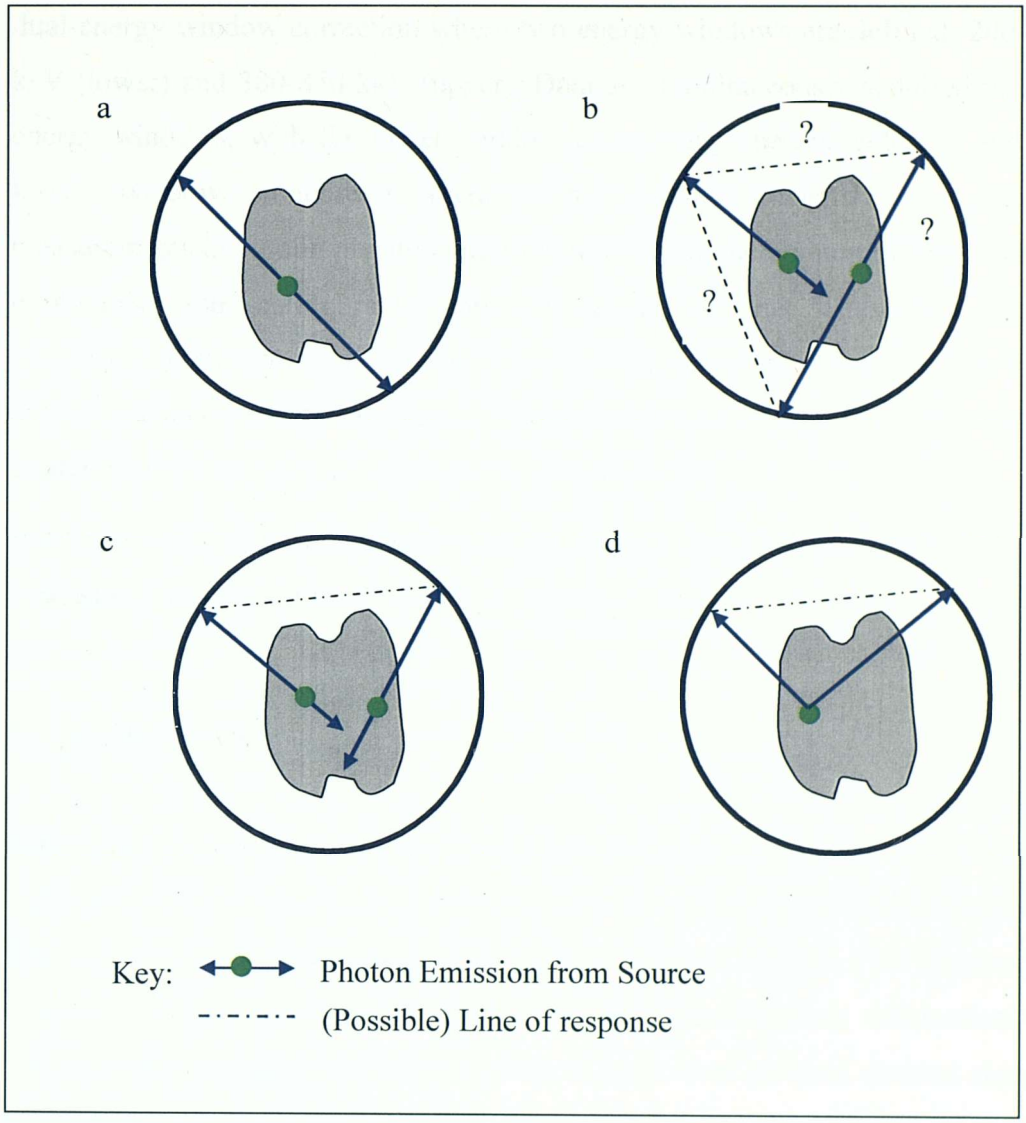


Figure 3: Coincidence Events Detected During PET Scanning

(a) True coincidence (b) Multiple coincidence (c) Random or accidental coincidence (d) Scattered coincidence

Scattered events can be reduced by the inclusion of septa between the ring detectors and by using shields at the end of the scanner to impede scattered coincidences from other parts of the body. Another strategy to diminish scattered events is to decrease the solid angle for detection of coincidence events as the number of scattered events produced is related to this angle. However, this method will make the sensitivity of the scanner worse.

Scatter events must be removed in order to derive quantitative data from the PET

scan. Several methods are available to correct for scatter. One method employs a dual-energy window correction where two energy windows are defined: 200-380 keV (lower) and 380-850 keV (upper). Data are simultaneously acquired in both energy windows, with the upper window comprising true coincidences and the lower window containing predominantly scatter events. Line source measurements in air and phantom are used to estimate the amount of scatter in the photo peak and scaling factors are calculated from this. These are used to calculate a scatter sinogram, which is subtracted from the photo peak sinogram to obtain a scatter corrected sonogram (Grootoonk *et al.*, 1992). With this method scatter events are reduced to within 6% of true values.

Whilst the dual-window method produces better out of field scatter correction, it is sensitive to temperature fluctuations which can affect crystal efficiency.

2.2.3.4 Attenuation

Attenuation occurs when the photon emitted from the radioisotope interacts with the object by photoelectric absorption or are scattered out of the field of view by Compton scatter. Whilst attenuation is less for PET than SPECT, PET requires the detection of two photons emerging from the object without attenuation for imaging purposes. In the brain, only 20% of coincident photons emitted along a line through the centre reach the PET detector and in the chest around 80 to 90% of photons are scattered or absorbed by the object (Daube-Witherspoon, 1995).

A unique feature of PET is that for a given coincidence line, the probability of photon attenuation is the same from any source, independent of its location along the line joining the two detectors. This is true even when the source lies outside the object which facilitates attenuation correction using an external transmission source. This concept can be explained by considering a point source situated at x cm, within the boundary of a cylinder with diameter, D and μ representing the linear attenuation coefficient of the material of the cylinder (Figure 4). The proportion of emitted photons that reach the detector closest to the source at point a, is $e^{-\mu x}$ and those reaching the detector furthest away, is $e^{-\mu (d-x)}$ (Figure 4a). If the

number of detected coincidences is N (without an object in the field of view), and the initial count rate is N_o, then:

$$N = N_o[e^{-\mu x} \times e^{-\mu (d-x)}]$$

$$= N_o e^{-\mu d}$$

This demonstrates that the probability of coincidence detection is independent of the source depth, x cm. If the source is external to the object at point b, then the probability terms for the nearest and furthest detectors are e^o and $e^{-\mu d}$, respectively (Figure 4 b). In this situation, the number of detected coincidences is given by:

$$N = N_o[e^o \times e^{-\mu d}]$$

$$= N_o e^{-\mu d}$$

This is the same as that obtained for the internal source, as shown in the equation above.

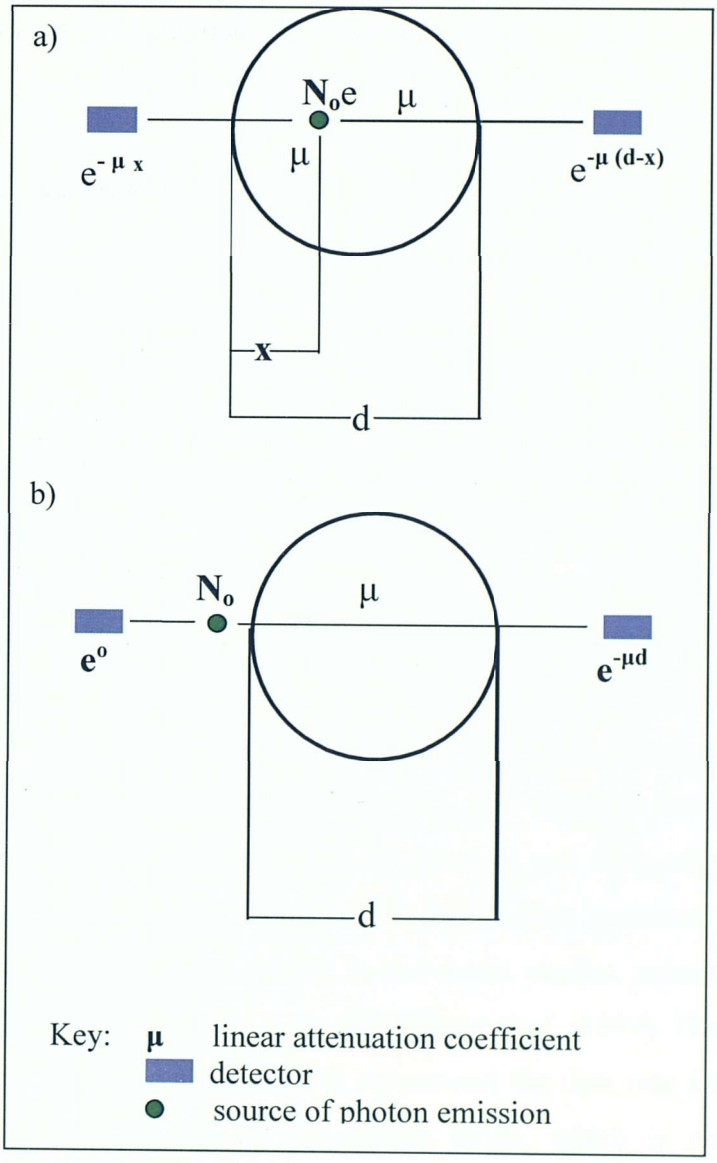


Figure 4: Diagram Showing Attenuation Probabilities used in PET Scanning a) Attenuation for an internal source b) Attenuation for an external source

Attenuation correction is therefore relatively straightforward. A scan using an external source is obtained with the patient in the scanner (attenuated transmission scan) and another, unattenuated scan using the same external source is taken when the scanner is empty (blank scan). The count rate from the attenuated transmission scan is compared to the blank scan to give a measure of attenuation which is used to correct the PET data. A transmission scan is usually performed prior to the PET

tracer scan. The transmission source contains a long-lived positron emitter such as germanium-68 (^{68}Ge) which has a half-life of 275 days. ^{68}Ge is housed in one or more retractable rods that rotate around the patient to measure the transmission count rate from all possible lines of response.

2.2.4 Three-Dimensional PET

Most modern PET scanners have the capability of providing information about the 3-D distribution of radioactivity in an object. The difference between 2D and 3D images lies in data acquisition and reconstruction. In 2D scans, lead or tungsten septa are normally used to separate adjacent imaging planes. These inter-ring septa were originally designed to reduce the registration of unwanted random and scatter coincidences. In 2-D mode, data are acquired as a number of contiguous slices, with contributions for each slice arising from within an individual or closely associated ring. However, whilst diminishing the number of invalid coincidences, this method also removes many true coincidences and increases statistical noise (see next section). In 3D PET, the septa are retracted allowing coincidences between all possible pairs of detectors and increasing the effective sensitivity by a factor of eight (Spinks *et al.*, 1992). This increased efficiency can be used to improve the image quality in low count studies, reduce the radiation dose administered and reduce scan times (Ollinger *et al.*, 1997). The development and availability of image algorithms to reconstruct the data into a 3D image has allowed exploitation of the 3D acquisition mode, which is now frequently employed particularly in neuro-imaging.

One disadvantage of 3D imaging is the significant increase in scatter coincidences recorded. Of all coincidences measured approximately 45% are due to scatter in the 3-D mode compared to 15% in 2-D. Despite this, 3-D PET offers great potential in nuclear imaging.

2.2.5 PET Image Reconstruction

The goal of image reconstruction is to recover the regional tissue concentrations of radiotracer measured during the PET scan. Raw PET data consists of a number of views (or projections) obtained from around the patient which consists of the sum of activity along a LOR but gives no information about the actual distribution and depth in the patient. There are many methods of image reconstruction with all of them involving back projection of the views across the FOV (Kak *et al.*, 1988), a technique utilised routinely in CT and SPECT scans as well. The image formation process conventionally divides the 'image space' into a matrix of square boxes called pixels, and puts counts in each pixel that are proportional to the counts from a particular LOR and places them in an area of overlap of the LOR and pixel. The data is back projected equally across the image grid for all angles subtended by each detector. The back-projected profiles will intersect for each projection at the position of the source of activity, but the image will be of a poor representation of the original because of the background generated by this procedure. Furthermore, back projection has the effect of amplifying the intensity of signal in large structures with low spatial frequencies.

This can be improved by the use of spatial filters which aims to suppress these amplifications and restore the true distribution. The Fournier transform is one such technique which subjects the data profile and data to a filter to weight each component in proportion to its own frequency so that increased weight is given to small structures that have high frequency. Problems associated with this technique include an increase in statistical uncertainty and noise in the projection data (Ollinger *et al.*, 1997). Filtering causes each pixel in the image to be associated with every other pixel, resulting in correlation of noise between pixels (Alpert *et al.*, 1982). After data filtering, an inverse transform is performed to produce a quantitative image. An alternative method of reconstruction so called iterative, enables a more superior form of image reconstruction in which the image data is successively reconstructed with different algorithms to be consistent with the projection data.

2.2.6 PET Performance Characteristics

2.2.6.1 Spatial Resolution

There are several main characteristics that determine the spatial resolution of PET images which include the physical size and shape of the detector element, positron movement in the tissue before annihilation and deviation from the strict collinear pathway that affect some emitted photons.

Detector dimension is fundamental in determining the spatial resolution of the PET image. In-plane spatial (transverse) resolution is characterised by two values of the spread of a point source in the image: radial (width) resolution, a line of spread from a point source in the directions along a line from the centre of the gantry to the source position, and tangential resolution, which is perpendicular to that line. Both these resolutions give a count profile curve that is approximately Gaussian in shape (see Figure 5). The width of this curve at one-half maximum value (the full width at half-maximum [FWHM]) is the most commonly used parameter to describe spatial resolution. FWHM is the minimum separation required for two points to be resolved and is primarily limited by individual detector size. The major advances in spatial resolution in the last few years have been due to the reduction in detector size.

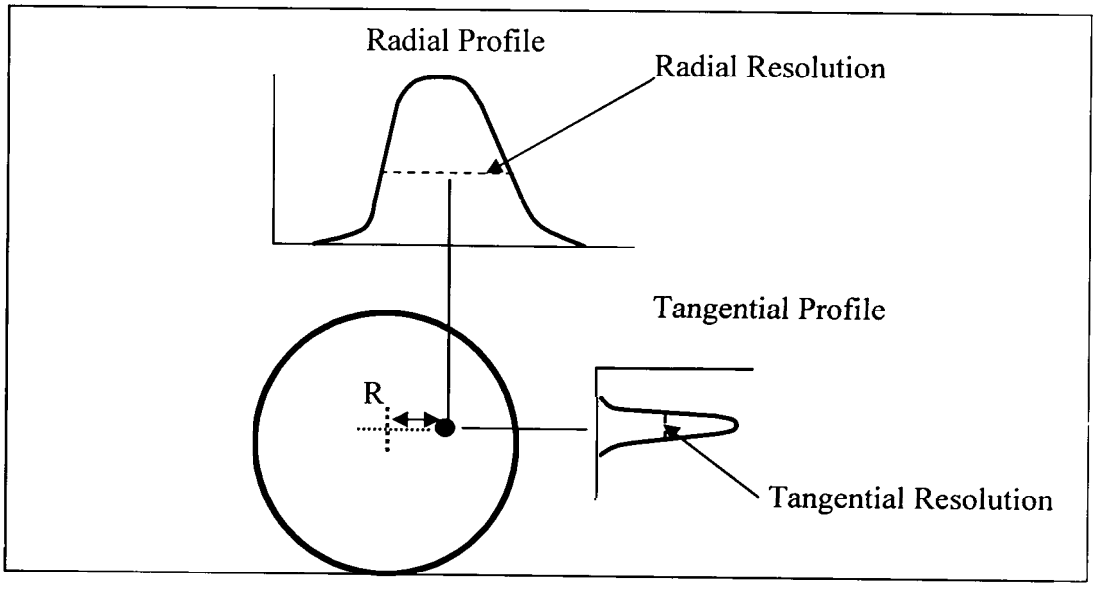


Figure 5: Parameters of Transverse Resolution

Transverse resolution is characterised by two values of the spread of a point or line source in the image. The radial resolution is the width of a profile from the centre of the gantry to the source

position at distance, R. The tangential resolution is the width of the profile perpendicular to the radial direction (Daube-Witherspoon, 1995) .

Positron energy imposes another restriction on spatial resolution. When a positron is emitted from the radioisotope, it has a range of energies and travels a finite distance before combining with an electron. A positron released form ^{18}F isotope may travel 2-3mm prior to annihilation (Cho *et al.*, 1975). If the positron travels in the direction of the coincidence detector no error is introduced. However, the error is maximised when the positron travels in a direction orthogonal to a line joining the two detectors. On average, the error introduced is 0.2mm for ^{18}F, for example (Phelps *et al.*, 1975) (Table 2.1).

Another factor that limits spatial resolution is non-colinearity of annihilation photons. This refers to a property of the positron- electron pair which does not come to complete rest before annihilation. In this situation the positron-electron particle still has residual momentum when it annihilates. As momentum has to be conserved the emitted annihilation photons deviate from the 180^{o} degree pathway. This introduces a small error (< 0.5%) in positioning of the annihilation event. The impact of this error is dependent on the diameter of the detector ring and not on photon energy. For a detector ring diameter of 80cm, the limit imposed by theses effects is less than 2mm, and for a diameter of 20cm, is less than 1mm.

2.2.6.2 Counting Efficiency

This refers to the proportion of emitted photons that are detected and contribute to the final image. The higher the counting efficiency the lower the noise level in the images. The counting efficiency of a 3-D mode PET scanner is higher than for 2-D PET mode. However, both compare favourably to a single head SPECT scanner with PET conferring a 30-fold advantage in efficiency over SPECT.

2.2.6.3 Count Rate Performance

This describes the response of the detector apparatus to increasing levels of radioactivity within the field of view. In an ideal situation, the count rate would increase linearly in response to increased activity. However, as discussed, a point is reached where the detector system is unable to process all events due to the rapidity of incoming events. As a result, the count rate response becomes non-linear. Corrections are available in commercial scanners to account for dead-time loss.

2.2.6.4 Statistical Noise

Statistical noise in PET scans is a result of the limited number of counts in each pixel and the random nature of radioactive decay. In general, the greater the number of image counts acquired, the better the quality and quantitative precision of the data. The radioactive decay process obeys the Poisson probability of distribution, where the standard deviation (SD) is defined as the square root of the mean number of counts (N):

$$SD = \sqrt{N}$$

Mean number of counts represents signal and SD is used as a measure of noise. For total counts of 10 000, 1 000 and 100, noise is 1%, 3% and 10% respectively, thereby demonstrating that noise increases as the number of counts decreases.

Statistical noise is also affected by the reconstruction process, which correlates noise between pixels (Alpert *et al.*, 1982) and corrections made for random, multiple and scatter coincidences, attenuation and detector non-uniformities and the size and location of the region of interest (Carson *et al.*, 1993).

The number of image counts detected is dependent on injected radiotracer activity, camera sensitivity and scan duration. The amount of radioactivity injected in clinical studies is limited by the requirement to limit radioactive exposure to the patient and by the characteristics of the scanner. Increasing injected radioactive dose results in more dead-time losses and random coincidences and camera sensitivity is influenced by detector counting efficiency as discussed. Scan duration takes into account the biological and physical half-

lives of the radiotracer and consideration must be made of patient discomfort and potential motion errors with longer scanning schedules.

2.2.6.5 Noise Equivalent Count Rate

The noise equivalent rate (NEC) is a parameter calculated to determine the effect of combining the degrading effects of dead-time loss, random and scatter coincidences on image quality:

$$NEC = \frac{T}{1 + \frac{S}{T} + \frac{kR}{T}}$$

where T, S and R are true, scattered and random coincidence rates respectively, and k is a factor of 1 or 2 depending on the method used to estimate random coincidences (Strother *et al.*, 1990). NEC is the count rate that would have resulted in the same signal-to-noise ratio in the data in the absence of scatter and random events and is always less than the observed count rate. NEC provides an overall factor to examine statistical quality and noise in the reconstructed image.

2.3 PET Calibration

PET systems detect only a fraction of the photons emitted from the radiotracers, and therefore the efficiency of the PET must be assessed and calibrated. This is usually achieved by first measuring the activity of a source of positron emission in the scanner followed by measurement of an aliquot from that source with a calibrated radiation detector such as a well counter. The well counter is calibrated in the UK by measurement of a standard source from the National Physical Laboratory, Teddington. As the measurements will be made at different times, a decay correction factor is applied to data sets from the scanner and well counter. If arterial blood samples are taken during the duration of the PET scan, the on-line detectors are calibrated in a similar fashion. A relationship is therefore established

between the radioactive concentrations in the tissue, derived from the PET image, and blood. This is important in modelling PET data to derive quantitative parameters.

2.4 Radioisotope Production

Positron emitting radionuclides are not usually present in nature and must be produced artificially, which most often occurs in a cyclotron. The production of radioactive atoms was first demonstrated in 1934 by Curie and Joliot after bombarding magnesium and aluminium with alpha particles from radium or polonium. They observed that positron emission from the target continued after the bombardment had stopped. In 1930, E. Lawrence conceived the idea of accelerating particles between two D-shaped magnets, called a cyclotron, in order to produce progressively higher energy particles for bombarding atoms. Cyclotrons in use today harness powerful and electric magnetic fields to accelerate charged particles such as protons, deutrons or alpha particles, which are created by the ionisation of the gases hydrogen, deuterium and helium, respectively. These particles are accelerated to such high speeds (2-5% of the speed of light) that they overcome the forces of repulsion from a positively charged nucleus and bombard a target containing stable atoms, to give rise to radionuclides. The radioisotopes generated have an excessive positive charge and decay by positron emission as previously described.

A limited number of radioisotopes with short half-lives are not produced in a cyclotron and can be formed in an on-site generator. Gallium-68 (^{68}Ga) and rubidium-82 (^{82}Rb) are extracted as decay products from their parents, germanium-68 (half-life = 275 days) and strontium-82 (half-life = 25 days), respectively.

2.5 Radiochemistry of Radioactive Tracers

This describes the process of labelling the compound of interest or radiotracer to be studied using PET with the radioisotope after it has been produced in the

cyclotron. An advantage of PET is that positron emitting radioisotopes are available for commonly occurring elements such as carbon (^{11}C), oxygen (^{15}O), nitrogen (^{13}N) and fluorine (^{18}F) which are used as substitution of an element in the compound to be radiolabelled. Fluorine-18 is commonly used to replace fluorine present in 5-fluorouracil for PET imaging studies (Brown G. *et al.*, 1993), though ^{18}F can also be used to replace hydrogen atoms with which it is isoteric, or hydroxyl groups with which it is isoelectronic (Brooks *et al.*, 1992; Inoue *et al.*, 1997).

Many of the radioisotopes have a short half-life (Table 2.2), requiring rapid methods of radiochemical synthesis and necessitating the need for an on-site cyclotron. Difficulties will also be encountered when longer studies need to be performed. Radioisotopes with longer half-lives can be transported from their site of production to the administration site.

The aim of radiochemistry is the simple and fast production of radiotracers to ensure sufficient quantities of radiotracer with high specific activity. Radiotracers with a very high specific activity of the order 150-600 GBq/mmol are required to ensure that concentrations of the non-radioactive part of the compound are low so as not to interfere pharmacologically with the *in vivo* measurement of the kinetics of the radiotracer. In general, radiotracer production should be quick enough to allow the radiolabelled target drug/compound to be isolated, purified and formulated as a pyrogen-free, sterile isotonic solution within 2 to 3 half-lives of the radionuclide.

High levels of radioactivity have to be handled in the production of radiotracers, particularly those utilising short-lived radioisotopes. To limit the exposure of personnel to this high radioactivity, single-step synthesis methods have been developed. In addition, radiochemistry now incorporates remote controlled and robotic-based chemistry techniques, though this necessitates complicated machinery and expertise to be on site.

Table 2.2: A list of positron emitters and their half-lives

Radioisotope	Half-life	Positron decay (%)
Bromine-75	98 min	76
Bromine-76	16.1 hrs	57
Carbon-11	20.4 min	99.8
Cobalt-55	17.5 hrs	77
Copper-62	9.7 min	97.8
Copper-64	12.7 hrs	19.3
Fluorine-18	109.8 min	96.9
Gallium-68	68.1 min	90
Iodine-124	4.2 days	25
Iron-52	8.3 hrs	57
Nitrogen-13	10 min	100
Oxygen-15	2.03 min	99.9
Rubidium-82	1.25 min	96
Technetium-94m	53 min	72
Yttrium-86	14.7 min	34
Zirconium-89	78.4 min	25

2.6 PET Modelling Techniques

The aim of modelling the behaviour of radiotracers in PET studies is to interpret kinetic data in terms of standard physiological, biological and pharmacological parameters. PET modelling allows the response of tissue and subsequent dynamic changes in radiotracer concentration to an injected dose of radioactivity to be observed and analysed to derive a parameter to describe the tissue kinetic of the radiotracer. Temporal resolution of tissue radioactivity is high and is determined by the frame durations of the dynamic scans which are shorter early on in the scan, to ensure the inclusion of rapidly changing radiotracer kinetics in the measurement. Mathematical modelling of tissue radioactivity alone is known as

semi-quantitative analysis, as the input of the radiotracer is not accounted for in this methodology. An example of this is integral analysis, which is discussed later in this chapter.

In other PET models, arterial blood radiotracer concentrations are recorded and are related to the radioactivity concentrations in tissue via an appropriate model. This enables the determination of plasma and tissue rates of exchange and provides an *in vivo* method of calculating quantitative regional tissue radiotracer kinetics. Arterial blood sampling in dynamic PET scans is derived from a combination of continuous on-line monitoring (second by second measurements) of whole blood radioactivity and discrete blood samples (5-10 samples per PET scan). From these measurements, a plasma input function for the radiotracer can be acquired from blood/plasma radioactivity portioning and plasma metabolite analysis. Blood data acquisition is sufficiently rapid to ensure that the fast kinetic profile of the radiotracer can be detected, as with radiotracer tissue data. The convolution operator is used to enable time-dependent changes in arterial radioactivity (input) and tissue radioactivity (output) to be assessed together and thereby generate a quantitative parameter of interest.

Modelling, when using both arterial and tissue radioactivity inputs, requires that two factors, delay and dispersion, be considered. Delay is the result of the temporal lag (~ 10 s) between injection time into a vein in the arm or hand, and time to reach the target organ such as tumour or liver. Dispersion occurs as a result of spreading of the bolus after injection in the BGO detectors and is corrected for by modelling measured and actual arterial concentration time courses.

Quantitative PET analysis can be divided into two categories: model led or data led analysis. Model led techniques themselves form a broad spectrum of methods ranging from a rigid compartmental model to more flexible approaches such as spectral analysis. In compartmental modelling, the potential distribution of the radiotracer is assigned to a limited number of discrete compartments, within which it can be free, specifically or non-specifically bound. This method requires *a priori* knowledge of the radiotracer. Spectral analysis on the other hand requires few *a priori* assumptions. An alternative technique is graphical analysis which lies between compartmental and spectral analysis. Data led methods include principle

component analysis which employs orthonormal transformation of standard coordinate axes to obtain key temporal components from dynamic data. Another technique is cluster analysis which allows natural groupings in data to be uncovered and provides estimates of association in PET data (Gunn *et al.*, 1998).

In this thesis, the principal analyses used are integral, compartmental, graphical and spectral methods, which are discussed below.

2.6.1 Semi-Quantitative Modelling Methods

2.6.1.1 Integral Methods

Two important parameters, standardised uptake value and area under the curve, are obtained relatively simply from the injected radioactivity dose, tissue radioactivity data and patient weight, using integral methodology. The radioactivity must be decay corrected (described below) to take into account the decay of the radioisotopes over the duration of the scan.

2.6.1.2 Decay Correction

Although the amount of radioactive material decreases with time the rate of radioactive decay remains the same. Different radioisotopes decay at different rates, but they all follow the exponential law of decay for radioactivity which depends on the initial radioactive count. The equation for exponential decay is:

$$N = N_0 e^{-\lambda t},$$

Where, N and N_0 are the number of radioactive nuclei present initially and after time t, respectively. λ (lambda) is the disintegration constant and is the probability that an atom will decay in a second. λ is characteristic for each radioisotope, and for the isotopes used in this thesis are shown in Table 2.3.

Table 2.3: Radio isotopes and their λ constants

Radioisotope	λ constant
[^{18}F]	1.053×10^{-4}
[^{11}C]	5.663×10^{-4}
[^{15}O])	5.6896×10^{-3}

2.6.1.3 Standardised Uptake Value

Standardise uptake value (SUV) is a relatively simple mathematical model in PET and therefore one of the most frequently employed. SUV is defined as the decay corrected tissue activity as measured by PET divided by the radioactivity injected divided by body weight (Zasadny *et al.*, 1993). Variability of SUV has been reduced by normalisation with body surface area (BSA) rather than body weight.

$$SUV_{(t)}\ [m^2/ml] = \frac{\text{Measured activity at time (t) [kBq/ml] x } e^{-\lambda t}}{\text{Injected dose [kBq] / BSA}}$$

In oncology studies SUV is used to compare normal and malignant tissue tracer pharmacokinetics. In dynamic PET scans, the SUV is the integral over a time frame of decay corrected tissue radioactivity normalised to injected activity and BSA. When the SUV for each time frame is plotted against mid-frame times (MFT, see Chapter 4), the so called time *versus* radioactivity curve (TAC) is generated. SUVs can be calculated at various time points during the scan. Early time points such as at 3 minutes ($SUV_{3.75mins}$), before metabolism of parent radiotracer, can give a measure of delivery of radiotracer e.g. of 5-[^{18}F]fluorouracil to tissue. For radiotracers that are 'trapped' in tissue, e.g. 2-floro-2-deoxy-glucose ([^{18}F]-FDG, see chapter 3) a later time point of SUV gives an indication of retention of radiotracer by tissue.

2.6.1.4 Area under the Radioactivity Curve

Area under the radioactivity curve (AUC) is another commonly used parameter which describes exposure of tissue to the radiotracer (parent and radiolabelled metabolite). It is calculated from the TAC, by integrating the activity in all time

frames for the full duration of the dynamic scan. AUC is expressed as m^2/ml x sec, after correction for radioactive decay and normalisation for body surface area.

2.6.2 Quantitative Modelling Methods

2.6.2.1 Compartmental Modelling

Compartmental analysis, as mentioned, requires some *a priori* knowledge of the behaviour of the radiotracer in tissue. A system is then constructed using a single or a series of interacting compartments between blood and tissue which are representative, although a simplification, of the underlying biological/physiological/pharmacological process. The compartments may either define physical distinct parts if the 'system' or the behaviour of chemical species within it. If there is direct proportionality between the model variable and the predicted response, the optimal set of variables can be computed directly using linear regression. The transfer of radiotracer between compartments is proportional to the amount of material within each compartment and is described by rate constants.

A number of assumptions are imposed when using a linear compartmental model:

i) The tracer must mix instantaneously within the compartment and be of uniform concentration.

ii) The quantity of tracer must be small compared to the 'system' being measured.

iii) The rate constants between the compartments do not change.

In oncology, a single tissue compartment model is used in radiolabelled water (H_2 [^{15}O]) blood flow modelling (see below).

2.6.2.2 Blood Flow Modelling

2.6.2.2.1 Fick Principle

Blood flow modelling is based on the Fick principle, originally described for the indicator dilution method to assess cardiac output. This postulates that the quantity of any tracer taken up by an organ from blood that perfuses it in a given period of time is equal to the amount of tracer carried to the organ by the arterial

in-flow minus the quantity removed from by venous drainage, during the same time interval. The basic equation expressing this is:

$$\frac{dQ}{dt} = \Phi C_a - \Phi C_v$$

Where, Φ is the blood flow of the organ (ml/min), dQ is the amount of the radiotracer in the organ of interest (mol), and C_a and C_v the concentrations of tracer in arterial blood and in venous blood respectively.

2.6.2.2.2 Non-Dynamic Methods

Methods for measuring regional blood flow with PET are based on a model originally developed by Landau et al. (Landau *et al.*, 1955), and Kety (Kety, 1965), who measured regional cerebral blood flow with diffusible radiotracers (nitrous oxide) and tissue autoradiography.

The first quantitative PET techniques used were developed by Raichle and his group in St. Louis (Herscovitch *et al.*, 1983; Raichle *et al.*, 1983) and Frackowiak and co-workers at the Hammersmith Hospital (Frackowiak *et al.*, 1980). Raichle used ^{15}O-labelled water which was injected intravenously as a bolus and the PET image acquired over 40 seconds. Frackowiak et al. developed the steady-state inhalation method to estimate blood flow, oxygen extraction, oxygen utilisation and blood volume in the brain. In this method the patient inhales ^{15}O-labelled CO_2 which is converted rapidly in the lung by carbonic anhydrase to radiolabelled water. After an inhalation of several minutes equilibrium is reached between radiotracer concentration in blood and tissue. Tissue perfusion can then be calculated from two measurements: tissue concentration, determined from the PET signal and arterial concentration, measured by arterial sampling using a cross calibrated well counter. In addition, radiolabelled water ($H_2[^{15}O]$) has several useful characteristics as a flow tracer as it is biologically inert as well as chemically stable with no physiological effects, and has a short half-life allowing rapid and repeatable studies to be performed. However, several assumptions are made to calculate blood flow using this model. First, it assumes that water is a completely and freely diffusible substance and that extraction of water from the circulation at different flow rates is always 100% (Frackowiak *et al.*, 1980). It also

makes assumptions about partition co-efficient. Partition co-efficient (or volume of distribution as it is called in PET) is the fraction of the volume of tumour in which the radiolabelled water is distributed at equilibrium. In this model, it is assumed that the partition co-efficient of water in healthy and diseased tissue is the same and that the volume of distribution of radiolabelled water is 1. Subsequent analyses (Herscovitch *et al.*, 1983; Lammertsma *et al.*, 1992; Lammertsma *et al.*, 1981) found that these assumptions led to underestimation of blood flow in heterogeneous tissue and in homogeneous tissue with volume of distribution less than 1. This is particularly important in tumours where the tissue is frequently heterogeneous.

2.6.2.2.3 Dynamic Methods

As a consequence of these limitations of perfusion estimation and coinciding with the development of faster scanners, these methods were modified and adopted for use in a dynamic procedure which employed kinetic information from the arterial input curve and tissue radioactivity. This method was initially developed for measuring blood flow and oxygen utilization in the brain and heart (Frackowiak *et al.*, 1980). It has subsequently been modified and used to measure blood flow and exchanging water space in breast tumours (Wilson *et al.*, 1992). In this technique, the behaviour of ^{15}O-labelled water, which is metabolically inert and freely diffusible, can be described by the following differential equation for a single-compartment model (Fig. 6).

$$dC_t(t)/dt = F.C_a(t) - (F/V_d + \lambda).C_t(t)$$

Where, $C_t(t)$ is the regional tissue concentration of $H_2[^{15}O]$ (kBq/ml of tissue) as a function of time and $C_a(t)$ is the arterial whole blood concentration of $H_2[^{15}O]$ (kBq/ml of blood). F is the regional blood flow (perfusion) in ml (blood)/min/ml (tissue), V_d is the volume of distribution of water (ml_{blood}/ml_{tissue}) and λ is the decay constant of ^{15}O.

The solution to this differential equation is given by:

$$C_t(t) = F.\ C_a(t) \otimes \exp^{-[F/Vd + \lambda]t}$$

Where $\otimes$ is the convolution operator and $C_t(t)$ represents the tissue response to an arterial input function $C_a(t)$. As $C_a(t)$ and $C_t(t)$ are measured over time with dynamic PET, best estimates of both F and V_d can be obtained using non-linear regression analysis (Wilson *et al.*, 1992).

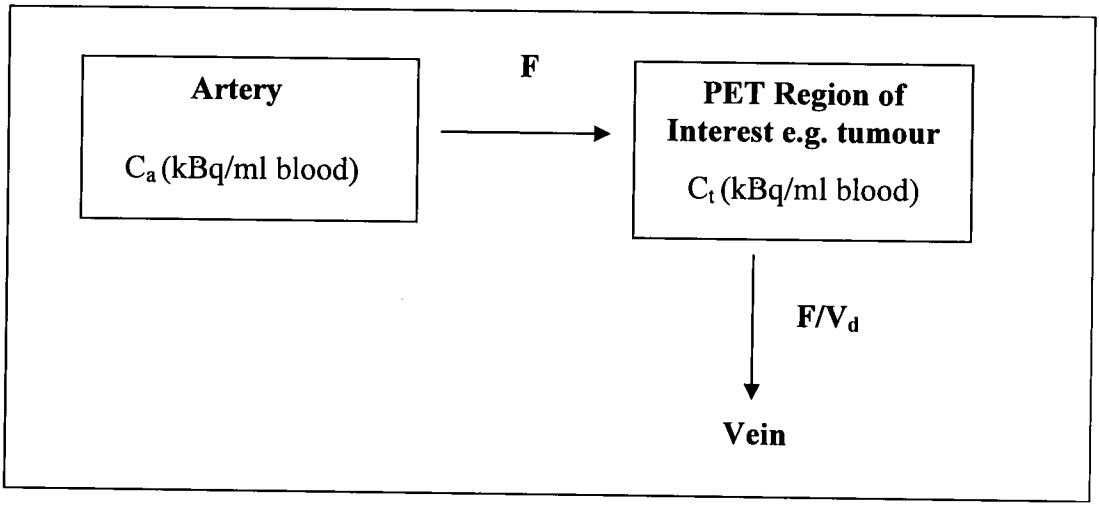


Figure 6: One-tissue compartment blood flow model.

Amongst the advantages to the dynamic model are that the acquisition of data is quicker and can be repeated easily. The faster acquisition with a shorter build up means a lower effective dose is delivered to the patient in addition to the lower total dose of radioactivity needed to acquire the data. In addition, V_d can be derived from the dynamic model, which may be a useful parameter particularly when measuring heterogeneous tissues such as tumours. One of the major disadvantages of the ^{15}O blood flow model is that it becomes unreliable at high flow rates. This is because the model depends on a difference between the arterial and tissue time activity curves. At high flow rates the arterial curves approaches the tissue curve and the data cannot be modelled. This is usually not a problem when measuring tumours as perfusion in such tissues is characteristically low.

Apart from measuring blood flow in breast cancer, PET has also been used to measure regional perfusion in primary and secondary brain tumours, pancreatic and hepatic malignancies including hepatocellular cancer and metastases (Anderson *et al.*, 2002).

2.6.2.3 Graphical Analysis

This method of analysis was largely developed by Patlak and his associates, based on mathematical principles exploited earlier by Patlak and Rutland, who used it in nuclear imaging (Patlak CS. *et al.*, 1983). The purpose of graphical analysis is to derive the unidirectional and irreversible uptake of tracer from plasma into tissue and was originally utilised to study solute exchange across the blood-brain barrier.

The general theoretical model behind graphical analysis describes tracer exchange between a plasma compartment, a reversible tissue region with an arbitrary number of compartments, and one or more tissue compartments in which the uptake of tracer is irreversible. A number of assumptions are required in this analysis:

i) There is a single point source, the plasma, for the radiotracer in the system.

ii) The concentration of the radiotracer in plasma may vary with time.

iii) Relatively rapid exchange occurs between the radiotracer in plasma and the tissue region which is made up of *n* number of compartments, where radiotracer exchange among plasma and this first region of tissue compartments is reversible.

iv) The radiotracer can enter a second tissue or compartment distribution region from the plasma or first region compartments. However, after entering the second region, the radiotracer cannot leave, and the radiotracer uptake is irreversible. The irreversible region may consist of more than one compartment, but these are mathematically lumped together to form a single compartment.

v) The radiotracer does not alter the system and the exchange of radiotracer within the system obeys first-order kinetics.

vi) If there is any metabolism of the parent in the plasma or exchangeable regions, the metabolites must behave in the same pattern as the parent.

vii) Generation of metabolites within the irreversible region must not leave this tissue compartment and must be measurable.

viii) The radiotracer is not initially present in either the exchangeable or irreversibly bound compartments.

In Patlak analysis, the data are first transformed and can then be depicted graphically. Data on the y-axis represents tissue concentration divided by plasma concentration for that time point. The normalisation of data on the x-axis effectively transforms the bolus input function into an infusion function of the arterial plasma activity. This is achieved by taking the integral of the plasma signal up to each measured time point and dividing by the actual plasma concentration at that time point. This normalised time is known as 'stretched time'.

In a typical Patlak plot using a two-tissue compartment model (Fig 7), the initial slope is curved upwards and is attributed to the radiotracer reaching equilibrium between plasma and reversible compartments while continuing to be taken up by the irreversible compartment. The gradient of the final linear upslope of the curve is proportional to the irreversible tissue uptake of radiotracer from plasma and reversible tissue regions and is known as K_I, the net clearance of radiotracer from plasma into tissue. If there is no trapping of radiotracer by the tissue, tissue levels follow plasma levels and the tissue over plasma curve bends and becomes horizontal. After transformation of the data, the Patlak model equation is defined as:

$$A_{tiss}(t) / C_x(t) = K_I \int_0^t C_x(t) d\tau / C_x(t) + (V_{ox} + V_b)$$

Where $A_{tiss}(t)$ and $C_x(t)$ are the time concentrations of radiotracer in tissue and plasma respectively, V_{ox} is the volume of the exchangeable regions, and V_b is the blood volume within the tissue. K_I is net unidirectional influx constant or net irreversible uptake constant as described.

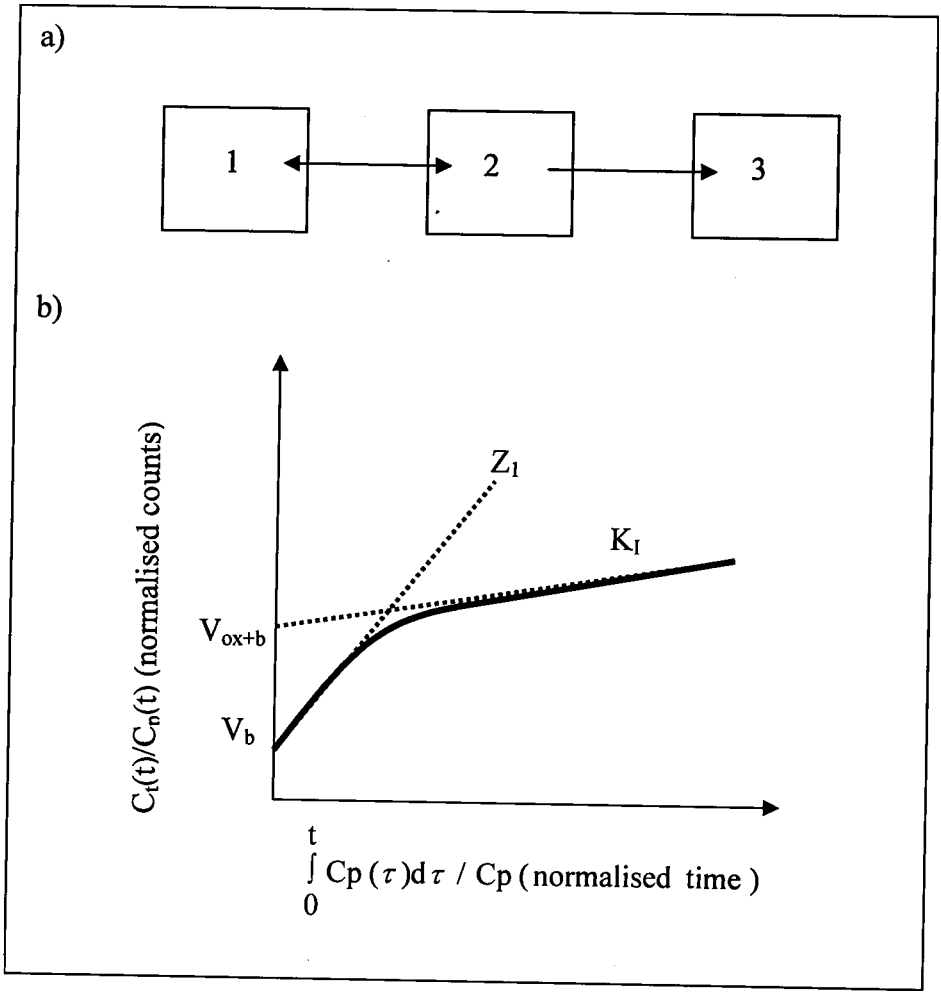


Figure 7: Graphical Representation of Radiotracer Transfer and Typical Patlak Plot

a) Transfer of radiotracer from plasma (compartment 1) and exchangeable regions (compartment 2) and unidirectionally into tissue (compartment 3).

b) Patlak plot showing the initial upslope gradient Z_I, proportional to the clearance of radiotracer from plasma to exchangeable regions and K_I, proportional to the net unidirectional clearance from plasma and exchangeable compartments into tissue

The original Patlak model described above has been modified to allow analysis of radiotracer which has labelled metabolites that do not behave in an identical manner to the parent. In modified Patlak (Mankoff *et al.*, 1996), the following additional assumptions are made:

i).The blood concentrations of tracer and its metabolites are known over time. In tissue, only the sum of the concentration of tracer and metabolites is known.

ii).The blood is the only source of metabolites i.e. a tissue other than the tissue of interest is principally responsible for the generation of metabolites.

iii) The metabolites are fully reversible between blood and tissue and are not taken up irreversibly by the tissue of interest.

In this extended Patlak, the equation is modified to the following:

$$A_{tiss}(t)/C_{tot}(t) = K_I \int_0^t C_x(\mathrm{t})\, d\tau / C_{tot}(t) + V_{ox}[C_x(t)/C_{tot}(t)] + \sum V_{om}[C_m(t)/C_{tot}(t)] + V_b$$

Where, $A_{tiss}(t)$ and $C_{tot}(t)$ are the time concentrations of total radiotracer (parent and metabolite) in tissue and plasma respectively, $C_x(t)$ and $C_m(t)$ are the time concentration of parent radiotracer and metabolite respectively in plasma, V_{ox} and V_{om} are the distribution volumes of parent and metabolite respectively and V_b is the blood volume within the tissue. From this, the parameter K_I can be calculated.

2.6.2.4 Spectral Analysis

Spectral analysis is a general modelling technique that enables the determination of pharmacokinetic and pharmacodynamic parameters, with relatively few modelling assumptions (Cunningham VJ. *et al.*, 1993). This technique is based on identifying a spectrum of kinetic components within a given data set which are involved in the regional uptake and portioning of radiotracer from blood to the tissue, rather than being restricted to a predefined compartment model. No *a priori* assumptions are required and the technique allows the distinction between transient components, associated with tracer in the tissue vasculature, and reversible and irreversible components comprising the tissue response to the administered radiotracer.

The fundamental process of spectral analysis is the method by which it relates the tissue radioactivity-time curve and arterial plasma input function. It does this by modelling the tissue data as a positive linear combination of basis functions, each of which is a single exponential in time convolved with the arterial input function.

$$C_{tiss}(t_i) = \sum_{i=1}^{i=k} \alpha_i \cdot C_m(t) \otimes \exp(-\beta_i \cdot t)$$

Where, $C_{tiss}(t)$ and $C_m(t)$ are radioactracer concentrations in tissue and arterial blood or plasma respectively at time (t_i), $\otimes$ denotes convolution operator, k is the

upper limit of the number of non-negative functions allowed in the model (typically 100). α and β parameters may be positive or zero, due to the constraint of the assumptions of first order tracer kinetics.

β values are predetermined, and are selected to cover the spectrum of expected kinetic behaviour. For short-lived radioisotopes, the range incorporates the slowest possible loss of radioactivity (indicative of the radioactive half-life of the radioisotope) up to the fastest measurable dynamic (e.g. the transient passage of activity through the vasculature). The use of PET data which are not decay corrected provides a natural constraint on the values for β. For example, for studies using [^{18}F] with a decay constant of 0.000105s^{-1}, a suitable range is 10^{-4} to I s^{-1}. Kinetic componenets may take any value between 0 to λ. Therefore, a β value of I s^{-1} is associated with the fastest component and is usually due to blood volume effects whilst a value closer to λ reflects retention of radiotracer in the tissue.

α indicates the relative contribution and intensity of each of the the components. Values for α may be obtained from a fit of the model to the measured time-activity data from the tissue being analysed using the non-negative least-squares algorithm (Meikle SR. *et al.*, 1998).

The fitted values of α and the corresponding pre-chosen values of β define the tissue unit impulse response function (IRF). The IRF describes the time course of the radiotracer that would be expected if it were possible to deliver the tracer instantaneously to tissue, and is represented by the following equation:

$$h(t_i) = \sum_{i=1}^{i=k} \alpha_i \exp(-(\beta_i - \lambda)t)$$

An alternative way of displaying the data is as a log frequency of β values, which shows the spectrum of individual kinetic components that adequately describe the tissue response and their amplitude. From this, the three parameters that are listed below, can be identified and calculated:

i) K_I, which is the clearance of radiotracer from plasma to tissue and is represented by:

$$K_1 = h(0) = \sum_{i=1}^{i=k} \alpha_i$$

ii) The fractional volume of distribution (VD) of the radiotracer (i.e. the steady state ratio of concentration of tracer in tissue and plasma) is given as:

$$VD \int_0^{\infty} h(t)dt = \sum_{i=1}^{i=k} \frac{\alpha_j}{\beta_j - \lambda}$$

iii) The mean residence time (MRT) of radiotracer in the sampled tissue, and is obtained by:

$$MRT = \frac{VD}{K_1}$$

2.6.2.4.1 Permeability and Surface Area Product

Transport across the capillary endothelial cell is known as the permeability and surface area product (PS), and is a product of the capillary surface area and permeability (Cunningham VJ. *et al.*, 1994). According to the Renkin-Cronin model, K_1 incorporates PS and two other related components (i) the rate of plasma flow through capillaries and (ii) the change in concentration of the radiotracer as it passes across the capillary bed from artery to vein. The Renkin-Cronin model was originally formulated to describe the unidirectional uptake of tracer from the capillary in terms of properties of an ideal unit capillary in the brain (Crone, 1963). Furthermore, certain assumptions are imposed on the model such as assuming that the capillary transit time is negligible and ignoring the exchange of label between red blood cells and plasma which can occur during transit through the capillaries. However, this model can be extended to other tissue systems to derive PS product if K_1 and regional blood flow are known. If extravascular concentration of the

radiotracer is negligible and influx of the tracer from plasma to tissue is greater than efflux, then:

$$E = (C_a - C_v)/C_a$$

Where C_a and C_v are the concentrations of the radiotracer in the arterial and venous ends of the capillary respectively and E denotes extraction.

$$K_1 = F \times E \qquad \text{Equation 1}$$

Where F is the regional blood flow and calculated using a one-compartment model and modified Kety-Schmidt equation (Kety *et al.*, 1948). If there is exponential decline of radiotracer concentration between C_a and C_v, then the following equation applies:

$$E = 1 - e^{-PS/F} \qquad \text{Equation 2}$$

Therefore PS product can be calculated if K_1 and regional blood flow values are known, using Equations 1 and 2 as follows:

$$K_1/F = 1 - e^{-PS/F}$$

$$e^{-PS/F} = 1 - K_1/F$$

$$-PS/F = \ln(1 - K_1/F)$$

$$PS = -F \times \ln(1 - K_1/F)$$

2.7 Summary

PET is a complex, multi-step technique requiring contributions from experts in a wide range of specialties. Advances have been made in PET scanners, detectors and software involved in image reconstruction which has improved the quality of PET scans.

Clinically, PET can give non-invasive information on the temporal and spatial distribution of radiotracers. Various models have been formulated to help interpret these data making it a valuable technique in clinical medicine.

Chapter 3 Molecular Imaging in Oncology

3.1 Introduction

The term molecular imaging can be broadly defined as the '*in vivo* characterisation and measurement of biological processes at the cellular and molecular level' (Weissleder *et al.*, 2001). PET is an ideal tool with which to explore biochemical, physiological, pharmacological and genetic pathways that are altered in the development of cancer or can be manipulated in its treatment.

PET imaging with [^{18}F]fluoro-2-deoxy-D-glucose ([^{18}F]FDG) has dominated the field of oncology for the last two decades. An observation by Warburg (Warburg, 1956) in the 1930's that malignant tumours have increased gylcolytic rate compared to normal tissue was followed in the 1980's with studies by Di Chiro, who showed that the degree of malignancy of cerebral tumours was correlated with their FDG uptake (Di Chiro, 1985; Di Chiro *et al.*, 1982). After systemic delivery, [^{18}F]FDG initially follows the same metabolic pathway as glucose, and is transferred into cells by specific glucose transporters (GLUT-1) and is then phosphorylated into [^{18}F]FDG-6-phosphate by hexokinase. Unlike glucose, [^{18}F]FDG-6-phosphate is trapped and accumulates within the cell as it lacks a hydroxyl group and cannot act as a substrate for further glycolysis (Nelson *et al.*, 1996). Although FDG uptake is not specific to neoplastic cells, the role of [^{18}F]FDG in current clinical applications in oncology is diverse and includes: pre-operative detection and staging of discase, detection of recurrence, differentiation between recurrence and scarring post treatment, evaluating response to treatment (Young *et al.*, 1999) and determination of biopsy site.

Despite the fact that 95% of all clinical PET scans use [^{18}F]FDG (Gambhir, 2002), the future challenge for PET imaging lies in the development of novel PET radiotracers (or molecular PET probes) to fulfil its expectation in the arena of molecular imaging and cancer treatment.

This chapter will give an overview of new advances in various molecular processes in oncology such as angiogenesis, gene expression, hypoxia, apoptosis, and receptor interactions that have been identified as important determinants of cancer prognosis and treatment, and the utilisation of novel, investigative PET radiotracers with which to image them. The pharmacological processes of pharmacokinetics and pharmacodynamic endpoint assessment using 5-[^{18}F]fluorouracil and 2-[^{11}C]thymidine PET will be discussed in subsequent chapters.

3.2 Angiogenesis

Tumours do not grow beyond 1-2mm^3 in size without the development of new blood vessels (Folkman, 1971). Angiogenesis, which is the growth of blood vessels either from existing vasculature or from *de novo* generation of blood vessels, is imperative to allow tumour cells to increase their nutrient supply, proliferate and survive even though the new vessels often have structural and functional abnormalities compared to normal tissue. Numerous experimental animal models have demonstrated that angiogenesis is one of the most critical steps for progression of the primary tumour, as well as metastatic dissemination (Folkman, 1990). Though angiogenesis remains a complex, multistep process, great strides have been made in the last few years to elucidate its molecular mechanism in much greater detail. Many cytokines implicated in this pathway have been discovered including vascular endothelial growth factor (VEGF), whose levels are upregulated in several cancers such as breast, colon, ovarian and lung, and which may have prognostic significance (Miller *et al.*, 2001). There are two evolving categories of treatment that interfere with tumour vasculature for therapeutic benefit:

i) Antiangiogenic agents that inhibit new endothelial cell development and subsequent formation of capillary networks.
ii) Antivascular drugs that disrupt existing endothelial cells leading to destruction of the tumour blood vessel architecture.

Both treatment strategies have proved attractive with the development of numerous therapeutic agents with antiangiogenic or antivascular activity.

3.2.1 Antiangiogenesis

The main restriction in the increasing number of new antiangiogenic drugs is the limited availability of surrogate markers of therapeutic efficacy. The outcome of antiangiogenic drugs is difficult to determine as there is a wide range of mechanisms by which they can prevent neogenesis or neovacularisation. Effective therapy may not lead to any substantial reduction in tumour size, rendering conventional imaging modalities unable to determine response. PET methods are being developed to measure parameters related to the angiogenic phenotype. VEGF is one of the most potent cytokines mediating angiogenesis (Ferrara, 2002), and is secreted in response to hypoxia by tumour cells (Shweiki *et al.*, 1992). One study has demonstrated the feasibility of imaging VEGF using an anti-VEGF antibody labelled with iodine 124 (^{124}I-VG76e) in mice bearing human xenografts. *Ex vivo* biodistribution confirmed antibody localisation within tumour (Collingridge *et al.*, 2002). Such PET imaging may help identify patients with high tumoural expression of VEGF allowing appropriate selection for treatment with antiangiogenic drugs and provide an accurate marker of treatment response. Recent effort has concentrated on developing radiolabelled antagonists to the integrin $\alpha_v\beta_3$. $\alpha_v\beta_3$ is highly expressed on activated endothelial cells and plays a crucial part in new vessel formation (Stromblad *et al.*, 1996). It binds to the tripeptide sequence arginine-glycine-aspartic acid (RGD) of various extracellular matrix proteins and by blocking these interactions can result in inhibition of tumour-induced angiogenesis (Brooks *et al.*, 1995; Westlin, 2001). A radiolabelled glycopeptide of RGD, [^{18}F]Galacto-RGD, showed accumulation in $\alpha_v\beta_3$ receptor positive tumours in mice using small animal PET scanning (Haubner *et al.*, 2001). Further studies need to be undertaken to determine the clinical potential of [^{18}F]Galacto-RGD PET imaging in patients undergoing antiangiogenic treatment.

3.2.2 Antivascular

The endpoint of antivascular activity is easier to define as the direct consequence of destruction of tumour vasculature is a reduction in tumour perfusion. Therefore the effect of newer antivascular agents may be monitored by changes in blood flow. [^{15}O]-labelled water ($H_2[^{15}O]$) has been utilised extensively and with good reproducibility in dynamic PET studies to quantify normal tissue and tumour blood flow *in vivo* using an input function derived from continuous arterial sampling over the period of imaging (Anderson *et al.*, 2002; Beaney *et al.*, 1984; Lammertsma, 1987; Wilson *et al.*, 1992). PET blood flow scans have contributed to the clinical evaluation of a novel antivascular agent, Combretastatin A4 Phosphate (CA4P), a tubulin binding agent, which induces rapid and selective blood flow reductions in experimental tumour systems by possible cytotoxic effects on proliferating endothelial cells (Chaplin *et al.*, 2002; Dark *et al.*, 1997; Prise *et al.*, 2002; Tozer *et al.*, 1999). 8 patients treated with CA4P in a phase 1 trial had $H_2[^{15}O]$ PET scanning before, 30 minutes and 24 hours after the first infusion of CA4P. Results showed a 30-60% temporary reduction in tumour blood flow at the higher dose level of CA4P, corroborating data obtained in animal studies (Anderson *et al.*, 2003; Griggs *et al.*, 2001).

3.3 Gene Expression

Remarkable progress in genetic engineering has been made to develop and clarify knowledge about cascades of gene expression and interaction between gene and gene products. This has been accompanied by the exciting prospect of gene manipulation in cancer treatment by either transferring appropriate genes into abnormal cells or by detection of endogenous gene expression for clinical translation and diagnosis (Gillies, 2002). However, without improving the ability to monitor and quantitate the degree of gene expression, which can currently only be achieved with biopsy specimens, the field of gene therapy would continue to face significant obstacles for routine use. Imaging gene expression is important for monitoring the location(s), magnitude and time variation of gene expression

from gene-therapy vectors, and can be important to measure efficacy of treatment and to answer questions pertaining to optimisation of treatment (Blasberg, 2002):

1. Has gene transfer been successful?
2. Is gene expression localised to the target tissue or organ, and is this optimal?
3. Is there sufficient transgene expression to obtain a therapeutic effect?
4. Are there any unwanted toxicities resulting from gene expression?
5. When pro-drug treatment is to be initiated, when is the most effective time to commence it?
6. How long does the gene expression persist in the target or any other tissues?

Two major approaches have been developed for monitoring gene expression using PET methodology:

(i) Direct imaging of endogenous genes or molecules
(ii) Indirect imaging, where there is 'linking' of the expressed therapeutic gene to a 'PET reporter gene' which 'reports' back on the status of expression of the gene of interest when properly linked.

3.3.1 Direct Imaging

Direct imaging of gene expression can be accomplished by developing radiolabelled probes that bind selectively to highly specific regions of the product of the expressed gene (e.g. protein, mRNA, or DNA) (Tavitian, 2000; Tavitian *et al.*, 1998). However, the advancement of this method of gene expression imaging is limited by the lack of specific and suitably labelled PET probes currently available (Younes *et al.*, 2002).

3.3.2 Indirect Imaging

More progress has been made with indirect imaging of gene expression utilising reporter genes despite its greater complexity (Tjuvajev *et al.*, 1995). Indirect imaging falls into two distinct categories: enzyme-based or receptor-based. In both cases, indirect imaging involves simultaneous expression between both the reporter gene and therapeutic gene product after construction of a cassette linking these genes that can be transfected into specific cells using a vector. This can be achieved in several ways:

- A single vector encoding for both transcribed genes in one mRNA, which is then translated into 2 proteins, labelled via an internal ribosome entry site (IRES) sequence (Pelletier *et al.*, 1988).
- An inducible bi-directional vector can be used which initiates the transcription of both the therapeutic and the reporter gene.
- The reporter and therapeutic gene can be delivered using 2 separate vectors.
- A fusion protein containing both the therapeutic and reporter protein can be used.

All of these approaches are dependent on having a useful PET reporter gene and radiolabelled probe (Gambhir, 2002). The paradigm for enzyme-based gene expression is the herpes simplex virus type 1 thymidine kinase gene (HSV1-tk), and is illustrated in Fig 8. The HSV1-tk gene encodes for the enzyme, HSV1-TK that can phosphorylate radiolabelled derivatives of thymidine (e.g. iodinated 2'-fluoro-2'-deoxy-1-β-D-arabinofuranosyl-5-iodo-uracil or [^{124}I]-FIAU) which acts as the PET probe after transportation into cells. In cells where HSV1-TK has been expressed, the radiolabelled phosphorylated probe (i.e. [^{124}I]-FIAU (PO_4)) is effectively 'trapped' (as it does not readily cross the cell membrane), and so accumulates within the cell, emitting a radioactive signal that reflects level of HSV1-TK enzyme activity and HSV1-tk gene expression (Tjuvajev *et al.*, 1995). The HSV1-tk gene vector with [^{124}I]-FIAU as the tracer has imaged gene expression in the liver and in transfected tumour cells (Gambhir *et al.*, 2000).

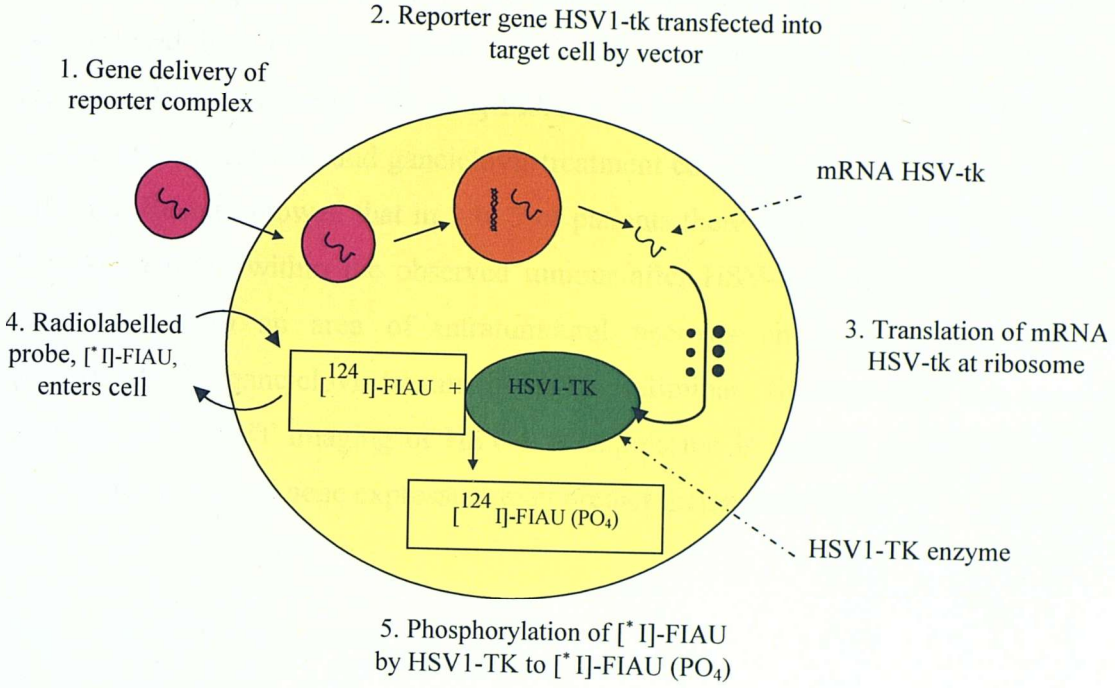


Figure 8: Diagram illustrating the paradigm of imaging gene expression with the PET reporter gene, HSV1-tk

Where gene expression uses the model of receptor imaging, the reporter gene is a cell surface receptor that 'binds' (and may internalise) the complimentary radiolabelled PET probe in the transduced cell. An example of a receptor PET reporter gene is the dopamine type 2 receptor (DR2) (MacLaren *et al.*, 1999) which has been validated in animals. Other reporter genes including those that encode stomatostatin receptor (Rogers *et al.*, 1999) and Na/I symporter (NIS gene) (Groot-Wassink *et al.*, 2002) have been examined in preliminary studies. All of these PET reporter genes work on the premise of binding to a suitable radiotracer producing sufficient, proportional accumulation of PET signal within the region for further analysis.

Studies in imaging reporter-gene expression in human subjects have only recently started. The HSV-1 tk gene vector can also be used as a therapeutic 'suicide' gene in combination with the pro-drug, ganciclovir. In this scenario, a cell expressing HSV-1 TK enzyme will commit suicide on exposure to ganciclovir under

appropriate conditions (Moolten, 1994). To assess the extent of gene expression and predict therapeutic potency, intratumoural liposomal HSV-1 tk gene vector was infused into recurrent glioblastomas of 5 patients (Jacobs *et al.*, 2001). Dynamic PET scanning with [^{124}I]-FIAU was performed at baseline and after gene vector application and ganciclovir treatment commenced 4 days after vector infusion. Results showed that in 1 in 5 of patients there was accumulation of [^{124} I]-FIAU activity within the observed tumour after HSV-1 tk infusion, and this corresponded to an area of intratumoural necrosis on an FDG-PET scan performed after ganciclovir treatment. These preliminary findings show that non-invasive FIAU-PET imaging of HSV-1 tk expression is feasible in patients and that vector-mediated gene expression may predict therapeutic effect.

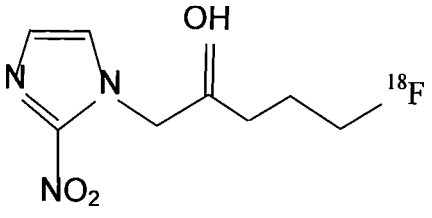
3.4 Markers of Hypoxia

Tumour hypoxia, resulting from inadequate and chaotic blood supply to neoplastic tissue, is an important prognostic indicator and a crucial factor in cancer therapy outcome to radiotherapy and some chemotherapy treatments. Oxygen mediates the biological effects of ionizing radiation and the response of cells to radiation depends strongly on the availability of oxygen. This 'oxygen effect' was first recognized by Mottram (Mottram, 1936) in 1936. Gray (Gray *et al.*, 1953) studied the influence of oxygen in mammalian tissue in detail and discovered that typically, hypoxic cells were 2.5-3 times more radioresistant than well-oxygenated cells. Assessment of tumour hypoxia prior to radiation therapy would provide a rational means to identify the outcome of radiation therapy in patients and to offer alternative radiotherapy strategies that may be more effective.

Preliminary clinical studies with Eppendorf pO_2 histographs have shown significant correlation between median pO_2 of tumours and their response to therapy (Brizel *et al.*, 1999; Brizel *et al.*, 1995; Hockel *et al.*, 1996). However, limitations of microelectrode probes to measure tumour hypoxia are that it is invasive, has poor reproducibility, can only access superficial tumours and may overestimate degree of hypoxia in necrotic tissue (Khalil *et al.*, 1995).

Non-invasive markers of hypoxia for PET imaging fall into 2 categories: 2-nitroimidazole analogues and non-nitroimidazole agents. 2-nitroimidazole analogues contain a nitro group that can bind covalently to cellular molecules upon reduction in hypoxic cells e.g. ^{18}fluorine-labelled misonidazole ([^{18}F]FMISO). Non-nitroimidazole markers such as Cu(II)-diacetyl-bis(N^4-methylthiosemicarabaone) (Cu-ATSM), are a complex of copper bis(thiosemicarbazones) that rely on the reduction of chelated metal for their selective deposition in hypoxic tissue (Lewis *et al.*, 1999).

In PET, the most experimental and clinical experience of hypoxic imaging has been gained by studying [^{18}F]FMISO (see Fig 9a).



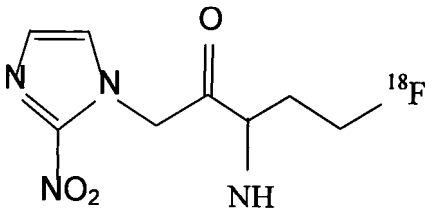


Figure 9: (a): [^{18}F]MISO; (b): [^{18}F]FETA

[^{18}F]MISO has been shown to accumulate in hypoxic tissue in an inverse proportion to tissue oxygenation (Yeh *et al.*, 1996). Under hypoxic conditions the rate of [^{18}F]MISO binding can be up to 28 times than in normoxic cells (Rasey *et al.*, 1989). Subsequent biodistribution studies defined hypoxia as tissue-to-blood [^{18}F]MISO ratio of 1.4, 2 hours after radiotracer administration (Rasey *et al.*, 1989). In a study of 37 patients with lung, head and neck and prostate cancer, hypoxia was present in 97% of the tumours studied and the extent of hypoxia varied markedly between tumours in the same site or of the same histology. Hypoxia was also distributed heterogeneously between regions within a single tumour. The intra- and intertumour variability indicate the importance of making oxygenation measures in individual tumours and the necessity to sample as much of the tumour volume as possible (Rasey *et al.*, 1996). However, there are 3 main problems with imaging with [^{18}F]MISO:

(i) There is lack of contrast between tumour and normal tissue uptake of [^{18}F]MISO due to poor cellular uptake of [^{18}F]MISO *in vivo* (Lewis *et al.*, 2001b).

(ii) [^{18}F]MISO is cleared from normal tissue over a 2 hour period. These slow kinetics delay imaging and result in low count rate studies with images of reduced quality (Lewis *et al.*, 2001b).

(iii) High rates of metabolism of [^{18}F]MISO limit its use to permit quantitative analysis (Varagnolo *et al.*, 2000).

Current research has reported on the synthesis of a new 2-nitroimidazole derivative, [^{18}F] fluoroetanidazole ([^{18}F]FETA) (Fig 6b), a monofluorinated congener of etanidazole. [^{18}F]FETA demonstrates oxygen-dependent binding and retention in tumours that are very similar to that for [^{18}F]MISO *in vitro*, and may offer the advantage in imaging hypoxic tumours because it is less rapidly metabolised *in vivo* and has had validation studies recently performed in mice (Barthel *et al.*, 2004). In addition brain-to-blood ratios indicate that [^{18}F]FETA readily crosses the blood-brain barrier and may have a role in assessment of gliomas (Rasey *et al.*, 1999).

The latest development in nitroimidazole imaging of hypoxia with PET is fluorine -labelled 2-(2-nitro-1[H]-imidazol-1-yl) - N-(2,2,3,3,3-pentafluoropropyl)-acetamide ([^{18}F]-EF5). In rat tumour models, [^{18}F]-EF5 distributed evenly in normal tissues with higher uptake in tumours visualized. Again, activity was located in the brain, and plans are underway to initiate a research project to determine the safety and preliminary evidence for the efficacy of this preparation in patients with brain tumours (Ziemer *et al.*, 2003).

Several recent studies have concentrated on the use of Cu-ATSM as a hypoxic marker. Cu-ATSM is retained in ischaemic tissue but rapidly diffuses out of normoxic tissue and uptake has been correlated with tumour pO_2 in small animal models (Lewis *et al.*, 2001a). Compared with [^{18}F]MISO, Cu-ATSM exhibits more efficient uptake and superior washout kinetics in hypoxic and normoxic cells with higher contrast levels obtained 10-15 minutes post injection. The positron emitting isotope ^{60}CU-ATSM has been used to predict response in

patients with NSCLC with encouraging results (Dehdashti *et al.*, 2003). Systems are being developed to integrate Cu-ATSM delineated hypoxic regions in tumours and delivering higher doses of radiotherapy to these smaller subvolumes using intensity modulated radiotherapy (IMRT) (Chao *et al.*, 2001).

3.5 Receptor Detection and Drug Interactions

Advances in tumour biology characteristics have revealed that many cell-surface and intracellular receptors are upregulated in cancer cells. The detection of these receptors can provide important information that can aid diagnosis and prognosis. As they are often the targets of inhibitory effects of hormones and growth factors that exert their therapeutic effect by interacting with these receptors, identification might help in selection of patients suitable for hormonal therapy and in assessing response. PET can be used to image relevant receptors and study drug-receptor interactions *in vivo* with either appropriately radiolabelled receptor binding hormones or antibodies, avoiding the necessity of recurrent invasive tumour biopsies which may also be prone to errors of tumour sampling. Receptor studies can either be direct (labelling the molecule of interest) or indirect (displacement of radioligand by the molecule of interest). The regional kinetics of radioligands can be used to derive values for receptor number (B_{max}), affinity (K_d) and binding potential (B_{max}/K_d) (Cunningham VJ. *et al.*, 1994). With the production and availability of radioligands of different receptors in various types of cancers, (e.g. breast, prostate, and neuroendocrine), receptor studies are now being performed in oncology.

3.5.1 Oestrogen

The most extensively studied receptor is the intracellular steroid oestrogen receptor (ER). 16α-[^{18}F] fluoro-17β-oestradiol (FES), an oestrogen analogue has been widely used to assess ER status in breast tumours *in vivo* (Figs 10a and b).

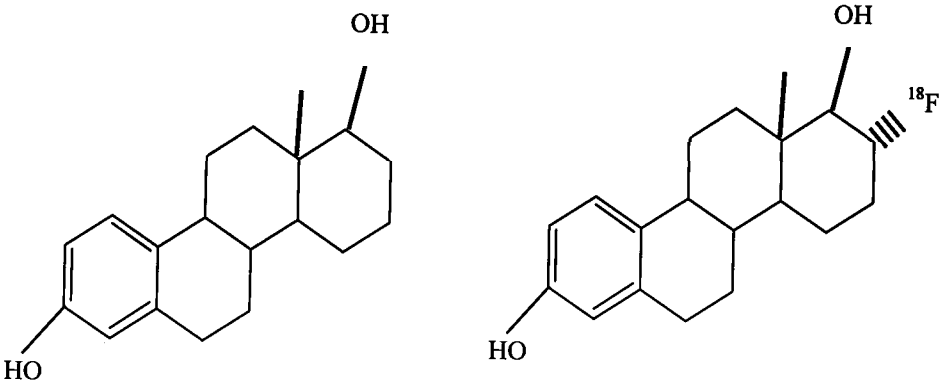


Figure 10 (a): Oestrogen **(b): 16α-[^{18}F] fluoro-17β-oestradiol (FES)**

Good overall agreement between *ex vivo* ER assays and FES uptake has led to the conclusion that FES-PET provides direct information on ER status (Dehdashti *et al.*, 1995). A decrease in the uptake of FES in metastatic breast cancers after the administration of tamoxifen has been visualised, demonstrating the presence of functional oestrogen receptors in the tumour (McGuire *et al.*, 1991). The reduction in FES uptake after tamoxifen was significantly greater in patients who responded to hormonal therapy (Dehdashti *et al.*, 1995). A further study correlating ER status with treatment response observed a group of patients with ER positive biopsies but FES negative PET scans who had poor response to hormone therapy, suggesting identification of a subset of patients with hormone refractory disease despite ER positive biopsies (Mortimer *et al.*, 1996). FES-PET imaging has therefore opened up an intriguing new way to monitor receptor function and response to hormonal therapy in patients with breast cancer at a cellular level (Flanagan *et al.*, 1998). In addition, FES has also been utilised in meningiomas where FES uptake correlated with in immunohistochemichal measurement of ER status from biopsies (Moresco *et al.*, 1997).

3.5.2 Androgen

The androgen receptor (AR) is a key biomolecule in the biology of prostate cancer and has been targeted by PET for radiolabelling and subsequent imaging to aid diagnosis and therapeutic planning. ^{18}F has been used to label several hormone analogues including 16β-[^{18}F]fluoro-5a-dihydrotestosterone (FDHT), 16β-[^{18}F]-

substituted testosterone, 16α- and 16β-[^{18}F]7α-methyl-nortestosterone, 20-[^{18}F]fluoro-R1881 (metribolone) and 20-[^{18}F]fluoromiboloerone (Bonasera *et al.*, 1996; Liu *et al.*, 1992). In man, AR expression has been studied with PET using FDHT. In a group of patients with progressive androgen independent prostate cancer, the majority of active lesions were visualised with FDHT using PET imaging. The impact of the expression of the AR on response of individual lesions to AR targeted anti-cancer drug therapies is being explored (Larson, 2002).

3.5.3 Neuroendocrine

Neuroendocrine tumours expressing stomatostatin receptors have been imaged using PET with radiolabelled ocreotide, a stomatostatin analogue. ^{64}Cu-labelled octreotide PET scanning has shown promising results in patients with carcinoid and islet cell tumours (Anderson *et al.*, 2001). ^{68}Gallium- and ^{66}Gallium-labelled octreotide analogues are currently undergoing imaging trials in patients and animals, respectively (Henze *et al.*, 2001; Ugur *et al.*, 2002). [^{18}F]fluoro-ethyl-siperone, a PET tracer with a high affinity for D_2 dopamine receptors has been used to image non-functioning pituitary adenomas to distinguish them from craniopharyngiomas and meningiomas, *in vivo*, which do not possess these receptors (Lucignani *et al.*, 1997).

3.5.4 Epidermal Growth Factor

Epidermal growth factor receptor (EFGR) is frequently overexpressed in malignancies. Strategies to target EGFR include monoclonal antibodies to prevent ligand binding and small molecule inhibitors of the tyrosine kinase activity to stop autophosphorylation and downstream intracellular signalling e.g. gefitinib. (Van de Wiele *et al.*, 2003a). A preliminary *in vitro* study has successfully prepared [^{11}C]-6-acrylomido-4-(3,4-dichloro-6-fluoroa-nilino)quinazoline (MLO3) as a potential PET biomarker for EGFR (Ben-David *et al.*, 2003). *In vivo* visualisation of EGFR expressing tumours could allow for non-invasive patient selection and response assessment for those undergoing such treatment.

3.5.5 Antibodies

Antibodies are also a potential tracer for targeting cell-surface receptors. Although primarily explored for imaging with gamma cameras and SPECT, newer small-animal studies and clinical trials are starting using positron-labelled antibody fragments. Monoclonal antibodies developed against specific antigen targets are problematic because their relatively slow clearance from blood leads to images with very high background signals, even up to one week after injection. Systematic construction of engineered antibody fragments for e.g. CEA has developed. Though they have less affinity to CEA antigen, they are more rapidly cleared in blood because of their smaller size. Humanised versions of these engineered antibodies have been labelled with ^{76}bromine and ^{64}copper, and mouse tumour xenografts imaging has been performed with micro PET (Lovqvist *et al.*, 1995; Lovqvist *et al.*, 1997; Wu *et al.*, 2000).

Radiolabelled antibody fragments have also been developed to identify the cell surface antigen receptor to C-erb2, a proto-oncogene product, that has prognostic and therapeutic implications in breast cancer, with ^{124}iodine for PET imaging (Bakir *et al.*, 1992). Again, this may assist in targeting appropriate patient therapy.

3.6 Apoptosis

Deregulation of cellular proliferation and suppression of mechanisms controlling programmed cell death (apoptosis) are believed to be important preliminary molecular events in the development of cancer (Evan *et al.*, 2001). Therapeutic strategies in cancer treatment are commonly mediated by initiation of apoptotic pathways, and apoptosis is thought to be the likely mechanism behind the cytoreductive effects of standard chemotherapy and radiotherapy regimes. A measure of apoptosis is desirable to predict and monitor tumour response to therapy. An early occurrence in the apoptotic cascade is the selective exposure of phosphatidylserine (PS) on the external surface of the cell; PS is a membrane associated intracellular phospholipid normally expressed internally on the plasma bilayer membrane (Blankenberg *et al.*, 2000; Verhoven *et al.*, 1999).

Recombinant human Annexin V (rh-Annexin V), an endogenous protein, has been shown to bind avidly to membrane-bound PS (van Heerde *et al.*, 1995) and was labelled initially with fluorescein for *in vitro, ex vivo* apoptotic assays, but then, with ^{99m}Technetium (^{99m}Tc-Annexin V) to permit imaging of apoptosis *in vivo* using single photon emission tomography (SPECT) (Blankenberg *et al.*, 1998; Blankenberg *et al.*, 1999). A recent study in 15 patients (with lung, lymphoma and breast cancer) evaluating early response following 1 cycle of chemotherapy by ^{99m}Tc-Annexin V imaging found no uptake of ^{99m}Tc-Annexin V in tumour pre-chemotherapy. However, 1-3 days post-treatment, 7 patients showed uptake of ^{99m}Tc-Annexin V at tumour sites, in whom 4 had complete response and 3 had partial response as correlated with FDG-PET and CT images. Conversely, 6 out of 8 patients with no significant post-chemotherapy uptake of ^{99m}Tc-Annexin V had progressive disease. The 2 breast cancer patients demonstrated poor tracer uptake but actually had partial response suggesting selective use of ^{99m}Tc-Annexin V apoptotic imaging in lymphoma and lung follow-up only (Belhocine *et al.*, 2002). However, ^{99m}Tc-Annexin V SPECT analysis relies on visual interpretation of static and planar images, resulting in qualitative or semi-quantitative data. Current developments are emerging to radiolabel Annexin V with iodine 124 (Glaser *et al.*, 2003) and fluorine 18 (Zijlstra *et al.*, 2003) for use as potential apoptotic probes in PET studies. This will have the added advantage of not only allowing quantitative analysis but also producing dynamic, 3-D images. These radiotracers are being validated in pre-clinical studies, and will be of greater benefit in assessing the efficacy of treatment options at an early time point.

3.7 Other Applications of PET Imaging

3.7.1 Choline

Alteration of choline metabolism, a constituent of the phospholipid bilayer cell membrane, has recently been evaluated as a marker of malignant transformation (Aboagye *et al.*, 1999). Extracellular choline is phosphorylated to phosphocholine by choline kinase after it is transported into cells. This commits choline to

phosphatidylcholine biosynthesis which is an essential signalling molecule for cell growth and essentially 'traps' the extracellular choline within the cell, hence its attraction for PET imaging. Whilst little is known of the mechanisms that regulate choline kinase activity or phosphocholine production, choline kinase dysregualtion is frequently found in a variety of human tumours such as lung, colorectal and prostate tumours and increased activity of choline kinase is found in panels of human cancer-derived cell lines compared to non-malignant cells (Ramirez de Molina *et al.*, 2002). This has supported the role of PET imaging with radiolabelled choline as a tumour marker.

Clinical studies have been conducted with methyl-^{11}carbon (methyl-[^{11}C]) labelled choline. It appears to be of particular interest in urological tumours where methyl-[^{11}C]-choline has higher uptake in bladder and prostate cancer than [^{18}F]FDG (de Jong *et al.*, 2002a; de Jong *et al.*, 2002b; Picchio *et al.*, 2002). In addition, better visualisation is obtained of urinary tract malignancies as there is minimal renal excretion of the tracer (de Jong *et al.*, 2002b).

Another study has compared methyl-^{11}C-choline uptake with histopathological specimens and gadolinium enhanced MRI, in 22 patients with brain tumours. The methyl-^{11}C-choline PET scans differentiated between high and low grade gliomas, and areas of methyl-^{11}C-choline accumulation were larger than areas enhanced with MR in some patients. However, methyl-^{11}C-choline was unable to distinguish low grade gliomas from benign lesions (Ohtani *et al.*, 2001). This suggests that a combination of methyl-^{11}C-choline PET scanning and MRI will allow more accurate diagnosis of high grade gliomas.

3.7.2 Multi-Drug Resistance

Acquired multi-drug resistance (MDR) represents a major cause of chemotherapy failure in cancer treatment with certain classes of drugs, in particular, compounds such as anthracyclines, vinca alkaloids and taxanes (Bellamy *et al.*, 1990; Zijlstra *et al.*, 1987). The molecular mechanism for this resistance has been identified as overexpression of the P-glycoprotein (Pgp), a plasma membrane transporter,

encoded for by the MDR gene (Germann *et al.*, 1993; Gottesman *et al.*, 1993). These proteins reduce intracellular accumulation of cytotoxic agents and diminish the efficacy of chemotherapy. Attempts have been made to examine this process further using radiolabelled pharmaceuticals, in conjunction with strategies to decrease the activity of Pgp. Technetium-99m Sestamibi (^{99m}Tc-Sestamibi), a substrate for Pgp, has been utilised in SPECT studies to image the blockade of the Pgp-mediated transport after suppression of the Pgp pump (Hendrikse *et al.*, 1999). *In vivo* PET studies involved in evaluation of MDR have been confined to experimentation in animals. ^{11}carbon ([^{11}C]-) labelled drugs such as ^{11}C-verapamil and ^{11}C-daunorubicin (Elsinga *et al.*, 1996) and ^{11}C-colchicine (Levchenko *et al.*, 2000) have been investigated and are additional tools for the quantification of Pgp-mediated transport with PET. A potential use of such agents would be to select patients who could benefit from the addition of Pgp modulators which are being designed (Brady *et al.*, 2001).

3.8 Summary

Huge advances have been made in molecular science to determine the complex processes underlying tumour biology with abnormal cellular and molecular pathways are being targeted to provide a novel and rational basis for cancer treatment. A fundamental change in the requirements of imaging is required to meet the current challenges posed by these new treatment strategies in cancer medicine and molecular imaging with PET is a valuable technique that can address many questions related to this emerging field.

Chapter 4 Methodology

4.1 Introduction

This chapter will describe the steps involved in the production of radionuclides, the scanning procedure and data acquisition that were required for the studies in this thesis. The methodology presented here is common to all studies but any deviations from the protocol will be outlined in the relevant chapters.

PET requires an expert, multi-disciplinary team and contributions made by other clinicians, chemists, physicists and technicians to the study are credited in the 'Acknowledgements' section.

All PET scans were performed in IMANET (formerly MRC) Cyclotron Building, Hammersmith Hospital, London, UK.

The projects reported in this thesis and radiotracers required for each are listed below:

1. Carbogen and nicotinamide modulation of 5-FU Pharmacokinetics and Perfusion.
    - 5-[^{18}F]FU and $H_2[^{15}O]$
2. Interferon-α modulation of 5-FU Pharmacokinetics and Perfusion.
    - 5-[^{18}F]FU and $C[^{15}O]_2$
3. Thymidine to Assess the Pharmacodynamic End-Point of Anti-Cancer Drugs.
    - 2-[^{11}C]thymidine, $H_2[^{15}O]$ and $H[^{11}C]O_3$

4.2 Ethics and ARSAC Approval

All study proposals were approved by the Hammersmith and Riverside Hospitals NHS Trust Research and Ethics Committee by for careful consideration and

alteration if necessary, before obtaining approval to commence the project and recruit patients. Permission was also granted from the Administration of Radioactive Substances Advisory Committee (ARSAC, UK) for the administration of radionuclides to ensure that the biological effective dose (BED) of radioactivity in the study was appropriate and relevant to the hypotheses being pursued in the studies.

4.3 Production of Radionuclides

The positron-emitting radionuclides required for PET imaging are produced by bombarding stable elements with high-energy beams of ionic particles accelerated by a cyclotron. Proton (p) bombardment of a nitrogen target results in the production of carbon-11 ([^{11}C] for thymidine studies) and an alpha (α) particle. Oxygen-15 (perfusion studies) results from deutron bombardment of a nitrogen target and fluorine-18 (for pharmacokinetic modulation studies) from proton bombardment of an oxygen target. Both reactions produce neutrons (n) in addition to the radionuclide. The nuclear reactions are summarised in Table 4.1.

Table 4.1: Summary of Nuclear Reactions for Production of Radionuclides used in the Studies

Nuclear Reaction	Radiolabelled Compound Produced
^{14}N (p,n) ^{11}C	[^{11}C] bicarbonate [^{11}C] thymidine
^{14}N (d,n) ^{15}O	[^{15}O] water [^{15}O] carbon dioxide
^{18}O (p,n)	[^{18}F] 5-fluoruracil

The Imanet Cyclotron Unit has two cyclotrons in use. The Scaditronix MC40 MK II cyclotron has a variable particle and energy machine capable of accelerating

helium-4 and helium-3 nuclei, protons and deutrons to produce several radionuclides (^{11}C, ^{18}F, ^{13}N, ^{15}O etc). This has now been replaced by the GE system. The second cyclotron is the smaller Cyclone 3D IBA cyclotron that is used only for the production of on-line ^{15}O-labelled compounds (carbon dioxide, $C[^{15}O]_2$ and water, $H_2[^{15}O]$).

4.4 Radiopharmaceutical Production

All radiopharmaceuticals in this study were produced on site using remote handling apparatus or automated synthesis techniques to ensure operator safety, as starting activities were high, at > 100GBq.

4.4.1 5-[^{18}F]Fluorouracil

In both 5-FU modulation studies, [^{18}F]fluorine produced in the cyclotron was passed through a suspension of the precursor, uracil (in acetic acid), which after rotatory evaporation (to remove acetic acid), was washed with ethanol (which was then evaporated). After the addition of KH_2PO_4 the mixture was heated and injected onto a high performance liquid chromatography (HPLC), from which the 5-[^{18}F]fluorouracil peak was eluted and filtered using Millipore® (see Figure 11 below).

This method, developed in the Cyclotron Unit by Dr Gavin Brown (Brown G. *et al.*, 1993) gave reliable yields of 5-[^{18}F]fluorouracil with high radiochemical purity and specific activity.

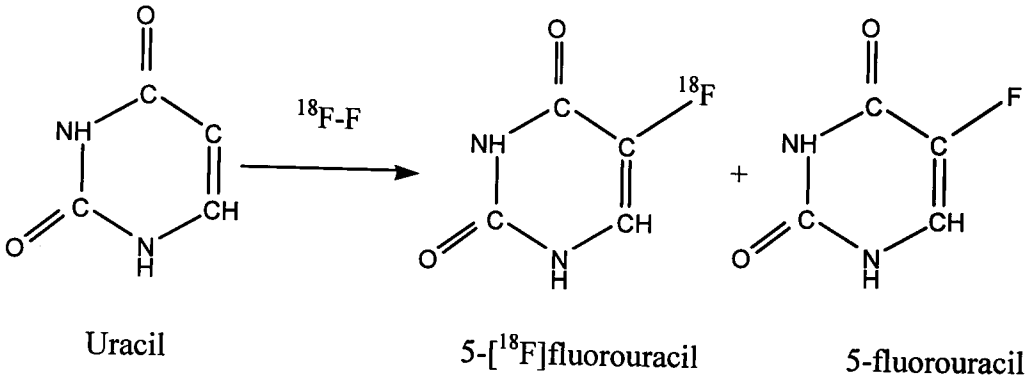


Figure 11: Radiosynthesis of 5-[^{18}F] fluorouracil

4.4.2 $H_2[^{15}O]$ and $C[^{15}O]_2$

Radiolabelled water ($H_2[^{15}O]$) was produced in a lead-shielded bed side unit by mixing [^{15}O] from the cyclotron with hydrogen over a palladium catalyst in an oven at 150^0 C. The gaseous output is led through a semi-permeable membrane on the other side of which is sterile saline which leads to the production of aqueous $H_2[^{15}O]$, which can then be given as an intravenous infusion.

For $C[^{15}O]_2$ production the [^{15}O] is exposed to a mixture of nitrogen and 1% CO_2 to produce radiolabelled carbon dioxide ($C[^{15}O_2]$).

4.4.3 2-[^{11}C]thymidine

Cyclotron produced [^{11}C] was exposed to a mixture of nitrogen and 5% hydrogen, to form [^{11}C]methane. From this, dry urea (the precursor of thymidine), is made by a number of steps via the production of phosphogene. 2-[^{11}C]thymine is converted to 2-[^{11}C]thymidine by a process of simple acid neutralisation, which is performed at room temperature (Steel *et al.*, 1999).

4.4.4 [^{11}C]HCO_3

Carbon dioxide ([^{11}C]O_2) was produced after bombardment of nitrogen containing 1% O_2 with protons. [^{11}C]O_2 from the cyclotron was then bubbled through an aqueous mixture of sodium bicarbonate for injection (8.4% BP) diluted with isotonic solution for approximately 2 minutes. The resulting solution was radiolabelled sodium bicarbonate ([^{11}C] sodium bicarbonate).

4.5 Quality Control

Radiotracers were transferred directly to the Quality Control (QC) laboratory after production to ensure the radiotracer fulfilled all the predetermined specifications required for injection or inhalation by the patient. Initially the radiotracer (5-[^{18}F]fluorouracil or 2-[^{11}C]thymidine) was analysed by HPLC and spectrometry to check for radiochemical purity. Any stable (i.e. non-radioactive) compounds were noted as well as the presence of other known or unknown impurities. Radioactivity was measured using a calibrated ionisation chamber. The radiotracer was then injected through a disposable filter in an exclusion chamber to obtain a sterile injectate. The pH of the radiotracer was quantified using pH indicator strips. Pyrogen assessments were performed after every 10 radiopharmaceuticals productions retrospectively using the Limulus amoebocyte lysate (LAL) pyrogen test.

[^{11}C]HCO_3 and C[^{15}O]$_2$ were tested for radiochemical purity and [^{11}C]HCO_3 and H_2[^{15}O] were tested for pH.

Only if the radiotracers met all the stringent requirements were they released for clinical injection or inhalation.

4.6 Quality Assurance

Each radiotracer had a detailed sheet listing every chemical necessary for its production and the conditions required to ensure stability (e.g. temperature, pH, expiry date etc) with a requirement by the relevant chemist to check each element during every run of radiotracer production.

4.7 Patient Recruitment and Preparation

Patients were recruited from Oncology out-patient clinics or wards at Charing Cross or Hammersmith Hospitals after permission from the Consultant Oncologist supervising the patients' treatment. On the initial meeting with the prospective patient details of the study and procedures were discussed and an information sheet given to them with a contact number for the investigators in case of further queries. At least 24 hours were given to allow for a decision to be made regarding participation. A similar procedure was undertaken for the study not conducted by the author. A consent form was signed by each patient for participation in the study with the understanding that the patient was free to withdraw from the trial at any time. All scans were performed as an out-patient at the Cyclotron Unit, Hammersmith Hospital, London, UK.

Each patient had a recent, diagnostic imaging scan (either CT or MRI) at the time of recruitment and this was used to locate the selected area to be scanned by PET. The central plane of this region was identified by x-ray simulation and was marked by a skin tattoo. The patients lay supine on the PET couch and were positioned by matching the skin tattoo to laser beams in the scanner. Patients were made comfortable on the scanning table with bolsters for knee supports and had the choice of listening to music or lying quietly. Patients were advised to keep still for the duration of the scan and were monitored by close circuit cameras to monitor any movement, which was documented as necessary. Before the radiotracer scan, a 20 minute transmission scan was performed for correction of tissue attenuation.

Prior to the scan patients had a 21 gauge Venflon inserted into their radial artery after performing the Allen's test to ensure patency of the ipsi-lateral artery and

infiltration of the skin with 1% bupivocaine for local analgesia. In the contra-lateral arm, a venous Venflon was inserted for radiotracer administration.

After receiving the radiotracer from QC, the radiotracer was either injected alone or in combination with unlabelled drug.

4.8 PET scanners

Studies were performed on two PET scan machines. Both 5-[^{18}F]FU modulation studies were carried out on the ECAT 931 scanner and the 2-[^{11}C]thymidine study on the ECAT 962 HR^{+} scanner.

4.8.1 ECAT 931 Scanner

The ECAT 931-08/12 PET scanner (CTI/Siemens , Knoxville, TN, USA) obtains images in a 2 dimensional (2D) mode and consists of eight rings of bismuth germanate (BGO) detectors which allow simultaneous acquisition from fifteen planes of data, eight from coincidences in the same plane (direct) and seven from coincidences in adjacent planes (cross). Each ring contains 512 BGO detector elements (4 096 in total), of the following dimensions: 5.6mm (transaxial), 12.9mm (axial) and 30mm (depth) and is separated from its neighbour by annular lead-tungsten septum with a retractable transmission source. Though the septa result in reduced camera sensitivity, they reduce registration of random and scatter coincidences and detector dead time. The axial field of view (FOV) is 10.8cm.

4.8.2 ECAT HR^{+} 962 Scanner

The ECAT EXACT HR+ 962 (CTI/Siemens, Knoxville, TN, USA) can acquire images in either 2D or 3D modes, but in the thymidine study only the 2D mode was utilised. The ECAT HR+ has 4 rings of detector blocks, with 8 rings of detector blocks each i.e. 32, with arrays of 8 x 8 elements each. Each ring block

has 72 blocks, composed of 576 elements, giving a total of 18 432 elements in all. Each element has dimensions of: 4.05mm (transaxial), 4.39mm (axial) and 30mm (depth). Again, each element is separated from its neighbour by annular lead-tungsten septum with a retractable transmission source. Furthermore, when the HR^+ scanner is operated in a 3D mode, the septa can also be removed. Images are simultaneously acquired in 63 planes, with an axial total detector length (FOV) is 15.5 cm. The transaxial FOV is 58.3 cm, with each detector element in coincidence with 288 elements i.e. half a ring.

4.9 Tissue Acquisition Protocols

Data from the dynamic PET scans were collected into specific time frame protocols for each radiotracer for the duration of the scan. At the beginning of the scan, time frames were short to permit sufficient temporal resolution of the early and rapid tissue activity. In the latter stages of the scan, time frames were longer to allow adequate and reliable counting from the detector system to maximise spatial resolution. This was because decay of the isotope contributes to poor counting statistics that occur particularly at the end of the study, and in order to reduce this effect, longer time frames are required at later time points.

Patients had the 10 minute perfusion scans ($H_2[^{15}O]$ or $C[^{15}O_2]$) first, followed by the 5-[^{18}F]FU, with a predetermined delay of 10 minutes between them, to ensure maximum decay of any residual $H_2[^{15}O]$ ($t_{1/2}$ = 2.03 minutes) radioactivity. Scanning protocols for radiotracer in each study is outlined below.

4.9.1 Carbogen and Nicotinamide Modulation Study

The perfusion study used $H_2[^{15}O]$ which was produced by a bed-side water generator and injected as a 20 second automated infusion followed by a 2 minute flush. The infusion was preceded by a 30 second background acquisition frame (see Table 4.3) and the scan lasted 10 minutes.

Table 4.3: $H_2[^{15}O]$ Scan Frame Protocol

Frame number	Frame duration (seconds)
1	30
2-18	5
19-21	10
22-26	30
27-32	60

5-[^{18}F]FU was combined with unlabelled 5-FU producing approximately 10mls of mixture which was injected over 30 seconds. Again, this was preceded by a 30 second background frame with shorter frames initially followed by frames of longer duration. The 5-[^{18}F]FU scan lasted 90 minutes.

Table 4.4: 5-[^{18}F]FU Scan Frame Protocol

Frame number	Frame duration (seconds)
1	30
2-10	30
11-15	60
16-20	120
21-25	180
26-31	600

4.9.2 Interferon-α Modulation Study

This study was performed in 1991 to1992 by Dr Robert Harte and differs from the current protocols used in the other two studies.

Perfusion was measured using C[$^{15}O_2$] (subsequently replaced by $H_2[^{15}O]$ since 1997 for ease of administration) and delivered via a light face mask (MC™

oxygen mask, Henley's medical, Welwyn, UK) at an activity of 4MBq/ml and a constant flow rate of 500 ml/min for 5 minutes. The scan lasted 10 minutes and time frames are shown below.

$C[^{15}O_2]$ is rapidly converted to $H_2[^{15}O]$ after inhalation by the action of carbonic anhydrase present in red blood cells making it a suitable radiotracer for measuring perfusion.

Table 4.5: $C[^{15}O_2]$ Scan Time Frames

Frame number	Frame duration (seconds)
1	30
2-7	5
8-13	10
14-19	20
20-21	10
22-23	20
24-27	30
28-30	60

5-[^{18}F]FU was administered as a 30 second bolus either alone or in conjunction with unlabelled 5-FU. The scan lasted 60 minutes and time frames are given below. The frame timings are slightly different from those in the carbogen and nicotinamide modulation study above. In the latter study, there is better temporal resolution of earlier data and a longer acquisition time as the 5-[^{18}F]FU scanning protocol was refined.

Table 4.6: 5-[^{18}F]FU Scan Frame Protocol

Frame number	Frame duration (seconds)
1-10	30
11-15	60
16-20	120
21-25	180
26-30	300

4.9.3 2-[^{11}C]thymidine Study

2-[^{11}C]thymidine was injected as a bolus over 30 sec after a 30 sec background scan. The scan lasted 60 min and the frames and durations are shown below.

Table 4.7: 2-[^{11}C]thymidine Scan Frame Protocol

Frame number	Frame duration (seconds)
1	30
2-10	30
11-15	60
16-20	120
21-25	180
26-30	300

After a 20 minute delay to allow for radioactive decay of 2-[^{11}C]thymidine ($t_{1/2}$ = 20.4 min) the 2nd radiotracer, [^{11}C]HCO_3, was injected as a 30 second bolus. Frame details are given in Table 4.8 and were designed to detect early rapid delivery of tracer to tissue followed by a plateau phase. Total scanning time was 62 minutes.

Table 4.8: [^{11}C]HCO_3 Scan Frame Protocol

Frame number	Frame duration (seconds)
1	30
2-7	30
8-13	10
14-19	20
20-25	30
26-29	300
30-33	600

4.10 Tissue Data Calibration and Reconstruction

Acquired coincidences described above were stored as two-dimensional matrices referred to as a sinogram. However, before reconstruction the sinogram data had to be corrected to take into account factors such as detector non-uniformity of response, scatter and attenuation of photons within the body, random counts and dead time correction and calibration.

4.10.1 ECAT 931 PET scanner

On this scanner normalisation factors were calculated on a daily basis after the acquisition of a 'blank' scan and used to correct for detector non-uniformity. The 20 minute transmission scan performed with the patient in position on the scanner before radiotracer administration was used as a ratio with the 'blank' scan to provide a factor for tissue attenuation. Both transmission and 'blank' scan were performed using eight retractable ^{68}Ge sources encased in steel rings. No scatter correction was applied to images acquired on the ECAT 931 machine.

Sinograms were reconstructed into tomographic images using a filtered back projection technique after transfer to Sun SPARC® Workstations (Sun Microsystems, Mountain View, CA, USA). A Hann filter with 0.5 of the Nyquist frequency was used as cut-off for reconstruction of the images. After

reconstruction each frame was presented as a 128 x 128 pixel image, with a voxel dimension of 2.1 mm x 2.1 mm. Spatial resolution of the final reconstructed image was 8 mm (FWHM) at the centre of the FOV with slice thickness of 6.4mm.

Tissue data was calibrated to obtain quantitative data. Calibration was checked every 3 months by scanning a ^{68}Ge containing phantom over a weekend and comparing radioactivity concentration obtained from the tomograph with that measured in a cross calibrated well counter.

4.10.2 ECAT HR+ 962 PET scanner

Again, normalisation factors were calculated on a daily basis after the acquisition of a 'blank' scan and used to correct for detector non-uniformity. The 20 minute transmission scan performed as on the ECAT 931 scanner.

As described above, sinograms were reconstructed into tomographic images using a filtered back projection technique after transfer to Sun SPARC® Workstations (Sun Microsystems, Mountain View, CA, USA) using a ramp filter. After reconstruction each frame was presented as a 128 x 128 pixel image, and using a zoom factor of 2, the in plane voxel size is 2.62 mm x 2.62 mm. Spatial resolution is 8 mm at the centre of the FOV. Slice thickness is 4.2 mm (FWHM) at the centre of the FOV and 5.2 mm at a 10 cm radius.

4.11 Blood Data Acquisition

Arterial blood samples were obtained from the indwelling radial catheter. Arterial blood sampling gives the closest approximation of the delivered concentration of radiotracer and metabolites to the capillaries in tissue.

Continuous blood sampling was performed for the duration of the scan using a peristaltic IVAC® pump which drew blood from the patient via a short length of plastic tubing (PTFE) to a calibrated BGO scintillation detector, to obtain a continuous measure of whole blood radioactivity (Ranicar ASO. *et al.*, 1991). The

pump was set at different rates according to the radiotracer injected (see Table 4.9 below).

Table 4.9: Pump Settings for Radiotracers Used in the Studies

Radiotracer	Pump Velocity and Duration
$H_2[^{15}O]$	• 5 ml/min for 10 min
$C[^{15}O_2]$	• 5ml/min for 10 min
5-[^{18}F]FU (Carbogen and Nicotinamide study)	• 5 ml/min for first 10 min • 2.5ml/min for last 80 min
5-[^{18}F]FU (Interferon-α study)	• 5 ml/min for first 10 min • 2.5ml/min for last 50 min
2-[^{11}C]thymidine	• 5 ml/min for first 10 min • 2.5ml/min for last 50 min
[^{11}C]HCO_3	• 5 ml/min for first 10:30 min • 2.5ml/min for last 51:30 min

The continuous blood sampling was interrupted at specific times to collect discrete blood samples of approximately 5 ml each down stream from the BGO counter through a 3-way tap, according to the radiotracer injected.

Table 4.10: Pump Settings for Radiotracers Used in the Studies

Radiotracer	Time of Discrete Sample(s) After Scan Start
$H_2[^{15}O]$	6 min
$C[^{15}O_2]$	6 min
5-[^{18}F]FU (Carbogen and Nicotinamide study)	5, 10, 15, 30, 45, 60, and 90 min
5-[^{18}F]FU (Interferon-α study)	5, 10, 20, 30 40 and 60 min
2-[^{11}C]thymidine	1.30, 2.30, 3, 6, 7.30, 9, 15, 30 and 60 min
$[^{11}C]HCO_3$	1.30, 5, 10:30,15,30 and 60 min

The discrete blood samples were collected for several purposes: (1), to determine the partitioning of radioactivity between whole blood and plasma, (2), to analyse the percentage of radiolabelled parent and metabolite in the plasma (where necessary) and (3), to calibrate the radioactive counts of the continual on-line system. In addition, in the 5-[^{18}F]FU (carbogen and nicotinamide study), each discrete blood sample was analysed for haematocrit, pO2 (mmHg), pCO2 (mmHg), glucose (mmol/l) and pH using an AVL electrolyte analyser (AVL Medical Instruments UK Ltd). In the 5-[^{18}F]FU studies, the initial discrete samples were obtained as drip samples to prevent disruption of the rapidly altering early continuous radioactive counts.

The start and finish of collection of the discrete blood samples was documented by the press of a foot switch attached to a computer, which recorded times from scan start. The mid-withdrawal time was single point taken to represent sampling time. All samples were corrected for radioactive decay, counter dead time, background activity, sample volume and density.

To preserve the patency of the arterial cannula during the scan, 10 ml of heparinised saline was periodically used to flush the indwelling Venflon. This involved suspending the on-line radioactivity counts for approximately 15-30 second whilst injecting the flush.

Regular calibrations were performed on the well counters, BGO detectors and PET cameras to produce quantitative blood data.

4.11.1 Metabolite Analysis of Discrete Blood Samples

Metabolite analysis was necessary immediately after collection due to the short $t_{1/2}$ of the radiotracer employing on-site technicians and facilities. After centrifugation of discrete samples, metabolite analysis was performed on the plasma samples obtained using HPLC, and was monitored by ultraviolet (UV) absorbance and radioactivity detection. The UV and radioactivity detectors were connected to a PC-based integrator (Labchrome software: Lablogic), which enables correction for background activity, radioactive decay and can calculate peak area for both radiolabelled parent and metabolites.

4.11.2 5-[^{18}F]FU analysis

5-[^{18}F]FU is metabolised to various cytotoxic anabolites and catabolised principally to the inactive α-fluoro-β-alanine or FBAL (see Chapter 5). To measure the contribution of parent 5-[^{18}F]FU radioactivity alone, the plasma samples were processed and analysed. Each plasma sample was deproteinised with ice cold methanol and then centrifuged again. The supernatant was concentrated by rotatory evaporation and the residue dissolved in HPLC mobile phase and filtered. The filtrate was analysed on a reverse-phase C_{18}μ-Bondapak column (300 x 7.8 mm; 10 μm), using a mobile phase comprising 5mM octane sulphonic acid and phosphoric acid (pH = 3.0), delivered at a flow rate of 3ml/min, to identify and quantify parent 5-[^{18}F]FU.

4.11.3 2-[^{11}C]thymidine metabolite analysis

2-[^{11}C]thymidine is rapidly degraded to four main metabolites: thymine, dihydrothymine (DHT), β aminobutyric acid and finally, carbon dioxide

($[^{11}C]O_2$). The main metabolite is $[^{11}C]O_2$, which accumulates in blood and expired air and is the major labelled metabolite signal in tissue. Its contribution to the blood signal was measured in discrete samples using Shields' method (Shields AF. *et al.*, 1998b). An aliquot of blood is taken from the discrete sample and mixed with sodium hydroxide, which traps the $[^{11}C]O_2$, such that all the radioactivity is attributable to $[^{11}C]$ (C_{total}). A second aliquot of blood is taken from the same sample to which isopropanol is added, following which the mixture is acidified with hydrochloric acid and nitrogen bubbled through it to release the available $[^{11}C]O_2$ (C_{rem}). From this, the percentage of $[^{11}C]O_2$ (C_{CO2}) in the sample can be given as:

$$C_{CO2} = C_{total} - C_{rem} / C_{total}$$

Parent radiotracer and remaining radioactive metabolites were quantified in a third aliquot of blood by removing plasma proteins by mixing with methanol, which extracts 98% of the radioactivity into the methanol supernatant. This supernatant was then concentrated and the residue containing 2-$[^{11}C]$thymidine and radioactive metabolites was injected onto a HPLC column, analysed and quantified.

4.11.4 Processing Blood Data

From the arterial blood data, the following measurements were made:

- a continuous measure of total blood radioactivity collected on-line from the patient for the entire scan
- a measure of the portioning of radioactive counts between plasma and whole blood at certain time points, which does not remain constant through the study, but is dependent on the radiotracer
- a measure of the plasma parent and metabolite radioactivity at certain time points

From these measurements it is possible to derive plasma activity of (P) from whole blood at time (t) by the following equation;

$$P(t) = PBR_{counts}(t) \times WB(t)$$

Where, $PBR_{counts}(t)$ = ratio of radioactivity in plasma/ radioactivity in whole blood, at time (t) and WB (t) = radioactivity in whole blood from on-line counter, at time (t).

A continuous plasma input function could then be generated. This first required the continuous radioactivity count to be modified to remove the discontinuations incurred from flushing the catheter, as described previously. This was corrected for by linear interpolation between the gaps where radioactivity count recording were interrupted. The plasma input function was generated with in-house software GENIF (Version 3, MRC UK) using the continuous radioactivity curve and plasma/blood radioactivity ratio. A continuous parent plasma input function could then be produced using the parent (and metabolite fractions if required) analysed also from discrete samples, with GENIF 3.

4.12 Analysis of PET Tissue Data

4.12.1 Tissue sampling and analysis

Tumour and normal tissue were sampled using a 'Region of Interest' (ROI) technique on a Sun Solaris workstation (Sun Microsystems, Mountain View, CA, USA). To define a ROI on the PET image, a recent CT or MRI scan was used to assist delineation of tumour and normal tissue areas. The ROIs were drawn manually on composite PET images (or 'add' image) which were created from the summation of individual PET time frames for each plane. This produced less noise and gave better anatomical detail than separate frames from the dynamic scan.

The ROIs defined on the composite image, the 'object map' was then applied to the dynamic scan for sampling, and the mean pixel radioactivity count from individual time frames was calculated, at the mid-frame time point.

ROIs were analysed using Analyze® (Biomedical Imaging Resource, Mayo Foundation, Rochester, MN, USA). Statistics generated from this were used to produce independent dependent weight code (.idwc) for every ROI using

Interactive Data Language (ILL, Research Systems Inc) on which PET analysis could be performed.

4.12.2 ROIs

Accurate ROI definition is essential to avoid errors in sampling or blurring of edges due to partial volume effect. Manually drawn ROIs are prone to operator subjectivity though Harte et al (Harte R. *et al.*, 1998) showed that inter-observer variations were small compared to actual differences between studies.

To minimise sampling variability, certain principles were implemented when defining a ROI:

- the top and bottom plane of the scan were not used for sampling
- the same person drew all ROIs in the studies (i.e. the author)
- a ROI was defined according to anatomical information and not on 'hot' or 'cold' spots on the PET image.

4.13 Modelling Of Tissue Data

Analysis of tissue data alone is called semi-quantitative analysis and gives rise to standardised uptake value (SUV) and area under the curve (AUC) as described in chapter 3 and were obtained for both 5-[^{18}F]FU and 2-[^{11}C]thymidine. To derive these parameters, first a tissue radioactivity curve (TAC) was generated by plotting the mean tissue radioactivity versus mid-frame time (MFT) for each ROI, using Microsoft Excel software (Microsoft Corporation, USA). The TAC was corrected for radioisotope decay, injected dose and body surface area (BSA) for each patient. From this, an early time point of 3.75 min i.e. $SUV_{3.75min}$ (m^2/ml) was calculated to give a measure of delivery of radiotracer to tissue. AUC (m^2/ml/sec) was determined by summating the mean radioactivity at all MFTs for the duration of the scan, to give a measure of tissue exposure to the radiotracer.

4.14 Modelling of Tissue and Blood Data

4.14.1 Tissue Perfusion

Tissue perfusion was quantified from the $H_2[O^{15}]$ and $[^{11}C]O_2$ scans combining tissue and blood data by the dynamic flow method (see Chapter 3 for details) using GENIF3, an in-house software. Two parameters were obtained: flow, a measure of tissue perfusion ($ml_{blood}/min/ml_{tissue}$) and volume of distribution (V_d; ml_{blood}/ml_{tissue}), for tumour, spleen and kidney where possible. These parameters were also calculated for the liver, but give only an index of perfusion and V_d as the liver has a dual blood supply (see Chapter 6).

4.14.2 5-[^{18}F]FU Studies

4.14.2.1 Patlak Analysis

This graphical, non-compartmental modelling approach is discussed in detail in Chapter 2. As 5-[^{18}F]FU is metabolised, the modified version of Patlak (Mankoff *et al.*, 1996) was performed after generating a Patlak plasma input function (comprising cumulative parent 5-[^{18}F]FU and total 5-[^{18}F]FU in plasma over time) and utilising tissue ROIs already obtained using in-house software. K_I ($ml_{blood}/min/ml_{tissue}$) was derived from this analysis and represents the net irreversible clearance of radiotracer form plasma into tissue and represents retention of radiotracer in tissue.

4.14.2.2Spectral Analysis

This data-led modelling technique requiring few *a priori* assumptions is fully outlined in Chapter 2 and was performed using in house soft-ware. Spectral analysis was used to determine K_1 ($ml_{blood}/min/ml_{tissue}$), which is the unidirectional clearance of radiotracer form plasma to tissue i.e. delivery of radiotracer to tissue. K_1 was analysed using ROI data and two input functions: parent plasma and total

plasma, and is discussed in chapters 6 and 7. Fractional retention of 5-[^{18}F]FU (FRF) was calculated from spectral analysis by dividing an early impulse response function (i.e. IRF_{1min}) by a late IRF according to scan duration (i.e. IRF_{90min} or IRF_{60min}) to exclude the influence of delivery of the radiotracer on retention. The permeability and surface area product (PS) a combination of two variables: capillary surface area and capillary permeability, was calculated from K_1 and tissue perfusion.

4.14.3 2-[^{11}C]thymidine Study

4.14.3.1Spectral Analysis

As mentioned previously, 2-[^{11}C]thymidine is rapidly catabolised via a series of intermediate metabolites to [^{11}C]O_2, the main metabolite. Whilst blood data can be corrected for the contribution of [^{11}C]O_2, PET tissue data cannot distinguish radiolabelled parent from radiolabelled metabolites. This necessitates a tissue metabolite scan to provide information on tissue handling of [^{11}C]O_2 and hence the [^{11}C]HCO_3 was performed as a metabolite correction scan. Injected [^{11}C]HCO_3 rapidly equilibrates with [^{11}C]O_2 by the action of carbonic anhydrase (present in red blood cells) in the following equation:

$$[^{11}C]HCO_3 \xleftrightarrow{\text{carbonic anhydrase}} H_2O + [^{11}C]O_2$$

Analysis of the 2-[^{11}C]thymidine is complex and will be discussed in depth in chapter 8. Briefly however, an IRF for the [^{11}C]HCO_3 scan is derived as above, from which the metabolite contribution of [^{11}C]HCO_3 is convolved using the IRF from the [^{11}C]HCO_3 scan and the metabolite input function from the 2-[^{11}C]thymidine scan. Subtraction of the tissue [^{11}C]HCO_3 activity from the total tissue activity in the 2-[^{11}C]thymidine leaves tissue thymidine activity (and intermediate catabolites) only. From this, K_1 and fractional retention of thymidine (FRT) using IRF_{1min}/IRF_{60min} is calculated again on in-house software.

4.15 Statistical Analysis

Statistical analysis was performed using STATA® version 5.0 software (Stata Corporation, College Station, TX, USA). In the 5-[^{18}F]FU biomodulation studies data is presented as mean and standard error of the mean (SEM) and 95% confidence limits ([95%CI]). The null hypothesis of no difference between the paired studies after modulation was tested using the Wilcoxon matched pairs signed rank test. A probability of a p value ≤ 0.05 was considered significant. The mean percentage difference was also calculated for paired data pre and post modulation. Within the same data sets, two different input functions were used to calculate parameters derived from spectral analysis. This was analysed using the Mann Whitney U test, a non-parametric test for unpaired data.

Chapter 5 PET Pharmacokinetics and 5-[^{18}F]fluorouracil

5.1 Introduction

Pharmacokinetics is the study of absorption, distribution, metabolism and excretion (ADME), processes that are responsible for the fate of the drug in the body. Drug studies to obtain tissue pharmacokinetics are conventionally acquired from serial plasma samples or urine collection which are analysed using sensitive and specific techniques such as high performance liquid chromatography (HPLC) and gas- or liquid spectrometry, from which tissue kinetics can be inferred. Alternatively, tissue biopsies can be performed to directly measure tissue pharmacokinetics. However, this is associated with several difficulties. Tissue biopsies, whether single or multiple, are not practical for clinical studies and may not even be possible in certain tumour sites, with the inherent problem of tissue heterogeneity present. Problems also exist in analysing multiple sites of disease and normal tissue such as kidney and liver.

Radiolabelled 5-fluorouracil (5-FU) in the form 5-[^{18}F]fluorouracil (5-[^{18}F]FU) has been extensively studied in some centres using PET to derive tissue pharmacokinetics in tumour and normal tissues. This chapter will discuss 5-FU, its modes of action, metabolism, clinical results and need for manipulation to improve effectiveness. The background of 5-[^{18}F]FU will also be discussed with particular relevance to its role in assessing the modification of 5-FU which will be discussed in subsequent chapters.

5.2 5-Fluorouracil

5.2.1 Mechanism of Action

5-Fluorouracil (5-FU) is a cytotoxic chemotherapeutic agent that has been in use in clinical oncology for over 40 years (Schilsky RL. *et al.*, 2002). 5-FU has been

employed in the treatment of a wide range of cancers, including gastrointestinal, breast and most frequently, in colorectal cancer for which it is the single most important drug. 5-FU is a fluorinated pyrimidine that was developed following the observation that in rat hepatomas, the pyrimidine uracil was utilised more rapidly than in normal tissue, indicating that uracil metabolism was a potential source for antineoplastic chemotherapy (Rutman *et al.*, 1954). 5-FU is classified as an anti-metabolite due to its ability to inhibit biosynthetic processes and/or by its incorporation into DNA and RNA with disruption of their normal function.

5-FU requires conversion to a number of nucleotides to exert its effect on DNA or RNA. After entering a cell using the same facilitated transport mechanism as uracil, 5-FU undergoes anabolism via a number of pathways (see Fig 12). 5-fluorouridine-5'-triphosphate (FUTP) formed directly or indirectly is misincorporated into different RNA fractions (Shani *et al.*, 1984) causing impaired synthesis of RNA at several levels including errors of base pairing during RNA transcription.

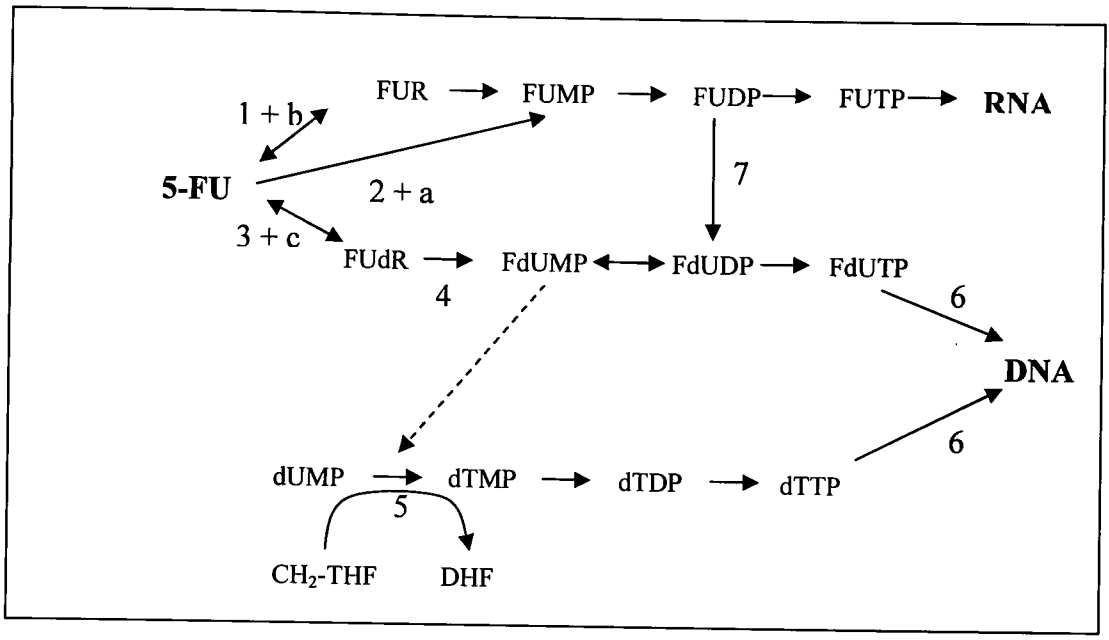


Figure 12: Anabolism of 5-FU

Enzymes: 1. Uridine Phosphorylase; 2. Orotate phosphoribosyltransferase; 3.Thymidine Phosphorylase; 4. Thymidine kinase; 5. Thymidylate synthase; 6. DNA polymerase; 7. Ribonucleotide reductase

Co-factors: a. Phosphoribosyl pyrophosphate; b. ribose-1-phosphate; c. deoxyribose-1-phosphate; DHF: dihydrofolate; CH_2-THF: 5,10-methylenetetrahydrfolate

Abbreviations: FUR: 5-fluorouridine; FUMP: 5-fluorouridine-5'-monophosphate; FUDP: 5-fluorouridine-5'-diphosphate; FUTP: 5-fluorouridine-5'-triphosphate; FUdR: 5-fluoro-2'-deoxyuridine; FdUMP: 5-fluoro-2'-deoxyuridine-5'-monophosphate; FdUTP: 5-fluoro-2'-deoxyuridine-5'-diphosphate; FdUTP: 5-fluoro-2'-deoxyuridine-5'-triphosphate; dUMP: 2'-deoxyuridine-5'-monophosphate; dTDP: 2'-deoxythymidine-5'-diphosphate; dTTP: 2'-deoxythymidine-5'-triphosphate

It has long been recognized that inhibition of thymidylate synthase (TS) by FdUMP is the principle mechanism of cytotoxicity of 5-FU (Danenberg, 1977). TS catalyses the reductive methylation of deoxyuridine monophosphate (dUMP) to deoxythymidine monophosphate (dTMP), with the reduced folate 5,10-methylenetetrahydrfolate (CH_2-THF) as the methyl donor and, as can be seen from Figure 12, this is a pivotal step in the synthesis of thymidine and eventually DNA. FdUMP forms a stable ternary complex with TS and CH_2-THF thus

preventing the normal substrate dUMP, from binding to it (Santi *et al.*, 1974). The exact molecular mechanisms that mediate events downstream of TS inhibition are not fully understood. Reduced levels of dTMP and subsequently dTTP induce imbalances in the pool of other deoxynucleotides (dATP, dGTP, dTTP). This disturbance is thought to disrupt DNA synthesis and repair leading to lethal DNA damage (Houghton *et al.*, 1995). Furthermore, elevated levels of dUMP may result in an increase in deoxyuridine triphospahte (dUTP). Both dTTP and FdUTP can be incorrectly incorporated into DNA and if not successfully repaired, ultimately results in DNA strand breaks and cell death (Longley *et al.*, 2003).

5.2.2 Plasma Pharmacokinetics

The plasma half-life of 5-FU is approximately 6 to 20 minutes though this varies between patients. After 6 hours of administration, plasma concentrations fall to below 1 μM, which is below the threshold for *in vitro* cytotoxicity (Abernethy *et al.*, 1989) and can be detected for several days (Peters *et al.*, 1993). Increasing the dose of 5-FU leads to a non-linear increase in plasma half-life probably as a result of saturation of metabolic or transport mechanisms. 5-FU clearance rates vary reflecting administration by intravenous bolus or as a continuous infusion. A linear increase in steady state concentration (C_{ss}) with dose is seen with protracted continuous infusions (Erlichman *et al.*, 1986).

5.2.3 Catabolism and Excretion

Up to 80% of systemic 5-FU is primarily catabolised by dihydropyrimidine dehydrogenase (DPD) to α-fluoro-β-alanine (FBAL), urea and CO_2 via 5-fluorodihydrouracil (F-DHU). DPD is a NADPH-dependent, rate limiting enzyme and is involved in the degradation of other pyrimidine bases including 5-FU (Pinedo, 1988). The highest levels of DPD are found in liver (which contributes to the majority of 5-FU metabolism) and peripheral blood lymphocytes as well as in the kidney, intestine and lung with small amounts present in tumours (Naguib *et*

al., 1985). Variable levels of DPD are found in gastrointestinal mucosa which is likely to contribute to the high variability in bioavailabilty of oral 5-FU. In addition, DPD exhibits a circadian cycle and may be responsible for the differences in 5-FU clearance in 5-FU infusions. A small percentage of the population have a profound deficiency of DPD and experience severe toxicity with standard doses of 5-FU (Milano *et al.*, 1994). FBAL is excreted in urine and has a plasma half-life of approximately 33 hours. 20% of 5-FU is excreted unchanged in urine and this is increased to 90% in those patients with DPD deficiency.

5.2.4 5-FU and Use in Oncology

5-FU has been used in the treatment of many tumour types including breast and gastrointestinal tumours. Although it dominates the treatment of colorectal cancer, the response rates when 5-FU is given as a single agent in advanced disease remains poor, at 15% (Cancer *et al.*, 1992; Meta-analysis *et al.*, 1998). This poor response rate has initiated research into approaches to increase therapeutic index. Increasing the plasma levels of 5-FU can improve response and survival in patients (Milano *et al.*, 1994). However, additional improvements in 5-FU efficacy by increasing plasma drug levels further are limited by dose-limiting normal tissue toxicity, and other approaches for enhancing the efficacy of 5-FU are required. Strategies were therefore developed to address and attempt to overcome the pharmacokinetic restrictions of systemic 5-FU, namely short biological half-life and S-phase dependency, which limit the drugs exposure and tumour cell kill (Leichman, 1999; Lokich *et al.*, 1989). Schedule alteration was one strategy employed to overcome this comparing intravenous bolus administration to continuous infusions of 5-FU. A meta-analysis examining this found response rates of 14% for bolus compared to 22% continuous infusion which also produced less toxicity, but overall survival rates were similar in both groups (Meta-analysis *et al.*, 1998). Other tactics have explored chronomodulation (Levi *et al.*, 1995) to coincide chemotherapy delivery with circadian variation in drug metabolism and cell cycle metabolism, but even though this approach has

produced superior results, the complexity of this technique has impeded clinical use. Another meta-analysis looking at biochemical modulation of 5-FU found that the addition of leucovorin or folinic acid, (which potentiates the inhibition of thymidylate synthase), doubled tumour response rates but without any substantial improvement in survival. This combination is now widely used as first line treatment in the adjuvant and metastatic setting (Cancer *et al.*, 1992). Recent data suggest that combining 5-FU and folinic acid with irinotecan and oxaliplatin, two relatively new chemotherapy agents, lead to an increase in response rates with a modest but significant improvement in survival compared to 5-FU and folinic acid alone (de Gramont *et al.*, 2000; Douillard *et al.*, 2000; Saltz *et al.*, 2000).

There is still a continuing clinical need to develop strategies to enhance 5-FU efficacy. The following section will discuss the development of PET imaging of 5-[^{18}F]FU and the contribution it has made to understanding 5-FU pharmacokinetics.

5.3 [^{18}F] Radiolabelled 5-FU and PET Imaging

5-[^{18}F]FU has been the most studied anti-cancer drug by PET in animals and man. One reason is that the chemical synthesis of 5-[^{18}F]FU is fully automated, leading to rapid and efficient production of 5-[^{18}F]FU with high specific activity and radiochemical purity (Brown G. *et al.*, 1993). 5-[^{18}F]FU has a favourable half-life of 110 minutes allowing kinetic studies to be performed.

5-[^{18}F]FU biodistribution was first measured in mice (Shani J. *et al.*, 1977) with subsequent studies to establish 5-[^{18}F]FU dosimetry and pharmacokinetics in humans (Shani J. *et al.*, 1982). Harte et al has produced good reproducibility data for 5-[^{18}F]FU kinetic studies (Harte R. *et al.*, 1998), confirming that PET imaging could be used to monitor *in vivo*, 5-[^{18}F]FU pharmacokinetics in tumour and normal tissue.

Pharmacokinetic studies with 5-[^{18}F]FU have shown a high signal intensity in normal liver which has been attributed to formation and retention of [^{18}F]FBAL from 5-[^{18}F]FU metabolism in the liver . Analysis of arterial plasma confirmed the presence of 5-[^{18}F]FU and high levels of [^{18}F]FBAL in the circulation (Kissel *et al.*, 1997). This is consistent with data obtained with 19F-magnetic resonance spectroscopy (19F-MRS) which detected high levels of FBAL in the liver (Brix G. *et al.*, 1998). 5-[^{18}F]FU PET scans have shown increased uptake in the kidney with time (Saleem A. *et al.*, 2000), reflecting the established route of elimination of 5-FU and associated metabolites (Heggie G. *et al.*, 1987). Dimitrakopoulou et al evaluated 50 patients with colorectal cancer and hepatic metastasis using PET scanning after infusion of 5-[^{18}F]FU in which they demonstrated a low but highly variable uptake of 5-[^{18}F]FU in the liver metastases (Dimitrakopoulou *et al.*, 1993). In addition they found a correlation between SUV at 20 minutes (reflecting 5-FU transport or influx of drug) and SUV at 120 minutes (representing trapped 5-FU). This was also significantly correlated with regional blood flow measured with ^{15}O-water in a subgroup of patients.

Similar results were found in a study using 5-[^{18}F]FU PET scanning to assess the biomodulation of 5-FU pharmacokinetics by N-phosphonoacetyl-L-aspartate (PALA), folinic acid and α-interferon in tumour and normal tissue in patients with gastrointestinal malignancy. In this study by Harte et al, pooled data demonstrated a significant correlation between tumour blood flow, early tissue exposure (AUC_{8min}) and late tissue exposure (AUC_{60mins}) of 5-[^{18}F]FU, suggesting the importance of drug delivery in initial drug uptake and its intratumoural retention up to 1 hour after administration (Harte R. *et al.*, 1999).

A pharmacodynamic relationship between tumour uptake of 5-FU and response first seen in mice (Shani J. *et al.*, 1977) has been reproduced in man using PET methodology. A group in Heidelberg found that colorectal liver metastasis with a high uptake of 5-[^{18}F]FU at 2 hours, as indicated by a standardised uptake value (SUV) of more than 3, had a negative growth rate, whereas those with an SUV of less than 2, had tumour progression (Dimitrakopoulo-Strauss A. *et al.*, 1998). This was further supported by work from Kissel et al who first demonstrated the ability to perform complex mathematical modelling on clinical oncology PET data to

obtain tumour and normal tissue pharmacokinetic parameters using a six-compartment model to quantify intracellular 5-[^{18}F]FU concentrations in hepatic metastases after 5-[^{18}F]FU PET scanning. This group found the rate constants for transport into (k_{in}) and out (k_{out}) of the intracellular compartment were the most sensitive parameters to describe tumour response. The criteria for 'trapping' of 5-FU in tumours ($k_{in} > k_{out}$) was met in 6/27 metastases in patients receiving 5-FU and in 5/6 metastases showing 'trapping' of 5-FU, were in patients receiving 5-FU and folinic acid (Kissel *et al.*, 1997). ^{19}F MRS studies have validated the PET association of 5-FU trapping and tumour response by showing that an increase in intra-tumoural half-life of 5-FU was correlated with clinical response in man (Presant C. *et al.*, 1990; Presant C. *et al.*, 1994).

Saleem *et al* investigated the mechanism of action of eniluracil, a known inactivator of the proximal and rate limiting enzyme, dihydropyrimidine dehydrogenase (responsible for the degradation of 5-FU) using 5-[^{18}F]FU PET scans (Saleem A. *et al.*, 2000). In eniluracil-naïve patients, there was strong localisation of 5-[^{18}F]FU derived radioactivity in the liver as expected due to rapid formation and retention of [^{18}F]FBAL. Following eniluracil administration, there was a marked reduction in radiotracer uptake in the liver and kidney suggesting a decrease in production of FBAL due to eniluracil activity, which was corroborated by a corresponding increase in plasma uracil and unmetabolised 5-[^{18}F]FU. In tumour, the half-life of 5-[^{18}F]FU increased from 2.3 to over 4 hours after eniluracil administration. Following metabolite correction, the levels of 5-[^{18}F] FU and anabolites in plasma were found to be higher after eniluracil treatment. This study provided proof of principle of the mechanism of action of eniluracil. The data was analysed further using spectral and Patlak models, which have less inherent assumptions than a compartmental approach, to calculate other pharmacokinetic parameters of 5-FU. Aboagye et al found that net clearance of 5FU from plasma to tumour was 0.0033 ± 0.0005 ml_{plasma}/ min/ml_{tissue} and was 200-fold less than the initial (10 min) clearance through catabolism by the liver. This study has shown that the cytotoxicity of 5-FU in patients with gastro-intestinal cancer could be compromised by its intrinsically low uptake by tumours, as well as decreased systemic availability from hepatic clearance (Aboagye EO. *et al.*, 2001).

In this thesis, PET imaging using 5-[^{18}F]FU has been used to measure the effect of physiological (with carbogen and nicotinamide) and biochemical (with α-interferon) modulation on 5-FU pharmacokinetic parameters and will be discussed in the following two chapters.

Chapter 6 Carbogen and Nicotinamide Modulation of 5-FU

6.1 Introduction

Solid tumour masses typically exhibit abnormal blood vessel networks. The blood flow associated with this heterogeneous vasculature is often disordered compared with normal tissues because of a variety of functional and structural irregularities created in the malignant tissue by new vessel formation (Vaupel P. *et al.*, 1989). This can substantially reduce perfusion in tumours which results in restricted and impaired drug delivery, and has been postulated as one reason for poor response rates of solid tumours to systemic chemotherapy (Siemann, 1998). Previous work by the MRC Hammersmith has underlined the importance of blood flow in determining initial 5-[^{18}F]FU uptake and retention in tumour at 1 hour (Harte R. *et al.*, 1999). Strategies to investigate improvements in drug delivery to tumours by altering tumour blood flow, without affecting systemic exposure to the drug, are being explored.

Carbogen, a gas comprising either 95% oxygen and 5% carbon dioxide or 98% oxygen and 2% carbon dioxide, in combination with nicotinamide, the amide derivative of vitamin B_3, have generated interest in this area. Carbogen and nicotinamide have so far primarily been used in conjunction with radiotherapy as an approach to reducing tumour hypoxia (Rojas A. *et al.*, 1996), an important factor in cancer treatment resistance (Gray *et al.*, 1953; Mottram, 1936), and for improving radiotherapy response (Bernier *et al.*, 2000; Hoskin *et al.*, 1999; Rubin *et al.*, 1979). Whilst the use of carbogen and nicotinamide in radiotherapy stems from their independent ability to increase blood oxygenation in tumours by a variety of pathways, using this combination as an adjunct to improving drug delivery lies in their probable inherently related mechanisms of action on blood vessels and tissue perfusion.

Carbogen has been documented to have an influence on blood flow since 1967 (Kruuv *et al.*, 1967), and is generally considered to inhibit hyperoxia induced vasoconstriction by the action of the carbon dioxide component (Kety S. *et al.*, 1948) and to facilitate capillary recruitment (Chen J. *et al.*, 1994) as a way of altering blood vasculature dynamics in normal tissues. There have been

conflicting reports on the outcome of carbogen breathing on blood flow in tumours. An overall increase in perfusion in implanted rat prolactinomas (Robinson *et al.*, 1995; Robinson *et al.*, 1997), chemically induced mammary cancer in rats (Robinson *et al.*, 1997) and murine RIF-1 tumours (Honess *et al.*, 1995) has been observed. However, no changes in perfusion were documented using carbogen alone in other tumour models (Dunn *et al.*, 1999; Grau *et al.*, 1992; Hirst *et al.*, 1994), or on microregional blood flow in advanced cancer in man (Powell MEB. *et al.*, 1996). This infers that amongst other factors, tumour type dependence on carbogen may be relevant (Dunn *et al.*, 1999) and also within the same tumour heterogeneity exists, with increases and decreases in blood flow observed in response to carbogen in the same tumour (Powell MEB. *et al.*, 1996) .

Nicotinamide is thought to act by eliminating transient closure of vessels in the microvasculature thereby stabilising blood flow (Chaplin D. *et al.*, 1990; Hirst *et al.*, 1994) and by decreasing interstitial fluid pressure (Peters CE. *et al.*, 1997). Other theories have suggested that nicotinamide is implicated in modulating tumour metabolism following its conversion to nicotinamide adenine dinucleotide (NAD^+). NAD^+ is a co-enzyme for over a 100 different dehydrogenases, which are responsible for many processes including oxidative metabolism and glycolysis. An increase in NAD^+ could have secondary effects on tumour blood flow and oxygenation (Kaanders *et al.*, 2002; Robinson *et al.*, 2000). Again, there have been contradictory reports of the effect of nicotinamide alone on tumour perfusion. An improvement in blood flow was seen in murine squamous cell tumours (Chaplin D. *et al.*, 1990). However, in radiation-induced fibrosarcomas (RIF-1) there was no change in blood flow with nicotinamide (Honess *et al.*, 1995) or in human tumours (Powell MEB. *et al.*, 1997), though this may reflect the lower dose of nicotinamide that was used. Alternatively, nicotinamide may affect only small blood vessels that are too small to be visualised by these imaging techniques. Intermittent hypoxia only occurs in blood vessels < 0.1 mm (Kimura *et al.*, 1996) and contribution to actual tissue perfusion may only be marginal, and hence unquantifiable, (Robinson *et al.*, 2000), and may be complementary to other agents influencing blood flow.

As carbogen and nicotinamide appear to act independently of one another in manipulating blood flow, studies have focused on the combination of carbogen and nicotinamide to assess blood flow response. In superficial human tumours, carbogen and nicotinamide together increased blood flow by 20% compared with baseline values, as measured using Laser doppler probes (Powell MEB. *et al.*, 1997). This increase in blood flow suggests that carbogen and nicotinamide can act synergistically.

In order to assess the effects of altering tumour blood flow on systemically administered chemotherapy, carbogen was administered to mice bearing subcutaneous RIF-1 tumours whilst receiving 5-FU chemotherapy (McSheehy *et al.*, 1998). The study found an increase in 5-FU uptake attributed not only to changes in tumour perfusion, but also to pH differences, resulting in an increased formation of anabolites detected by MRS and enhanced cytotoxicity in the larger tumours.

To address the question whether a similar relationship exists in man, this study was conducted to investigate the effects of carbogen and nicotinamide modulation on 5-FU pharmacokinetics in patients with metastatic colorectal cancer.

6.2 Study Aims

The study aims were as follows:

1) To investigate whether the combination of carbogen and nicotinamide modulated tissue perfusion in normal tissue and tumour *in vivo*.

2) To establish if other physiological factors measurable in blood or by PET are altered in response to carbogen and nicotinamide.

3). To investigate change in tumour and normal tissue handling of 5-[^{18}F]FU when carbogen and nicotinamide are co-administered.

6.3 Methods

6.3.1 Patient Selection

Patients with metastatic colorectal cancer due to undergo first line palliative treatment with 5-FU/folinic acid chemotherapy attending the Department of Oncology at either Charing Cross or Hammersmith hospitals, were entered into this study. Patients all had imageable metastases $\geq$ 2 cm in size in at least 1 axis of dimension, as measured on CT scan.

Patients were excluded if they had a history of chronic obstructive pulmonary disease (COPD). These patients would not tolerate the high O_2 content of carbogen as it would impair their hypoxic respiratory drive. Patients unable to consume oral medication were also ineligible as they would have been incapable of swallowing nicotinamide tablets.

Eligibility criteria included a life expectancy of $\geq$ 3 months, performance status $\geq$ 2 (Appendix A), satisfactory full blood count (FBC), with neutrophils $\geq 1.5 \times 10^9$ and platelets $\geq 100 \times 10^9$, and adequate renal and hepatic function (serum creatinine, < 125 $\mu mol \cdot L^{-1}$; bilirubin < 17 mmol $\cdot L^{-1}$; and aspartate transaminase, < 35 $\mu mol \cdot L^{-1}$).

Ethics approval was obtained from the Hammersmith Hospital Research Ethics Committee and authorization for the use of radionuclides was given by Administration of Radioactive Substances Advisory Committee (UK). Patients were given information sheets (Appendix B) and a minimum of 24 hours to decide whether to enter the trial. Written consent for study participation was obtained.

6.3.2 Study Design

Patients underwent two PET scanning sessions coinciding with the start of two separate chemotherapy cycles (see Figure 13). Chemotherapy consisted of 5-FU plus FA given as either the de Gramont regime (FA 200 mg/m^2 (maximum 350mg) 2 hour infusion, 5-FU 400 mg/m^2 bolus and 600 mg/m^2 22 hour continuous infusion, days 1 and 2, repeated every 2 weeks) or modified de

Gramont regime (FA 350 mg, 5-FU 400 mg/m^2 bolus and 2,800 mg/m^2 46 hour continuous infusion, repeated every 2 weeks). Scanning was performed in the early afternoon to avoid diurnal variation in the metabolism of 5-FU (Harris BE. *et al.*, 1988). Prior to embarking on each scanning session, all patients had a FBC (as above) and clinical examination to ensure they were fit for chemotherapy. The first scanning session occurred on day 1 of the de Gramont regimen, and did not involve administration of nicotinamide and carbogen. The $H_2[^{15}O]$ scan was followed by the 5-[^{18}F]FU scan. 5-[^{18}F]FU was given concurrently with the administration of therapeutic 5-FU and injected as a 30 second bolus for the 90 minute scan. The second scanning session occurred during a subsequent cycle of chemotherapy and patients were given 60 mg/kg nicotinamide orally 2–3 hours before scanning commenced. Carbogen (BOC Limited) inhalation began 5 minutes before the start of both the $H_2[^{15}O]$ and 5-[^{18}F]FU scans and continued for a further 5 minutes during each scan. Patients breathed carbogen, comprising 95% oxygen and 5% carbon dioxide, delivered at 10 litres/minute through tightly fitting masks (Intersurgical UK cushion flex mask) which were strapped to the patients' faces using a two-tailed rubber harness (supplied by Mount Vernon Hospital, UK). The mask was attached to a two litre reservoir re-breathing bag and was connected to the gas cylinder via a one-way valve.

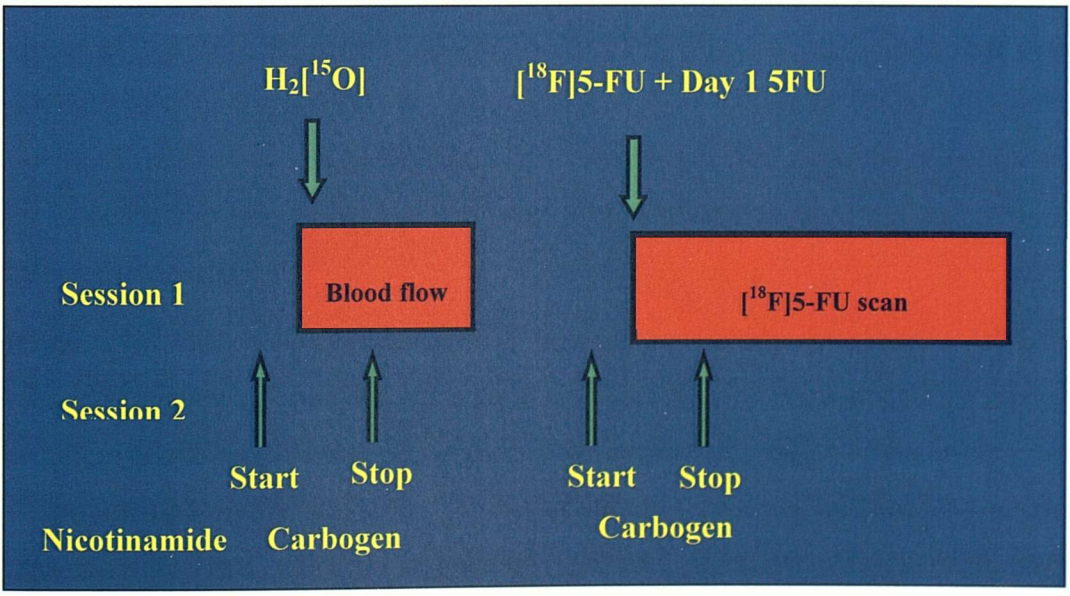


Figure 13: Study Design

6.3.3 Procedures

Prior to the first scanning session patients had a pinprick tattoo applied to their skin to ensure accurate and reproducible positioning on the ECAT 931 scanning couch. This was performed after simulation on a x-ray scanner, using a recent CT scan for location of the metastasis. Patients were positioned in the scanner by matching skin marks with laser beams.

On the patient's second visit to the scanner, they were aligned according to the tattoo, and a short transmission scan performed to ensure accuracy of position.

For the duration of the scan, continuous arterial blood sampling and discrete samples were collected with an average total of 325 ml of blood taken per scanning session. Details of $H_2[^{15}O]$ and 5-[^{18}F]FU synthesis and scanning protocols are in Chapter 4.

6.4 Data Analysis and Statistics

Discrete blood samples were analysed using a blood gas machine to obtain pO_2 (mmHg), pCO_2 (mmHg), glucose (mmol/l) and pH. Cardiac output was calculated using the indicator dilution technique. This method has been adapted for use in dynamic PET $H_2[^{15}O]$ scan (Yap JT. *et al.*, 2000). The integral of the first pass arterial phase of the $H_2[^{15}O]$ bolus was estimated by fitting the initial decline in the input function to a single exponential function. Cardiac output was calculated by dividing the integral of the 1st pass arterial phase by total radioactivity of injected dose.

Regions of interest were drawn on each scan as previously described. 5-[^{18}F]FU scans were analysed using a semi-quantitative technique in tumour, spleen, kidney and liver ROIs. Additional spectral and modified Patlak analyses were performed in tumour and spleen ROIs only. For spectral analysis, total plasma and parent plasma, to evaluate effect of metabolites, were used as input functions to calculate K_1, fractional retention of 5-[^{18}F]FU and permeability and surface area product.

$H_2[O^{15}]$ scans were analysed using the modified Kety-Schmidt equation (Wilson *et al.*, 1992). Details of data analysis are given in Chapters 2 and 4.

For statistical analysis, Wilcoxon signed rank test was used for matched pairs, and the Mann-Whitney test used for unmatched pairs. Data were also analysed using Pearson's correlation coefficient. All statistical tests were two sided and the significance level was set at ≤ 0.05.

6.5 Results

6.5.1 Patient characteristics

8 patients entered the study (4 male and 4 female), with a mean age of 65 years (range 59–78 years). 5/8 patients presented with metastatic disease and had not previously received chemotherapy. Of the 3 patients who had been diagnosed previously, 2/3 had been given adjuvant treatment with a 5-FU based chemotherapy, but with a greater than 2 year gap elapsing before entering this study.

2 patients did not complete the full study: 1 patient had disease progression and only had one cycle of chemotherapy; the other patient did not receive carbogen because of a high carboxyhaemoglobin level which is indicative of a being a heavy smoker and having sub-optimal respiratory function, although denying symptoms of COPD.

6 patients underwent two PET scanning sessions, separated by a minimum of 2 weeks and a maximum of two months. Clinical characteristics of these patients are given in Tables 6.1 and 6.2.

All 6 patients tolerated breathing carbogen with only minimal discomfort experienced from tightness of the mask. A mean dose of 3530 mg of nicotinamide (range = 2820 to 4680 mg) was given with no side effects reported.

Table 6.1: Patient Characteristics

Patient number	Patient scan number Pre C/N	Patient scan number Post C/N	Primary site of disease	Sex	Age (Years)	Body surface area
1	p06479	p06490	colorectal	M	74	1.7
2	p06493	p06526	colorectal	M	75	2
3	p06538	p06550	colorectal	F	59	1.43
4	p06553	p06594	colorectal	F	48	1.46
5	p06588	p06606	colorectal	M	52	1.68
6	p06558	p06567	colorectal	F	78	1.56

Table 6.2: Regions of Interest Sampled

Patient	Metastases	Size	Regions sampled			
			LK	RK	S	L
1	Liver:1a Liver:1b	4cm 2cm	√	√	√	√
2	Liver :2a Liver:2a	10cm 2cm	√	√	√	√
3	Liver:3a Liver:3b Liver:3c Liver:3d	3cm 3cm 3cm 2cm	√	√	√	√
4	Liver:4a Liver:4b	6cm 4cm	√	√	√	√
5	Liver:5a Liver:5b Liver:5c	6cm 3cm 3cm	√	√	√	√
6	Lymph node:6a Lymph Node:6b	2cm 2cm	√	√	√	√

Abbreviations: LM, liver metastasis; LNM, lymph node metastasis; LK, Left kidney; RK, right kidney; S, spleen; L, liver; M, metastasis.

6.5.2 Scan Details

Table 6.3 gives details of radionuclides and therapeutic 5-FU doses injected into individual patients. The mean injected activity of 5-[^{18}F]FU was 345 MBq (range 136–403 MBq) and the mean injected dose of 5-FU was 380 mg/m^2 (range 300–400 mg/m^2). In one patient (p06594) the injected dose of 5-[^{18}F]FU was only 135.6 MBq though this was deemed acceptable as her BSA was small at 1.46. Radiochemical purity was > 95.5% with the precursor uracil the only identified impurity.

The mean injected dose of $H_2[^{15}O]$ was 995.3 MBq (range = 880.6 - 1106.3 MBq).

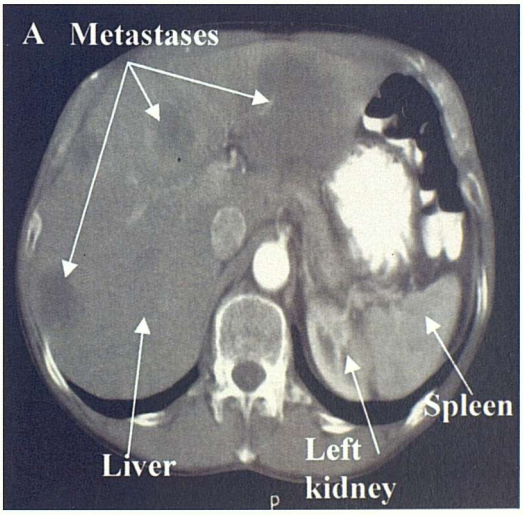
There was a 36% (8/14 scans) failure rate in radiotracer production resulting from 1/8 $H_2[^{15}O]$ and 7/8 5-[^{18}F]FU production failures.

Table 6.3: Scan Details for 5-^{18}F]FU and $H_2[O^{15}]$

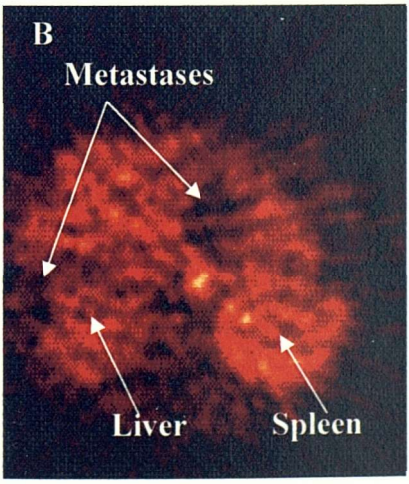
Patient scan number	Patient number	Bolus dose of 5-FU injected (mg)	Injected 5-^{18}F]FU activity (MBq)	5-[^{18}F]FU radiochemical purity (%)	$H_2[O^{15}]$ activity injected (MBq)
p06479	1	680	362.6	95.8	954.6
p06490	1	680	380	99.5	999
p06493	2	605	344	99.5	1006.4
p06526	2	650	384.8	100	1043.4
p06538	3	570	375	100	880.6
p06550	3	570	403.5	100	939.8
p06553	4	585	349.6	100	995.3
p06594	4	585	135.6	100	1065.6
p06588	5	670	373.7	100	976.8
p06606	5	670	387.4	100	1106.3
p06558	6	500	375.9	100	947.2
p06567	6	500	395.5	100	1028.6

6.5.3 Localisation of $H_2[^{15}O]$ and 5-[^{18}F]FU in Tumour and Normal Tissue

Perfusion, uptake and localisation of 5-[^{18}F]FU in different tissues were analysed by PET imaging. An axial CT scan and corresponding static images from $H_2[^{15}O]$ and 5-[^{18}F]FU scans pre C/N administration are shown in Figure 14. In the 5-[^{18}F]FU image, tissue radioactivity comprises fluorine-18-labelled parent 5-FU, anabolites and catabolites. As can be seen in both studies, hyperintense regions in normal liver and kidney probably represent the high blood flow to these organs as well as 5-[^{18}F]FU metabolism (catabolism and excretion, respectively). On the other hand, liver metastases appear hypointense on both scans, indicative of poor tumour perfusion and inferior drug penetration.



A) Typical transabdominal CT scan
B) Perfusion scan and
C) 5-[^{18}F] FU drug scan, showing multiple liver metastases, liver, left kidney and spleen.



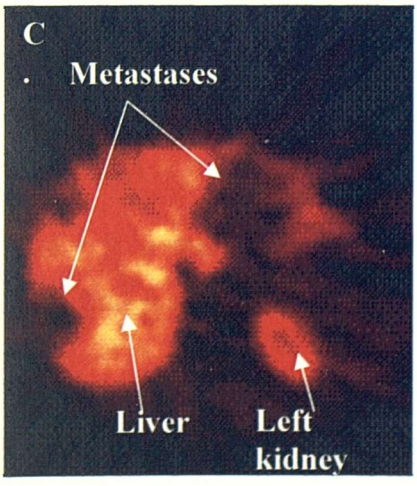
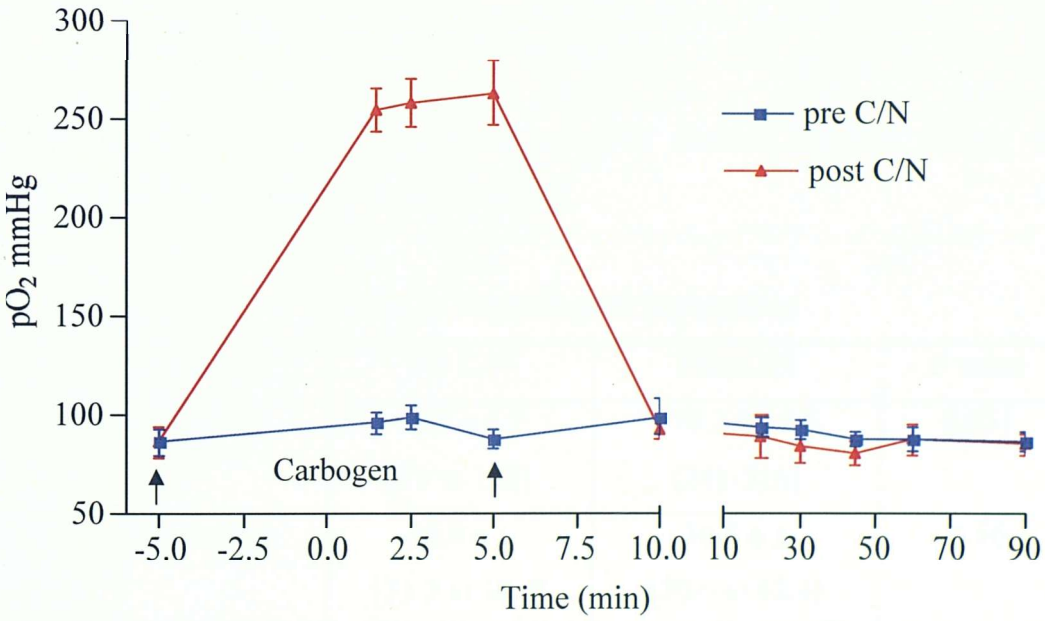


Figure 14: CT and PET Images

6.5.4 Physiological results

The data show that in this study pO_2 increased 5 minutes after commencing carbogen inhalation (2-3 hours after nicotinamide) and after 10 minutes of carbogen inhalation blood pO_2 increased from 93 mmHg (range 77–117 mmHg) to 278 mmHg (range 213–319 mmHg), which was statistically significant ($p = 0.031$). pO_2 levels decreased rapidly after cessation of carbogen breathing and were similar to pre-modulated levels within 5 minutes of stopping carbogen (see Figure 15).



Data are mean ± SEM; C/N, carbogen and nicotinamide; number = 6

Figure 15: Arterial pO2 before and after Carbogen and Nicotinamide

Though there was a slight increase in arterial pCO_2 in response to carbogen breathing this was not statistically significant (Table.6.5).

In the 6 paired $H_2[^{15}O]$ studies of cardiac output there was a non-significant reduction in values ($p = 0.43$) by 7 % after carbogen and nicotinamide (see Table 6.4 below).

Table 6.4: Values for Cardiac Output

Patient Number	[1]Cardiac output pre C/N	[1]Cardiac output pre C/N
1	2.79	2.69
2	3.01	4.38
3	3.28	2.41
4	3.94	2.91
5	3.66	2.73
6	3.81	3.56

[1], L/min; C/N, carbogen and nicotinamide

The other physiological parameters measured showed minimal change with carbogen and nicotinamide (see Table 6.5).

Table 6.5: Physiological Parameters

Parameter	Pre C/N	Post C/N	P value
pO_2 (mmHg)	93.3 ± 5.7 [79 to 108]	278.2 ± 14.6 [241-316]	0.031
pCO_2 (mmHg)	35.9 ± 1 [33.3 to 38.4]	36.3 ± 3 [30.6 to 42.4]	0.56
Glucose (mmol/L)	6.2 ± 0.58 [4.3 to 8.0]	6.2 ± 0.76 [3.8 to 8.6]	0.86
pH	7.45 ± 0.009 [7.42 to 7.47]	7.45 ± 0.02 [7.40 to 7.50]	1.00
Cardiac output (L/min)	3.42 ± 0.18 [2.93 to 3.90]	3.11 ± 0.3 [2.35 to 3.88]	0.43

Data for pO_2, CO_2, glucose and pH are for the 5 minute time point from scan start (i.e., after 10 minutes of carbogen inhalation), the time at which the pO_2 values during the second scan were highest; C/N, carbogen and nicotinamide. Data are mean ± SEM [95% CI]

6.5.5 Perfusion and Volume of Distribution (V_d)

Analysis of the $H_2[^{15}O]$ images yielded measurements of perfusion and the V_d of water for ROIs drawn in tumour and normal tissues before and after administration of nicotinamide plus carbogen (see Figures 16 to 23 below). A summary of results is given in Table 6.6

a) Tumour

15 metastases were analysed: 13 liver and 2 lymph node metastases. One liver metastasis (1b) responded to treatment and became too small for analysis of perfusion and V_d after nicotinamide and carbogen.

As expected, perfusion was lower in tumour than in normal tissues. Nicotinamide and carbogen administration led to an increase in tumour perfusion (Figure 16) in 10/12 metastasis, with a mean increase of 56% (range -32% to +261%; *P*=.0024; n=12). There was no change in tumour perfusion in 1/12 liver metastasis. In contrast, perfusion decreased in the 2 lymph node metastases and 1/12 liver metastasis.

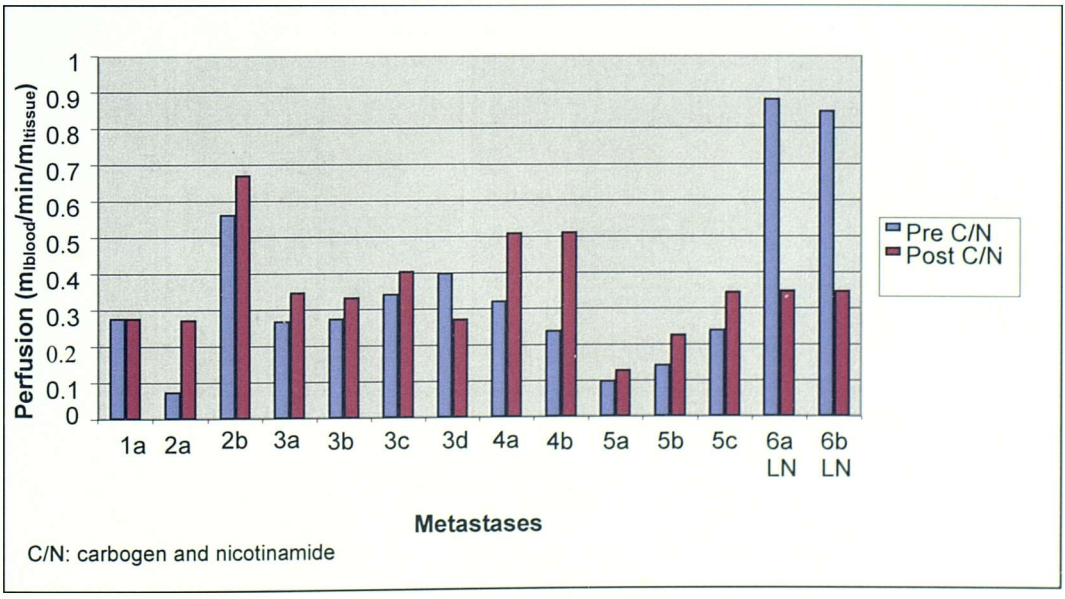


Figure 16: Tumour Perfusion Before and After Carbogen and Nicotinamide

There was no statistical difference in tumour V_d with pre carbogen and nicotinamide V_d of 0.78 ± 0.06 ml_{blood}/ml_{tissue}, and post carbogen and nicotinamide V_d of 0.73 ± 0.07 ml_{blood}/ml_{tissue} in the liver metastases. In the 2 lymph node metastases, Vd decreased after carbogen and nicotinamide.

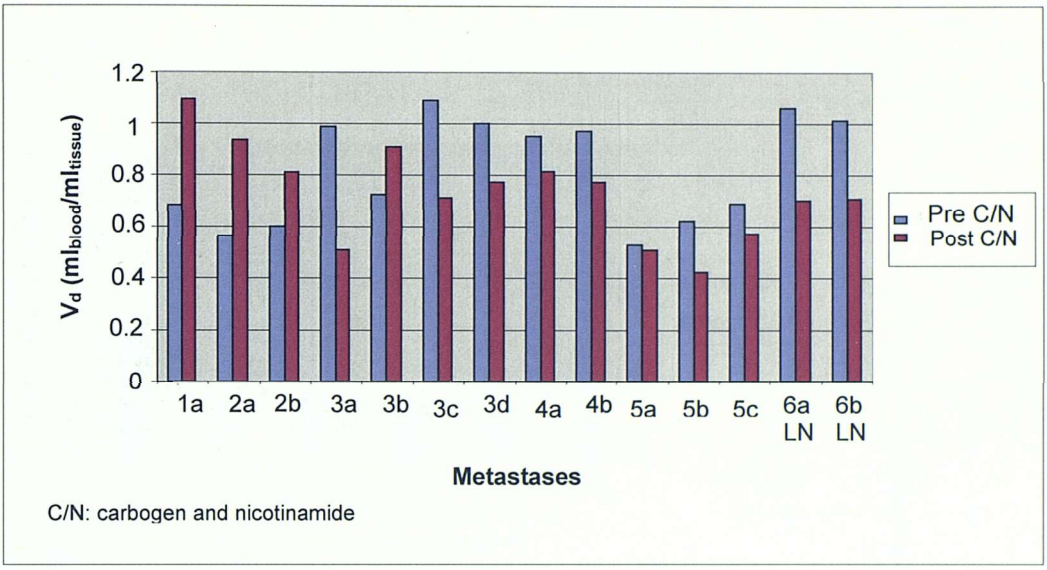


Figure 17: Tumour V_d Before and After Carbogen and Nicotinamide

b) Spleen

Spleen had the highest organ perfusion pre and post carbogen and nicotinamide with values of 1.88 ± 0.41 $ml_{blood}/min/ml_{tissue}$ and 1.78 ± 0.28 $ml_{blood}/min/ml_{tissue}$, respectively, with no significant difference.

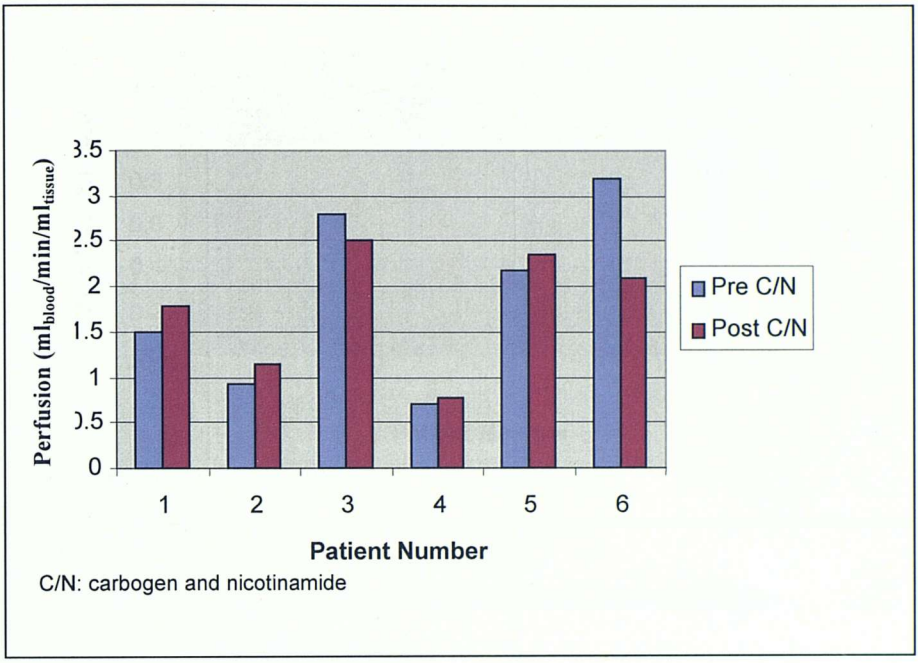


Figure 18: Spleen Perfusion Before and After Carbogen and Nicotinamide

Spleen V_d was the same pre and post carbogen and nicotinamide, with values of 0.94 ± 0.07 ml_{blood}/ml_{tissue} and 0.94 ± 0.41 ml_{blood}/ml_{tissue} respectively.

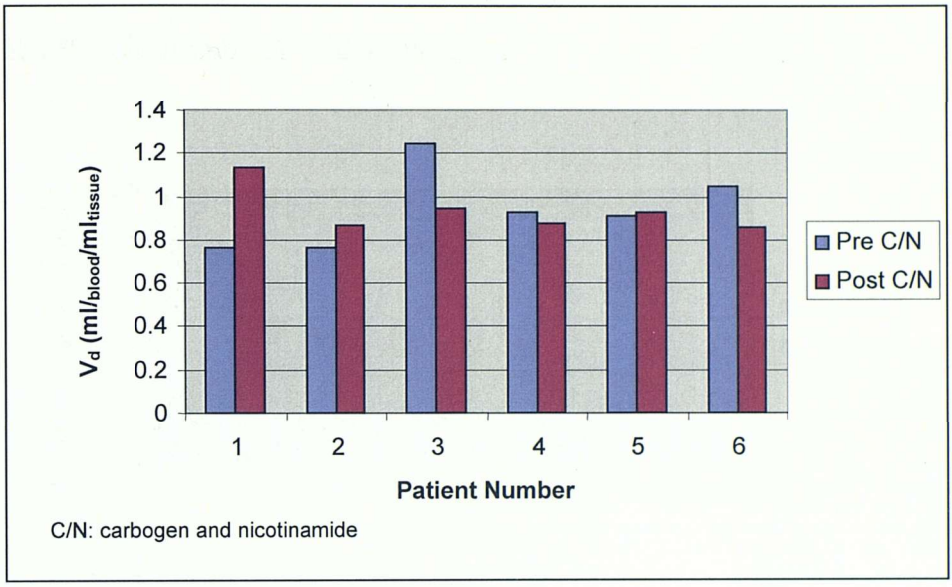


Figure 19: Spleen V_d Before and After Carbogen

c) Kidney

In all 12/12 kidney ROIs sampled, perfusion decreased with a mean change of -43% (range -82% to -11%) post carbogen and nicotinamide. The result was statistically significant with p=0.0005.

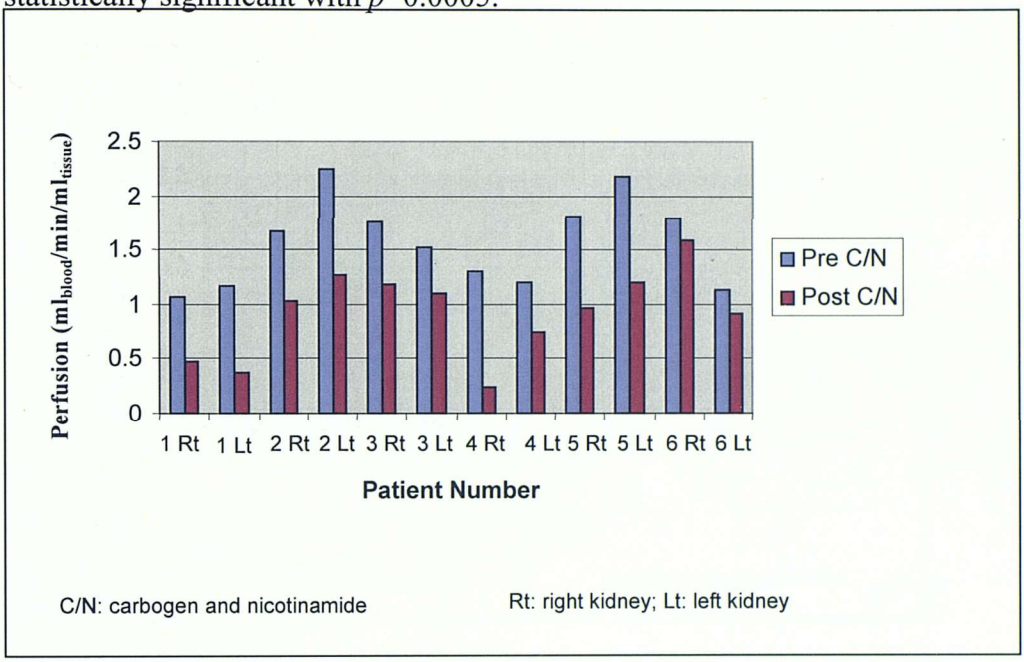


Figure 20: Kidney Perfusion Before and After Carbogen and Nicotinamide

Again, in all 12/12 kidneys sampled, V_d decreased with a mean change of -17% (range -44% to 2%) and this was statistically significant with p = 0.001.

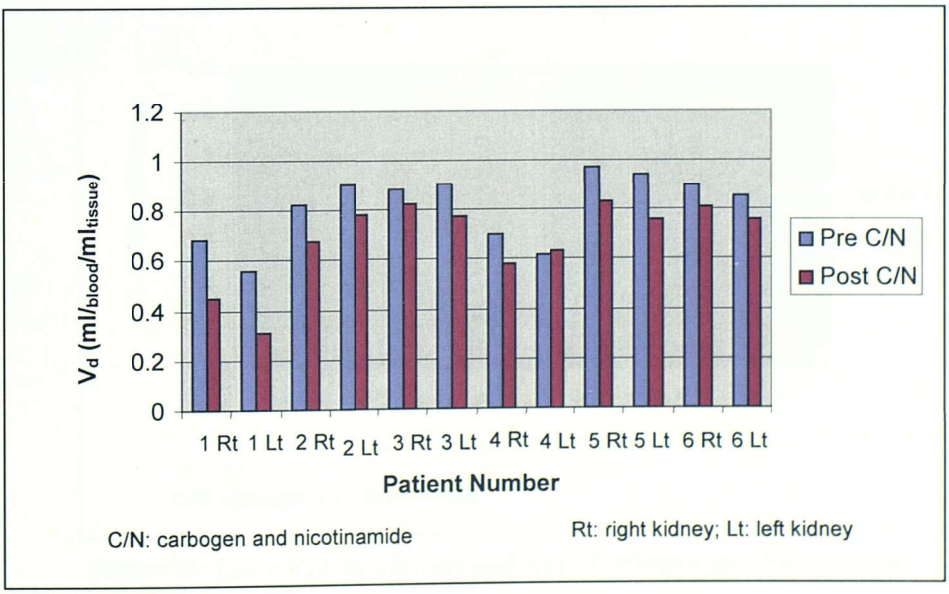


Figure 21: Kidney V_d Before and After Carbogen and Nicotinamide

d) Liver

Hepatic perfusion index also decreased in all 6 patients with a mean change of -29% (range -42% to -8%). This was also significant with $p = 0.031$.

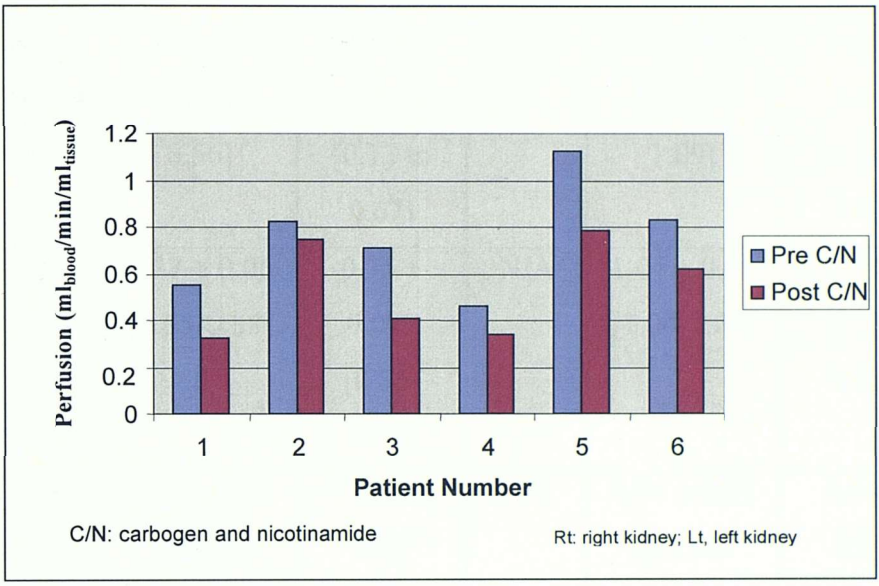


Figure 22: Liver Perfusion Index Before and After Carbogen and Nicotinamide

Liver V_d index was not significantly altered after carbon and nicotinamide with p = 0.56.

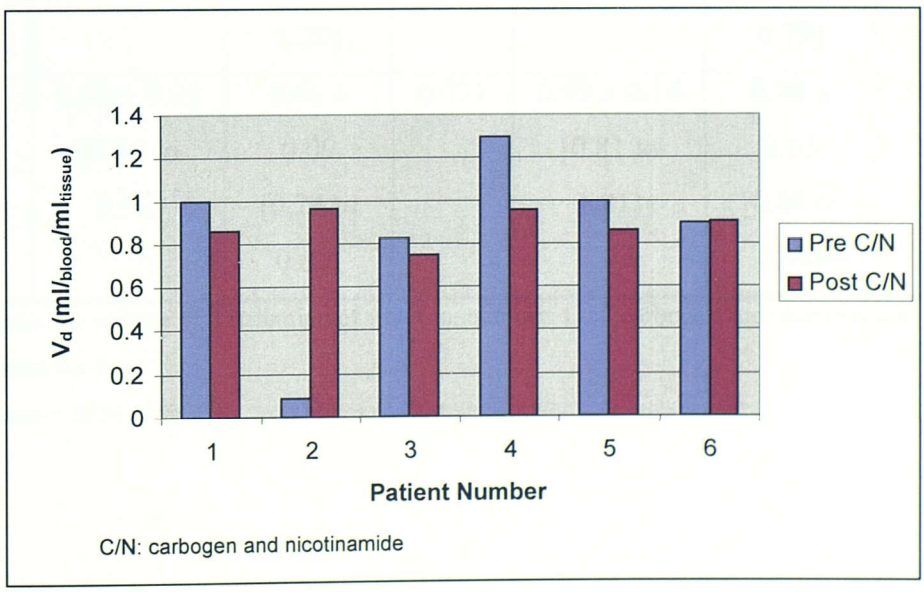


Figure 23: Liver V_d Index Before and After Carbogen and Nicotinamide

Table 6.6: Summary of Results for perfusion and V_d for Regions Sampled

Region	Regional perfusion ($ml_{blood}/min/ml_{tissue}$)			V_d (ml_{blood}/ml_{tissue})		
	Pre C/N	Post C/N	*P*	Pre C/N	Post C/N	*P*
Liver metastases (n=12)	0.27 ± 0.03 [0.08 to 0.56]	0.36 ± 0.03 [0.13 to 0.67]	0.0024	0.78 ± 0.06 [0.53 to 1.09]	0.73 ± 0.07 [0.41 to 1.02]	0.52
Lymph Node Metastases (n=2)	0.87 ± 0.06 [0.85-0.88]	0.35 ± 0.002 [0.35-0.35]	N/A	1.04 ± 0.01 [1.04-1.06]	0.7 ± 0.01 [0.70-0.71]	N/A
Spleen (n = 6)	1.88 ± 0.41 [0.82 to 2.94]	1.78 ± 0.28 [1.06 to 2.50]	1.00	0.94 ± 0.07 [0.75 to 1.14]	0.94 ± 0.04 [0.83 to 1.04]	1.00
Kidney (n = 12)	1.57 ± 0.12 [1.30 to 1.80]	0.92 ± 0.12 [0.60 to 1.20]	0.0005	0.81 ± 0.04 [0.73 to 0.90]	0.68 ± 0.05 [0.58 to 0.79]	0.001
*Liver (n = 6)	0.68 ± 0.09 [0.40 to 0.96]	0.46 ± 0.09 [0.24 to 0.67]	0.031	0.99 ± 0.16 [0.81 to 1.81]	0.90 ± 0.03 [0.80 to 0.99]	0.22

Abbreviations: V_d, volume of distribution of water; n, number; C/N, carbogen and nicotinamide; N/A, not applicable

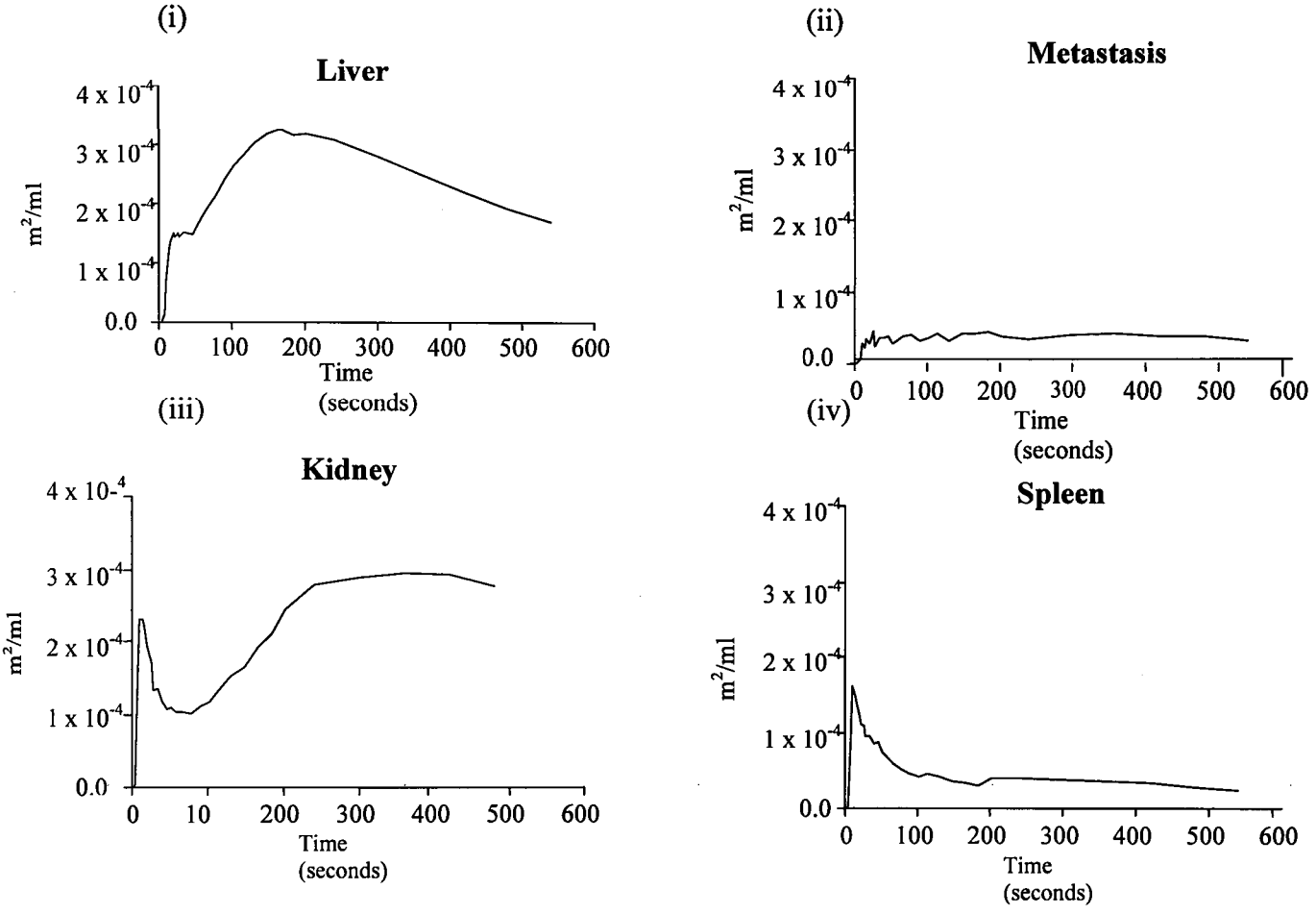
*, index values for liver

Data are mean ± SEM [95% CI].

6.5.6 Semi-quantitative Analysis

Figure 24 depicts characteristic time activity curves (TAC) for full dose 5-[^{18}F]FU, corrected for injected activity and BSA, for the organs illustrated in Figure 14C, without carbogen and nicotinamide. Liver TAC showed a gradual rise and peak in 5-[^{18}F]FU activity at around 30 minutes, attributed to the ability of the liver to convert intracellular fluorouracil to its catabolite α-fluoro-β-alanine (FBAL) as it is abundant in dihydropyrimidine dehydrogenase (DPD), the key enzyme in catabolism of 5-FU (Heggie G. *et al.*, 1987). The decline in liver TAC reflects the slow release of [^{18}F]BAL back into the circulation. The early peak in kidney TAC indicates initial high delivery of 5-[^{18}F]FU followed by a rapid decline probably representing saturation of metabolism of 5-[^{18}F]FU by the kidney, which also possesses relatively high DPD levels (Heggie G. *et al.*, 1987). The curve is then followed by a gradual rise, as 5-[^{18}F]FU is catabolised and excreted by this organ. The early peak in spleen TAC again indicates preliminary high delivery, followed by a reduction to a level sustained for the duration of the scan. This is consistent with both 5-[^{18}F]FU and ^{18}FBAL flowing freely through the spleen as the spleen does not participate in the metabolism of 5-FU. Finally, tumour TAC demonstrates a much smaller peak followed by constant levels suggesting trapping of 5-[^{18}F]FU and anabolites.

Figure 24: Representative Tissue Activity Curves for (i) liver (ii) metastasis (iii) kidney and (iv) spleen



6.5.6.1 $SUV_{3.75mins}$

The early uptake of 5[^{18}F]FU into tissues was measured at 3.75mins using $SUV_{3.75mins}$ to reflect predominantly delivery of the parent radiotracer ($t_{1/2}$ = 5 to 15 minutes (Presant C. *et al.*, 1990) and has been calculated for tumour, spleen, kidney and liver. A summary of results is given in Table 6.7.

a) Tumour

A total of 14 metastases were analysed: 12 liver and 2 lymph node metastases. One liver metastases (3d) identified on CT imaging was poorly visualised on the 5-[^{18}F]FU scan and could not be analysed. As seen in the relevant TAC curves, pre carbogen and nicotinamide $SUV_{3.75mins}$ was lower for tumour. $SUV_{3.75mins}$ increased in 9/12 liver metastases after carbogen and nicotinamide with a mean

increase of 39%, which was not statistically significant at p = 0.064. In the 2 lymph node metastases, there was no consistent change in $SUV_{3.75mins}$ after carbogen and nicotinamide.

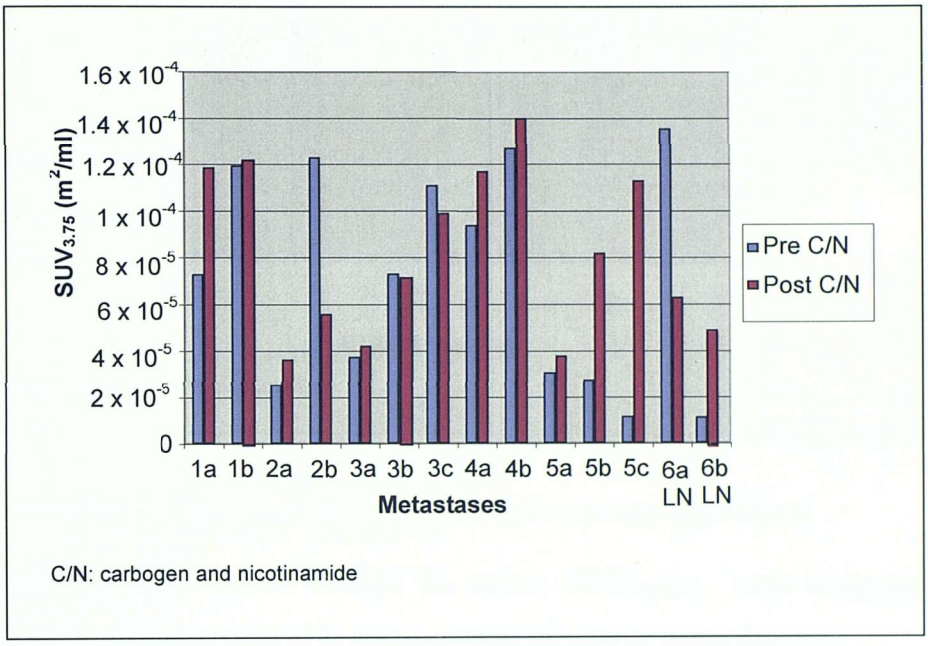


Figure 25: Tumour $SUV_{3.75mins}$ Before and After Carbogen and Nicotinamide

b) Spleen

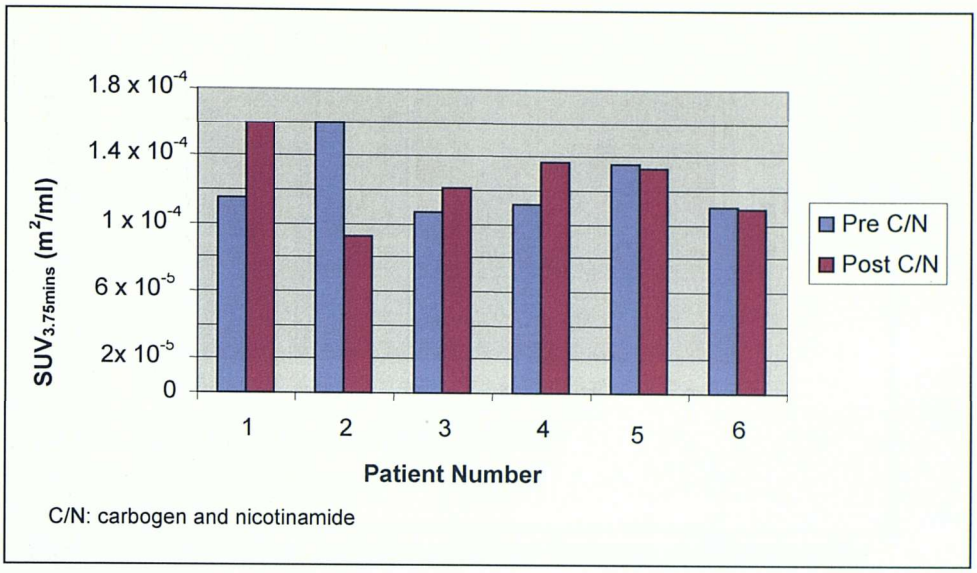


Figure 26: Spleen $SUV_{3.75mins}$ Before and After Carbogen and Nicotinamide

There was no significant change in spleen $SUV_{3.75mins}$ post carbogen and nicotinamide in agreement with measurement of splenic perfusion.

c) Kidney

In 4/6 patients $SUV_{3.75mins}$ decreased after carbogen and nicotinamide in both kidneys. The mean reduction in kidney $SUV_{3.75mins}$ was 45% and was statistically significant, $p = 0.043$.

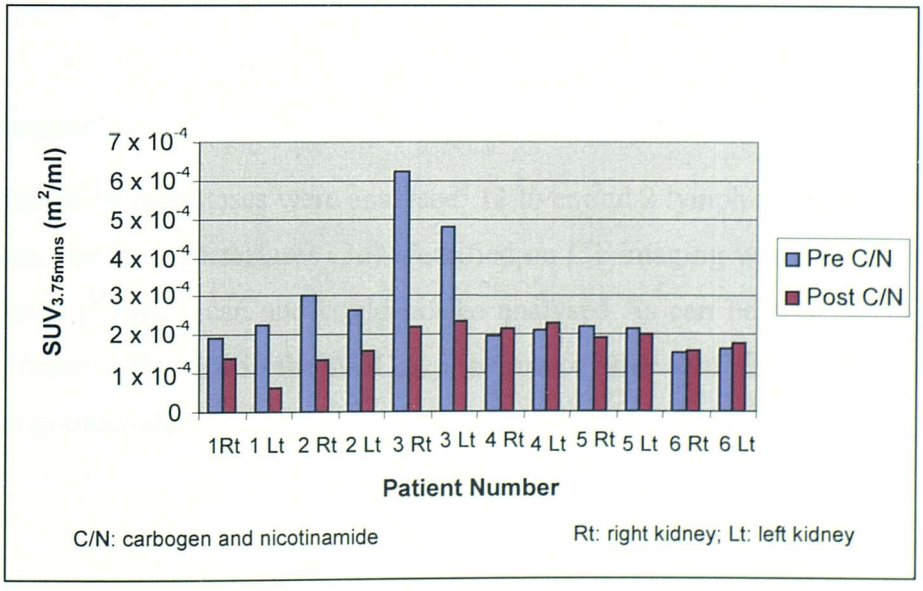


Figure 27: Kidney $SUV_{3.75mins}$ Before and After Nicotinamide

d) Liver

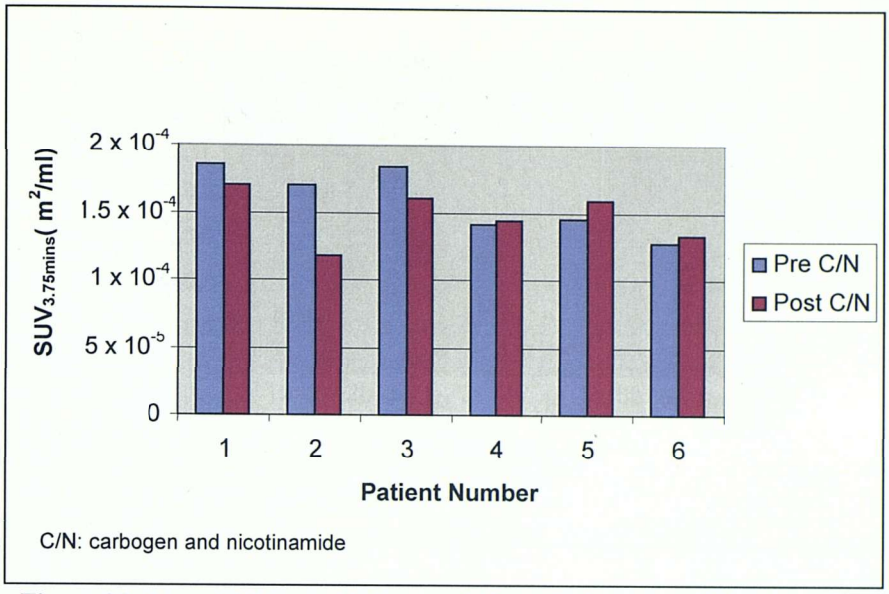


Figure 28: Liver $SUV_{3.75mins}$ Before and After Carbogen and Nicotinamide

There was no significant change in liver $SUV_{3.75mins}$ post carbogen and nicotinamide again in agreement with liver perfusion index.

6.5.6.2 AUC_{90mins}

The area under the curve (AUC) over 90 minutes was calculated for each region, with and without the modulation of carbogen/nicotinamide .This represents tissue exposure to 5-[^{18}F]FU for the period of the scan. A summary of results is given in Table 6.7.

a) Tumour

A total of 14 metastases were analysed: 12 liver and 2 lymph node metastases. As before, one liver metastases (3d) identified on CT imaging was poorly visualised on the 5-[^{18}F]FU scan and could not be analysed As can be seen, there was no significant difference in the AUC_{90mins} before or after administration of carbogen and nicotinamide.

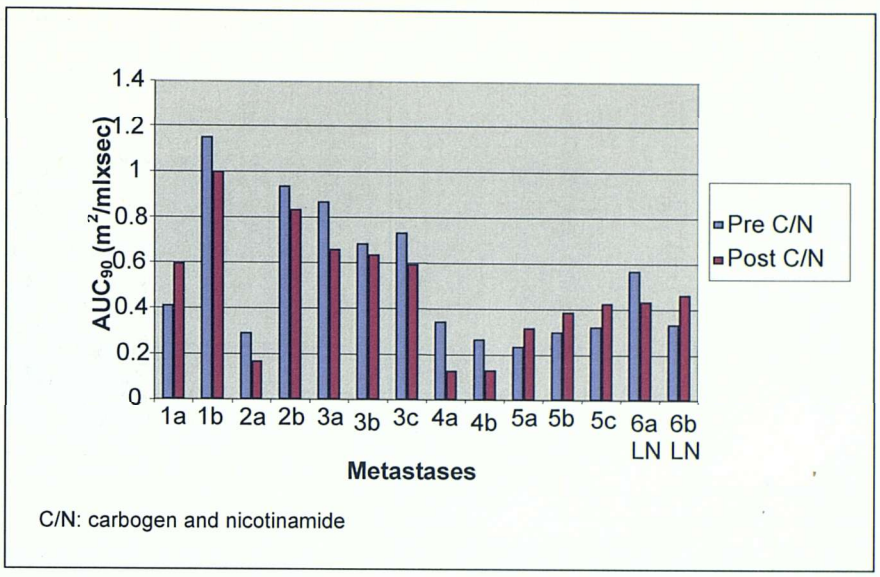


Figure 29: Tumour AUC_{90mins} Before and After Carbogen and Nicotinamide

b) Spleen

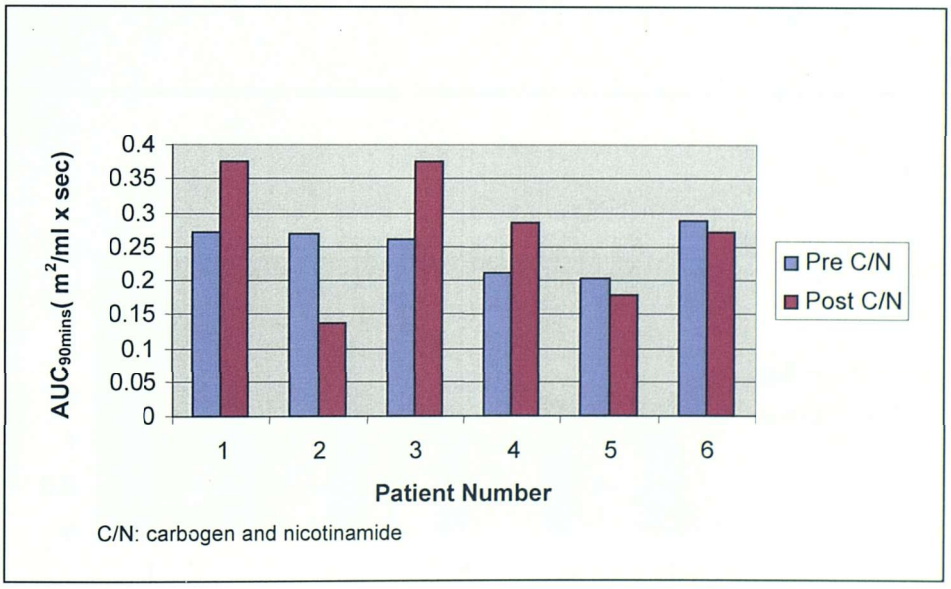


Figure 30: Spleen AUC_{90mins} Before and After Carbogen and Nicotinamide

AUC_{90mins} for spleen was the lowest, indicating poor retention of 5-[^{18}F]FU. There was no change in AUC_{90mins} in spleen after carbogen and nicotinamide.

c) Kidney

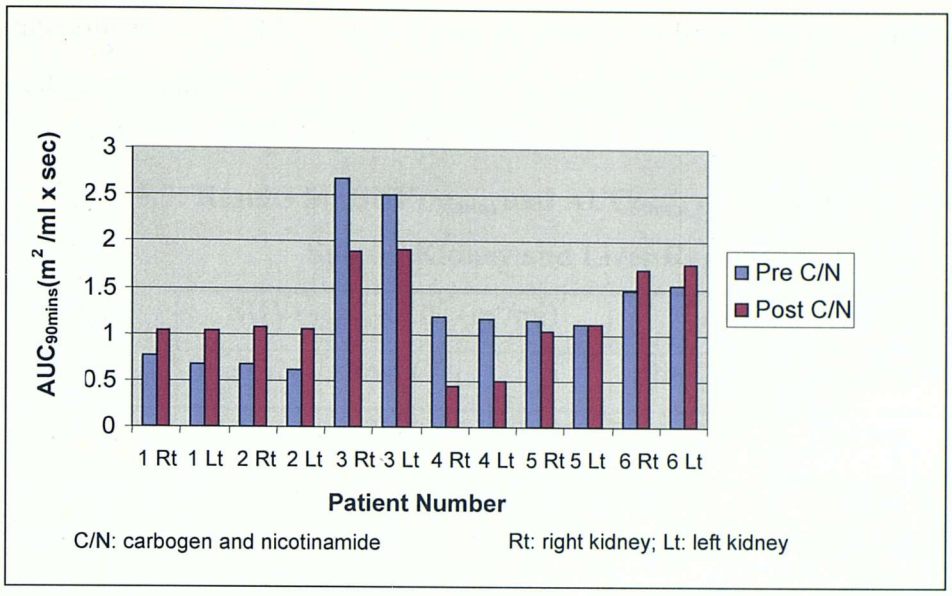


Figure 31: Kidney AUC_{90mins} Before and After Carbogen and Nicotinamide

Kidney had the second highest value for AUC_{90mins} consistent with its role in the excretion of catabolites of 5-[^{18}F]FU. There was no significant change in kidney AUC_{90mins} after carbogen and nicotinamide.

d) Liver

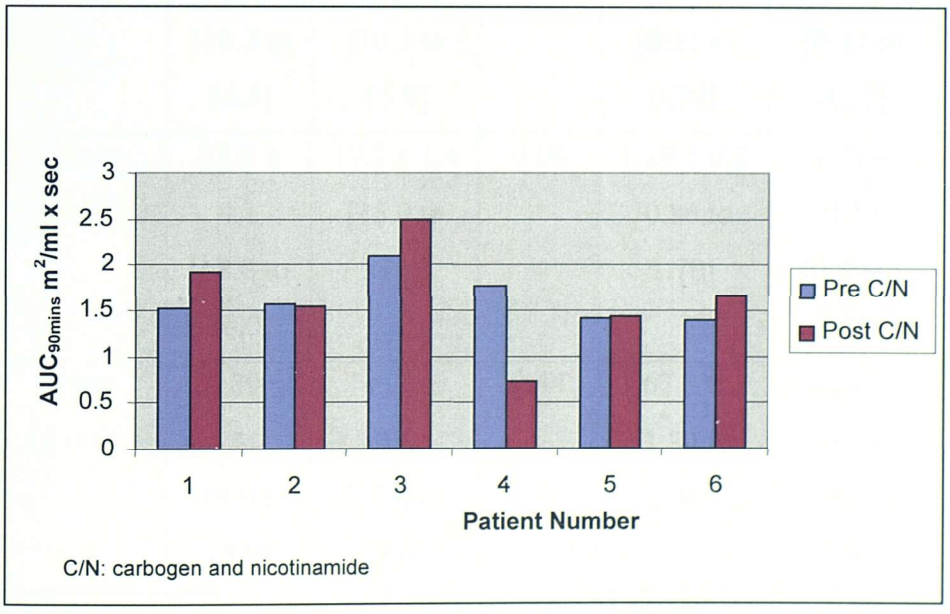


Figure 32: Liver AUC_{90mins} Before and After Carbogen and Nicotinamide

Liver had the highest AUC_{90mins}, which is probably because of its role in catabolism of 5-[^{18}F]FU. There was no change in liver AUC_{90mins} after carbogen and nicotinamide.

Table 6.7: Results for $SUV_{3.75mins}$ and AUC_{90min} of 5-[^{18}F]FU in Tumour, Spleen, Kidney and Liver Regions

Region	$SUV_{3.75mins}$ x 10^{-5} (m^2/ml)			AUC_{90min} (m^2/ml/sec)		
	Pre C/N	Post C/N	p	Pre C/N	Post C/N	p
Liver Metastases (n = 12)	7.01 ± 1.3 [3.2 to 9.0]	8.32 ± 1.2 [5.7 to 10.9]	0.06	0.45 ± 0.07 [0.28 to 0.60]	0.41 ± 0.07 [0.25 to 0.56]	0.32
Lymph Node Metastases (n = 2)	9.02 ± 2.35 [10.6 – 11.3]	7.07 ± 1.2 [5.6 – 6.3]	0. 78	0.52±0.06 [0.34-0.45]	0.51±0.07 [0.32-0.47]	0.76
Spleen (n = 6)	12.3 ± 0.83 [10.2 to 14.5]	12.52 ± 0.95 [10.1 to 15.0]	0.84	0.25 ± 0.014 [0.21 to 0.29]	0.27 ± 0.04 [0.17 to 0.37]	0.84
Kidney (n = 12)	27.0 ± 4.1 [18.0 to 36.0]	17.7 ± 1.4 [15.0 to 21.0]	0.04	1.29 ± 0.2 [0.86 to 1.70]	1.21 ± 0.14 [0.89 to 1.50]	0.67
Liver (n = 6)	15.89 ± 1 [13.0 to 18.0]	14.73 ± 0.8 [13.0 to 17.0]	0.44	1.62 ± 0.1 [1.30 to 1.90]	1.62 ± 0.24 [1.00 to 2.20]	0.56

n, number; $SUV_{3.75mins}$, standardised uptake value at 3.75 minutes; AUC_{90min}, area under the PET time activity curve; C/N, carbogen and nicotinamide.

Data are mean ± SEM [95% CI].

6.5.6.3 Relationship Between Tumour Perfusion and 5-[^{18}F]FU Pharmacokinetics

The relationship between tumour perfusion and 5-[^{18}F]FU pharmacokinetics was studied in 11 liver metastasis. 2 liver metastasis were not included as incomplete data had been obtained after carbogen and nicotinamide (1b and 3d).

Before intervention a significant correlation was found between $SUV_{3.75mins}$ ($r=0.69$, $p=0.013$) and AUC_{90min} ($r=0.74$, $p=0.0167$) and tumour perfusion. After carbogen and nicotinamide no correlation was seen with $SUV_{3.75mins}$ and tumour perfusion ($r=0.09$ $p=0.53$) or AUC_{90min} ($r=0.18$, $p=0.38$).

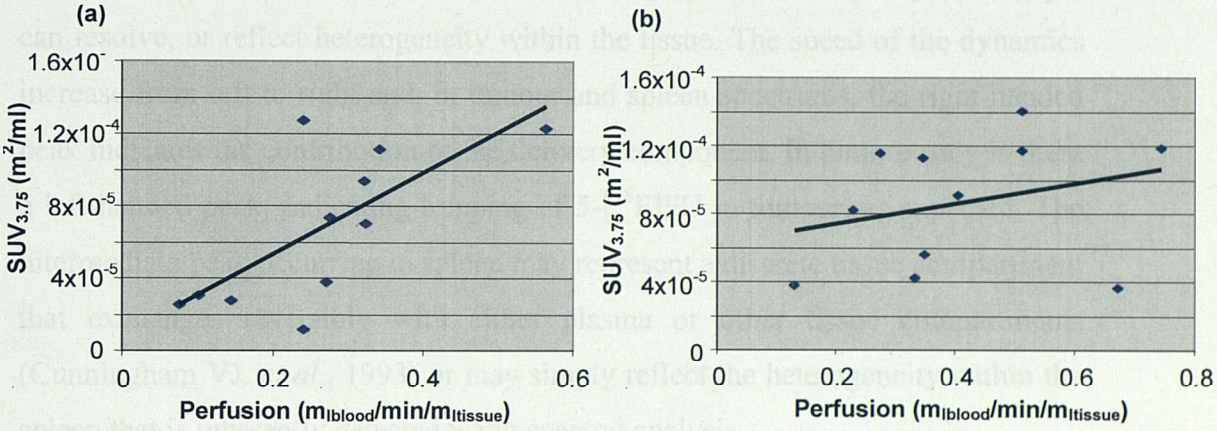


Figure 33: Correlation between perfusion and $SUV_{3.75min}$ in liver metastases (a) before and (b) after carbogen and nicotinamide

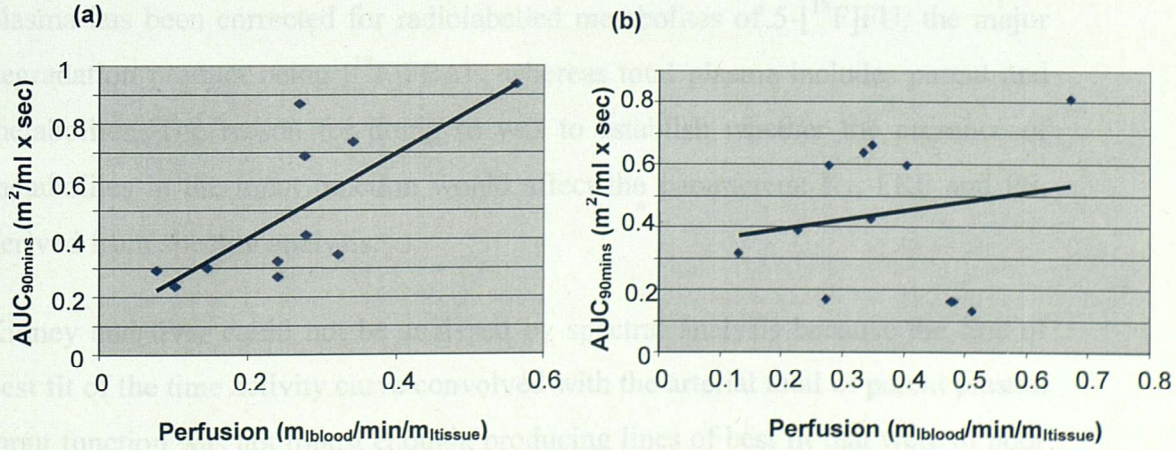


Figure 34: Correlation between perfusion and AUC_{90mins} in liver metastases (a) before and (b) after carbogen and nicotinamide

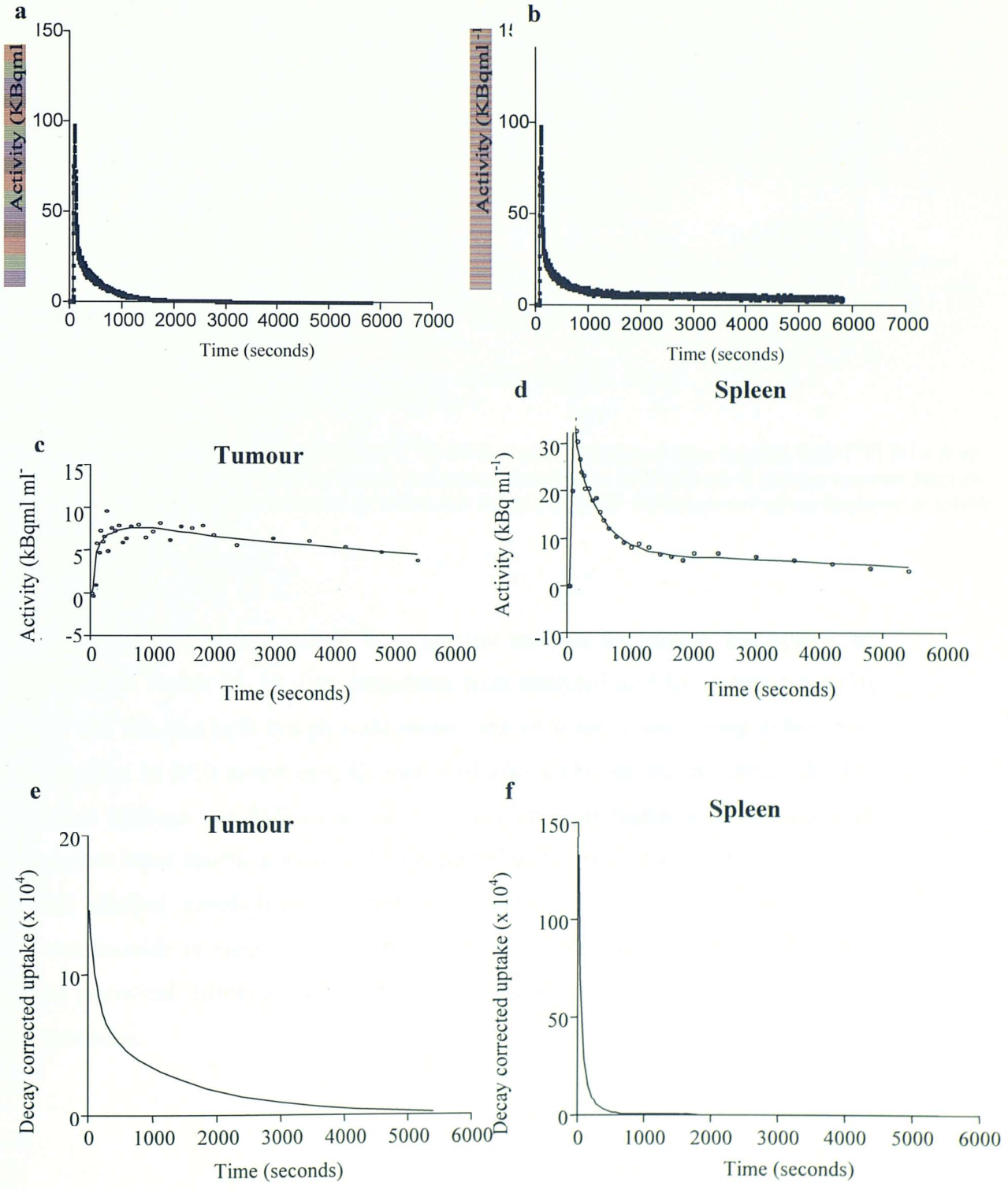
6.5.7 Spectral Analysis

Tissue fits and unit impulse response functions (IRF) were obtained from spectral analysis and are shown in Fig.35. IRF describes the time course of 5-[^{18}F]FU in tissue that would be expected if it had been possible to deliver 5-[^{18}F]FU instantaneously to the region of interest (Fig.35.c and f). The spectrum of kinetic results for a liver metastasis and spleen, shown in Figs.35.e and g reveal the number of kinetic components that adequately describe the data, and may correspond to the number of discrete tissue compartments that the PET technique can resolve, or reflect heterogeneity within the tissue. The speed of the dynamics increase from left to right and, in tumour and spleen spectrums, the right handed peak indicates the contribution of the delivery component. In tumour only is there a left handed peak, indicating trapping of 5-[^{18}F]FU in tumour, as expected. The intermediate peak occurring in spleen may represent a discrete tissue compartment that exchanges reversibly with either plasma or other tissue compartments (Cunningham VJ. *et al.*, 1993) or may simply reflect the heterogeneity within the spleen that is inherently detected using spectral analysis.

In this study, spectral analysis was performed in metastases and spleen using two different input functions: (i) total plasma arterial input function and (ii) parent plasma arterial input function. As suggested in the nomenclature, the parent plasma has been corrected for radiolabelled metabolites of 5-[^{18}F]FU, the major degradation product being [^{18}F]FBAL, whereas total plasma includes parent and metabolites. The reason for doing so was to establish whether the presence of metabolites in the input function would affect the parameters: K_1, FRF and PS, derived from spectral analysis.

Kidney and liver could not be analysed by spectral analysis because the line of best fit of the time activity curve convolved with the arterial total or parent plasma input function was not robust enough, producing lines of best fit that were of poor quality. With liver this may be explained by the vasculature as the liver receives a dual blood supply from portal vein and hepatic artery and may therefore result in discrepancy between measured arterial input and actual hepatic input. Liver

metastases are principally supplied by the hepatic artery and hence satisfactory fits were obtained as shown below.



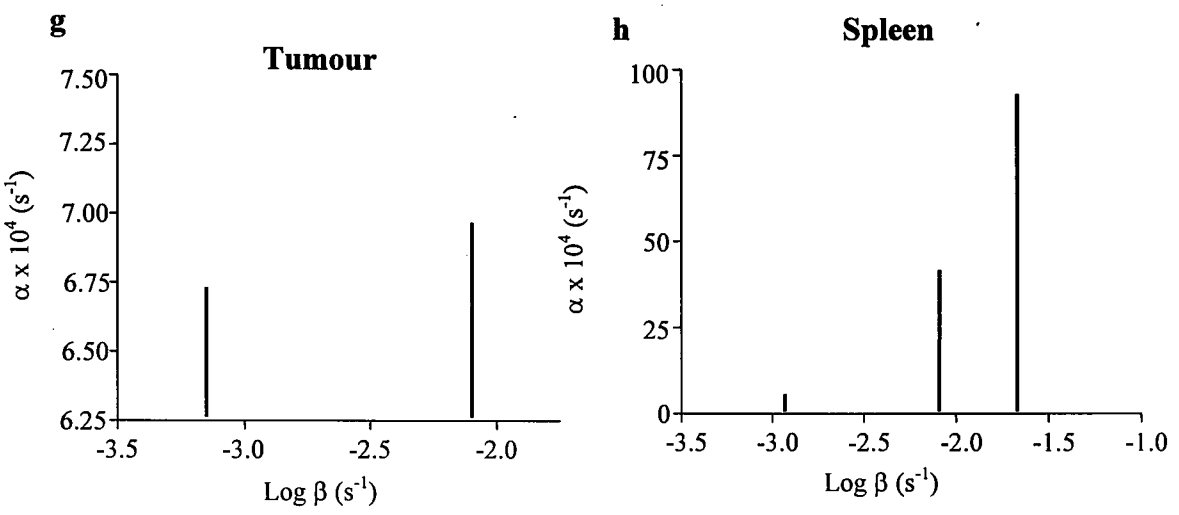


Figure 35: Results for Spectral Analysis Using Total Arterial Plasma Input

a) arterial parent plasma input function for 5-[^{18}F] FU b) arterial total plasma input function for 5-[^{18}F] FU c & d) corresponding time activity curve for tumour and spleen, showing line of best fit e & f) impulse response function (IRF) for tumour and spleen, corrected for radioactive decay g & h) IRF for tumour and spleen displayed as kinetic components

6.5.7.1 (i) K_1

K_1 values that were obtained from spectral analysis for tumour and spleen are shown in Figure 35. 10 liver metastases were analysed as 3 liver metastases (1b, 2b and 3d) and both lymph node metastases were too small. Using either input function, in 8/10 metastases, K_1 increased after carbogen and nicotinamide. The mean increase was 54% using parent plasma and was higher at 62% using total plasma input function, as would be expected as the latter has not been corrected for labelled metabolites. K_1 was significantly increased after carbogen and nicotinamide in metastases with both input functions (see Table 6.8). There was no statistical difference seen after comparing K_1 derived using the two input functions.

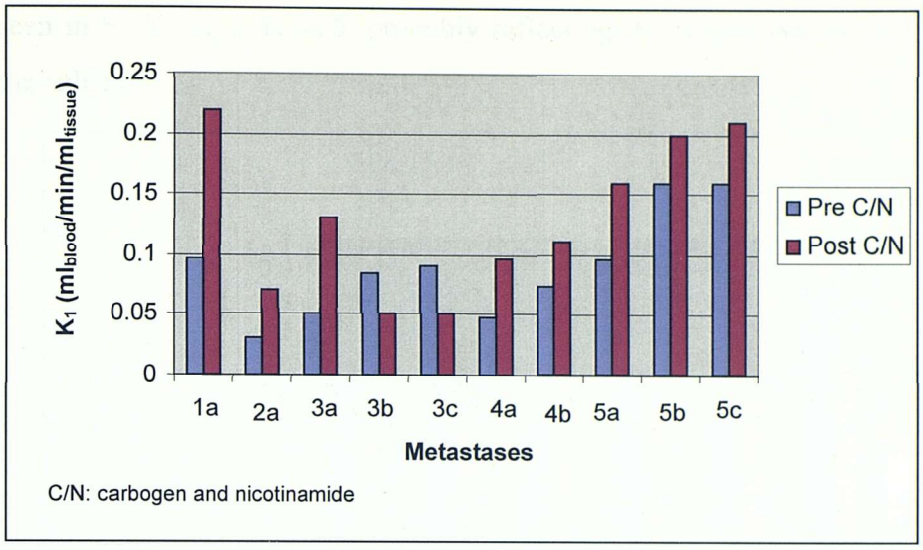


Figure 36: Tumour K_1 Before and After Carbogen and Nicotinamide Using Total Plasma Input

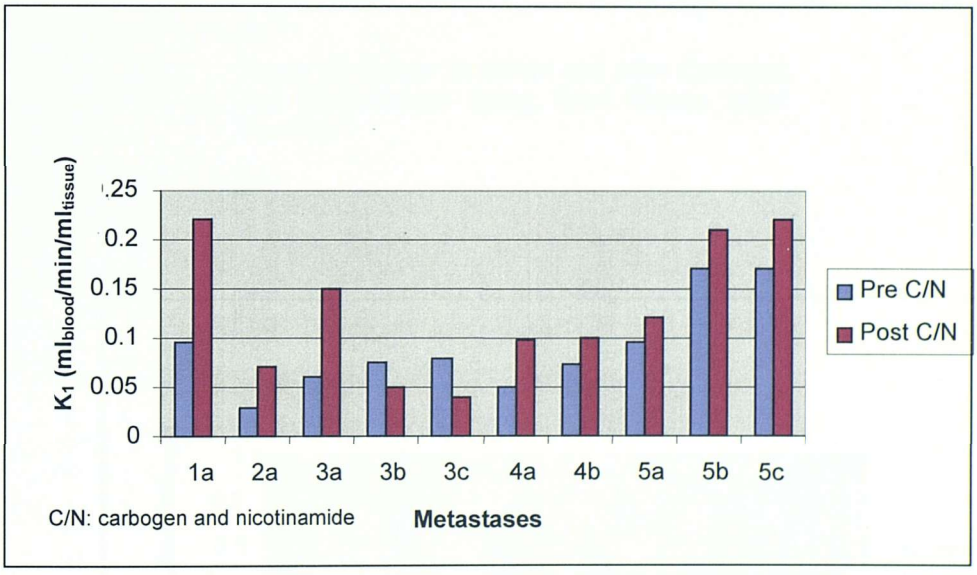


Figure 37: Tumour K_1 Before and After Carbogen and Nicotinamide Using Parent Plasma Input Function

In the spleen, K_1 was reduced in 4/6 patients with both input functions though the decrease was marginal and was not statistically significant (Table 6.8). Again, there was no statistical difference in K_1 obtained form total or parent plasma input functions (Table 6.9).

As seen in the summary Table.6.8, spleen K_1 was greater than tumour K_1 by approximately five-fold, pre and post carbogen and nicotinamide, with an increase

seen in $SUV_{3.75mins}$ as well, probably reflecting the higher perfusion measured in the spleen.

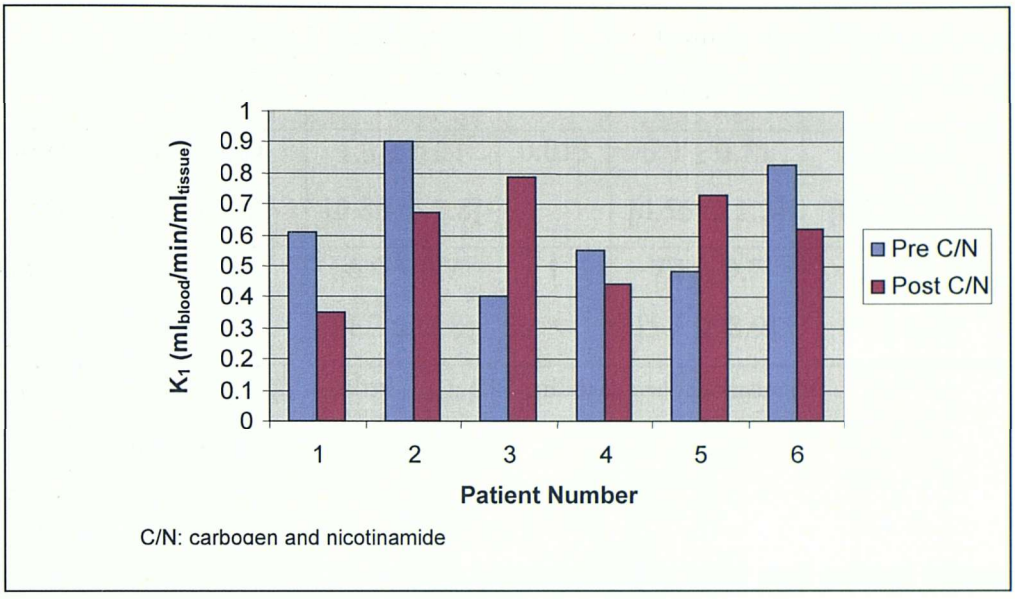


Figure 38: Spleen K_1 Before and After Carbogen and Nicotinamide Using Total Plasma Input Function

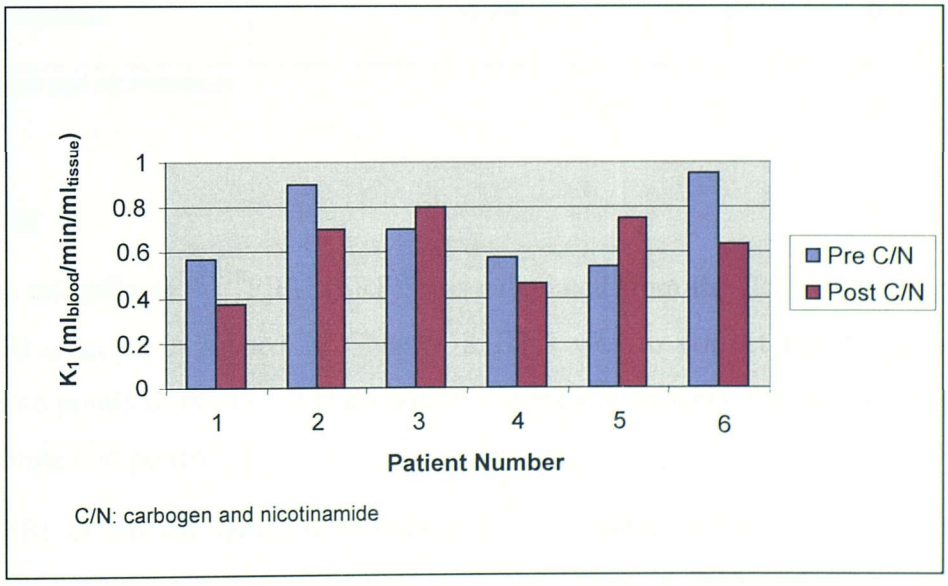


Figure 39: Spleen K_1 Before and After Carbogen and Nicotinamide Using Parent Plasma

Table 6.8: Table of K_1 for Tumour and Spleen Before and After Carbogen and Nicotinamide Using Total and Parent Plasma Input Functions

Region	$K_1 \times 10^{-1}$ ($ml_{blood}/min/ml_{tissue}$) Using Total Plasma Arterial IF			$K_1 \times 10^{-1}$ ($ml_{blood}/min/ml_{tissue}$) Using Parent Plasma Arterial IF		
	Pre C/N	Post C/N	P	Pre C/N	Post C/N	P
Tumour (n = 10)	0.89 ± 0.14 [0.57 to 1.2]	1.3 ± 0.21 [0.83 to 1.8]	0.013	0.9 ± 0.15 [0.56 to 1.2]	1.3 ± 0.2 [0.7 to 1.7]	0.037
Spleen (n = 6)	6.3 ± 0.81 [4.2 to 8.4]	6.0 ± 0.7 [4.2 to 7.8]	1	7.1 ± 0.7 [5.1 to 8.9]	6.2 ± 0.7 [4.4 to 8]	0.441

n, number; $K_1 \times 10^{-1}$ ($ml_{blood}/min/ml_{tissue}$); C/N, carbogen and nicotinamide.

Data are mean ± SEM [95% CI].

Table 6.9: Comparison of K_1 values obtained using total and parent plasma arterial input functions

Region	*p value for K_1 with no C/N*	*p value for K_1 with C/N*
Tumour	*0.56*	*0.94*
Spleen	*0.19*	*0.7*

C/N, carbogen and nicotinamide

6.5.7.2 FRF

Fractional retention of 5-[^{18}F]FU (FRF), was calculated from the IRF by dividing $IRF_{1min}/IRF_{60\ min}$ as explained in Chapter 2. This was to correct for the very earliest time points of the IRF that do not only represent delivery, but also have a blood volume component.

Tumour FRF calculated using either total or parent plasma showed no consistent change after carbogen and nicotinamide with no change in 2/10 metastases, an increase in 5/5 metastases and a decrease in 3/10 metastases and there was no statistical difference in FRF, in agreement with results from tumour AUC_{90mins}. The most obvious difference was seen in the actual values obtained for tumour FRF using total or parent plasma for pre and post carbogen and nicotinamide.

Tumour FRF was higher pre and post carbogen and nicotinamide using parent plasma arterial input function and this was statistically significant. The reason for this finding may be because of the difference in the 2 input functions, where it can be seen that the plasma arterial concentration at 60 minutes is higher for total plasma. This results in a lower IRF_{60mins} for total plasma than for parent plasma after convolution with tissue response and consequently lower FRF.

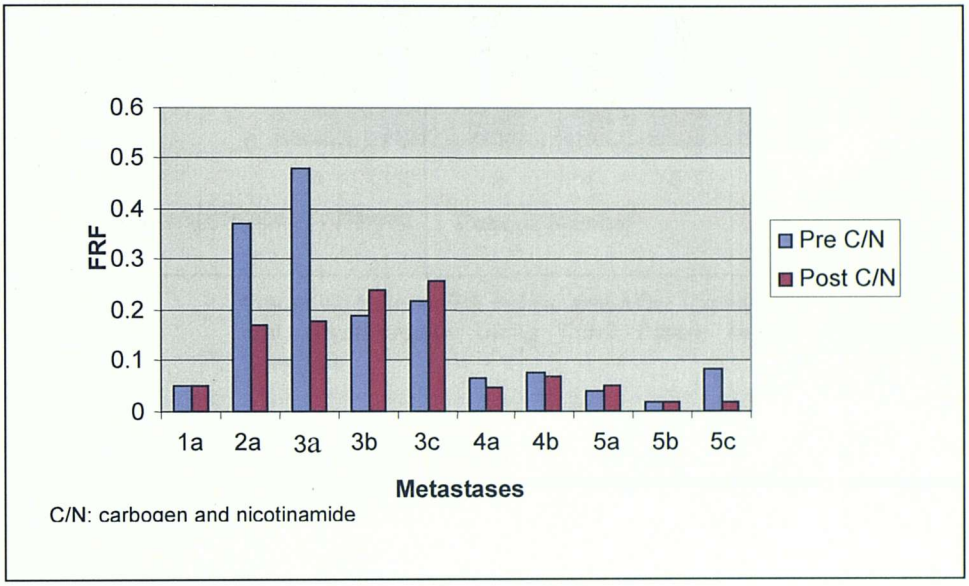


Figure 40: Tumour FRF Before and After Carbogen and Nicotinamide Using Total Plasma Input Function

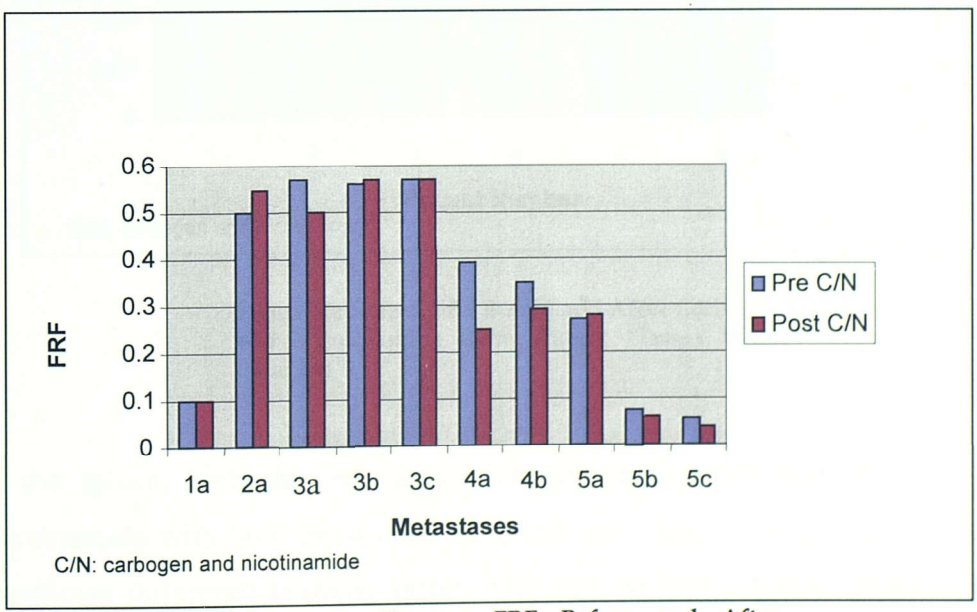


Figure 41: Tumour FRF Before and After Carbogen and Nicotinamide Using Parent Plasma Input Function

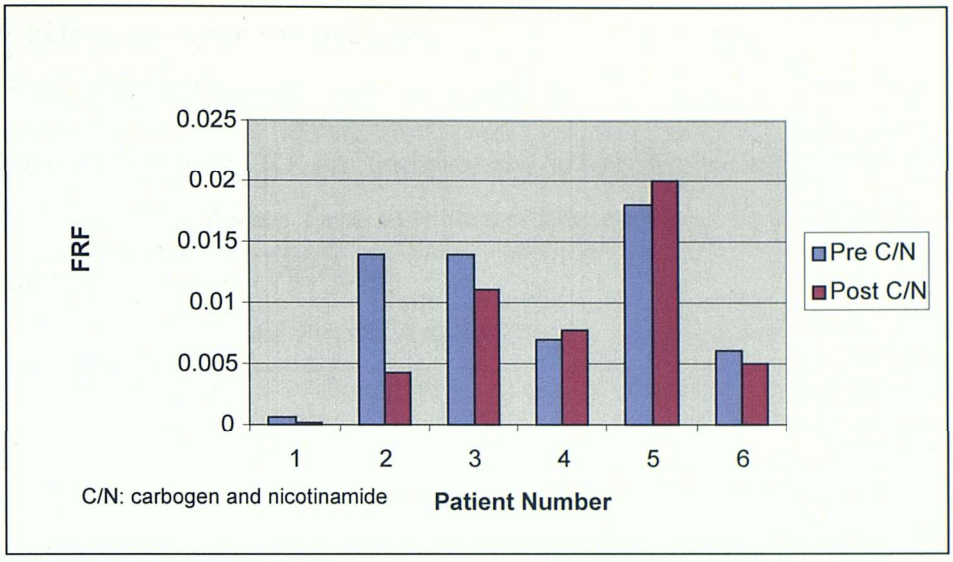


Figure 42: Spleen FRF Before and After Carbogen and Nicotinamide Using Total Parent Input Function

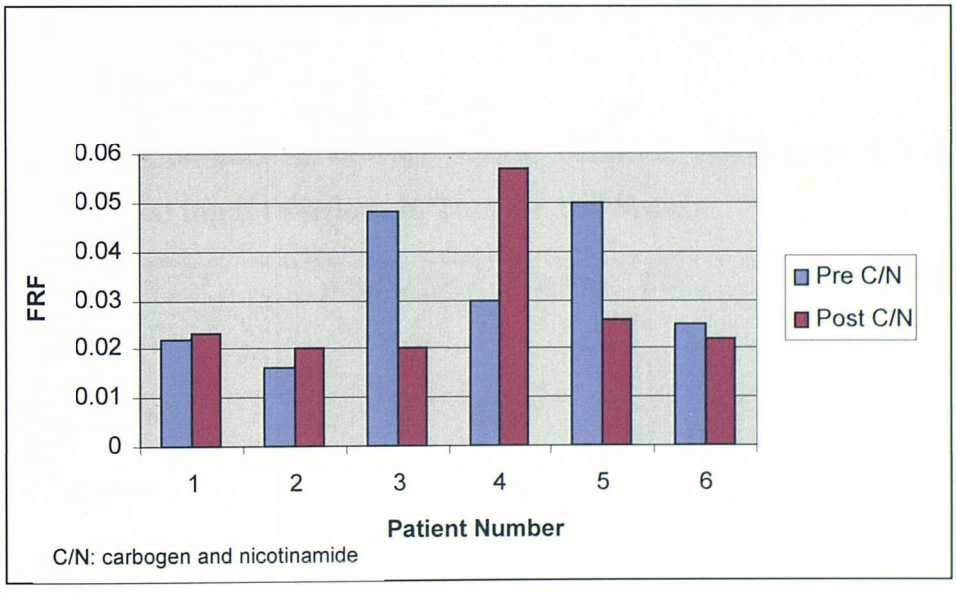


Figure 43: Spleen FRF Before and After Carbogen and Nicotinamide Using Parent Plasma Input Function

In the spleen, FRF showed variable changes before and after carbogen and nicotinamide with both input arms in agreement with AUC_{90mins}. There was no significant difference between spleen FRF derived using total or parent plasma input functions.

As can be seen from the summary Table 6.10, tumour FRF is higher than spleen FRF before and after carbogen and nicotinamide as expected from the results obtained from $AUC_{90mins.}$

Table 6.10: Table of FRF for Tumour and Spleen Before and After Carbogen and Nicotinamide Using Total and Parent Plasma Input Functions

Region	FRF x 10^1 Using Total Plasma Arterial IF			FRF x 10^1 Using Parent Plasma Arterial IF		
	Pre C/N	Post C/N	p	Pre C/N	Post C/N	p
Tumour (n = 10)	1.6 ± 0.49 [0.48 to 2.7]	1.1 ± 0.29 [0.45 to 1.8]	0.36	3.4 ± 0.66 [1.9 to 0.49]	3.2 ± 0.68 [1.7 to 4.7]	0.2
Spleen (n = 6)	0.10 ± 0.031 [0.22 to 0.19]	0.86 ± 0.03 [-0.007 to 0.18]	0.62	0.32 ± 0.057 [0.17 to 0.47]	0.28 ± 0.059 [0.13 to 0.43]	0.8

n, number; FRF, fractional retention of 5-[^{18}F]FU; C/N, carbogen and nicotinamide.

Data are mean ± SEM [95% CI].

Table 6.11: Comparison of FRF values obtained using total and parent plasma arterial input functions in Tumour and Spleen

Region	*p value for FRF with no C/N*	*p value for FRF with C/N*
Tumour	*0.039*	*0.002*
Spleen	*0.62*	*0.06*

C/N, carbogen and nicotinamide

6.5.7.3 Permeability Product Surface Area (PS)

PS is calculated from the K_1 parameter (which is the product of regional flow and extraction) derived from spectral analysis, and from the corresponding perfusion values. See Chapter 2 for equations and further explanation of PS derivation.

The PS for tumour increased in 8/10 liver metastases by a mean of 64% after carbogen and nicotinamide but did not achieve statistical significance with either

input functions. Interestingly, in the 2 metastases, (which were in the same patient), that had a reduction in PS, also had a reduction in $SUV_{3.75mins}$ and K_1 with carbogen and nicotinamide. There was no statistical difference between input function arms and PS after carbogen and nicotinamide.

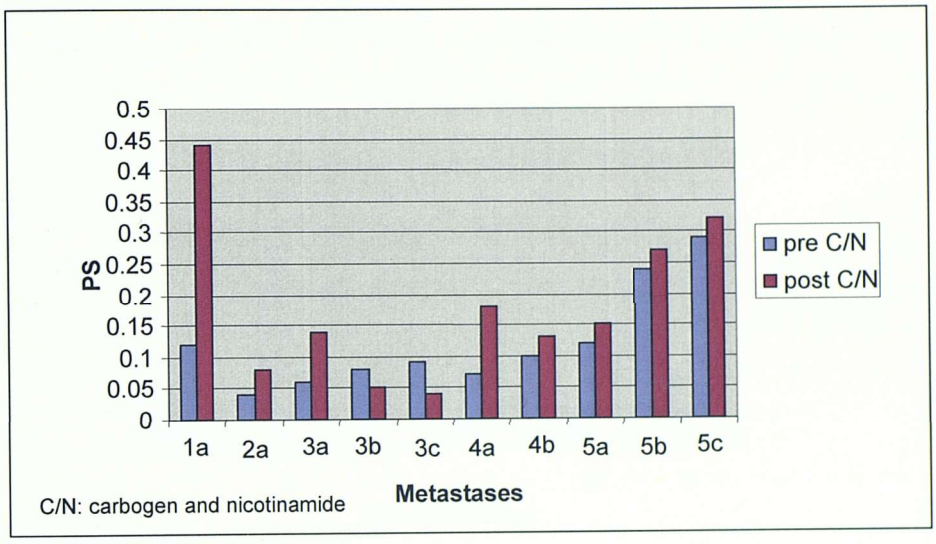


Figure 44: Tumour PS Before and After Carbogen and Nicotinamide Using Total Plasma Input Function

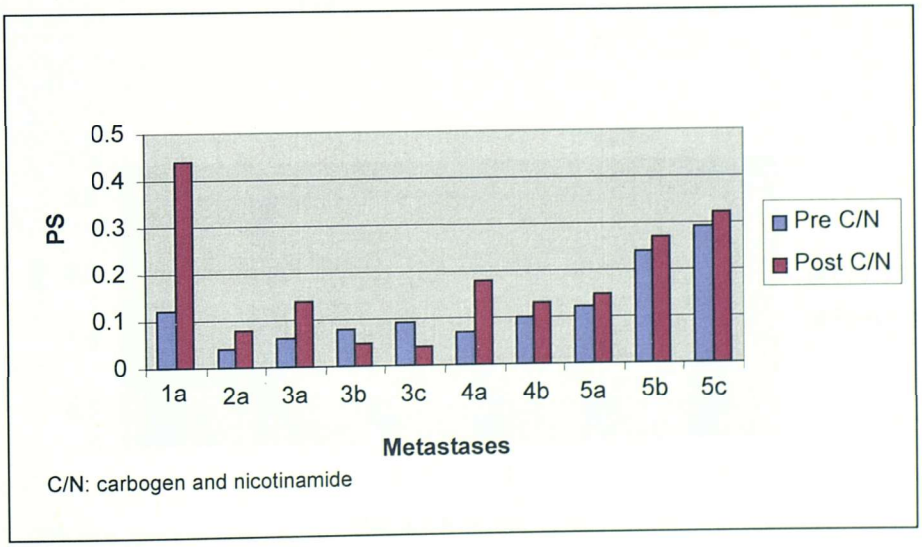


Figure 45: Tumour PS Before and After Carbogen and Nicotinamide Using Parent Plasma Input Function

Values for PS product in the spleen were similar before and after carbogen/nicotinamide (Table 6.12) with both inputs suggesting that there was no modulation of transmembrane transport of 5-[^{18}F]FU by carbogen/ nicotinamide. There was no statistical difference between PS calculated for spleen for the two input functions either.

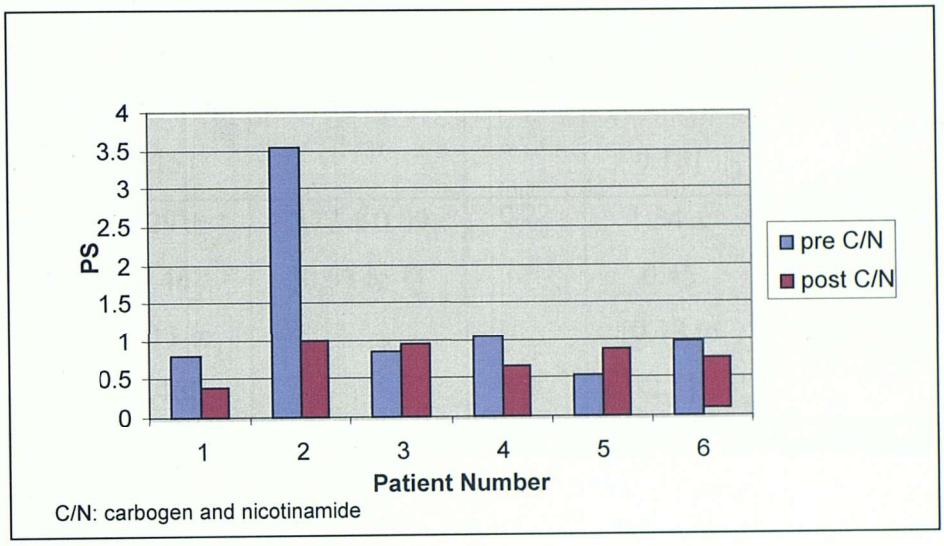


Figure 46: Spleen PS Before and After Carbogen and Nicotinamide Using Total Plasma Input Function

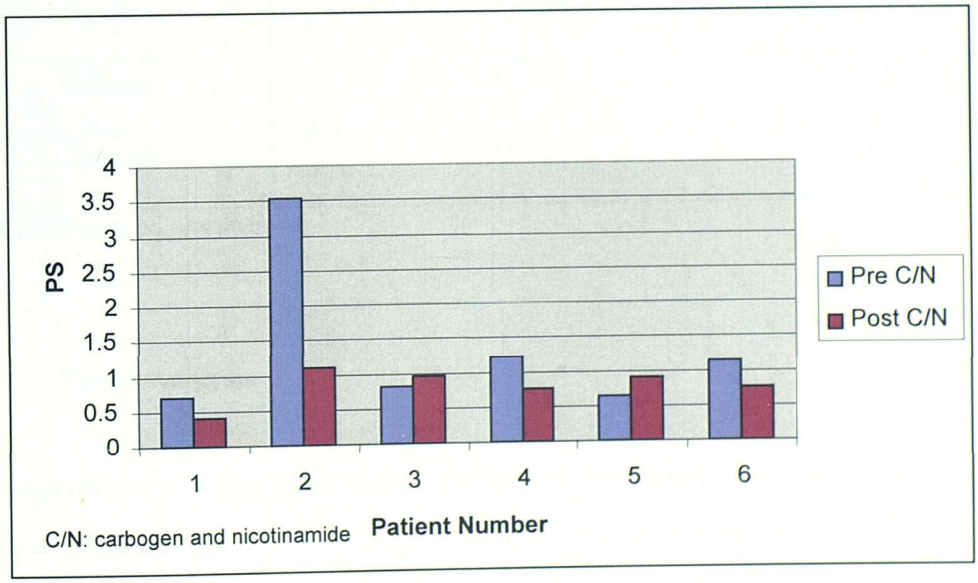


Figure 47: Spleen PS Before and After Carbogen and Nicotinamide Using Parent Plasma Input Function

Table 6.12: Table of PS for Tumour and Spleen Before and After Carbogen and Nicotinamide Using Total and Parent Plasma Input Functions

Region	PS Using Total Plasma Arterial IF			PS Using Parent Plasma Arterial IF		
	Pre C/N	Post C/N	p	Pre C/N	Post C/N	p
Tumour (n = 10)	0.11 ± 0.016 [0.072 to 0.15]	0.18 ± 0.037 [0.094 to 0.26]	0.052	0.12 ± 0.025 [0.063 to 0.18]	0.18 ± 0.04 [0.088 to 0.27]	0.065
Spleen (n = 6)	1.29 ± 0.46 [0.11 to 2.46]	0.77 ± 0.09 [0.53 to 1]	0.22	1.34 ± 0.45 [0.18 to 2.5]	0.82 ± 0.097 [0.57 to 1.1]	0.16

[1] permeability surface area product, ml of plasma/min/ml of tissue; C/N, carbogen/nicotinamide; n = number

Table 6.13: Comparison of PS values obtained using total and parent plasma arterial input functions in Tumour and Spleen

Region	*p value for FRF with no C/N*	*p value for FRF with C/N*
Tumour	*0.87*	*1*
Spleen	*0.31*	*0.06*

C/N, carbogen and nicotinamide

6.5.8 Patlak Analysis

K_I was obtained using an extended model led graphical analysis for spleen and tumour (Mankoff *et al.*, 1996). As before, in 3 liver metastases (1b, 2b and 3d) and 2 lymph node metastases analysis was not possible due to poor fit of data. K_I was unaffected by carbogen and nicotinamide modulation in the liver metastases and spleen. However, tumour K_I was greater for tumour than spleen. (Table 6.14). The negative K_I obtained in some patients for the spleen indicates that although

there is delivery and uptake of 5-[^{18}F] FU by the spleen, there is greater washout of the radiotracer.

Table 6.14: Summary of results for K_I in Tumour and Spleen

N	K_I ($ml/_{blood}/min/ml_{tissue}$)x 10^{-2}		
	Pre C/N	Post C/N	p
Tumour (n = 10)	3.0 ± 0.68 [1.5 to 4.6]	2.8 ± 0.37 [1.9 to 3.6]	0.86
Spleen (n = 6)	-0.00255 ± 0.017 [-0.43 to 0.43]	0.24 ± 0.02 [-0.42 to 0.89]	0.56

C/N, carbogen and nicotinamide

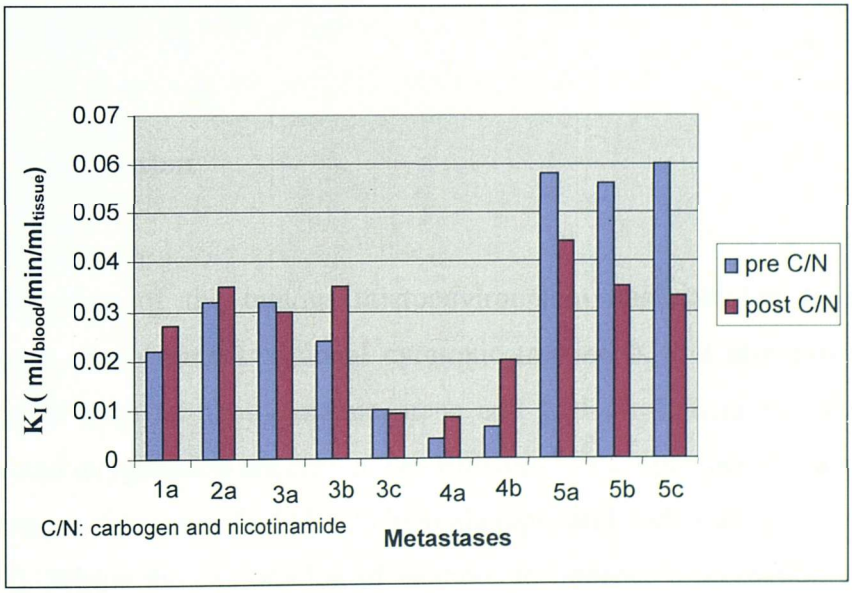


Figure 48: Tumour K_I Before and After Carbogen and Nicotinamide

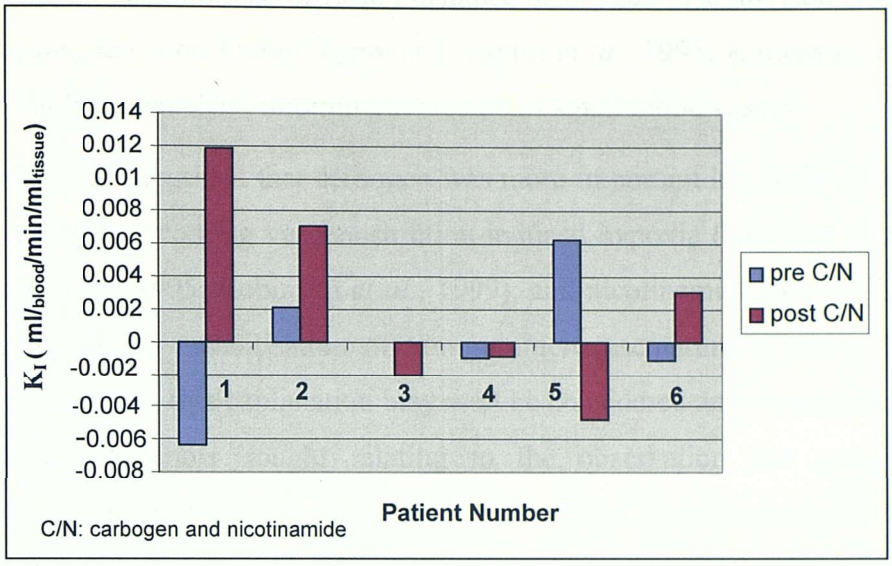


Figure 49: Spleen K_I Before and After Carbogen and Nicotinamide

Modified Patlak requires various assumptions to permit analysis and in kidney and liver these requirements are not fulfilled. One condition that is not satisfied is that both these tissues possess quantities of DPD and hence metabolise 5-[^{18}F]FU which is one explanation why modified Patlak analysis was predicted to fail in them.

6.6 Discussion

Modification of the tumour microenvironment has potential to improve the efficacy of not only traditional cytotoxic treatments, but also novel anticancer therapies such as photodynamic, gene and biological therapies. Tumour blood flow and oxygenation are critical determinants in the outcome of many such forms of cancer treatment including chemotherapy and radiotherapy (Vaupel *et al.*, 2001). Whilst the exploitation of methods to improve oxygenation is of primary concern in radiotherapy, the mechanisms involved are strongly linked to those affecting tissue blood flow and consequently have important implications for the delivery of systemically delivered chemotherapy.

Conventionally, tumour hypoxia is divided into two distinct categories: chronic, diffusion limited hypoxia, occurring in tumour cells > 150 μm from blood vessels

as this is the approximate diffusion distance of oxygen (Thomlinson *et al.*, 1955) and acute, perfusion-limited hypoxia (Chaplin *et al.*, 1995; Kimura *et al.*, 1996), resulting from transient, intermittent closure of small blood vessels.

Early studies suggested that carbogen was more important in overcoming chronic hypoxia by overcoming vasoconstriction-induced hypoxia (Griffiths *et al.*, 1997; Honess *et al.*, 1995; Robinson *et al.*, 1999), and nicotinamide thought to prevent acute hypoxia by stabilisation of tumour microvasculature (Chaplin D. *et al.*, 1990). However, this explanation may well be considered an oversimplification as clarification is now sought relating to the observation that carbogen and nicotinamide may not only effect tissue perfusion but also tumour metabolism and physiology (Robinson *et al.*, 2000).

Inhaled carbogen increased the delivery of intravenous ifosfamide and 5-FU in experimental tumours in rat models (Rodrigues *et al.*, 1997; Rodrigues *et al.*, 2002; Stubbs *et al.*, 1998; Thews *et al.*, 2002) using magnetic resonant spectroscopy (MRS). However, there is currently no data available on the effect of carbogen with or without nicotinamide on drug delivery in man. The purpose of this study was to demonstrate whether similar beneficial effects would occur in man following the administration of nicotinamide and carbogen to patients with metastatic colorectal cancer. The advantages of PET over MRS are its superior sensitivity, better spatial and temporal resolution and ability to image deep-seated tumours and organs, though both are non-invasive modalities. Although MRS can distinguish parent compounds from radiolabelled metabolites, arterial blood sampling and the application of kinetic modelling analysis with PET allows quantification of relevant pharmacokinetic parameters. In addition it was possible to record effects of carbogen and nicotinamide in normal tissue and on human physiology.

As expected there was a dramatic increase in pO_2 after carbogen inhalation. This started within 7 minutes of carbogen inhalation and peaked at 10 minutes, though arterial pO_2 was not continually measured during this period. Arterial pO_2 returned to baseline values 5 minutes after discontinuation of carbogen. These findings agree with results from non-clinical studies (Stubbs *et al.*, 1998; Thews *et al.*, 2002). The rapid increase in arterial pO_2 in response to carbogen reflects intra-

tumoural changes in O_2 observed in human tumours detected by Eppendorf pO_2 probes (Falk S. *et al.*, 1995; Powell *et al.*, 1999).

This study showed arterial pCO_2 was unaffected by carbogen although in animal models pCO_2 increased in response to inhalation of all gases containing differing proportions of CO_2 (1% to 5%) with the maximum pCO_2 increase occurring with the largest CO_2 component (Dunn *et al.*, 1999; Thews *et al.*, 2002). Furthermore, in a clinical study carbogen breathing induced a significant rise in arterial pCO_2 compared to breathing air or a combination of 98% O_2 and 2% CO_2 (Baddeley *et al.*, 2000). However, in the latter study carbogen breathing was through a very tightly fitting mask which 29% of volunteers were unable to endure. In this study the mask was looser but all subjects tolerated carbogen for the required time interval, and as a consequence the carbogen may have been diluted with air resulting in no change in arterial pCO_2 measurements.

Arterial pH was unaffected by carbogen in these patients, similar to findings from other clinical (Baddeley *et al.*, 2000) and animal studies (Thews *et al.*, 2002). Other animal studies have observed both increases (Dunn *et al.*, 1999; Honess *et al.*, 1995) and decreases (Stubbs *et al.*, 1998) in pH in response to carbogen. Also, a significant rise in blood glucose levels in response to nicotinamide and carbogen was seen in mice, raising the issue of the approach inducing hyperglycaemia in man (Robinson *et al.*, 2000). No such changes in arterial glucose were found in this study though.

The lack of change in arterial pCO_2, pH and glucose found in man suggests there may be species-related changes in pCO_2 and glucose in response to carbogen and. However, further work is needed to clarify the complex physiological changes that might occur in response to nicotinamide and carbogen administration in man.

Using PET we were able to investigate concurrently a number of normal tissues, namely kidney, liver and spleen. Tissue-type dependent changes in perfusion were seen, consistent with a study in an experimental tumour model, where perfusion of the liver and kidney significantly decreased and an increase in perfusion in the spleen was noted after carbogen inhalation (Honess *et al.*, 1995). In the animal study, the increase in splenic perfusion was further attenuated by the addition of nicotinamide and largest in treatment with nicotinamide only. We saw a dramatic

decrease in renal flow in response to nicotinamide and carbogen. This reduction in kidney perfusion, and corresponding decrease in water V_d, suggests that in man renal blood vessels shut down in response to carbogen and nicotinamide. A reduction in flow index was also seen in the liver where there was a tendency for V_d to decrease. As cardiac output was maintained, the effect on the kidney and liver perfusion indicate mechanisms of autoregulation in these organs, possibly resulting in the redistribution of blood flow from highly perfused organs (i.e., kidney and liver) to other tissues such as tumour. Acute local blood flow control is normally achieved by rapid changes in local constriction of arterioles to maintain a constant supply of oxygen to the tissue (Guyton *et al.*, 1996). As there was no significant increase of pCO_2 in this study, the changes seen in normal tissue are likely to stem from hyperoxia. This suggestion is further supported by the lack of changes in liver or kidney perfusion with nicotinamide only in the animal model. In analogy with the animal study, the lack of change in perfusion in the spleen could be explained by suspension of any improvement in flow with nicotinamide by the vasoconstricting affect of the increased pO_2. However, evaluation of the exact mechanism would have required separate studies with either nicotinamide or carbogen inhalation. The lack of significant change in cardiac output suggests systemic blood pressure could increase following nicotinamide and carbogen. Although blood pressure was not measured in our study due to positional constraints within the scanner, an increased blood pressure following carbogen was reported in experimental models (Braun R. *et al.*, 2001; Dunn *et al.*, 1999), while in normal human volunteers nicotinamide did not effect blood pressure (Stratford *et al.*, 1992).

Our study confirms the inferior blood flow in colorectal liver metastases compared with normal tissues such as spleen, kidney and liver and is of a similar magnitude to that reported in the literature using other measuring techniques (Vaupel P. *et al.*, 1989). As noted in previous studies, the effects of nicotinamide and carbogen on tumour perfusion seem to be site dependent (Dunn *et al.*, 1999). The 32% increase in tumour perfusion seen in response to nicotinamide and carbogen administration is in keeping with other studies, whereas perfusion of the two lymph node metastases decreased. A 22% increase was measured by Laser doppler probes in superficial, advanced human tumours (Powell MEB. *et al.*,

1997) and in experimental tumours a 75% increase in perfusion was documented following high-dose nicotinamide administration of 500 mg/kg (Braun R. *et al.*, 2001), a dose much higher than the maximum tolerated human dose. There is always concern that doppler measurements of tissue flow do not discriminate tissue perfusion from blood that flows through arterial-venous shunts (this can result in an overestimation of tissue perfusion). In this study with examination of liver metastases, consideration must be made of a dual blood supply to the liver and subsequently to the liver metastases, when using a technique that requires the assumption that the data are modelled using a one compartment model (Kety *et al.*, 1948). A study by Ziegler et al in 1996 (Ziegler *et al.*, 1996) used a dual input model to estimate liver blood flow compared with direct measurements of both inputs using microspheres in dogs. Flow values from the single input model were found to be closest to the microsphere values. Although the dual input in the liver may have introduced a source of inaccuracy the available data suggest that human tumour perfusion does increase in response to nicotinamide and carbogen. Also, any concern that the diverted blood flow might pass through vascular shunts in tumours can be negated because of the use of $H_2[^{15}O]$ which is deposited in tissues by capillary exchange.

The changes in perfusion in normal tissues and tumour in this study suggests an augmentation of blood flow in tissues less capable of local vascular control mechanisms, such as tumour. This finding is consistent with the theory that that the 'steal' phenomenon is the dominant mechanism for redistribution of host blood flow to tumour (Jirtle, 1988). The 'steal' effect originally describes the reduced tumour blood flow in response to drugs such as hydralazine, where normal tissue vasculature relaxes after administration of vasodilating agents thereby diverting blood flow from tumours which are not capable of further vessel dilatation. In this study, we have demonstrated a 'reverse steal' or 'gain' effect (Robinson *et al.*, 1995) with apparent diversion of perfusion from normal tissue to the liver metastases, though not in lymph node metastases, suggesting differential tumour response. In this study however, the V_d of water in tumours did not alter in response to nicotinamide and carbogen administration, suggesting that there was no recruitment of previously non-functioning vessels in the liver metastases. In animal models, vasoconstrictor-induced increases in the mean blood pressure has

led to increases in tumour blood flow but also interstitial fluid pressure (Zlotecki *et al.*, 1995). High interstitial fluid pressure may also explain the lack of correlation between tumour blood flow and K_1. However, the tumour is likely to be responding in a heterogeneous manner. Parts of the tumour might be responding by an increase in flow with an increase in 5-FU extraction, whereas others might respond with an increase in V_d but no changes in flow. For example, in one tumour, (liver metastasis 1a), there was a large increase in K_1, no change in perfusion, but an increase in V_d and therefore more of tumour tissue being perfused. In another tumour, (liver metastasis 2a), there was a large increase in flow and V_d, but only a modest increase in K_1, which is likely to be due to a low single-pass extraction fraction (Crone, 1963) due to the high flow.

The available data suggest that in humans, perfusion of liver metastases increases in response to nicotinamide and carbogen, but the underlying mechanisms remain complex. Whilst, the mode of action of carbogen and nicotinamide on tumour blood vessels is still unclear, it is likely to involve a complex interaction between tumour cells, tumour vasculature and the tumour microenvironment (Powell MEB. *et al.*, 1997). Alteration in the concentration of vasodilators such as nitric oxide (NO) and its antagonist, endothelin, a peptide vasoconstrictor, have been speculated as other causes in the changes of tumour blood flow (Sibtain *et al.*, 2002). CO_2 itself is a direct and powerful mediator of these substances and a local increase in CO_2 leads to an increase in NO and a concomitant decrease in endothelin (Yoshimoto *et al.*, 1991); conversely, a high O_2 reacts rapidly with NO by scavenging NO produced by endothelial cells (Ganong WF., 2001). Nicotinamide has also been found to independently affect the production of NO and endothelin and has been found to inhibit nitric acid synthase mRNA induction in activated macrophages (Pellat-Deceunynck *et al.*, 1994). It would appear that a balance of NO and endothelin is of importance in manipulating tumour blood flow.

The early uptake and delivery of 5-[^{18}F]FU (measured as $SUV_{3.75mins}$ and K_1 respectively) was higher in the normal tissues studied than in the liver metastases, a finding that mirrored the higher normal tissue perfusion. This observation, together with a significant correlation between tumour perfusion and $SUV_{3.75mins}$ before intervention, suggests that 5-[^{18}F]FU uptake is related to tissue perfusion in

liver metastases. The data show that nicotinamide and carbogen can increase tumour perfusion, although the effect on 5-[^{18}F]FU uptake and delivery varied between individual metastases. These findings are similar to changes observed in mice, where only large tumours showed increased uptake of 5-FU in response to carbogen (McSheehy *et al.*, 1998). In our study, all 5 liver metastases larger than 4cm had increased $SUV_{3.75mins}$ and K_1 values (liver metastases: 1a, 2a, 4a, 4b and 5a). In contrast, the effect of carbogen uptake and delivery in tumours less than 4cm in size was variable and was not consistent with changes in regional perfusion. In normal tissue, changes in perfusion also reflected the uptake of 5-[^{18}F]FU with a significantly reduced perfusion and $SUV_{3.75mins}$ in kidneys after nicotinamide and carbogen, though no change in either parameter in the spleen.

The tissue exposure measured as $AUC_{90min,}$ retention of ^{18}F-5FU measured as FRF and net clearance measured as K_1 was higher in tumour than spleen, both before and after nicotinamide and carbogen. This indicates tumour trapping of 5-FU by the metastases, similar to the observation made using magnetic resonance spectroscopy (Presant C. *et al.*, 1994). Differences in the retention of 5-FU in tumour and spleen might relate to differences in the gradients of extra- and intracellular pH between tissues (Ojugo ASE. *et al.*, 1998), and/or differences in tissue proliferation (Wells *et al.*, 2002a) with the formation of more 5-FU nucleosides in tumour than in normal tissue. In this study, tumour fractional retention and AUC_{90min} of 5-[^{18}F]FU was unaffected by nicotinamide and carbogen. This finding contrasts with that of McSheehy *et al* who showed a carbogen-induced increase in 5-FU retention measured using MRS in murine RIF-1 tumours (McSheehy *et al.*, 1998). The group related the increase in 5-FU retention to a differential rise in extracellular *versus* intracellular pH, thus creating a proton pump gradient favouring intracellular retention of 5-FU in tumours (McSheehy *et al.*, 2000). The lack of change in intratumoral retention of 5-[^{18}F]FU may be due to the 20-minute shorter duration of carbogen breathing in our study or a cancellation of the increased delivery because of an increased rate of washout. It remains to be seen whether a longer carbogen breathing time in humans might increase 5-[^{18}F]FU retention, or a short breathing time to exploit the initial increase in delivery while minimizing the enhanced extraction. Future studies with MRS would also be of interest to identify any chemical species for

which there might be an increased exposure or retention. However, further study is required to examine the effects of nicotinamide and carbogen on 5-FU extraction from tissues.

Permeability and surface area product (PS) measures transport or diffusion across capillary endothelial cells and was higher in spleen than tumour before and after carbogen and nicotinamide administration implying either differences in tissue capillary permeability or capillary surface area. There was a non-significant increase in tumour in response to carbogen and nicotinamide. However, the increase does suggest that carbogen and nicotinamide may influence vascular permeability of 5-FU from plasma to tissue in tumours that has hitherto been undetectable in studies using MRS imaging, particularly as this study has shown that increased capillary surface area is unlikely as tumour V_d was unchanged.

Comparing spectral analysis using total plasma and parent plasma arterial radioactivity as input functions showed that the only statistical difference was seen in FRF because of differences in the profile of the curves at later time points i.e. at 60 minutes. K_1 and PS were unaffected by this and suggests that correction for labelled metabolites is not necessary to derive these parameters. Therefore, it may be possible to obtain K_1 and PS for 5-[^{18}F]FU without the use of arterial blood sampling, as the input function can be obtained directly from the PET image if a pool of arterial blood is within the field of view of the PET scanner during imaging .

Other than discomfort in carbogen breathing, an important criterion to be considered is the potential effect of nicotinamide and carbogen on normal tissue toxicity. An earlier study in rats bearing GH3 prolactinomas found no carbogen-induced enhancement of ifosfamide uptake, measured using MRS, in tissue extracts of liver, spleen, kidney, muscle and heart (Rodrigues *et al.*, 1997). A more recent paper highlighted an unexpected MRS detection of 5-FU anabolites in the metastasis-free liver of a patient, raising the issue of increased hepatocellular toxicity with concurrent carbogen breathing (Griffiths JR. *et al.*, 2001). However, studies in rats did not find any carbogen-induced change in the liver or small intestine levels of 5-fluoro-2'-deoxyuridine-5'-monophosphate (FdUMP) measured using MRS. Our own study has corroborated the rat studies and indicates a lack of increased delivery and retention of ^{18}F-5FU in kidney,

spleen and liver. The effects on renal perfusion suggest that angiotensin-converting enzyme (ACE) inhibitors, which also affect renovascular function, should be avoided.

This study has shown that carbogen and nicotinamide can alter perfusion and 5-[^{18}F]FU delivery in tumour and normal tissue. However, further studies are needed to assess whether varying the duration of carbogen breathing can enhance 5-[^{18}F]FU extraction and retention by metastases, and ultimately improve response and survival rates in patients undergoing 5-FU treatment for metastatic colorectal cancer.

6.7 Summary

1. Carbogen and nicotinamide can alter tumour and normal tissue perfusion in man resulting in tissue dependent effects.

2. Carbogen and nicotinamide increase perfusion of colorectal cancer metastases in liver indirectly, by redistribution of blood from vascular tissues such as the kidney.

3. The dramatic reduction of renal perfusion following carbogen and nicotinamide warrants further investigation into the possible mechanism(s) that may be involved.

4. 5-[^{18}F]FU pharmacokinetic profile can also be modified by carbogen and nicotinamide with enhanced delivery to tumour reflecting the changes seen in perfusion.

5. No deleterious effects were observed in 5-[^{18}F]FU pharmacokinetics in normal tissue, an important consideration when evaluating chemotherapeutic agents.

6. The methodology presented in this study will be helpful in appraising other agents postulated to improve the delivery and retention of systemically administered anti-cancer drugs in humans.

Chapter 7 5-FU and Interferon

7.1 Introduction

Interferons are pleiotropic cytokines, discovered almost 50 years ago, (Isaacs *et al.*, 1957) and have been evaluated as potential therapeutic modalities as they exert antiproliferative and immunomodulatory effects on malignant cells (Jonasch *et al.*, 2001) through cell surface receptor binding and signal transduction pathways (Wadler *et al.*, 1997a). Two major subgroups are recognized depending on chromosomal location and receptor specificity; Type 1, to which interferon-α (IFN-α) and –β (IFN-β) subtypes belong and Type 2, which consists of interferon-γ (Wadler *et al.*, 1997b).

Numerous *in vitro* studies have reported enhanced cytotoxicity of 5-FU in various cell lines by interferon although the actual mechanism of interaction is still unclear. An early study demonstrated growth inhibition in MC 38 adenocarcinoma and HL-60 human leukaemic cells, most marked when 5-FU was preceded by IFN-α (Elias *et al.*, 1988). However, a number of possible steps that may be responsible for interferon enhancing 5-FU cytotoxicity have been identified.

Elias et al demonstrated an elevation in 5-fluoro-2'-deoxyuridine-5'-monophosphate (FdUMP) *in vitro* following IFN-α and 5-FU compared to 5-FU alone (Elias *et al.*, 1989). One possible explanation for the increase in FdUMP could be an IFN-α dose-dependent induction of thymidine phosphorylase (TP) (Schwartz *et al.*, 1995; Schwartz *et al.*, 1992). An *in vivo* study has shown a two fold elevation in TP in peripheral blood mononuclear cells following treatment with 5-FU and a single dose of IFN-α or IFN-β (given 1 to 2 hours before 5-FU), which persisted for 48 hours (Makower *et al.*, 1997).

Other studies have shown DNA damage in colon cancer cells, measured as single and double strand breaks induced by 5-FU, is increased by IFN-α modulation (Houghton *et al.*, 1993; van der Wilt *et al.*, 1997; Wadler *et al.*, 1996).

Milano et al showed inhibition of dihydropyrimidine dehydrogenase catabolism of 5-FU by interferon-α *in vitro* in various cell lines resulting in potentiation of 5-FU cytotoxicity (Milano *et al.*, 1994).

A study by Chu et al has shown that IFN-γ can abrogate the 3-fold 5-FU induced expression of thymidylate synthase *in vitro* in the human colon cancer cell line H630, thereby enhancing the sensitivity of the cell to 5-FU in an otherwise relatively resistant 5-FU cell line (Chu *et al.*, 1990). However, only minimal 5-FU induced TS over expression in human (Grem *et al.*, 1995) and murine colon cancer cell lines was observed in other studies, with no effect on this by either IFN-γ or IFN-α (van der Wilt *et al.*, 1997).

There is still no agreed consensus as to the mode of action of IFN-α on 5-FU despite the many studies and results in the literature. As response rates for the treatment of metastatic colorectal with 5-FU are dismally low, it is important to fully evaluate the enhanced efficacy that IFN-α potentially could bring.

7.2 Study Aims

7.2.1 Primary Aim

1) To assess 5-[^{18}F]FU pharmacokinetic changes following biomodulation by IFN-α *in vivo* in metastases and normal tissue, as the precise mode of their interaction with 5-FU is still not fully understood.

2) To relate any PET detected pharmacokinetic changes to known mechanisms of activity or to provide insight into novel modes of activity.

7.2.2 Secondary Aims

1) To establish whether the combination of 5-[^{18}F]FU and IFN-α had any effect on normal tissue and tumour perfusion.

2) To establish whether dose of 5-FU had any effect on IFN-α biomodulation.

7.3 Methods

7.3.1 Patient Selection

Patients with gastrointestinal (one patient) or colorectal cancer (five patients) with metastasis scheduled palliative chemotherapy with a 5-FU based treatment regime were enrolled in this study. All 6 patients had not had any previous treatment with chemotherapy and had metastases that were ≥ 3 cm in size in at least 1 axis of dimension, as measured on CT scan.

Eligibility criteria included a life expectancy of ≥ 3 months, performance status ≥ 2, and adequate renal and hepatic function (serum creatinine, < 125 $\mu mol \cdot L^{-1}$; bilirubin < 17 $mmol \cdot L^{-1}$; and aspartate transaminase, < 35 $\mu mol \cdot L^{-1}$).

Ethics approval was obtained from the Hammersmith Hospital Research Ethics Committee and authorization for the use of radionuclides was given by UK Administration of Radioactive Substances Advisory Committee (ARSAC). All patients gave written and informed consent for participation in the study.

Dr Robert A Harte collected the data and the author analysed and interpreted the data.

7.3.2 Study Design

Patients underwent two 5-[^{18}F]FU pharmacokinetics studies at the same time of day, one week apart: the first on day 1, while biomodulator-naïve and the second on day 8 after administration of IFNα (either IFNα-2a or -2b). IFNα (3 million units subcutaneously) was injected on days 1, 4, 7, and 8. IFNα was given after the PET study on day 1 and 30 minutes before the 5-[^{18}F]FU scan on day 8. Patients were assigned to either have tracer dose of 5-FU (4.8 to 8.4 mg/m^2) or full dose 5-FU (375-400mg/m^2) for both scans in the study. The radiotracer 5-[^{18}F]FU was administered intravenously either alone or co-injected with 5-FU in the full dose studies in all patients. The 5-[^{18}F]FU radionuclide was injected as a bolus over 30 second to 1 minute and the scan duration was 60 minutes.

Tissue perfusion was obtained from $C[^{15}O]_2$ scans performed immediately before the 5-[^{18}F]-FU scan on day 1 and day 8. Each patient received $C[^{15}O]_2$ via a face mask at a rate of 4MBq per millilitre at 500mls/min for 5 minutes. The scan lasted 10 minutes in total.

7.4 Procedures

Patients were positioned in the scanner on successive weeks using anatomical landmarks with a recent CT scan to locate metastasis and after insertion of a cannula. The patients' positioning was verified at the start of the second scan by a short transmission scan.

Continual arterial blood sampling was performed during both scans with additional discrete samples obtained for metabolite analysis.

7.5 Data Analysis and Statistics

The data sets were transformed into analyzable formats. This involved reformatting the header folder of the dynamic image scans, converting well counts from ECAT counts into KBq using a conversion factor, and the application of a calibration factor for [^{15}O] and 5-[^{18}F] decay.

The perfusion scans were analysed using the modified Kety-Schmidt equation (Wilson *et al.*, 1992).

Tracer and full dose 5-[^{18}F]FU scans were both analysed using a semi-quantitative model to derive $SUV_{3.75mins}$ and AUC_{60mins}. Spectral analysis methods were used to obtain K_1 and fractional retention of 5-FU (FRF) utilizing two input functions: (i) total plasma (parent and labelled metabolites) and (ii) parent plasma (parent alone). In addition, full dose 5-[^{18}F]FU scans only were analysed using modified Patlak methodology to acquire K_1.

Mann-Whitney for unmatched pairs or Wilcoxon signed rank test for matched pairs were used for statistical analysis.

7.6 Results

7.6.1 Patient Characteristics

6 patients were recruited into the study, three each to receive tracer (1 male; 2 females) and full dose (2 males; 1 female). All 6 patients had liver metastases from their primary tumour. Mean age was 61 years (range 46 to 80 years). All patients had $C[^{15}O]_2$ and 5-[^{18}F]FU scans before and after IFNα modulation. Patient characteristics are shown below in Tables 7.1. Table 7.2 gives details of the number and size of liver metastasis and normal tissue regions that were sampled in each patient.

Table 7.1: Patient Details

Patient number	Patient scan number Pre [1]IFN-α	Patient scan number Post [1]IFN-α	Primary site of disease	Sex	Age (Years)	Body surface area
Tracer Dose 5-FU						
1	p03185	p03195	colorectal	F	54	1.64
2	p03210	p03225	colorectal	F	80	1.46
3	p03239	p03251	colorectal	M	59	1.75
Full Dose 5-FU						
4	p02696	p02711	colorectal	M	67	2
5	p02741	p02754	colorectal	F	46	1.68
6	p02784	p02795	gastric	M	61	1.87

[1], Interferon-α

Table 7.2: Regions Sampled

Patient	[1]Number of liver metastases	Maximum size of liver metastases (cm)	[1]Spleen	[1]Liver	[1]Kidney
1	2 (1a and 1b)	1a = 10; 1b = 7	✓	✓	x
2	1 (2a)	2a = 5	✓	✓	Rt.
3	2 (3a and 3b)	3a = 5; 3b = 6	✓	✓	x
4	2 (4a and 4b)	4a = 3; 4b = 3	✓	✓	x
5	3 (5a, 5b and 5c)	5a = 7; 5b = 5; 5c = 3	✓	✓	Rt.
6	1 (6a)	6a = 3.5	✓	✓	Rt. and Lt.

[1], regions sampled on PET scan; ✓, sampled; x, not sampled because not visible in area scanned

7.6.2 Scan Details

Table 7.3 gives details of the quantity of 5-FU administered and of the 5-[^{18}F]FU activity injected. Mean 5-FU given in full dose studies was 724mg and in the tracer dose studies was 10.4mg. Mean injected activity of 5-[^{18}F]FU was 347 MBq (range 176 to 416 MBq). The patient with the lowest 5-[^{18}F]FU activity of 176 MBq also had a comparatively small BSA of 1.46 which meant that there was reasonable radiotracer uptake in the ROIs to permit quantitative analysis. Mean radiochemical purity was 97.6% (range 95.7 to 100%) with uracil identified as the only impurity. Blood sampling during C[^{15}O]$_2$ and 5-[^{18}F]FU scans resulted in an estimated blood loss of 275 mls during each PET session.

Table 7.3: Scan Details

Patient scan number	Patient number	Dose of 5-FU injected (mg/m^2)	Injected 5-[^{18}F]FU activity (MBq)	5-[^{18}F]FU radiochemical purity %
p03185	1	14 mg (8.4)	349	95.7
p03195	1	14 mg (8.4)	348	97.9
p03210	2	7 mg (4.8)	176	90.8
p03225	2	7 mg (4.8)	343	99.5
p03239	3	10.3 mg (5.9)	348	98.6
p03251	3	10.3 mg (5.9)	299	98.1
p02696	4	800mg (400)	355	96.3
p02711	4	800mg (400)	416	97.4
p02741	5	672 mg (400)	359	98.9
p02754	5	672 mg (400)	392	99.6
p02784	6	701 mg (375)	375	98.9
p02795	6	701 mg (375)	413	100

7.6.3 5-[F^{18}]FU Pharmacokinetic Results

Semi-quantitative and spectral analyses were performed in full and tracer dose studies in tumours. Patlak analysis was performed only on full dose patient data in tumours.

7.6.4 Semi-Quantitative Analysis

Using this methodology, $SUV_{3.75mins}$ as an indication of 5-[^{18}F]FU delivery and AUC_{60mins} as a measure of tissue exposure to 5-[^{18}F]FU, were derived. Similar tissue activity curve (TAC) shapes that were seen in tumours in chapter 6 were derived for tumours in this study.

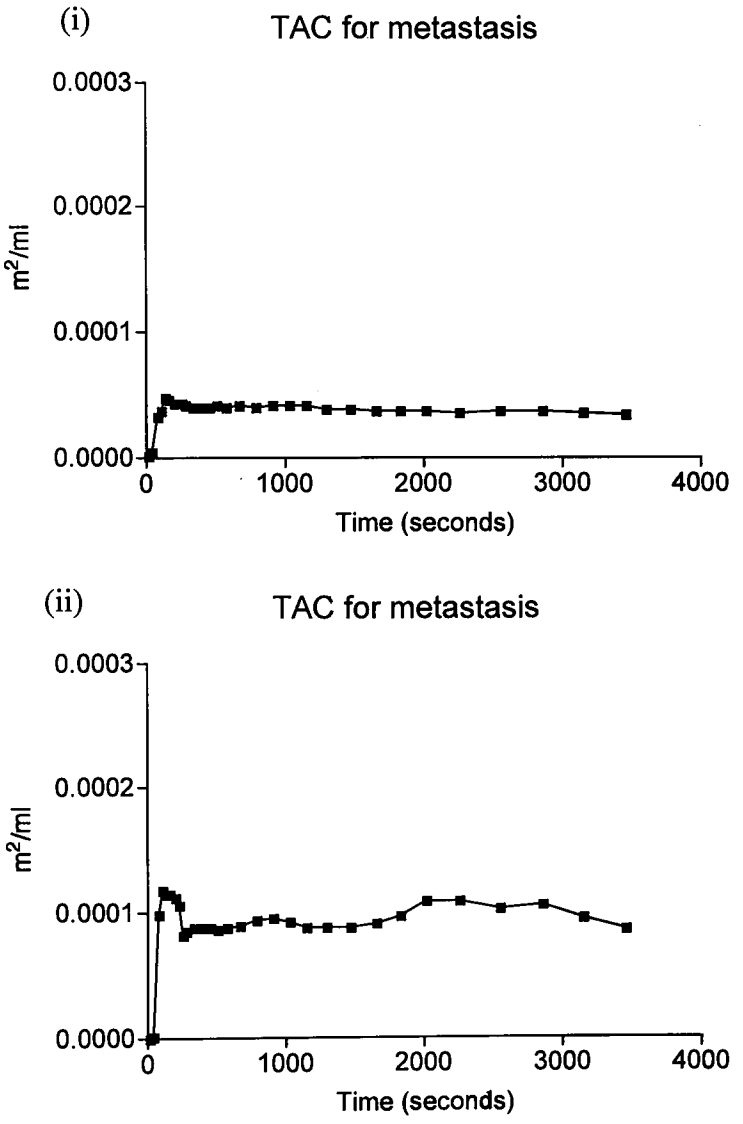


Figure 50: Typical Tissue Activity Curves for 5-[18F]FU in (i) Tracer Dose and (ii) Full Dose Studies

As can be seen from the TACs there was a difference in magnitude for tracer and full dose studies. This is reflected in the mean values for AUC_{60mins} for full dose which are higher than for tracer dose (see Table 7.4). This shows that the tracer dose falls below saturation pharmacokinetics for 5-FU. At tracer dose, 4/5 metastases had an increase in AUC_{60mins} and at full dose, 4/6 had an increase. However, there was no statistical difference with the addition of IFN-α for AUC_{60mins} at both dose levels. Mean AUC_{60mins} before IFN-α was $0.17 \pm 2.5 \times 10^{-2}$ and $0.27 \pm 0\ 6 \times 10^{-2}$ m^2/ml x sec for tracer and full dose respectively. After IFN-α, AUC_{60mins} was $0.19 \pm 3.2 \times 10^{-2}$ and $0.27 \pm 4.7 \times 10^{-2}$ m^2/ml/sec for tracer and full dose respectively.

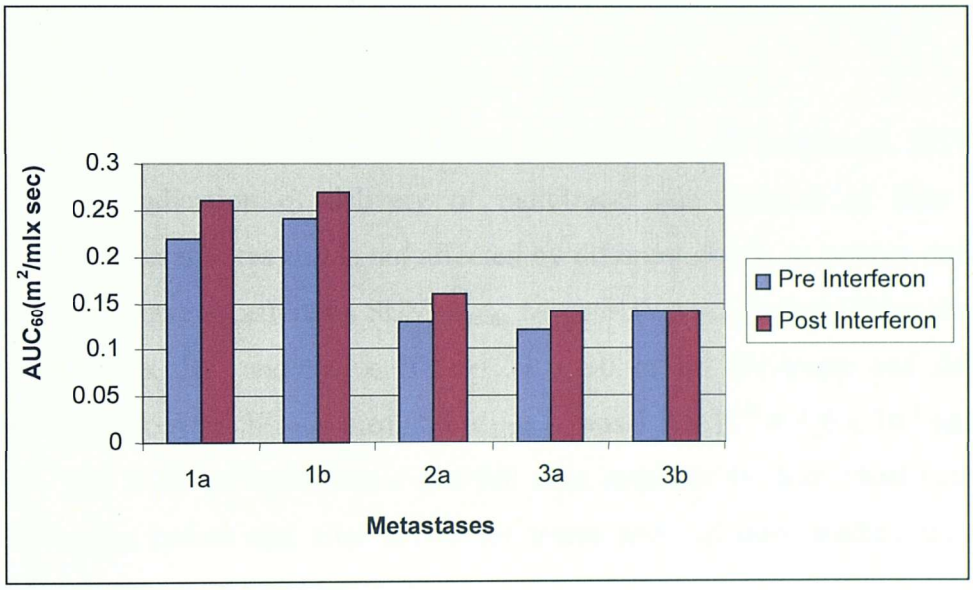


Figure 51: Tracer Dose: Tumour AUC_{60mins} before and after Interferon

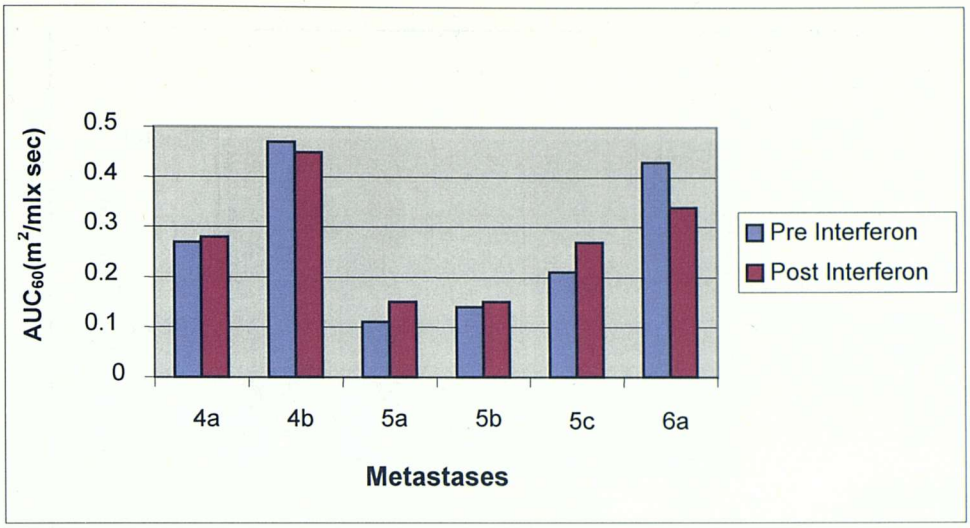


Figure 52: Full Dose: Tumour AUC_{60mins} Before and After Interferon

Mean $SUV_{3.75mins}$ was similar for tracer and full dose. As mentioned, $SUV_{3.75mins}$ gives an indication of delivery of radiotracer and consists of flow *versus* extraction parameters and is not affected by different doses. At neither dose level did IFN-α have an affect on $SUV_{3.75mins.}$ Mean $SUV_{3.75mins}$ before IFN-α was 2.4 x 10^{-4} ± 1.9.x 10^{-4} and 9.5 x 10^{-5} ± 2.3 x $10^{-5}m^2$/ml for tracer and full dose respectively. After IFN-α, mean $SUV_{3.75mins}$ was 7.9 x 10^{-5} ± 1.6 x 10^{-5} and 7.9 x 10^{-5} ± 2 x $10^{-5}m^2$/mlfor tracer and full dose respectively. Individual results for $SUV_{3.75mins}$ before and after IFN-α for tracer and full dose studies are shown below in Figures 53 and 54.

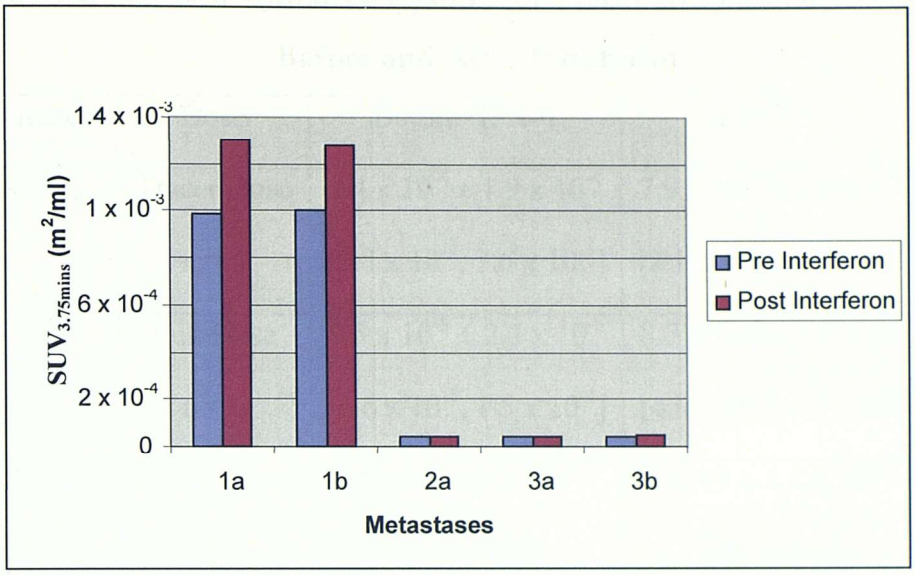


Figure 53: Tracer Dose: Tumour $SUV_{3.75mins}$ before and after Interferon

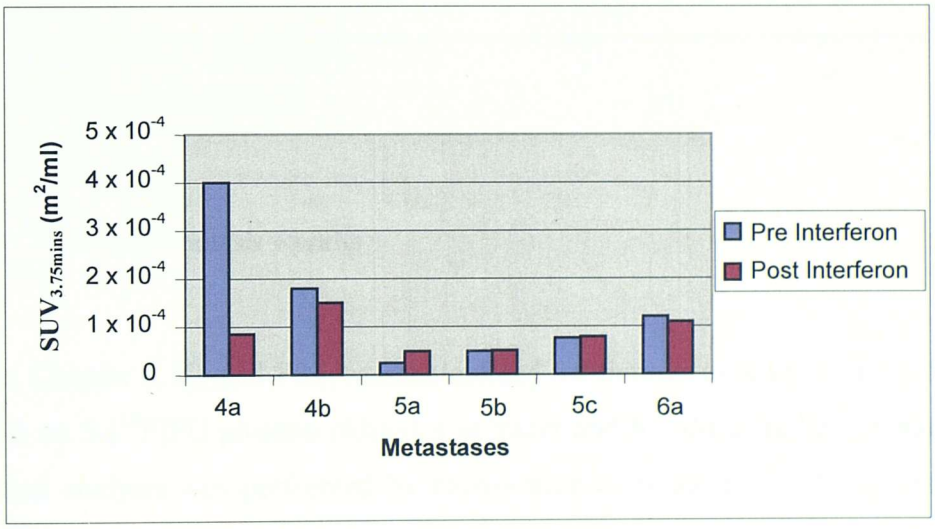


Figure 54: Full Dose: Tumour $SUV_{3.75mins}$ Before and After Interferon

Table 7.4: Semi-Quantitative Results for Tracer and Full Dose 5-[^{18}F]FU Before and After Interferon

Parameter	Dose	Before [3]IFN-α	After [3]IFN-α	p value
[1]$SUV_{3.75mins}$	Tracer Dose n = 5	$2.4 \times 10^{-4} \pm 1.9 \times 10^{-4}$ [2.8×10^{-4}, 7.6×10^{-4}]	$7.9 \times 10^{-5} \pm 2.0 \times 10^{-5}$ [2.1×10^{-5}, 1.3×10^{-4}]	0.63
	Full Dose n = 6	$9.5 \times 10^{-5} \pm 2.3 \times 10^{-5}$ [3.6×10^{-5}, 1.5×10^{-4}]	$8.7 \times 10^{-5} \pm 1.6 \times 10^{-5}$ [4.6×10^{-5}, 1.3×10^{-4}]	0.56
[2]AUC_{60mins}	Tracer Dose n = 5	$0.17 \pm 2.5 \times 10^{-2}$ [0.10, 0.24]	$0.19 \pm 3.2 \times 10^{-2}$ [0.10, 0.28]	0.25
	Full Dose n = 6	$0.27 \pm 0.6 \times 10^{-2}$ [0.11, 0.43]	0.27 ± 0.047 [0.15, 0.39]	0.83

[1], m^2/ml; [2], m^2/sec/ml; [3], Interferon- α

Data are mean ± SEM; [95% CI]

7.6.5 Spectral Analysis Results

As in Chapter 6, K_1 and FRF were calculated for tumour to observe any affect of IFN-α on 5-[^{18}F]FU pharmacokinetics in tracer and full dose studies. In addition, spectral analysis was performed by convolution of tissue radioactivity response and the two input functions, as described previously. This produced two data sets for K_1 and FRF for tracer and full dose studies with good model fits obtained as in chapter 6. As can be seen below differences were observed in the input function curves for parent and total plasma in tracer and full dose studies, see Figure 54 below.

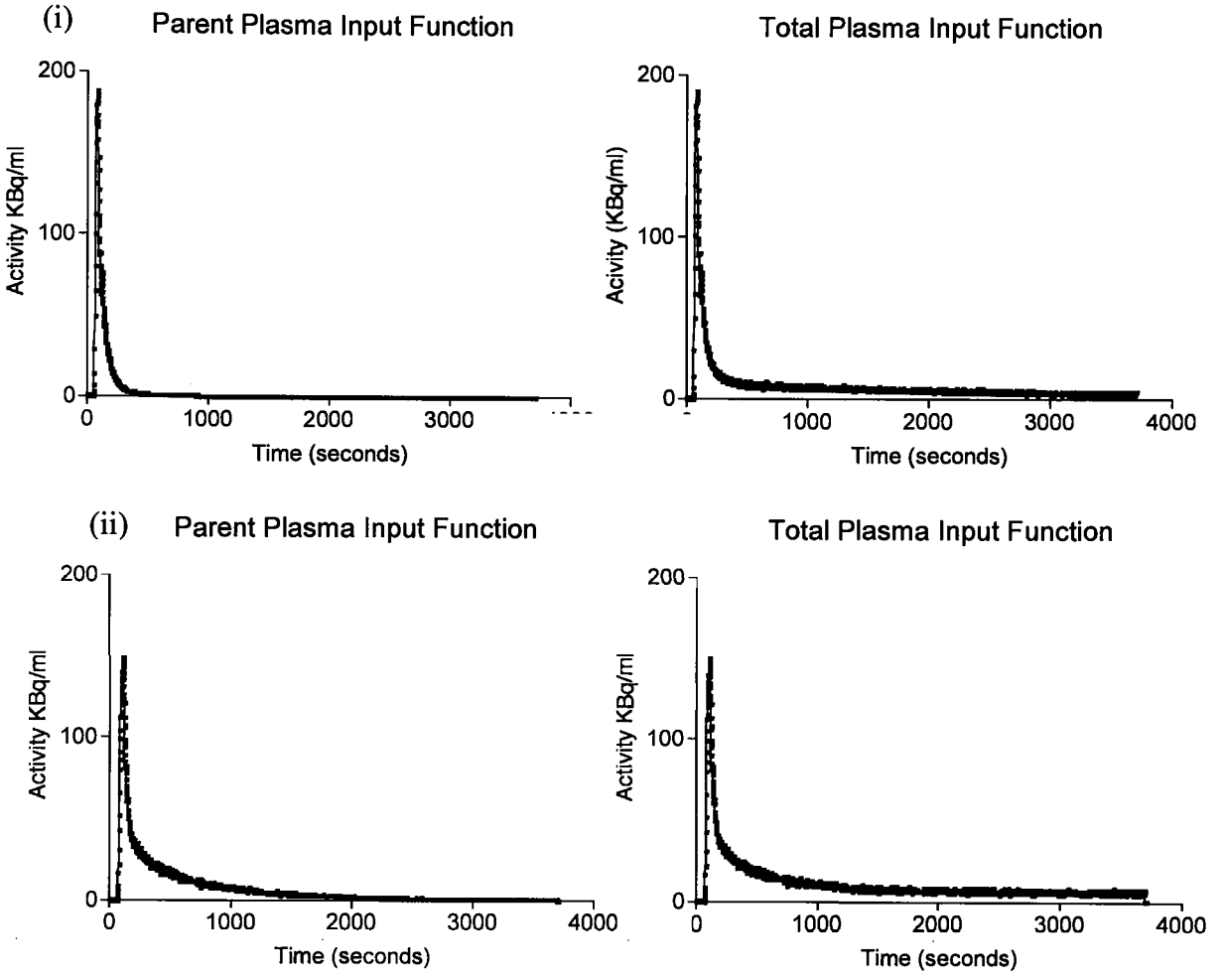


Figure 55: Parent Plasma and Total Plasma Input Functions for (i) Tracer Dose and (ii) Full Dose Tracer Dose 5-[^{18}F]FU Studies

The initial part of the curve is similar for both input functions as is to be expected as there has not been a significant amount of 5-[^{18}F]FU metabolism yet. The latter part of the curve reflects the subtraction of labelled metabolites in the parent plasma radiotracer curve which is apparent as the curve tends to fall to almost non-detectable levels at 2 000s, whereas in the corresponding total plasma input function, after 2 000s the curve is composed of radiolabelled parent and metabolites and hence levels remain higher.

7.6.5.1 K_1 Results

7.6.5.1.1 Tracer Dose Results

As can be seen from the table below, K_1 was slightly higher after IFN-α when using either parent plasma or total plasma input functions but suggesting no change in the delivery component as Mann-Witney statistics performed showed non-significant results obtained for parent plasma and total plasma before IFN-α ($p = 0.31$) and parent plasma and total plasma after IFN-α ($p = 1$). Mean values obtained for K_1 for parent and total plasma before IFN-α and after IFN-α were also similar with no statistical difference.

Table 7.5: K_1 for Tracer Dose before and after Interferon-α, Using Parent and Total Plasma Input Functions

Metastases	[1]K_1 before [2]IFN-α parent plasma	[1]K_1 before [2]IFN-α total plasma	[1]K_1 after [2]IFN-α parent plasma	[1]K_1 after [2]IFN-α total plasma
1a	0.24	0.25	0.4	0.27
1b	0.3	0.29	0.48	0.52
2a	0.57	0.75	0.2	0.085
3a	0.075	0.87	0.094	0.054
3b	0.088	0.06	0.052	0.29
Mean ± SEM	0.17 ± 0.066	0.15 ± 0.049	0.23 ± 0.076	0.24 ± 0.084

[1], $ml_{blood}/min/ml_{tissue}$; [2], Interferon- α

Data are mean ± SEM

7.6.5.1.2 Full Dose Results

Again, results for K_1 in both parent and total plasma analyses were not significantly different before and after IFN-α, $p = 0.69$ and 0.31 for parent and total plasma input functions respectively.

Table 7.6: K_1 for Full Dose Before and After Interferon-α, Using Parent and Total Plasma Input Functions

Metastases	[1]K_1 before [2]IFN-α parent plasma	[1]K_1 before [2]IFN-α total plasma	[1]K_1 after [2]IFN-α parent plasma	[1]K_1 after [2]IFN-α total plasma
4a	0.250	0.220	0.30	0.220
4b	0.300	0.290	0.35	0.300
5a	0.025	0.038	0.14	0.140
5b	0.500	0.500	0.16	0.160
5c	0.320	0.370	0.27	0.240
6a	0.530	0.410	0.30	0.300
Mean ± SEM	0.32 ± 0.07	0.3 ± 0.07	0.25 ± 0.03	0.23 ± 0.028

[1], $ml_{blood}/min/ml_{tissue}$; [2], Interferon- α

Data are mean ± SEM.

Table 7.7: Summary of Results for K_1

Input Function	Dose	[1]K_1 Before [2]IFN-α	[1]K_1 After [2]IFN-α	p value
Parent plasma	Tracer Dose	0.17 ± 0.066 [0.012, 0.53]	0.23 ± 0.076 [0.016, 0.44]	0.19
	Full Dose	0.32 ± 0.08 [0.13, 0.51]	0.25 ± 0.03 [0.16, 0.34]	0.69
Total plasma	Tracer Dose	0.15 ± 0.049 [0.07, 0.29]	0.24 ± 0.084 [0.011, 0.48]	0.31
	Full Dose	0.3 ± 0.066 [0.13, 0.47]	0.23 ± 0.028 [0.16, 0.30]	0.31

[1], $ml_{blood}/min/ml_{tissue}$; [2], Interferon- α

Data are mean ± SEM [95% CI].

7.6.5.2 Fractional Retention of 5-[^{18}F]FU

7.6.5.2.1 Tracer Studies

Fractional retention of 5-[^{18}F]FU (FRF) describes retention of radiotracer. As can be seen from individual values for tracer in Table 7.8 there was no change in mean FRF after IFN-α using either parent or total plasma input functions.

Table 7.8: Fractional Retention of 5-[^{18}F]FU for Tracer Dose before and after Interferon-α Using Parent and Total Plasma Input Functions

Metastases	[1]FRF before [2]IFN-α parent plasma	[1]FRF before [2]IFN-α total plasma	[1]FRF after [2]IFN-α parent plasma	[1]FRF after [2]IFN-α total plasma
1a	0.27	0.0027	0.27	0.0011
1b	0.23	0.0049	0.26	0.0076
2a	0.26	0.064	0.56	0.085
3a	0.42	0.04	0.29	0.03
3b	0.45	0.14	0.33	0.11
Mean ± SEM	0.38 ± 0.056	0.05 ± 0.025	0.34 ± 0.056	0.047 ± 0.022

[1], Fractional Retention of 5-[^{18}F]FU; [2], Interferon- α

The results also show that parent plasma FRF is higher than total plasma FRF before and after IFN-α. Mann-Witney statistics performed on these values showed a significant change obtained for parent plasma and total plasma before IFN-α ($p = 0.0079$) and parent plasma and total plasma after IFN-α ($p = 0.0079$). As explained before, FRF is derived using the ratio, IRF_{60mins}/ IRF_{1min}. Looking at the two input functions for tracer, it can be seen that the plasma arterial concentrations at 60 minutes is higher for total plasma. This results in a lower IRF_{60mins} for total plasma than for parent plasma after convolution with tissue response and consequently a lower FRF.

7.6.5.2.2 Full Dose Studies

In the full dose studies, again no change was seen on FRF of 5-[^{18}F]FU and the addition of IFN-α with analysis using parent and total plasma input functions as shown in Table 7.9.

Table 7.9: Fractional Retention of 5-[^{18}F]FU for Tracer Dose before and after Interferon-α Using Parent and Total Plasma Input Functions

Metastases	[1]FRF before IFN-α parent plasma	[1]FRF before IFN-α total plasma	[1]FRF after IFN-α parent plasma	[1]FRF after IFN-α total plasma
4a	0.150	0.078	0.150	0.06
4b	0.170	0.0605	0.560	0.0902
5a	0.260	0.1	0.140	0.088
5b	0.100	0.09	0.140	0.084
5c	0.120	0.078	0.160	0.13
6a	0.260	0.15	0.290	0.07
Mean ± SEM	0.18 ± 0.03	0.092 ± 0.013	0.24 ± 0.07	0.087 ± 0.01

[1], Fractional Retention of 5-[^{18}F]FU; [2], Interferon- α

FRF values using total plasma are lower than corresponding values calculated using parent plasma input functions. Mann-Witney statistical analysis comparing parent plasma and total plasma input functions for FRF was significant with p = 0.015 and p= 0.002 before and after IFN-α respectively. As explained before, the reason postulated for this lies in the differing input function curves (Figure 50) and their affect on FRF calculation.

Table 7.10 Summary of Results for FRF

Input Function	Dose	[1]FRF Before [2]IFN-α	[1]FRF After [2]IFN-α	p value
Parent plasma	Tracer Dose n = 5	0.38 ± 0.056 [0.22, 0.54]	0.34 ± 0.056 [0.19, 0.50]	0.65
	Full Dose n = 6	0.18 ± 0.028 [0.10, 0.25]	0.24 ± 0.068 [0.065 – 0.42]	0.44
Total plasma	Tracer Dose n = 5	$5 \times 10^{-2} \pm 2.5 \times 10^{-2}$ [-0.02, 0.12]	$4.7 \times 10^{-2} \pm 2.2 \times 10^{-2}$ [-0.013, 0.11]	0.81
	Full Dose n = 6	$9.2 \times 10^{-2} \pm 1.3 \times 10^{-2}$ [6.0×10^{-2}, 0.13]	$8.7 \times 10^{-2} \pm 9.8 \times 10^{-3}$ [6.2×10^{-2}, 0.11]	0.84

[1], Fractional Retention of 5-[^{18}F]FU; [2], Interferon- α

Data are mean ± SEM [95% CI].

7.6.6 Patlak Results

K_I describes the net clearance of radiotracer from plasma to tissue and is derived from modified Patlak methodology. This was only possible in the full dose however and not in tracer dose studies. This is probably because the requirement that in Patlak that parent reaches equilibrium between plasma and tissue before irreversible trapping (Mankoff *et al.*, 1996) is not achieved as there is insufficient parent drug initially or because the plasma curve goes to zero within a short time, in the tracer arm only Results for the full dose studies are shown in Figure 55. In all 6/6 metastasis K_I increased, giving a mean % change of +139%. Mean K_I before IFN- α was $1.6 \times 10^{-2} \pm 3.1 \times 10^{-3}$ and mean K_I after IFN- α was $3.4 \times 10^{-2} \pm 7.5 \times 10^{-3}$ $ml_{blood}/min/ml_{tissue}$. The p value was significant with p = 0.0313.

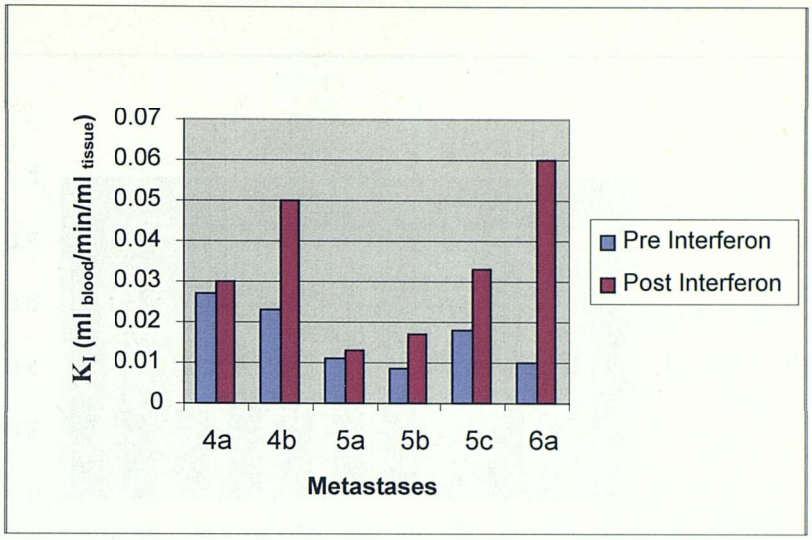


Figure 56: Tumour K_I Before and After Interferon

7.6.7 Tissue Perfusion and Volume of Distribution

Tissue perfusion data from the tracer and full dose 5-[FU] arms have been combined as the C[$^{15}O_2$] scans were performed before the 5-[^{18}F]FU scans and therefore will not be affected by the two different 5-[FU] dose schedules. Individual patient results for each region are shown below, and statistical results for all regions are summarized in Table 7.11.

7.6.7.1 Tumour Perfusion and Volume of Distribution

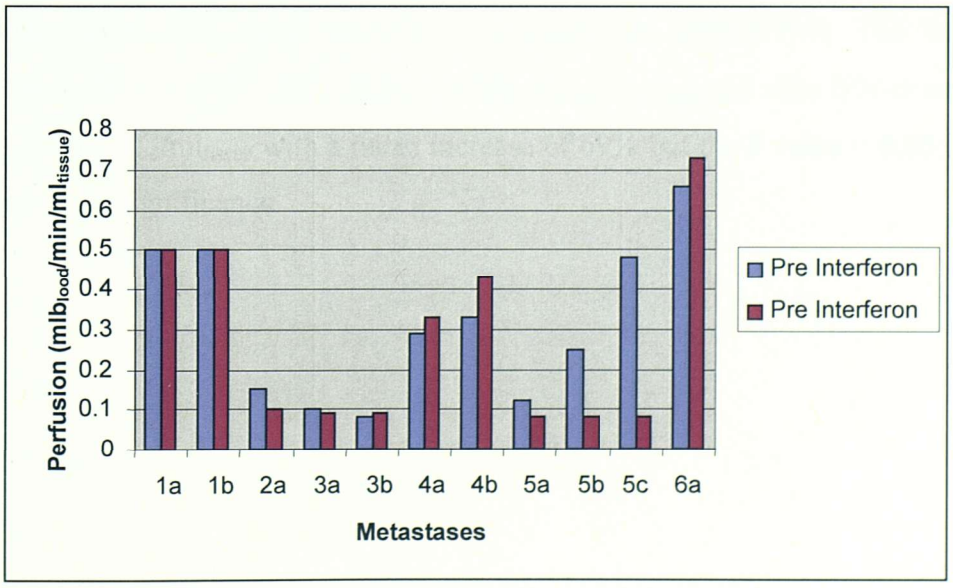


Figure 57: Tumour Blood Flow Before and After Interferon

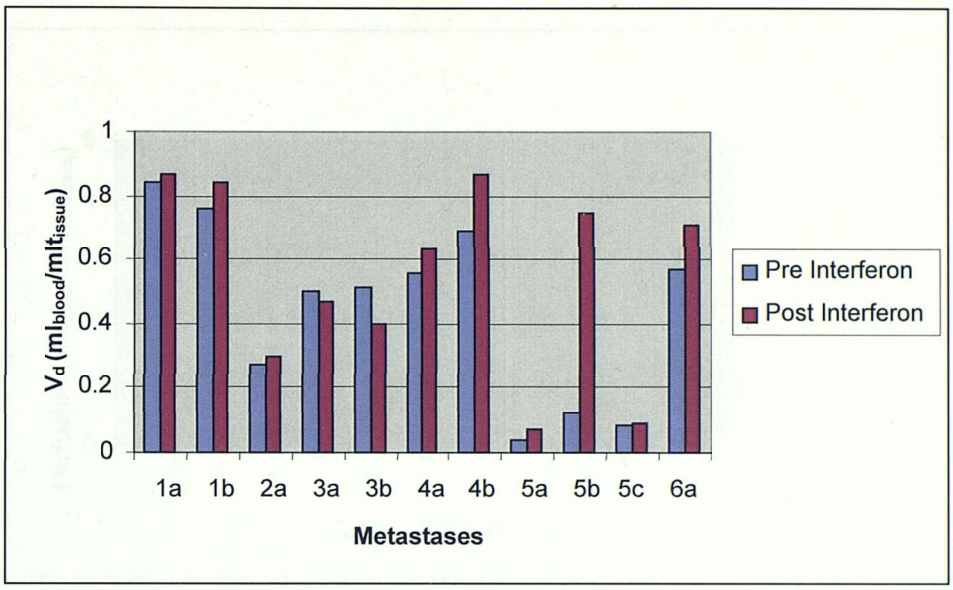


Figure 58: Tumour V_d Before and After Interferon

In 4/11 metastasis perfusion increased, in 4/11 metastasis perfusion decreased and in 3/11 metastasis there was no change in perfusion after IFN-α. The mean value pre IFN-α was 0.31 ± 0.059 $ml_{blood}/min/ml_{tissue}$ and post IFN-α was 0.27 ± 0.070 $ml_{blood}/min/ml_{tissue}$. However, there was considerable heterogeneity in individual tumour perfusion and the result was not significant. In 9/11 metastases V_d increased, and V_d decreased in 2/11 metastases after IFN-α. The volume of distribution pre IFN-α was 0.45 ± 0.084 ml_{blood}/ml_{tissue} and after IFN-α was 0.55 ± 0.090 ml_{blood}/ml_{tissue} with a mean increase of 69% but the P value = 0.05 indicated marginal significance.

7.6.7.2 Splenic Perfusion and Volume of Distribution

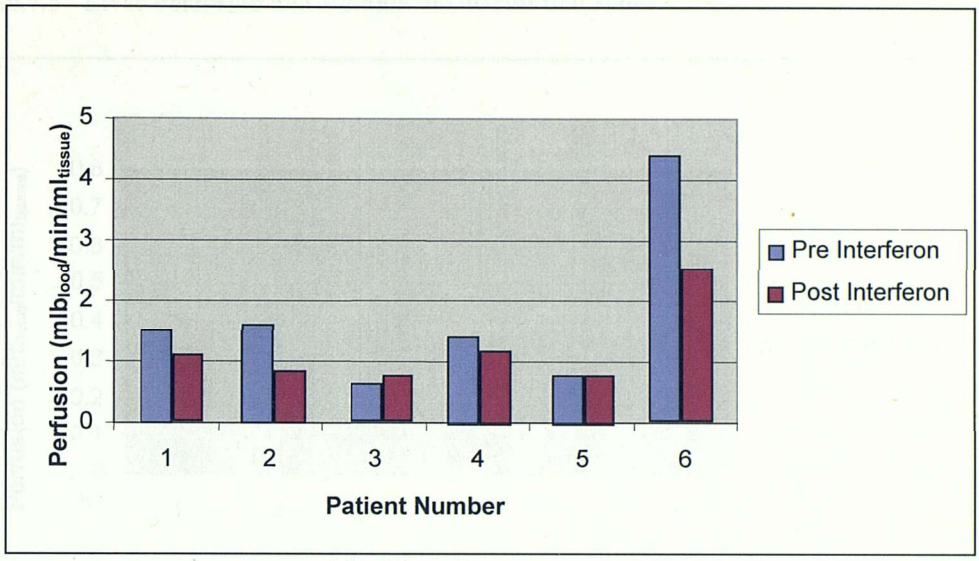


Figure 59: Spleen Perfusion Before and After Interferon-α

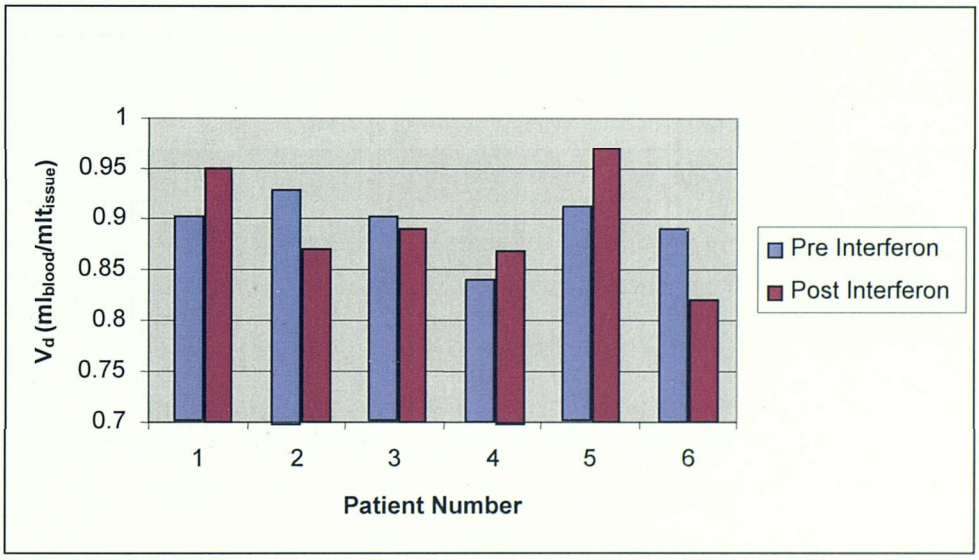


Figure 60: Spleen V_d Before and After Interferon-α

Splenic perfusion and volume of distribution showed inconsistent changes after IFN-α (Table 7.5). Mean perfusion pre IFN-α was 1.7 ± 0.56ml_{blood}/min/ml_{tissue} and mean perfusion post IFN-α was slightly less at 1.2 ± 0.27$_{blood}$/min/ml_{tissue}. Mean V_d in the spleen pre IFN-α was 0.89 ± 0.012 mlblood/mltissue and post IFN was unaltered at 0.89 ± 0.022$_{blood}$/min/ml_{tissue}.

7.6.7.3 Liver Perfusion and Volume of Distribution Index

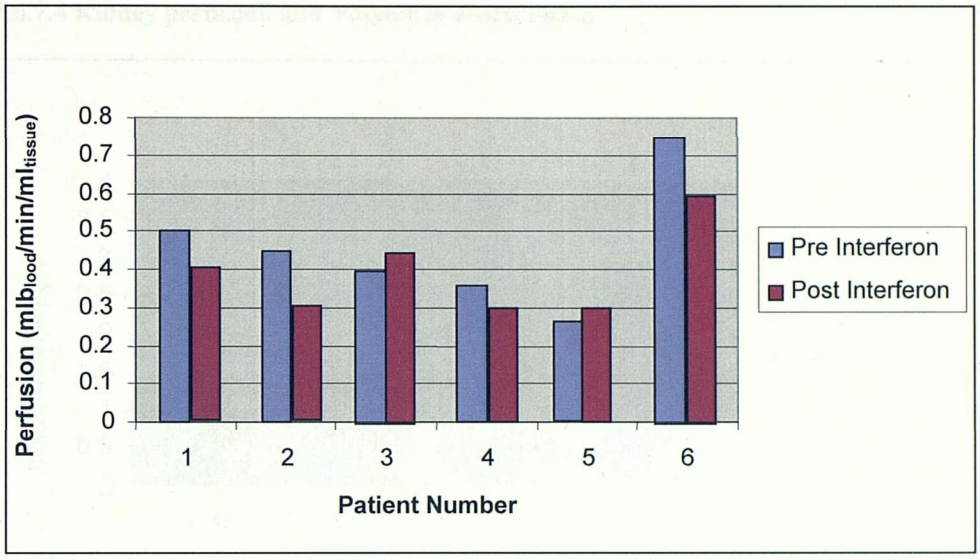


Figure 61: Liver Perfusion Index Before and After Interferon

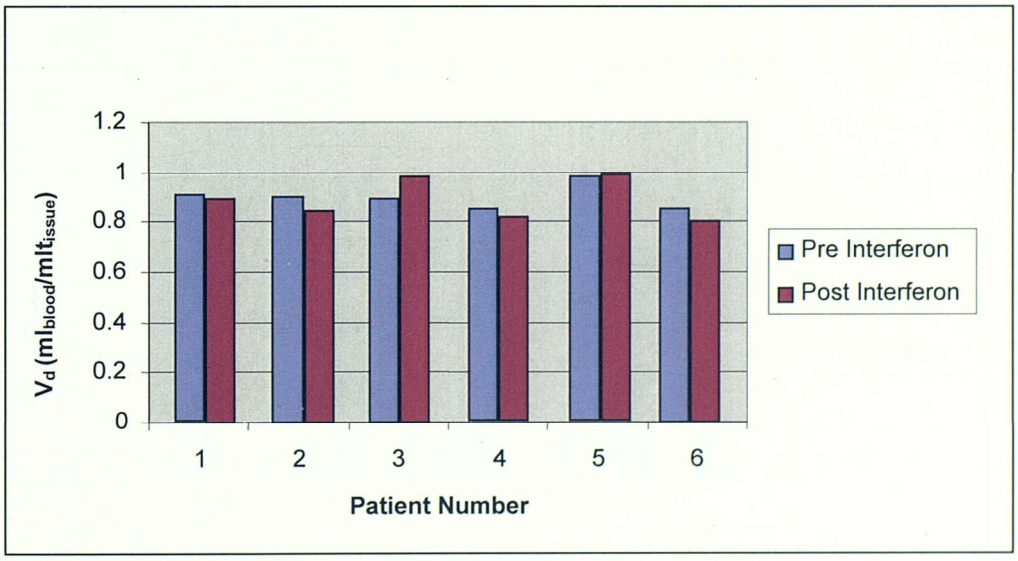


Figure 62: Liver V_d Index Before and After Interferon

As mentioned in Chapter 6, liver perfusion and volume of distribution are index values as this organ has a dual blood supply. In the 6 liver ROIs analysed, both parameters were not significantly altered by modulation with IFN-α. Mean liver perfusion values of 0.45 ± 0.068 $ml_{blood}/min/ml_{tissue}$ and 0.39 ± 0.049 $ml_{blood}/min/ml_{tissue}$ were obtained pre and post IFN-α, respectively. Values for Vd

in the liver were similar before and after IFN-α , with values of 0.89 ± 0.019 ml_{blood}/ml_{tissue} and 0.88 ± 0.033 ml_{blood}/ml_{tissue}, respectively.

7.6.7.4 Kidney perfusion and Volume of Distribution

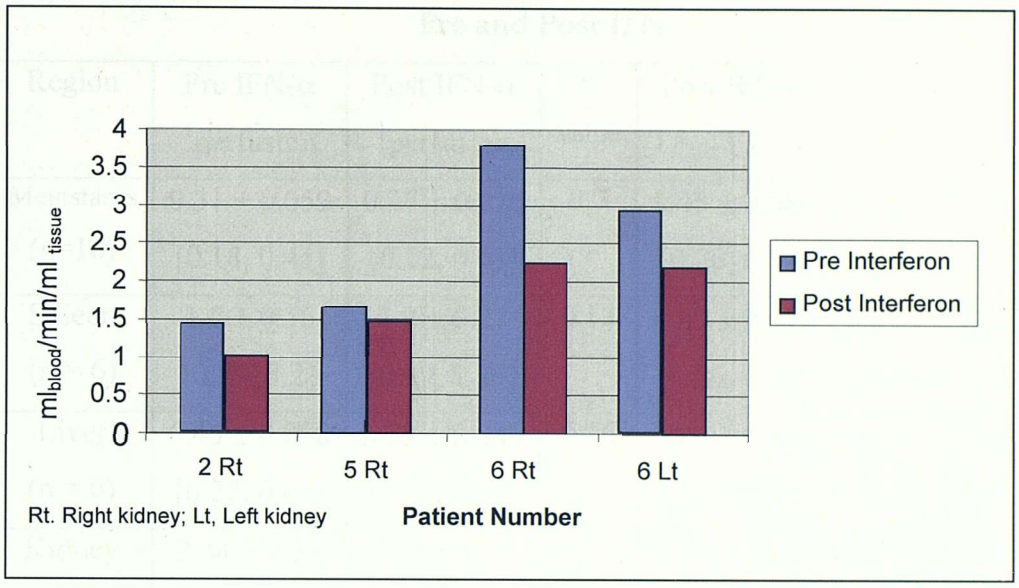


Figure 63: Kidney Perfusion Before and After Interferon

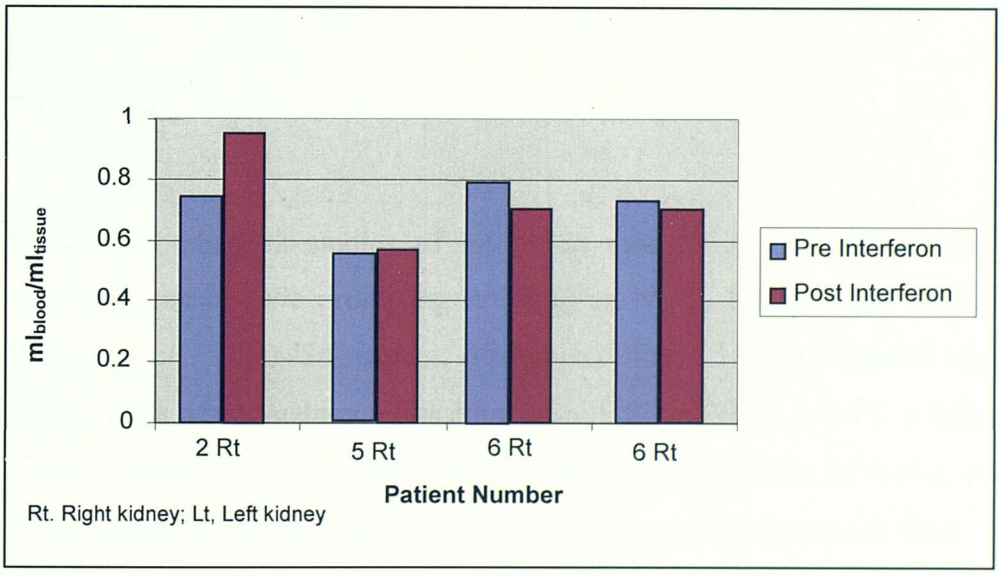


Figure 64: Kidney V_d Before and After Interferon

In all 4 kidneys sampled, perfusion decreased with the administration of IFN-α with a mean reduction of 27%. Pre IFN-α was 2.44 ± 0.56 $ml_{blood}/min/ml_{tissue}$ and post IFN-α was 1.72 ± 0.30 $ml_{blood}/min/ml_{tissue}$ though this was not significant (p =

0.13). Volume of distribution was unaltered with IFN-α, with pre IFN-α of 0.70 ± 0.05 ml_{blood}/ml_{tissue} and post IFN-α of 0.73 ± 0.079 ml_{blood}/ml_{tissue}.

Table 7.11: Summary of Perfusion and Volume of Distribution statistics Pre and Post IFN

Region	Pre IFN-α ^{1}perfusion	Post IFN-α ^{1}perfusion	p value	Post IFN-α $^{2}V_d$	Post IFN-α $^{2}V_d$	p value
Metastases (n=10)	0.31 ± 0.059 [0.18, 0.45]	0.27 ± 0.070 [0.12, 0.43]	0.7	0.45 ± 0.084 [0.26, 0.64]	0.55 ± 0.090 [0.34, 0.75]	0.05
Spleen (n = 6)	1.7 ± 0.56 [0.29, 3.2]	1.2 ± 0.27 [0.49, 1.89]	0.13	0.89 ± 0.012 [0.86, 0.93]	0.89 ± 0.022 [0.84, 0.95]	0.84
Liver (n = 6)	0.45 ± 0.068 [0.28, 0.63]	0.39 ± 0.049 [0.27, 0.52]	0.16	0.89 ± 0.019 [0.84, 0.94]	0.88 ± 0.033 [0.80, 0.97]	0.56
Kidney (n = 4)	2.44 ± 0.56 [0.68, 4.2]	1.72 ± 0.30 [0.76, 2.7]	0.13	0.70 ± 0.05 [0.54, 0.87]	0.73 ± 0.079 [0.48, 0.98]	1

n, number; ^{1}, $ml_{blood}/min/ml_{tissue}$; ^{2}Vd, volume of distribution, ml_{blood}/ml_{tissue}; Data are mean ± SEM [95% CI].

7.7 Discussion

Some early phase 2 studies of interferon modulation of 5-FU in metastatic colorectal cancer gave promising results (Patt *et al.*, 1997; Pazdur *et al.*, 1990; Wadler *et al.*, 1989). Subsequent randomized phase 3 trials produced equivocal results and a recent meta-analysis comparing 5-FU ± IFN-α or 5-FU ± folinic acid + IFN-α demonstrated no substantial benefit of the addition of IFN-α (Cancer, 2001). Although the clinical application of interferon has decreased, there is still a potential subset of patients who may yet benefit from the addition of interferon.

This study set out to evaluate the possible 5-FU pharmacokinetic parameters that may be affected by the biomodulation of IFN-α, as well as looking at effects of dose dependence. The potential effect of IFN-α on tumour and normal tissue perfusion was also examined.

The results from this study have shown that one pharmacokinetic parameter that IFN-α may modulate is retention of 5-[^{18}F]FU. This is suggested by the statistically significant increase in K_I that was seen in analysis of tumour in the full dose studies. K_I, represents the net unidirectional irreversible uptake of parent into tissue, and is derived using extended Patlak methodology which takes into account the presence of labelled 5-[^{18}F]FU metabolites but which are not retained by the tissue being analysed (Mankoff *et al.*, 1996). In the full dose study, there was an increase in all 6/6 tumour analysed, with a mean K_I before IFN-α of 1.6 x $10^{-2} \pm 3.1 \times 10^{-3}$ and post IFN-α of $3.4 \times 10^{-2} \pm 7.5 \times 10^{-3}$ ml $_{blood}$/min/ml $_{tissue}$, p = 0.03. This is consistent with a clinical study by Presant et al, in which 2/3 patients had an increase in intra-tumoural half-life after IFN-α modulation of 5-FU measured in liver metastasis, indicating trapping of 5-FU (Presant *et al.*, 2000), where 5-FU pharmacokinetics were measured with ^{19}F-MRS. The elevation in K_I post IFN-α corroborates the postulated mechanism of action in which there is an increase in thymidine phosphorylase and hence, FdUMP, following IFN-α (Schwartz *et al.*, 1994; Schwartz *et al.*, 1995), as there was no increase in radiotracer delivery in this study, which will be discussed later. Though the PET signal cannot distinguish between 5-[^{18}F]FU and metabolites, the increased net clearance of parent 5-[^{18}F]FU (i.e. K_I) in tumour after IFN-α suggests that the IFN-α induced increase in thymidine phosphorylase leads to a subsequent increase and retention of 5-[^{18}F]FU as FdUMP, as it forms a stable complex with thymine synthase and a folate co-factor.

In this study, another measure of retention, fractional retention of 5-[^{18}F]FU, was unaltered by IFN-α in tracer and full dose studies, using both parent and total plasma input functions. FRF is calculated using spectral analysis requiring relatively few assumptions to be upheld to allow analysis and differs from K_I. FRF gives a measure of tissue response relative to radiotracer concentration in plasma at 60 minutes after being normalized for variability in the delivery component (i.e. IRF_{1min}). One explanation for there being no change in FRF is that IFN-α may inhibit dihydropyrimidine dehydrogenase metabolism of 5-FU, which will decrease 5-FU clearance from plasma (Milano *et al.*, 1994). This will manifest as no change in IRF_{60mins} post IFN-α as any rise in tissue signal (possibly from enhanced 5-[^{18}F]FU anabolism) will correspond with a rise in plasma 5-

[^{18}F]FU levels. Another reason for a lack of difference in FRF after IFN-α could be because of the rapid loss of parent 5-[^{18}F]FU from plasma.

AUC_{60mins} was another parameter calculated in full dose and tracer studies and gives an indication of tissue exposure to 5-[^{18}F]FU over 60 minutes. There was no change in AUC_{60mins} after IFN-α in tracer or full dose tumour analysis. AUC_{60mins}, whilst normalised for injected radiotracer activity and decay, and body surface area, does not take into account radiotracer delivery to the tissue which can be highly variable, as seen by values for $SUV_{3.75mins}$ and K_1, and may effect the final estimate of AUC_{60mins}.

As expected however, both AUC_{60mins} and FRF were greater in the full dose 5-[^{18}F]FU studies pre and post IFN-α than the tracer dose 5-[^{18}F]FU studies, but this did not attain a significant value. This reflects that in the tracer dose studies, the injected levels of 5-[^{18}F]FU were below saturation kinetics for 5-FU metabolism. However, this study was limited by the use of only two dose levels of 5-FU.

Both FRF and K_1 were calculated using parent and total plasma input functions. As in the carbogen and nicotinamide modulation studies, K_1 was the same regardless of which input function was used before and after IFN-α but, FRF was significantly different. As stated previously, the accepted input function for spectral analysis is using parent plasma. The same argument applies as to why total plasma input function will not give an accurate measure of IRF_{60mins} as the radioactivity will predominantly consist of 5-[^{18}F]FU metabolites and not parent, which does not affect K_1 as this is derived from an earlier time point.

The results here show that there was no difference in 5-[^{18}F]FU delivery to tumours as represented by $SUV_{3.75mins}$ and K_1 in either tracer or full dose 5-[^{18}F]FU studies with IFN-α. This may be related to results from tissue perfusion observed in this study.

Perfusion and volume of distribution measured using inhaled C[^{15}O]$_2$ and calculated in tumour, spleen, kidney and liver (as an index). The results demonstrated that IFN-α did not modulate perfusion or V_d in any of these tissues.

However, IFN-α does exhibit anti-angiogenic properties in rodent tumour models alone (Wang *et al.*, 2003) or in conjunction with other anti-angiogenic agents and cytoctoxic agents (Wadler *et al.*, 1997a). IFN-α exerts its anti-angiogenic effect probably by inhibition of production of an angiogenic promoter, the basic fibroblast growth factor. IFN-α has been used successfully in children in the treatment of life threatening haemangiomas who received daily doses of IFN-α for several months (Folkman *et al.*, 1992; Greinwald *et al.*, 1999). Further studies are needed to establish the effect of IFN-α on normal tissue or tumour perfusion in humans. The reason no change was seen in perfusion here may be due to more complex reasons. Thymidine phosphorylase has been reported to be identical to platelet derived endothelial cell growth factor (PD-ECGF) an enzyme closely associated with tumour angiogenesis (Miyadera *et al.*, 1995; Moghaddam *et al.*, 1992). Thymidine phosphorylase (PD-ECGF) promotes tumour angiogenesis by inducing endothelial cell migration, particularly in the initial stages of tumour growth (Focher *et al.*, 2001; Marchetti *et al.*, 2001). There are many other tumour cytokines and growth factors involved in angiogenesis and subsequently tissue perfusion and the underlying mechanisms have not been fully elucidated.

Further discussion regarding thymidine phosphorylase (TP) is warranted as it appears to be one important step by which IFN-α modulates 5-FU. In addition to its essential role in converting 5-FU to FdUMP (via thymidine kinase), TP catalyses the reversible phosphorolytic cleavage of thymidine and analogues to their respective bases and deoxyribose-1-phosphate and maybe play a role in thymidine haemostasis (Fox *et al.*, 1995). It has been proposed that one role of TP is to control the intracellular levels of thymidine, which at higher concentrations become toxic to cells and cause replication errors in DNA (O'Brien *et al.*, 1996). TP, whilst present in a wide range of normal tissue, has elevated expression in many tumours and higher levels of TP are associated with a worse prognosis in some malignancies, colorectal cancer amongst them (Takebayashi *et al.*, 1996). The effect of TP on angiogenesis, as mentioned above, is one factor involved in the development of a more aggressive phenotype and subsequent increased resistance to cytotoxic agents. Indeed, a recent study looking at colorectal cancer biopsies has shown that tumours with a higher gene expression of TP are more likely to be non–responders to 5-FU chemotherapy (Metzger *et al.*, 1998). This

conflicts with previous studies where induction of TP has been associated with enhanced 5-FU activity in vitro (Schwartz *et al.*, 1994; Schwartz *et al.*, 1995). In contrast, Salonga et al found that colorectal tumours responding to 5-FU have low gene expression of TP (Salonga *et al.*, 2000). The same group found other factors that independently predict response to 5-FU are low gene expressions of both thymidylate synthase and dihydropyrimidine dehydrogenase (Salonga *et al.*, 2000) confirmed in studies by Soong (Soong *et al.*, 2008). Within this cohort though are a group of patients who despite having a low TP, are still non-responders to 5-FU based chemotherapy (Metzger *et al.*, 1998), which infers that TP expression does not uniformly identify responding tumours. It is in this group of patients who are of interest as they may benefit from IFN-α combined with 5-FU. Identification of these individuals may now be possible using a blood test. Braybrooke et al found that following a single dose of IFN-α, there was a rapid and sustained induction of TP in peripheral blood mononuclear cells in 64% of patients (Braybrooke J. *et al.*, 2000). However, it remains to be seen whether stratifying treatment in this specific cohort of patients for modulation of 5-FU with IFN-α is clinically beneficial.

7.8 Summary

1. *In vivo* analysis of IFN-α modulation of 5-FU normal tissue and tumour pharmacokinetics can be performed using PET.

2. In this study, a single dose of 3 million units of IFN-α did not have any effect on blood flow or volume of distribution in normal tissue or tumour.

3. IFN-α increases net clearance (K_I) of 5-FU from plasma to tumour. This substantiates one postulated mechanism where IFN-α induces thymidine phosphorylase resulting in elevated levels of FdUMP.

Chapter 8 2-[^{11}C]thymidine To Measure the Pharmacodynamic Endpoint of Anti-cancer Drugs

8.1 Introduction

A pivotal aspect of cancer treatment is determining tumour response as a measurement of the pharmacodynamic endpoint to cancer treatment. The standard technique to assess tumour response to anti cancer treatment in addition to clinical examination is with conventional imaging modalities such as x-ray, ultrasound, computed tomography, or MRI. These methods rely principally on changes in anatomical criteria such as tumour dimensions (unilateral or bilateral) or volume to determine whether therapy has been a success or failure. However, the dependence on changes in tumour size alone is unlikely to be the most accurate measure of response for several reasons. A negative radiological scan may not necessarily be indicative of a 'cure' as a radiological complete response may still be compatible with the survival of approximately 10^8 cells including replicating stem cell that could jeopardise an apparently successful treatment (Collins *et al.*, 1956). Alternatively, any residual tumour mass may be partially or completely composed of necrotic, apoptotic or inflammatory tissue as well as viable tumour cells, which can confound interpretation of results. After the instigation of chemotherapy or radiotherapy regimes, there may often be a delay of 2-3 months before any obvious signs of tumour response are apparent, which impedes decisions on rapid treatment modification when there has been no response. The new opportunities being offered in cancer medicine such as antiangiogenic agents or gene therapy may be cytostatic and treatment will not invariably lead to a reduction in tumour size. There is a clinical need for an alternative strategy of response assessment and with an emphasis on earlier prediction and detection of pharmacodynamic endpoints to facilitate faster screening of novel drugs.

Change in tumour size is preceded by important biochemical changes, including a decrease in cellular proliferation and/or an increase in cellular death rate and subsequent decline in the number of viable tumour cells (Krohn, 2001). One of

the most accurate measures of tumour growth remains serial biopsy (Chang *et al.*, 1999; Feldman *et al.*, 1986), but this is obviously impractical and has limitations in itself including potential sampling errors particularly in tumours, which are intrinsically heterogeneous.

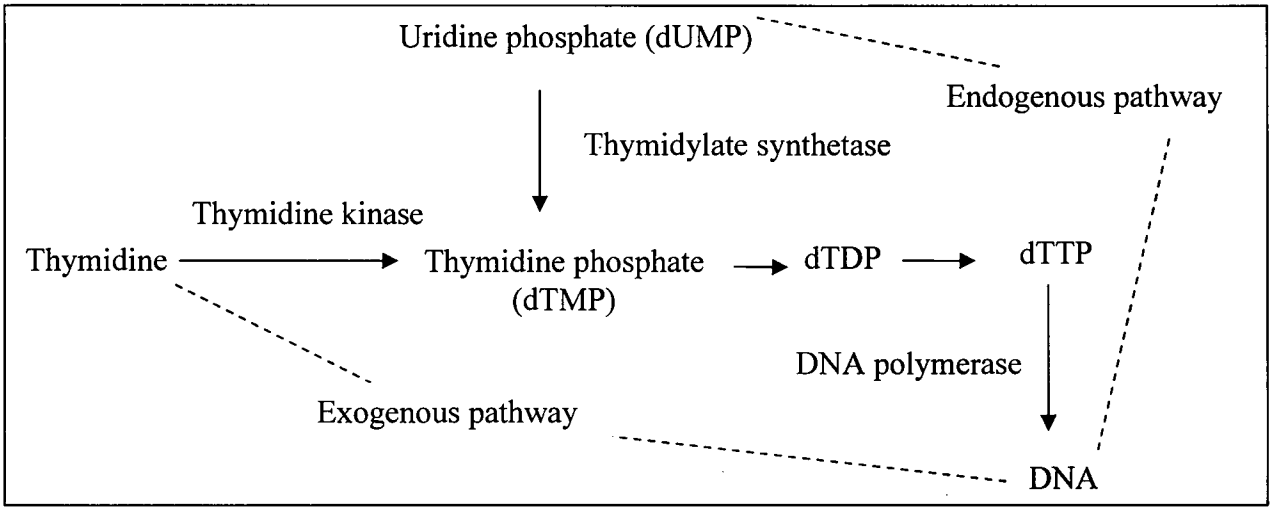
Measurement of tumour growth and DNA synthesis are attractive targets for PET imaging. 2-[^{11}C]thymidine is a novel PET radiotracer that is being explored as a method to measure cellular proliferation *in vivo*.

8.2 Thymidine Background

The use of thymidine in cell growth studies represents the gold standard measure of DNA synthesis and cellular proliferation. DNA is synthesised from four nucleotides: cytosine, guanine, adenine and thymidine. Thymidine is of great importance as it is the native pyrimidine base used in DNA synthesis and is not incorporated into RNA as are the others, making it a logical choice to act as a labelled marker to image DNA proliferation.

Thymidine utilised by the cell is either synthesised by the *de novo* (endogenous) or salvage (exogenous) pathway (Figure 65) both of which are tightly regulated. In the mammalian cell most of the thymidine used is produced from uridylate via the *de novo* pathway (Mankoff *et al.*, 2000). Thymidine is produced from deoxyuridine monophosphate which is methylated to form thymidine monophosphate (TMP) by thymidylate synthase (TS). Labelling thymidine to image cellular kinetics exploits the salvage pathway. In this pathway, extracellular thymidine is rapidly transported into the cell using a facilitated, non-energy dependent transporter (Wohlhueter *et al.*, 1979), where it is converted to TMP by thymidine kinase (TK). Within the cell, TMP produced by the exogenous and endogenous pathways undergoes sequential phosphorylation before incorporation into DNA. Unless there is a shortage of the precursor, thymidine, the rate of DNA synthesis depends on the 'proliferative state' of the tissue and not on the concentration of the precursor. The flux of nucleotides through the precursor pool and into DNA is called the rate of synthesis (Cleaver JE., 1967). Levels of the

enzymes TK and TS are under strict control (Cleaver JE., 1967). TK exists in two forms: TK1, found in the cytoplasm but only in dividing cells, and TK2, found in mitochondria and is not cell-cycle regulated (Munch-Petersen *et al.*, 1991). The levels of both TK1 and TS are increased 5- to 10- fold prior to and during the S (synthesis) phase of the cell cycle (Cleaver JE., 1967; Tannock, 1992).



Key: dUMP, deoxyuridine monophosphate: dTMP, deoxythymidine monophosphate: dTDP, deoxythymidine diphosphate, dTTP, deoxythymidine triphosphate.

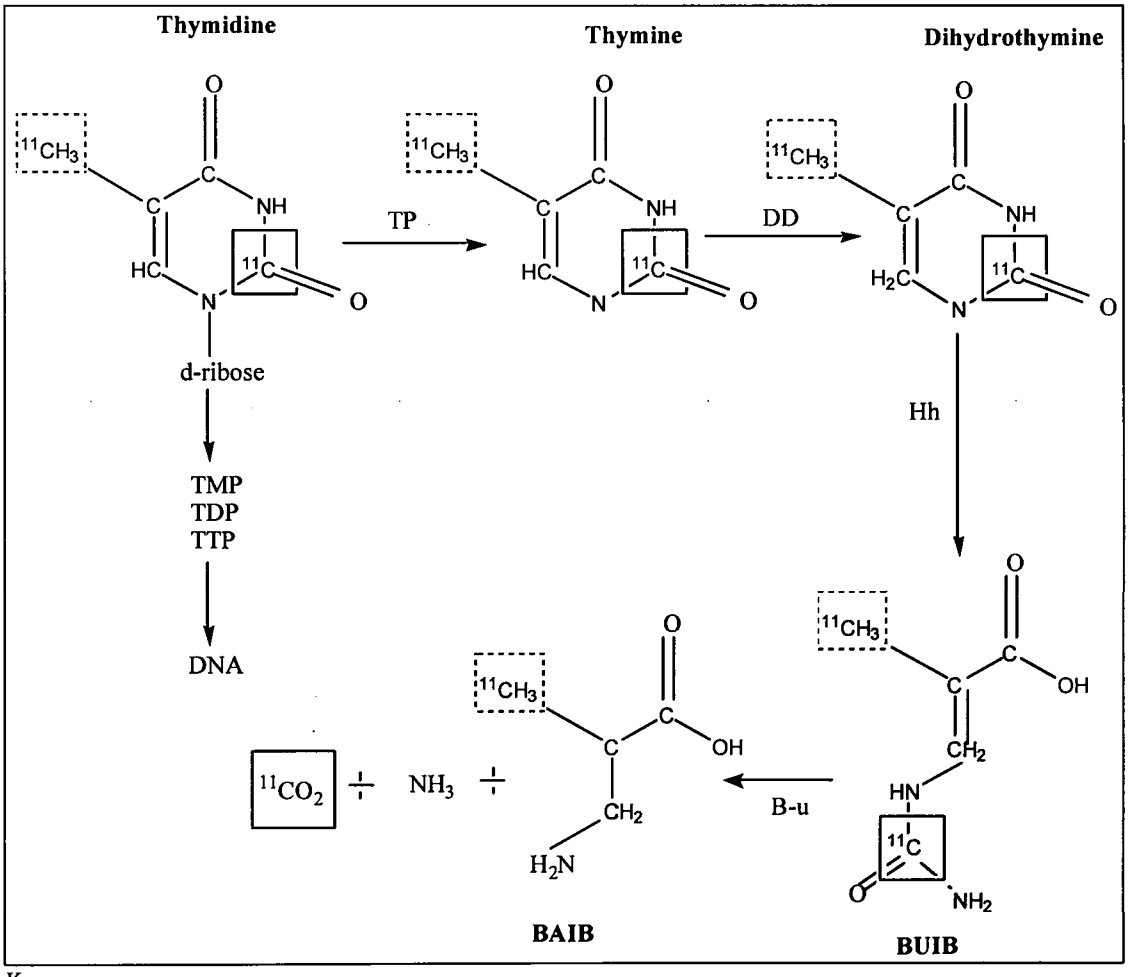
Figure 65: Diagram Showing Incorporation of Thymidine into DNA via Exogenous and Endogenous Pathways

Tritiated thymidine ([^{3}H]-thymidine) has been used for over 50 years in this capacity to measure cell growth and elucidate the cell cycle using autoradiography after injection of [^{3}H]-thymidine into animals and subsequent excision of a tissue sample.

8.3 Development of Thymidine in PET

PET obviously offers the advantage of *in vivo* measurement of cell proliferation using positron emitting radiolabelled thymidine. Preliminary feasibility studies by Larson et al investigated the use of [^{3}H]thymidine, [^{3}H]uridine, [^{14}C]-2-deoxyglucose, and [^{67}Ga]citrate which were injected intravenously into mice with solid subcutaneous EMT-6 sarcoma. High uptake of the radiotracers in tumour

demonstrated their potential for tumour imaging in PET (Larson SM. *et al.*, 1981). A further study by the same group examined [^{3}H]thymidine in mice, rats and canine tumours, either transplanted or spontaneous. They again observed a high tumour to tissue uptake ratio, with prolonged retention in tumours (Larson SM. *et al.*, 1981). For PET imaging, thymidine has been labelled with [^{11}C] in either the 5-methyl (Sundoro-Wu *et al.*, 1984) or 2-carbonyl position (Vander Borght *et al.*, 1991) and have both been used in pre-clinical studies and for *in vivo* imaging of tumours in man. The principle difference between the two radiotracers is in their *in vivo* labelled metabolite profiles (see Figure 66).



Key:

(i) Enzymes: TP, thymidine phosphorylase; DD, dihydrothymine dehydrogenase; Hh, hydropyrimidine hydrase; B-u, B-ureidopropianase

(ii) Metabolites: BUIB, β-ureiodoisobutyric acid; BAIB, R-β- aminoisobutyrate

Figure 66: Diagram showing catabolism of [^{11}C]thymidine Labelled in 5-Methyl- and 2-Carbonyl Positions, to Show Different Metabolite Profile

Thymidine is rapidly metabolised by thymidine phosphorylase which is found in many tissues including tumours and platelets (Cleaver JE., 1967). The labelled metabolites produced by this process are thymine, dihydrothymine, β-ureidoisobutyric acid and finally, carbon dioxide (CO_2). Tumours generate a small amount of these labelled metabolites, but the major source is the blood as a result of the degradation of thymidine by the liver and platelets. Methyl-[^{11}C]thymidine generates more radiolabelled metabolites that accumulate in the tissues that have already taken up thymidine, and therefore they may not contribute to the image background to the same extent as more freely distributed labelled metabolites. In contrast the principle metabolite of 2-[^{11}C]thymidine is [^{11}C]O_2, which is rapidly transported into tissues and is fairly ubiquitous. Initial investigators assumed, over simplistically, that [^{11}C]O_2 was rapidly cleared from the body by exhalation. However, a study by Shields et al has shown that [^{11}C]O_2 is relatively slowly cleared from the body. They found that whilst approximately 50% of the radiolabelled metabolite, [^{11}C]O_2, is exhaled after 60 minutes of scanning, a substantial amount of [^{11}C]O_2 is retained in tissue, with a smaller quantity (5-10%) present as intermediate labelled metabolites (Shields AF. *et al.*, 1992). [^{11}C]O_2 is reversibly transported between tissue and blood with which it equilibrates according to tissue pH, with the majority of [^{11}C]O_2 trapped in tissue as bicarbonate.

8.4 Pre-Clinical Studies

The rapid clearance of radiolabelled thymidine from the circulation as observed by Larson (Larson SM. *et al.*, 1980) led to concern that the distribution of thymidine might primarily reflect tissue blood flow rather than cellular proliferation. A study by Shields et al measured the uptake of methyl-[^{3}H]thymidine in mice and dogs and showed that between one and sixty minutes there was no correlation with blood flow as measured using [^{14}C]iodoantipyrine. The results were not affected by the type of radioisotope used or route of administration as comparable results were obtained using methyl-[^{3}H]thymidine and methyl-[^{14}C]thymidine, administered intravenously or by intraperitoneal injection (Shields *et al.*, 1984).

Studies by Goethal et al showed that in spite of intense *in vivo* metabolism of methyl- [^{11}C]thymidine, major radioactivity was found in rapidly dividing tissue of both the normal Wistar rat, and in rats with chemically induced tumours (Goethals *et al.*, 1999). In the duodenum and tumour, at least 55% of [^{11}C] was precipitated in the DNA fraction and about 60% as DNA precursors in the supernatant. However, despite theses findings the contribution of radiolabelled metabolites to the tissue signal is still important.

The need to evaluate the *in vivo* metabolism of thymidine was further emphasised in a study where the incorporation of exogenous hydrogen-3-[^{3}H]thymidine into DNA in human cell lines was found to vary enormously from 18-100%; the rest being metabolised (Taheri *et al.*, 1982).

Shields et al performed studies to examine the distribution and metabolism of methyl labelled thymidine in [^{3}H], [^{11}C] and [^{14}C] positions in normal mice and in dogs with and without lymphoma. They found that in rapidly proliferating tissue in mice, most of the radioactivity by sixty minutes was present in DNA with smaller amounts present in metabolites. Studies in dogs however, revealed more activity in metabolites rather than in the DNA of tumour and splenic tissues Significant differences were also observed in retention in mice of [^{3}H] labelled thymidine compared to carbon labelled thymidine. This was attributed to reutilisation of the radiolabelled carbon from the methyl group from metabolites prior to incorporation into proteins, whilst with [^{3}H]thymidine, tritium is lost, presumably in the form of tritiated water (Shields *et al.*, 1990).

After first describing the synthesis of 2-[^{14}C]thymidine (Vander Borght *et al.*, 1991), Vander-Borght performed a study to compare the *in vivo* distribution of 2-[^{14}C]thymidine with methyl-[^{3}H]thymidine in liver regeneration in partially hepatectamised Wister rats. A significantly higher accumulation of 2-[^{14}C]thymidine was seen in regenerating rather non-regenerating liver, with the amount of radioactivity in DNA giving a good correlation with the total tissue radioactivity. In contrast, no such correlation was evident with methyl-[^{3}H]thymidine. Further analysis of radioactive tissue showed that 72% of 2-

[^{14}C]thymidine accounted for DNA radioactivity compared to only 39% with methyl-[^{3}H]thymidine (Vander Borght *et al.*, 1990).

8.5 Clinical Studies

A wide variety of tumours have been imaged in clinical studies utilising either methyl- or 2-ring- [^{11}C]thymidine. One of the earliest studies by Martiat in 1988 investigated the uptake of methyl-[^{11}C]thymidine in Non-Hodgkins lymphoma (NHL). In this preliminary trial, methyl-[^{11}C]thymidine uptake was higher in patients with high grade (HG) NHL (Martiat *et al.*, 1988). A similar study was performed by Jamar et al in patients with primary or recurrent NHL, but using 2-[^{11}C]thymidine instead. Again increased uptake of 2-[^{11}C]thymidine was demonstrated in all 18 patients within ten minutes of administration with higher uptake observed in HG compared to low grade (LG) tumours, but no clear difference was seen between LG and intermediate grade tumours (Jamar F. *et al.*, 1992).

Several studies have imaged cerebral lesions with labelled thymidine. In a study comprising 20 patients; 10 patients with a malignant lesion and 10 patients with a benign tumour, methyl-[^{11}C]thymidine uptake was increased in 8/10 patients with malignancy, but in none of the 10 patents with benign tumours (Eary *et al.*, 1999). Pomper et al investigated the differentiating potential of methyl-[^{11}C]thymidine to distinguish primary central nervous system lymphomas from benign lesions in 10 patients with AIDS compared to magnetic resonance imaging (MRI) (Pomper *et al.*, 2002). All patients with lymphoma had a positive PET image and PET had a higher accuracy than MRI. 2-[^{11}C]thymidine has also been used in cerebral imaging studies. In one study, 2-[^{11}C]thymidine identified 11/14 untreated brain tumours with an average uptake twice that of normal brain. However, no correlation was seen between tumour grade and thymidine uptake. This was primarily affected by the high uptake in 4 patients with low grade meningioma (Vander Borght *et al.*, 1994).

Radiolabelled thymidine PET imaging has also been conducted in bronchial carcinomas. Lonneux et al found disappointing results when using methyl-[^{11}C]thymidine. Images obtained were uninterpretable because of accumulation of the radiolabelled metabolites (Lonneux M. *et al.*, 1996). A study by Shields et al in 4 patients with small cell lung cancer found that the tumours were easily identified with 2-[^{11}C]thymidine (Shields AF. *et al.*, 1998b). On the whole, these clinical results have led the way for the development of analytical models from which quantative information on cellular proliferation can be derived.

8.6 Analysis of [^{11}C]thymidine images

Analysis of PET thymidine images can provide quantative regional estimates of cellular proliferation. The least complex approach to [^{11}C]thymidine image analysis is the static uptake measures such as standardised uptake value (SUV). However, though this is simple to calculate, it leads to significant bias in estimating thymidine flux into DNA because it does not take into account the time course of imaging and does not consider the influence of labelled metabolites.

The production of radiolabelled metabolites that are not involved in DNA synthesis and are present in the region of interest confounds interpretation of the thymidine scan images as it is not possible to distinguish between different radiolabelled chemical species using PET. To overcome the problem of labelled metabolites, development of analytical models for quantitative measurement have favoured the use of 2-[^{11}C]thymidine rather than methyl-[^{11}C]thymidine. The pre-clinical (Vander Borght *et al.*, 1991) and clinical (Lonneux M. *et al.*, 1996) studies described above highlight the problems inherent with the radiolabelled metabolites produced by methyl-[^{11}C]thymidine leading to accumulation in tumour and poor resolution on clinical images. Though the principle metabolite of 2-[^{11}C]thymidine, labelled CO_2, has considerable retention in tissue (Shields AF. *et al.*, 1992), various strategies have evolved to correct for this metabolite.

Mankoff et al proposed a graphical model to determine thymidine flux from blood into DNA as a measure of cellular proliferation based on the assumption that

thymidine flux ($Flux_{TdR}$) can be described by the product of native thymidine blood concentration ($[TDR]_b$) and a flux constant (K_{TdR}) (Mankoff *et al.*, 1998):

$$Flux_{TdR} = [TDR]_b \cdot K_{TdR}$$

The exogenous pathway provides only a fraction of the thymidine used in DNA synthesis, with the remainder provided by the endogenous pathway. Previous studies have shown that the fraction of thymidine incorporated into DNA from the endogenous pathway (f_{ext}) is a function of thymidine in the extracellular fluid. As thymidine is readily permeable through tissue capillaries, then the extracellular concentration of thymidine should closely follow blood concentration. Therefore if thymidine blood concentration is known, then synthetic rate of DNA (SR_{DNA}) can be calculated from measurements of flux of thymidine from the external pathway. Assuming that half the nucleotides base pair contain thymidine (Cleaver JE., 1967), then:

$$SR_{DNA} = 2 \cdot \frac{1}{f_{ext}} \cdot Flux_{TdR}$$

The five compartment model devised by Mankoff requires on-line blood measurements to analyse metabolites from which three separate input functions (thymidine, intermediate metabolites and CO_2) are obtained, which are used to estimate eight rate constants (Mankoff *et al.*, 1998). Animal studies have validated this model's ability to predict the time course of 2-[^{11}C]thymidine incorporation into DNA, and stimulations in mice have shown that this analysis does provide reliable values of thymidine flux (Mankoff *et al.*, 1999). A modification was introduced by performing a sequential [^{11}C]O_2 scan in a clinical study with 20 patients with cerebral lesions to identify the transfer of metabolite across the blood brain barrier and provide an input function (Eary *et al.*, 1999). However, these approaches can potentially lead to a problem identifying parameters accurately due to the similarity in time course for each input function and the inherent noise in the data. Furthermore, the compartment model requires some *a priori* of the biological fate of the compounds *in vivo* in order to construct the

number of compartments and the relationship between them, and hence, is highly constrained. If the assumptions are incorrect then the model will be inaccurate.

An alternative approach was developed using spectral analysis which requires no *a priori* decision about the most appropriate compartmental structure (Cunningham VJ. *et al.*, 1993) which produces an impulse response function (IRF) from the plasma input function and tissue activity time curve (see Chapter 2). In a study by Wells et al, 2-[^{11}C]thymidine in regions of interest in tumours was described using the fractional retention of thymidine (FRT). This parameter is defined as the ratio of IRF at 60 minutes (IFR_{60mins}), which reflects retention, to that at one minute (IRF_{1min}), which reflects delivery. FRT is therefore normalised for tracer delivery to allow comparison between regions which have different clearances of tracer. In this study, Wells found a significant correlation between FRT and Ki-67 index, an *ex-vivo* histopathological marker of DNA proliferation, in 17 chemotherapy naïve patients with advanced intra-abdominal malignancy (Wells *et al.*, 2002b). Another study by Wells has shown good reproducibility of data in intra-patient 2-[^{11}C]thymidine scans performed 1 week apart (Wells *et al.*, 2005). Though the plasma input function was corrected for metabolites, no attempt was made to adjust for contribution of labelled metabolites in the 2-[^{11}C]thymidine PET image in either study. However, the same group have developed a dual- scan approach to correct for radiolabelled CO_2 to refine the analysis described above. In this dual-scan procedure, in addition to the 2-[^{11}C]thymidine scan, a supplementary metabolite scan is also performed which allows correction of the parent scan for the presence of systematically derived radiolabelled metabolites that are delivered to tissue (Gunn R. *et al.*, 2000).

8.7 2-[^{11}C]thymidine to Assess Pharmacodynamic End-Points

Shields et al studied response to treatment in four patients with small cell lung cancer (SCLC) and two patients with high grade sarcoma. All patients had a PET scan with 2-[^{11}C]thymidine before treatment and one week after chemotherapy. In 3 patients with a complete response (two patients with SCLC and one with sarcoma), all had a substantial reduction of 55-89% in 2-[^{11}C]thymidine uptake. In

one patient with SCLC who had a partial response, a smaller reduction of 48% was seen. Two patients with progressive disease, one patient each with SCLC and sarcoma had a minor reduction in 2-[^{11}C]thymidine uptake of 8% and 3%, respectively. However, these scans were analysed using limited modelling methods (Shields AF. *et al.*, 1998b).

In this study, the feasibility of using the dual scan approach and spectral analysis modelling to determine the pharmacodynamic end-point after chemotherapy using 2-[^{11}C]thymidine will be examined.

8.8 Study Aims

The primary aim is to assess the change in 2-[^{11}C]thymidine uptake in tumour before and after chemotherapy and to correlate this with conventional imaging in tumour.

A secondary aim is to assess the feasibility of using a dual scan approach in a clinical study.

Also, this study aims to assess cellular proliferation in normal tissue and to assess the effect of chemotherapy on these tissues.

8.9 Methods

8.9.1 Patient Selection

Any patient with histologically proven primary or metastatic (excluding cerebral metastases) lung cancer who was due radical or palliative treatment with a conventional intravenous chemotherapy regime was eligible for the study. The patient had to have had a recent CT scan of their thorax prior to commencement of

treatment with a lesion of greater than 3 cm in at least one dimension and that could be evaluated using the RECIST classification system (Appendix B).

Other eligibility criteria included a WHO performance status of greater than 2 (Appendix A), and adequate full blood count, renal and hepatic function to be able to tolerate chemotherapy.

Ethics approval was obtained from the Hammersmith Hospital Research Ethics Committee and authorisation for the use of radionuclides was given by the Administration of the Radioactive Substances Advisory Committee (ARSAC UK). Fully informed and written consent was given by the patient for participation in the study.

8.9.2 Study Design

The patient underwent two PET scanning sessions using 2-[^{11}C]thymidine and [^{11}C]HCO_3 (for metabolite correction) one week before commencing chemotherapy and one week after the third cycle of chemotherapy. In each scanning session, the 60 minute 2-[^{11}C]thymidine was performed first, following a 30 second intravenous bolus injection. After a twenty minute interval, the 62 minute [^{11}C]HCO_3 scan was performed, again after a 30 second intravenous bolus administration of the radiotracer.

Prior to the first PET scanning session and after one week after the third course of chemotherapy, the patient had conventional imaging i.e. CT or MRI, of the site of the disease and a blood test for full blood count.

8.10 Procedures

The patient was positioned on the PET scanner couch using the recent CT scan to locate the tumour to be imaged. Anatomical landmarks were noted and utilised to position the patient accurately for the subsequent PET scanning session.

Continuous arterial blood sampling was obtained during both scans via an arterial cannula which was also used to obtain discrete blood samples.

8.11 Data Analysis

PET image scans were analysed after drawing a region of interest (ROI) on tumour, normal lung and bone marrow manually, using the CT scan to help with organ identification and delineation.

2-[^{11}C]thymidine scans were analysed using semi-quantative methodology to obtain SUV_{3mins} and AUC_{60mins}.

Spectral analysis was also performed to obtain K_1 and fractional retention of thymidine (FRT), after metabolite correction. A number of steps are required in order to perform metabolite correction. Plasma arterial input functions for the 2-[^{11}C]thymidine and [^{11}C]HCO_3 scan from continuous and discrete blood samples, are generated. In the 2-[^{11}C]thymidine scan, two input functions are generated: (i) combined parent and intermediate metabolite input function ($Plasma_{Thy}$) and (ii) input function for the metabolite CO_2 that is measured in the discrete samples during the 2-[^{11}C]thymidine scan, ($Plasma_{ThyCO2}$). The $Plasma_{Thy}$ input function is created as a dying exponential. It was necessary to use combined parent and intermediate metabolite for $Plasma_{Thy}$ input function as after 20 minutes, (due to rapid metabolism) no parent 2-[^{11}C]thymidine is detected in the plasma, which limits analysis of data. A combined parent and intermediate metabolite $Plasma_{Thy}$ input function permits use of a non-zero input function and also intermediate metabolite levels are very small compared to the main metabolite, [^{11}C]O_2, at later time points, though we must assume that both parent and intermediate metabolite have similar phosphorylation. From the [^{11}C]HCO_3 scan, the a single input function is obtained from measurement of [^{11}C]O_2 in arterial plasma ($PlasmaCO_2$).

From the bicarbonate scan, the following is derived using spectral analysis and deconvolution:

$$Tiss_{HCO3} = Plasma_{CO2} \otimes IRF_{HCO3}$$

Where, $Tiss_{HCO3}$ is the region of interest in the [^{11}C]HCO_3 scan, and IRF_{HCO3} is the impulse response function that is generated from the tissue and blood data and $\otimes$ represents the deconvolution operator.

In the 2-[^{11}C]thymidine scan, the following derived using spectral analysis and deconvolution:

$$Tiss_{ThyCO2} = Plasma_{ThyCO2} \otimes IRF_{HCO3}$$

Where, the IRF_{HCO3} from the bicarbonate scan is deconvolved with the $Plasma_{ThyCO2}$ from the 2-[^{11}C]thymidine scan, to generate the CO_2 component in the region of interest in the 2-[^{11}C]thymidine scan, $Tiss_{ThyCO2}$.

Tissue thymidine and intermediate metabolite is calculated by subtraction:

$$Tiss_{Thy} = Tiss_{totalThy} - Tiss_{ThyCO2}$$

Where, $Tiss_{totalThy}$ is the total thymidine tissue activity from the ROI in the 2-[^{11}C]thymidine scan and $Tiss_{ThyCO2}$ is derived as outlined above. $Tiss_{Thy}$ represents the thymidine and intermediate metabolite content for the ROI from the 2-[^{11}C]thymidine scan after metabolite corrected tissue.

Finally, spectral analysis was used to generate the IRF (IRF_{Thy}) and K_1 for each ROI from the 2-[^{11}C]thymidine scan:

$$Tiss_{Thy} = Plasma_{Thy} \otimes IRF_{Thy}$$

From the IRF_{1min} and IRF_{60min}, the fractional retention of thymidine (FRF) is calculated by:

$$FRF = IRF_{60min} / IRF_{1min}$$

8.12 Results

8.12.1 Patient Characteristics

A 49 year old female, ex-smoker, entered the study. She had presented with a one week history of left shoulder pain and was found to have a mass on chest x-ray. A CT guided biopsy gave histology of non-small cell lung cancer. She had not had any previous treatment. After a staging CT scan, she was commenced on three courses of chemotherapy, given every 3 weeks and consisting of: Gemcitabine at $1gm/m^2$ (dose 1 900 mg administered) given on day 1 and day 8, and Carboplatin at 5 (Glomerular Filtration Rate + 25) (dose administered 750 mg) given on day 1 only.

PET scanning sessions were performed one week prior to commencement of chemotherapy, and one week after the third chemotherapy cycle. Total blood loss during each PET session was approximately 355 mls and she tolerated the scanning sessions well, without any adverse effects. A follow-up CT scan was also performed one week after the third cycle of chemotherapy.

8.12.2 PET Scan Details

The following table gives details of 2-[^{11}C]thymidine and [^{11}C]HCO_3 that were administered on each PET session.

Table 8.1: Scan Details

	Scan number	Injected 2-[^{11}C]thymidine activity (MBq)	2-[^{11}C]thymidine radiochemical purity %	Injected [^{11}C]HCO_3 Activity (MBq)
Pre ^{1}CT	t00057	288.6	100	407
Post ^{1}CT	t00075	329.3	100	355.2

^{1}, Chemotherapy

8.12.3 Conventional Radiology

The patient had a CT one week before and after three courses of chemotherapy. The initial CT scan showed two masses in the left lung. The larger mass was a 5cm x 4 cm lobulated tumour situated in the left apical region, invading the left brachiocephalic vein. The smaller mass, within the left side of the mediastinum, was greater than 3 cm. and irregular in outline. After chemotherapy, the largest mass had decreased to 3 cm x 3 cm and the smaller mass had decreased to 2 cm, giving a partial response.

8.12.4 Haematological Results

The patient had a full blood count prior to commencing, and one week after chemotherapy and the results are shown below in Table 8.2.

Table 8.2: Full Blood Count Before and After Chemotherapy

Haematological Indices	pre chemotherapy	1 week post chemotherapy
Haemoglobin	13.8	8.7
White Cell Count	8.1	3.7
Platelets	495	523

8.13 2-[^{11}C]thymidine Analysis

Three regions were analysed in the 2-[^{11}C]thymidine scans: lung tumour, normal lung and bone marrow, using the recent CT scan to help with organ delineation and drawing of regions of interest. An example of the lung cavity from summated 2-[^{11}C]thymidine PET images is shown in Figure 67.

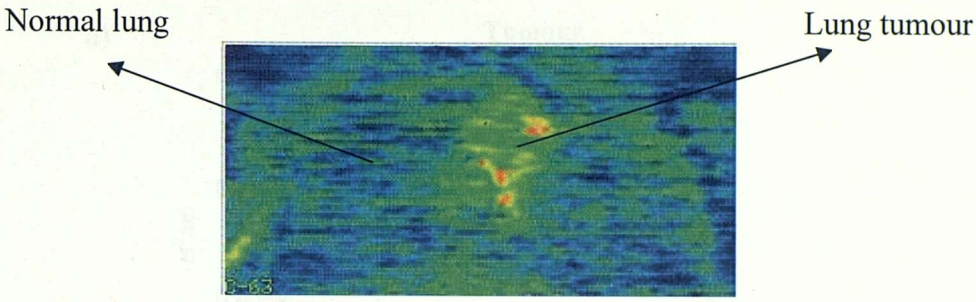


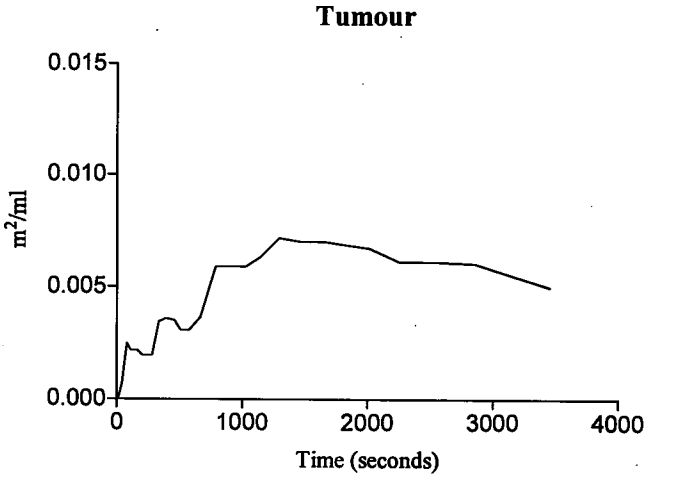
Figure 67: Coronal View of Thorax Using 2-[^{11}C]thymidine Imaging

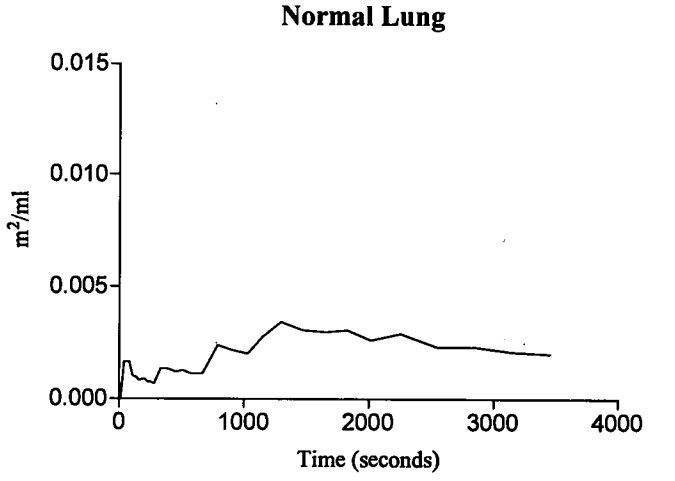
The regions of interest from the 2-[^{11}C]thymidine scans were analysed using semi-quantitative analysis to derive SUV_{3mins} and AUC_{60mins}. Analysis was also performed using spectral analysis after metabolite correction using the [^{11}C]HCO_3 scan data to derive K_1 and FRT

8.13.1 Semi-Quantitative Analysis

Tissue radioactivity versus time curves for lung tumour, normal lung and bone marrow were plotted pre and post chemotherapy. The curves looked similar for each region before and after treatment. Curves of the regions before chemotherapy are shown below.

a)





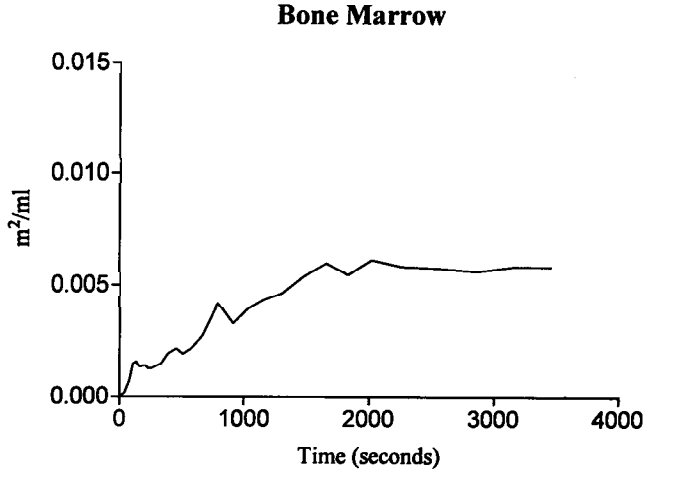


Figure 68: Tissue Radioactivity Versus Time Curves for (a) Tumour, (b) Normal Lung and (c) Bone Marrow

SUV_{3mins} and AUC_{60mins} were derived for each region and corrected for decay and body surface area (BSA) and the percentage change was calculated before and after chemotherapy (Table 8.3). SUV_{3mins} gives an indication of early uptake of 2-[^{11}C]thymidine, though is not corrected for labelled metabolites in the tissue. As can be seen, lung tumour > bone marrow > normal lung SUV_{3mins}, before and after chemotherapy. SUV_{3mins} post chemotherapy marginally increased in lung tumour by 2.1% and in normal lung by 8.8%. In bone marrow, there was an increase in delivery of 2-[^{11}C]thymidine of 30.4% after chemotherapy.

Table 8.3 SUV_{3mins} for 2-[^{11}C]thymidine Before and After Chemotherapy

	[1]SUV_{3mins} pre [2]CT t00057	[1]SUV_{3mins} post [2]CT t00075	% change after chemotherapy
Lung tumour	3.065×10^{-3}	3.728×10^{-3}	+ 2.1
Normal lung	1.224×10^{-3}	1.3311×10^{-3}	+ 8.8
Bone marrow	2.061×10^{-3}	2.687×10^{-3}	+ 30.4

[1], Standard uptake value at 3 minutes, m^2/ml; [2], Chemotherapy

AUC_{60mins} gives an indication of 2-[^{11}C]thymidine retention in regions of interest, though again there is no tissue correction for radiolabelled metabolites. Looking at Table 8.4, AUC_{60mins} it can be seen that lung tumour > bone marrow > normal lung before and after chemotherapy. Post chemotherapy, the largest reduction in AUC_{60mins} was seen in the bone marrow, with a decrease of 13.5%. Lung tumour retention of 2-[^{11}C]thymidine decreased by 6.8%, in keeping with the reduction in size of the tumour as observed on the CT image obtained post treatment. Normal lung AUC_{60mins} increased marginally by 2.5% post chemotherapy.

Table 8.4 AUC_{60mins} for 2-[^{11}C]thymidine Before and After Chemotherapy

	[1]AUC_{60mins} pre [2]CT t00057	[1]AUC_{60mins} post [2]CT t00075	% change after chemotherapy
Lung tumour	0.15	0.14	- 6.8
Normal lung	0.060	0.062	+ 2.5
Bone marrow	0.13	0.11	- 13.5

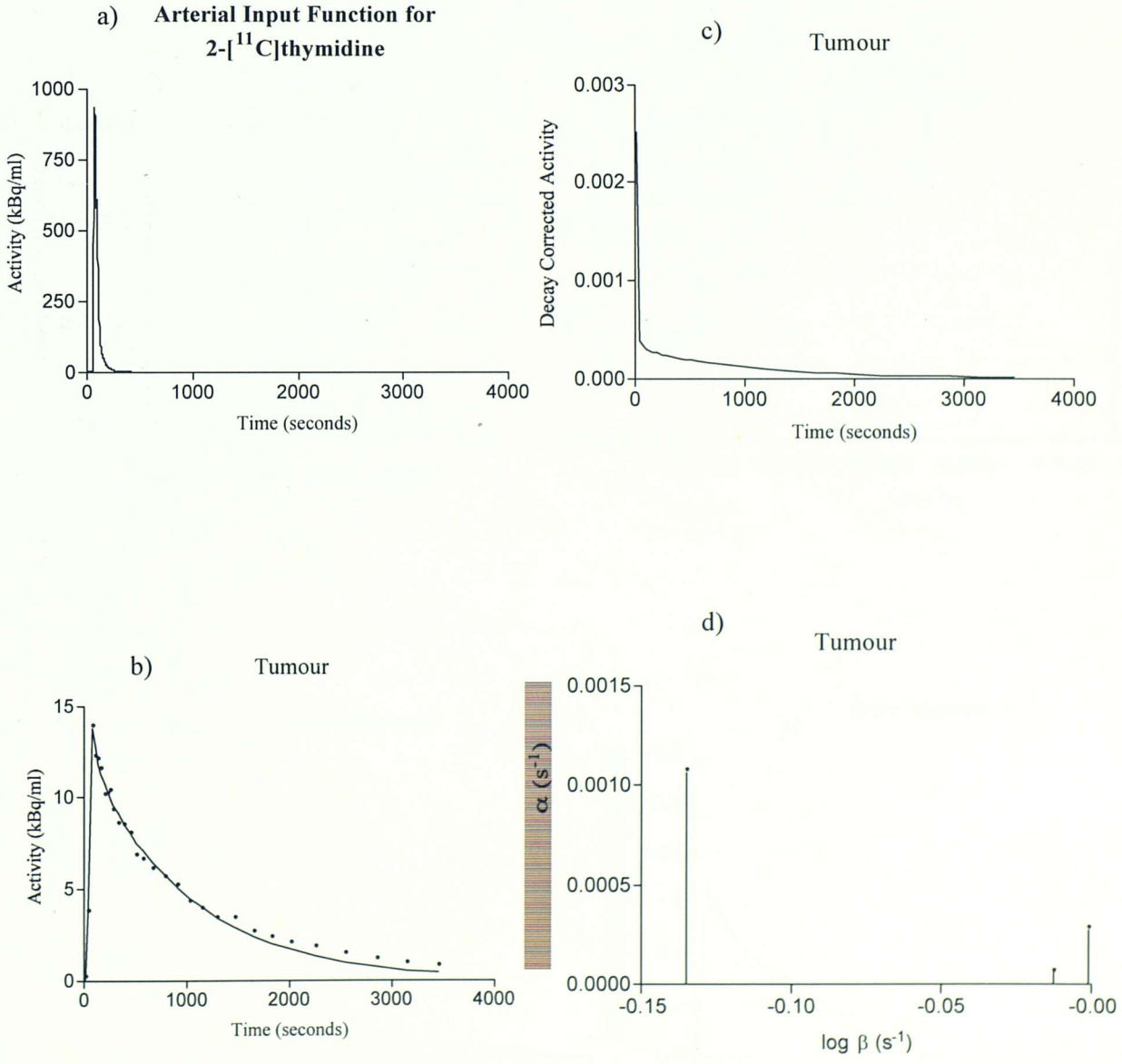
[1], Area under curve over 60 minutes, m^2/ml x sec; [2], Chemotherapy

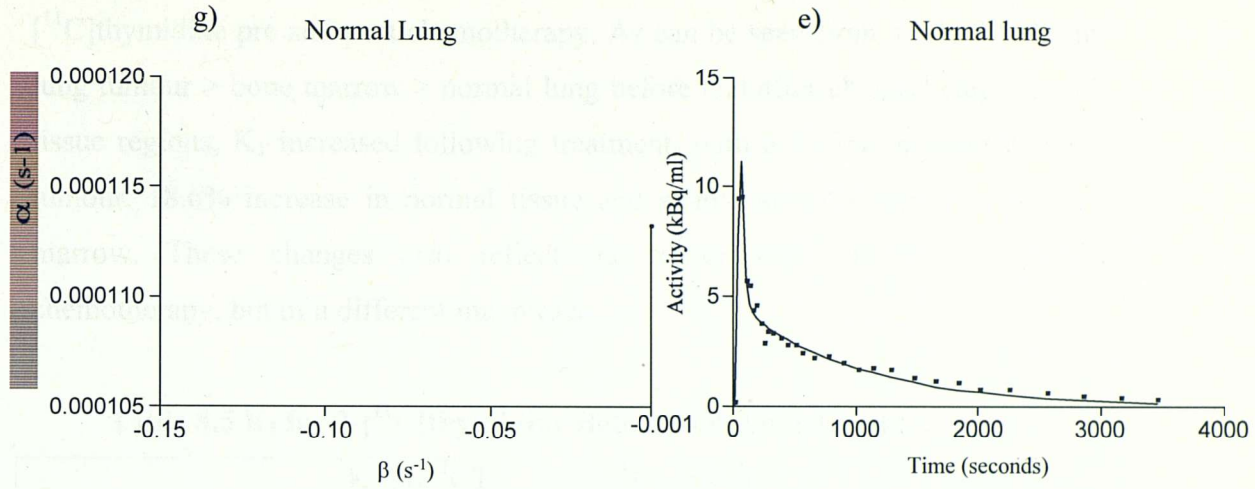
8.13.2 Spectral Analysis

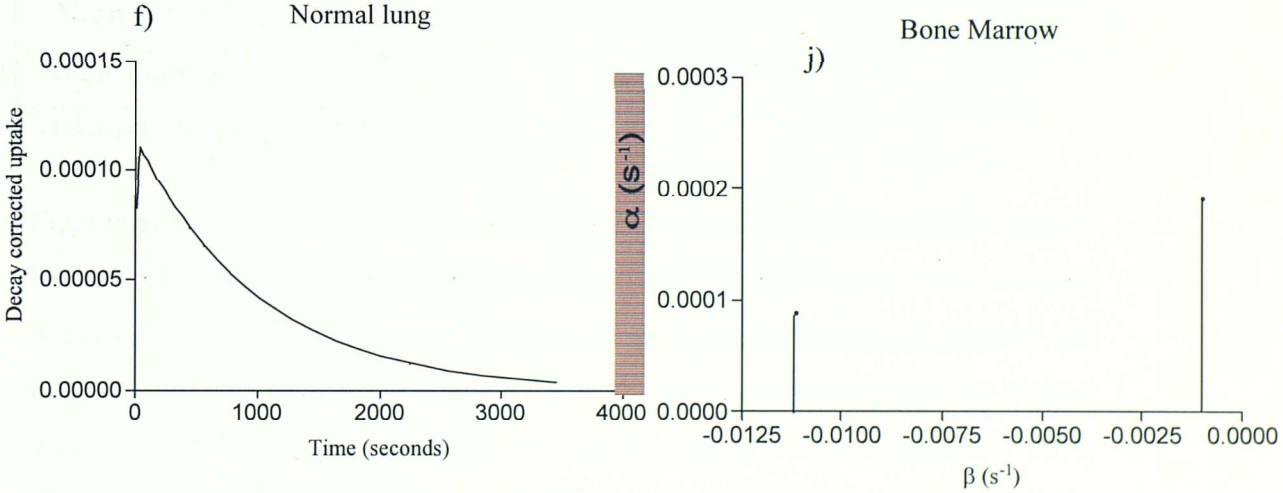
As described in methodology, spectral analysis was performed on the 2-[^{11}C]thymidine image data after [^{11}C]O_2 radiolabelled metabolite correction, and using a metabolite corrected 2-[^{11}C]thymidine arterial plasma input function. For each region of interest the tissue data was convolved with the arterial input function to produce a data fit as shown in Figure 69, which as can be seen was satisfactory for the organs analysed, and similar post chemotherapy. From this an impulse response function was derived, which is used to describe the tissue response of 2-[^{11}C]thymidine if it had been possible to deliver 2-[^{11}C]thymidine to the tissue instantaneously. The spectrum of kinetic results for lung tumour and normal lung and bone marrow, are also shown in Figure 69. Using a log scale, the number of kinetic components that adequately describe the data are revealed, and this corresponds to the number of discrete tissue compartments that the PET technique can resolve. The speed of the dynamics increase from left to right and, in all tissue regions, a right handed peak is present, indicating the contribution of the delivery component. In lung tumour and bone marrow regions, but not in normal lung, a left handed peak is seen, indicating trapping of 2-[^{11}C]thymidine in these regions. This was expected as both these tissues should have a high rate of DNA proliferative activity.

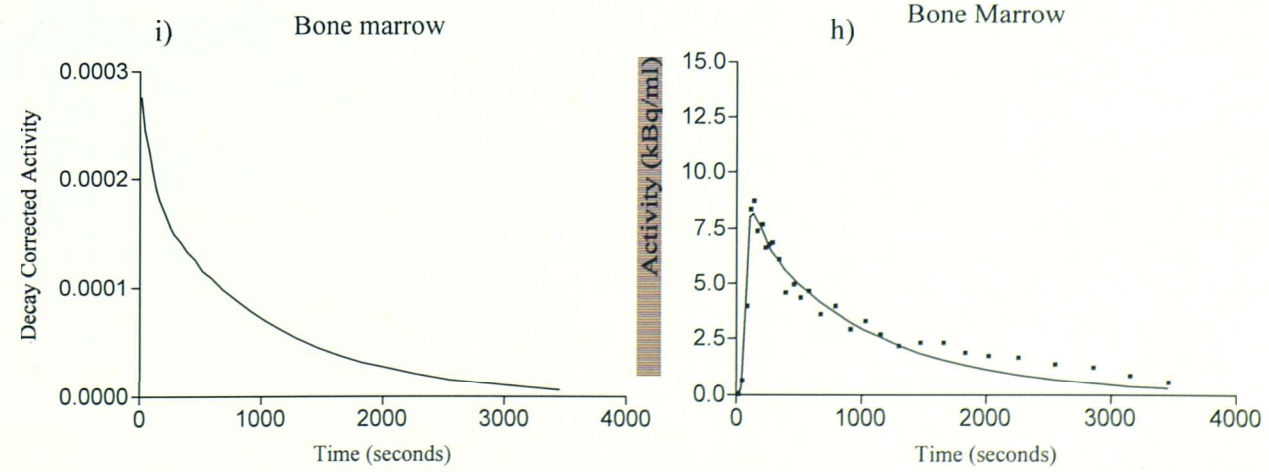
Figure 69: Spectral Analysis Curve for 2-[^{11}C]thymidine

a) arterial plasma input function for 2-[^{11}C]thymidine
b, e, h) corresponding time activity curve for tumour, normal lung and bone marrow, showing line of best fit
c, f, i) impulse response function (IRF) for tumour , normal lung and bone marrow corrected for radioactive decay,
d, g, j) IRF for tumour, normal lung and bone marrow displayed as kinetic components




g)
Normal Lung
α (s-1)
0.000120
0.000115
0.000110
0.000105
-0.15
-0.10
-0.05
-0.001
β (s-1)
e)
Normal lung
Activity (kBq/ml)
15
10
5
0
0
1000
2000
3000
4000
Time (seconds)


f)
Normal lung
Decay corrected uptake
0.00015
0.00010
0.00005
0.00000
0
1000
2000
3000
4000
Time (seconds)
Bone Marrow
j)
α (s-1)
0.0003
0.0002
0.0001
0.0000
-0.0125
-0.0100
-0.0075
-0.0050
-0.0025
0.0000
β (s-1)


i)
Bone marrow
Decay Corrected Activity
0.0003
0.0002
0.0001
0.0000
0
1000
2000
3000
4000
Time (seconds)
h)
Bone Marrow
Activity (kBq/ml)
15.0
12.5
10.0
7.5
5.0
2.5
0.0
0
1000
2000
3000
4000
Time (seconds)

For all regions, K_1 was calculated from spectral analysis, reflecting delivery of 2-[^{11}C]thymidine pre and post chemotherapy. As can be seen from Table 8.5, K_1 in lung tumour > bone marrow > normal lung before and after chemotherapy. In all tissue regions, K_1 increased following treatment, with a 33.3% increase in lung tumour, 18.6% increase in normal tissue and a modest 5.9% increase in bone marrow. These changes also reflect the effect seen on SUV_{3mins} after chemotherapy, but of a different magnitude.

Table 8.5 K_1 for 2-[^{11}C]thymidine Before and After Chemotherapy

	$^1K_1$ pre ^{2}CT t00057	$^1K_1$ post ^{2}CT t00075	% change after chemotherapy
Lung tumour	9×10^{-2}	1.2×10^{-1}	+ 33.3
Normal lung	7×10^{-3}	8.3×10^{-3}	+ 18.6
Bone marrow	1.7×10^{-2}	1.8×10^{-2}	+ 5.9

[1], $ml_{blood}/min/ml_{tissue}$; [2], Chemotherapy

Fractional retention of 2-[^{11}C]thymidine (FRT) has been calculated for the regions before and after chemotherapy. As expected, FRT in lung tumour > bone marrow > normal lung reflecting again the increase proliferative nature of tumour and bone marrow. After chemotherapy, FRT in the lung tumour still had the highest value, but FRT in normal lung was greater than in bone marrow. After chemotherapy, FRT decreased by 20.7% in lung tumour, in keeping with the changes observed in AUC_{60mins} and CT radiology. In bone marrow, FRT also decreased by 10.5%, similar to the decline in AUC_{60mins}, which is probably related to the known impact anti-cancer chemotherapy has on normal cellular myeloproliferation.

Table 8.6 Fractional Retention of 2-[^{11}C]thymidine Before and After Chemotherapy

	^{1}FRT pre ^{2}CT t00057	^{1}FRT post ^{2}CT t00075	% change after chemotherapy
Lung tumour	2.9×10^{-2}	2.3×10^{-2}	- 20.7
Normal lung	1.6×10^{-2}	1.8×10^{-2}	+ 13.2
Bone marrow	1.9×10^{-2}	1.7×10^{-2}	- 10.5

[1], Fractional Retention of 2-[^{11}C]thymidine; [2], Chemotherapy

8.14 Discussion

Functional imaging using PET can supplement information derived from clinical and radiological examinations that in themselves have limitations in assessing tumour response to anti-cancer treatment as outlined previously.

By far the commonest radiotracer used in PET to determine tumour response is [^{18}F]fluoro-2-deoxy-D-glucose ([^{18}F]FDG) (Young *et al.*, 1999). The increased demands of glycolysis in neoplastic cells compared to benign cells and consequent higher uptake of [^{18}F]FDG has been used to infer information on tumour growth and proliferation. Numerous *in vitro* and *in vivo* studies in humans have demonstrated that the uptake of [^{18}F]FDG is related to tumour grade in a range of malignancies. In general, low grade, slowly proliferating tumours have less [^{18}F]FDG uptake than is seen in poorly differentiated, rapidly growing tumours (Avril *et al.*, 2001; Buck *et al.*, 2002; Vesselle *et al.*, 2002). However, non-cell division related tumour cell activities require a supply of energy as do inflammatory cells such as macrophages and neutrophils (Kubota *et al.*, 1992). Other factors reported to influence [^{18}F]FDG uptake include upregulation of glucose transporter 1 receptors, number of viable tumour cells present, microvessel density and hexokinase expression, making glucose metabolism an ambiguous measure of tumour proliferation (van de Wiele *et al.*, 2003b).

Direct imaging of tumour proliferation with 2-[^{11}C]thymidine is being explored as a radiotracer that may circumvent the potential discrepancies associated with FDG-PET image interpretation. This study has demonstrated the feasibility of

clinical imaging to assess tumour response with 2-[^{11}C]thymidine using a dual scan approach with spectral analysis to correct for the radiolabelled metabolite, [^{11}C]O_2.

The most important parameters which were derived from analysis of the successive 2-[^{11}C]thymidine PET scans in this study to give an indication of thymidine utilisation and hence DNA synthesis and tissue proliferation are retention of thymidine or FRT and tissue exposure to thymidine, or AUC_{60mins}. From the results presented here, there was a reduction in both AUC_{60mins} and FRT in lung tumour following chemotherapy, consistent with results obtained from conventional imaging where according to the RECIST criteria a partial response i.e. a reduction in tumour size of 30%, was achieved on visual inspection of the post treatment CT scan. The reduction in FRT of 20% was greater than the reduction seen in AUC_{60mins} after chemotherapy. FRT is a quantitative parameter and more likely to give an accurate indication of decline in DNA synthesis in the lung tumour, as suggested in the study by P. Wells, where a significant correlation between Ki-67 and FRT was demonstrated (Wells *et al.*, 2002a). Furthermore, the FRT derived in this study is probably a more robust measure of DNA proliferation as the tissue sampled has been corrected for the metabolite [^{11}C]O_2.

In bone marrow, a reduction in FRT of 10.5% and in AUC_{60mins} of 13.5% was observed after chemotherapy corresponding with the changes in the peripheral blood profile indices, haemoglobin and white cell, whose values also decreased post therapy. The chemotherapeutic drugs, carboplatin and gemcitabine, are known to be myelosuppressive agents with cumulative reduction in haemoglobin levels but particularly affecting white cell and platelet counts, with the nadir seen within three weeks post carboplatin and seven to ten days post gemcitabine chemotherapy, which coincides with the second PET scanning session.

In normal lung, a small increase in FRT of 13.2% and AUC_{60mins} of 2.5% was seen after chemotherapy. Gemcitabine has been rarely reported to cause parenchymal lung toxicity resulting in interstitial pneumonitis, pulmonary fibrosis and oedema but there are no reports of adverse side effects on lung tissue

attributed to by carboplatin, so a predicted change in DNA proliferation and cell growth was not expected in normal lung.

The parameters K_1 and SUV_{3mins} calculated from the 2-[^{11}C]thymidine PET images give an indication of delivery of thymidine to the regions of interest. K_1 and SUV_{3mins} increased in the lung tumour, normal lung and bone marrow after chemotherapy. The increase in K_1 may simply be a reflection of perfusion to the region, though blood flow was not measured in this study. However, after one minute, thymidine delivery is independent of blood flow (Shields *et al.*, 1984) so it is unclear why SUV at three minutes increased in lung tumour and bone marrow as there was decreased retention of 2-[^{11}C]thymidine after chemotherapy. In the study by Wells et al no correlation was found between delivery of 2-[^{11}C]thymidine and Ki-67, an *in vitro* marker of DNA proliferation (Wells *et al.*, 2002a) and indeed the relationship between delivery and retention of thymidine in tissue has not been fully elucidated.

This study has demonstrated the feasibility of imaging pharmacodynamic endpoints using 2-[^{11}C]thymidine using a dual scan approach to correct for tissue metabolites. In addition to assessing tumour response to chemotherapy, it was possible to measure the effect of treatment on the proliferation of normal tissue such as bone marrow and lung which is an essential consideration when determining the toxicity profiles of anti-neoplastic drugs. A study by Shields et al has shown that changes in uptake of 2-[^{11}C]thymidine in tumours only one week after treatment can give an indication of tumour response to chemotherapy shortly after treatment initiation (Shields AF. *et al.*, 1998b). Using the dual scan technique as performed in this study, an actual measure of change in proliferative rate is achievable in normal tissue and tumour. This could potentially enable a physician to alter treatment earlier than is currently possible in non-responding tumour and spare excessive normal tissue toxicity in patients, if present.

Another use of imaging with 2-[^{11}C]thymidine that is being explored is to monitor thymidine salvage kinetics after treatment with Thymitaq^{TM}, a non-classical thymidine synthetase (TS) inhibitor. As previously mentioned, TS is a critical enzyme in DNA synthesis, and cells can overcome this cytotoxic effect by

incorporating thymidine from the extracellular or salvage pathway. Measurement of this salvage pathway was devised using 2-[^{11}C]thymidine imaging in patients with gastro-intestinal malignancies 1 hour after treatment with Thymitaq^{TM} who had an increase in intra-tumoural uptake compared to controls. This uptake coincided with the peak plasma concentrations of the drug in treated patients (Wells *et al.*, 2003).

A newer thymidine analogue, 3'-deoxy-3'-flurothymidine (FLT) has been developed as another promising radiotracer with which to measure cellular proliferation non-invasively using PET and was first studied in dogs for this purpose (Shields AF. *et al.*, 1998a). Labelled with [^{18}F], FLT has the advantages of a longer half-life than 2-[^{11}C]thymidine and therefore does not have to be manufactured on site for clinical use and is resistant to catabolism so it produces fewer radiolabelled metabolites that interfere with analysis. However, [^{18}F]FLT is not directly incorporated into DNA but rather its uptake and intracellular phosphorylation has been shown to correlate with thymidine kinase 1 (TK1) activity, an enzyme closely linked to cellular proliferation, as observed in A549 ling cancer cells *in vitro* (Rasey *et al.*, 2002). There have been several clinical studies using [^{18}F]FLT (Buck *et al.*, 2002; Shields AF. *et al.*, 1998a; Smyczek-Gargya *et al.*, 2004; Vesselle *et al.*, 2002) in a wide range of cancers. In a series of twenty-six patients with untreated solitary pulmonary nodules, the uptake of [^{18}F]FLT measured by SUV correlated significantly with Ki-67 ($r = 0.87$), with 100% specificity and 86% sensitivity. The lower sensitivity was attributed to false-negative scans in three patients with malignant lung lesions which all had a low rate of cellular proliferation (Buck *et al.*, 2002). In another study ten patients with biopsy or clinically suspected NSCLC underwent dynamic scanning with 2-[^{11}C]thymidine and correlated uptake of [^{18}F]FLT with Ki-67 immunohistochemistry. Using both SUV and Patlak analysis, to determine FLT flux, a strong correlation was found between [^{18}F]FLT uptake and Ki-67 (Vesselle *et al.*, 2002). In a more recent study twelve patients with primary breast cancer had static [^{18}F]FLT scans of 80 to 120 minutes duration. SUV was calculated and compared to Ki-67 labelling index, but no correlation was found between the two parameters. The absence of correlation between [^{18}F]FLT uptake and Ki-67 in breast compared to a positive association in lung tumours was assumed to be

because of differences in growth patterns in the two tumour types (Smyczek-Gargya *et al.*, 2004). Another study has demonstrated a correlation between K_I and fractional retention of [^{18}F]FLT and Ki-67 in breast tumours, suggesting superiority of quantative analysis when using [^{18}F]FLT PET to image cellular proliferation in breast cancer (Kenny *et al.*, 2005). There is also some literature available on [^{18}F]FLT uptake and tumour response assessment. A pre-clinical study investigating the response of tumours to 5-FU in mice with radiation-induced fibrosarcoma found a reduction of [^{18}F]FLT uptake after treatment and an association with proliferating cell nuclear antigen in tumours (Barthel *et al.*, 2005). A clinical study by Kenny et al has shown that [^{18}F]FLT PET can be used to distinguish between clinical response and stable disease in patients with breast cancer 1 week after chemotherapy (Kenny *et al.*, 2007).

FMAU or [1-(2'-fluoro-2'-deoxy-β-D-ribofuransonyl) thymine] is another thymidine analogue originally developed as an antiviral and anti-leukaemic drug that has been shown to be rapidly taken up by cells, phosphorylated by TK and variably incorporated into DNA, with little catabolism (Philips *et al.*, 1983). 2[^{14}C]FMAU uptake was high in tumour xenografts compared to normal tissue in pre-clinical studies (Conti *et al.*, 1995). Studies are on going to evaluate its full potential in human studies after it has been radiolabelled with fluorine-18 (Sun *et al.*, 2005).

Iodo- and bromodeoxyuridine (IUdR, BUdR) are formed after replacement of the methyl group in thymidine with iodine and bromine, respectively, and are incorporated into cells synthesising DNA. IUdR and BUdR have been used to measure cell cycle in biopsy specimens with flow cytometry after labelling with monoclonal antibodies or fluorescent dyes. IUdR and BUdR have been labelled with radioisotopes which have a long half-life: ^{124}I (half-life = 4.2 days) (Guenther *et al.*, 1998) and ^{76}Br (half-life = 16 hours) (Bergstrom *et al.*, 1998) for PET imaging studies. Though taken up in tumour, image analysis is complicated by rapid dehalogenation and liberation of the labelled halogen molecule. Imaging 24 to 48 hours after injection may allow for clearance of the free halogen, although this time lapse has led to a reduction in tumour activity. Clinical studies with [^{76}B]UdR have revealed conflicting results in brain tumours and melanoma,

with little radioactivity in brain tumour DNA, but in the melanoma group, uptake of [^{76}BUdR] correlated significantly with MIB-1 staining (Boni *et al.*, 1999; Gudjonssona *et al.*, 2001). Blasberg et al performed delayed imaging of 24 hours with ^{124} IUdR in meningiomas and gliomas. There were variable correlations between K_I, SUV, and tumour to brain activity ratios (Tm:Br) and other measures of tumour proliferation (tumour type and grade, labelling index, and patient survival) observed. However, greater image specificity and significance of the SUV and Tm:Br values would be obtained by achieving greater washout and clearance of the exchangeable fraction of residual (background) radioactivity in the tumours, *i.e.*, by increased hydration and urinary clearance and possibly by imaging later than 24 h after [^{124}I]IUdR administration (Blasberg *et al.*, 2000).

The study presented here provides encouraging results for the application of 2-[^{11}C]thymidine PET imaging of pharmacodynamic endpoints. Accurate and early *in vivo* response assessment to chemotherapy can avoid prolonged treatment with chemotherapy in unresponsive tumours and identify tumour response to cytostatic and molecular targeted drugs. Further studies may allow the construction of guidelines correlating early tumour response measured by 2-[^{11}C]thymidine with conventional methods as the EORTC has devised for FDG-PET. In normal tissue, changes in cellular proliferation may help determine toxicity profiles of conventional anti-proliferative drugs and novel drugs, as cytotoxicity is a major pharmacodynamic endpoint in phase 1 drug trials.

Imaging of cellular proliferation either directly using thymidine, such as 2-[^{11}C]thymidine or indirectly with an analogue, such as [^{18}F]FLT, could be of huge importance in cancer treatment and drug development.

8.15 Summary

- Dual scanning with 2-[^{11}C]thymidine and [^{11}C]bicarbonate is feasible in a clinical setting.

- Changes in 2-[^{11}C]thymidine uptake in tumour and normal tissue can provide a non-invasive measurement of DNA synthesis and cellular proliferation in response to chemotherapy.

Appendix A

WHO PERFORMANCE STATUS

Activity Performance Description	Score
Fully active, able to carry out all pre-disease performance without any restriction.	0
Restricted in physically strenuous activity by ambulatory and able to carry out work of a light or sedentary nature, such as light house work or office work.	1
Ambulatory and capable of all self-care, but unable to carry out any work activities. Up and about for more than 50% of waking hours.	2
Capable of only limited self-care. Confined to bed or chair for more than 50% of waking hours.	
Completely disabled and cannot carry out any self-care. Totally confined to bed or chair.	4

Appendix B

Response to Treatment of Solid Tumours (RECIST) Guidelines

Definitions

At baseline, all tumours are measurable, non-measurable or truly non-measurable.

Measurable Lesions

Measurable lesions are lesions that can be accurately measured in at least one dimension and are ≥ 20mm on conventional imaging techniques or ≥ 10mm using spiral CT.

Non-measurable

Non-measurable lesions are lesions that can be accurately measured in at least one dimension and are ≤ 20mm on conventional imaging techniques or ≤ 10mm using spiral CT.

Truly Non-measurable lesions

Immeasurable lesions are bone lesions, leptomeningeal disease, ascites, pleural/pericardial effusions and inflammatory breast disease.

Methods of Measurement

Clinical examination

Clinically detected lesions are only considered measurable if they are superficial (e.g. skin nodules and palpable lymph nodes.

Chest x-ray

Lesions on chest x-ray are accepted as measurable lesions when they are clearly defined and surrounded by aerated lung.

CT and MRI

CT and MRI are best currently available and the most reproducible methods for measuring target lesions selected for response assessment.

Ultrasound

When the primary end point of the study is objective response evaluation, ultrasound should not be used to measure tumour lesions that are clinically not easily accessible.

Endoscopy and laparoscopy

The utilisation of these for objective tumour evaluation has not yet been fully validated.

Tumour markers

Tumour markers alone cannot be used to assess response. However, if tumour markers are initially above the upper normal limit, they must return to normal levels for a patient to be considered in complete clinical response.

Cytology and histology

Cytological and histological techniques can be used to differentiate between partial and complete response in rare cases. Cytological confirmation of the neoplastic nature of any effusion that appears or worsens during treatment is required when the measurable tumour has met criteria for response or stable disease. Under such circumstances, the cytological examination of the fluid collected will permit differentiation between response or stable disease.

Tumour Response Evaluation

Baseline evaluation

All measurable lesions up to a maximum of 5 lesions per organ and 10 lesions in total, representative of all involved organs, should be recorded as target lesions and measured and recorded at baseline. Target lesions with the longest diameter should be selected. A sum of the longest diameter for all target lesions will be calculated and reported as sum of longest baseline diameter.
All other lesions are reported as non-target lesions and should be recorded but not measured.

Response Criteria

Evaluation of Target Lesions

Complete Response: the disappearance of all target lesions

Partial Response: at least a 30% decrease in sum of longest baseline diameter of target lesions, taking as reference the baseline sum longest diameter.

Progressive Disease: at least a 20% increase in the sum of the longest diameter of baseline lesion taking as reference the smallest sum longest diameter recorded since the treatment started or the appearance of one or more lesions.

Stable Disease: neither sufficient shrinkage to qualify for partial response or sufficient increase to qualify for progressive disease, taking as reference the smallest sum longest diameter recorded since the treatment started.

Evaluation of non-target lesions

Complete Response: the disappearance of all non-target lesions and the normalisation of tumour markers.

Incomplete response/stable disease: the persistence of one or more non-target lesion (s) and/or the maintenance of tumour marker level above normal limits.

Progressive disease: the appearance of one or more new lesions and/or unequivocal progression of non-target lesions.

Evaluation of best overall response

The best overall response is the best response recorded until disease progression or recurrence. Table 1 provides overall response for all possible combinations of tumour response in target and non-target lesions with or without the appearance of new lesions.

Table 1 Overall response for all possible combination of tumour responses*

Target lesion	Non-target lesion	New lesion	Overall response
CR	CR	No	CR
CR	Incomplete response/SD	No	CR
PR	Non-PD	No	PR
SD	Non-PD	No	SD
PD	Any	Yes or no	PD
Any	PD	Yes or no	PD
Any	Any	Yes	PD

*CR, complete response; PR, partial response; SD, stable disease; PD, progressive disease

Frequency of tumour re-evaluation

Frequency of tumour re-evaluation while on treatment should be protocol specific and adapted to the type and schedule of treatment.

Confirmation

Partial/Complete response: to be assigned this status, changes in tumour measurement must be confirmed by repeat assessment that should be made not less than 4 weeks after the criteria for response are first met.

Stable disease: measurements must have met the stable disease criteria at least once after start of treatment at a minimum interval in general, not less than 6 to 8 weeks.

Duration of Overall response

The duration of overall response is taken from the time that measurement criteria are met for complete or partial response (which ever status is recorded first) until the first date that progressive or recurrent disease is objectively documented.

Duration of stable disease

Stable disease is measured from the start of treatment until the criteria for disease progression is met.

Awards and Publications

Awards

2002 FECS/ASCO/AACR study award, Flims, Switzerland.

2002 ASCO Merit Award, Orlando, USA.

Publications

Book Chapter

N Gupta and PM Price. Molecular Imaging in Cancer Treatment: PET *Imaging in Oncology Ed.2: New Horizons in Oncology*

Original Papers and Reviews

N Gupta, PM Price, EO Aboagye. PET for *in vivo* pharmacokinetic and pharmacodynamic measurements *Eur J Cancer* 2002 **38** 2094-2107

Nishi Gupta, Azeem Saleem, Safiye Osman, Eric O. Aboagye, Robert Philips, Claire Vernon, Harpreet Wasson, Terry Jones, Peter J. Hoskin, Patricia P. Price. Carbogen and Nicotinamide Selectively Increase Blood Flow and 5-Fluorouracil Delivery in Colorectal Cancer Metastases *Clin Cancer Res* **12** 3115-3123

Oral Presentation

N Gupta, A Saleem, S Osman, P Hoskin, P Price and E Aboagye. Carbogen and nicotinamide selectively increase blood flow to liver metastasis. *BACR* 2002

Posters and Abstracts

N Gupta, E Aboagye, A Saleem, R Harte, S Osman, B Phillips, C Vernon, H Wasan and P Price. Delivery and Retention of 5-FU can be Modulated and Measured Independently in Vivo in Man. *Proc Am Soc Clin Onco* 2003 **22** p212, 850a

EO Aboagye, A Saleem, N Gupta, C Brock, P Price. What new pharmacokinetic information can molecular imaging provide us? *Eur J Cancer* 2002 **38** Supp 7 S12

N Gupta, A Saleem, S Osman, P Hoskin, P Price and E Aboagye. Carbogen and nicotinamide selectively increase blood flow index (BFI) and 5-fluorouracil (5-FU) delivery in human tumours. *Proc Am Soc Clin Onc* 2002 **21** p124, 493a

References

ABERNETHY, D.R., ALPER, J.C., WIEMANN, M.C., MCDONALD, C.J. & CALABRESI, P. (1989). Oral 5-fluorouracil in psoriasis: pharmacokinetic-pharmacodynamic relationships. *Pharmacology*, **39**, 78-88.

ABOAGYE, E.O. & BHUJWALLA, Z.M. (1999). Malignant transformation alters membrane choline phospholipid metabolism of human mammary epithelial cells. *Cancer Res*, **59**, 80-4.

ABOAGYE EO., SALEEM A., CUNNINGHAM VJ., OSMAN S. & PRICE PM. (2001). Extraction of 5-Fluorouracil by Tumor and Liver: A Noninvasive Positron Emission Tomography Study of Patients with Gastrointestinal Cancer. *Cancer Research*, **61**, 4937-41.

ALPERT, N.M., CHESLER, D.A., CORREIA, J.A., ACKERMAN, R.H., CHANG, J.Y., FINKLESTEIN, S., DAVIS, S.M., BROWNELL, G.L. & TAVERAS, J.M. (1982). Estimation of the local statistical noise in emission computed tomography. *IEEE Trans Med Imaging*, **M1-1**, 142-146.

ANDERSON, C.D. (1932). The Apparent Existence of Easily Deflectable Positives. *Science*, **76**, 238-239.

ANDERSON, C.J., DEHDASHTI, F., CUTLER, P.D., SCHWARZ, S.W., LAFOREST, R., BASS, L.A., LEWIS, J.S. & MCCARTHY, D.W. (2001). 64Cu-TETA-octreotide as a PET imaging agent for patients with neuroendocrine tumors. *J Nucl Med*, **42**, 213-21.

ANDERSON, H. & PRICE, P. (2002). Clinical measurement of blood flow in tumours using positron emission tomography: a review. *Nucl Med Commun*, **23**, 131-8.

ANDERSON, H.L., YAP, J.T., MILLER, M.P., ROBBINS, A., JONES, T. & PRICE, P.M. (2003). Assessment of pharmacodynamic vascular response in a phase I trial of combretastatin A4 phosphate. *J Clin Oncol*, **21**, 2823-30.

AVRIL, N., MENZEL, M., DOSE, J., SCHELLING, M., WEBER, W., JANICKE, F., NATHRATH, W. & SCHWAIGER, M. (2001). Glucose metabolism of breast cancer assessed by 18F-FDG PET: histologic and immunohistochemical tissue analysis. *J Nucl Med*, **42**, 9-16.

BADDELEY, H., BRODRICK, P.M., TAYLOR, N.J., ABDELATTI, M.O., JORDAN, L.C., VASUDEVAN, A.S., PHILLIPS, H., SAUNDERS, M.I. & HOSKIN, P.J. (2000). Gas exchange parameters in radiotherapy patients during breathing of 2%, 3.5% and 5% carbogen gas mixtures. *Br J Radiol*, **73**, 1100-4.

BAKIR, M.A., ECCLES, S., BABICH, J.W., AFTAB, N., STYLES, J., DEAN, C.J., LAMBRECHT, R.M. & OTT, R.J. (1992). c-erbB2 protein overexpression in breast cancer as a target for PET using iodine-124-labeled monoclonal antibodies. *J Nucl Med*, **33**, 2154-60.

BARTHEL, H., PERUMAL, M., LATIGO, J., HE, Q., BRADY, F., LUTHRA, S.K., PRICE, P.M. & ABOAGYE, E.O. (2005). The uptake of 3'-deoxy-3'-[18F]fluorothymidine into L5178Y tumours in vivo is dependent on thymidine kinase 1 protein levels. *Eur J Nucl Med Mol Imaging*, **32**, 257-63.

BARTHEL, H., WILSON, H., COLLINGRIDGE, D.R., BROWN, G., OSMAN, S., LUTHRA, S.K., BRADY, F., WORKMAN, P., PRICE, P.M. & ABOAGYE, E.O. (2004). In vivo evaluation of [18F]fluoroetanidazole as a new marker for imaging tumour hypoxia with positron emission tomography. *Br J Cancer*, **90**, 2232-42.

BEANEY, R.P., LAMMERTSMA, A.A., JONES, T., MCKENZIE, C.G. & HALNAN, K.E. (1984). Positron emission tomography for in-vivo measurement of regional blood flow, oxygen utilisation, and blood volume in patients with breast carcinoma. *Lancet*, **1**, 131-4.

BELHOCINE, T., STEINMETZ, N., HUSTINX, R., BARTSCH, P., JERUSALEM, G., SEIDEL, L., RIGO, P. & GREEN, A. (2002). Increased uptake of the apoptosis-imaging agent (99m)Tc recombinant human Annexin V in human tumors after one course of chemotherapy as a predictor of tumor response and patient prognosis. *Clin Cancer Res*, **8**, 2766-74.

BELLAMY, W.T., DALTON, W.S. & DORR, R.T. (1990). The clinical relevance of multidrug resistance. *Cancer Invest*, **8**, 547-62.

BEN-DAVID, I., ROZEN, Y., ORTU, G. & MISHANI, E. (2003). Radiosynthesis of ML03, a novel positron emission tomography biomarker for targeting epidermal growth factor receptor via the labeling synthon: [11C]acryloyl chloride. *Appl Radiat Isot*, **58**, 209-17.

BERGSTROM, M., LU, L., FASTH, K.J., WU, F., BERGSTROM-PETTERMANN, E., TOLMACHEV, V., HEDBERG, E., CHENG, A. & LANGSTROM, B. (1998). In vitro and animal validation of bromine-76-bromodeoxyuridine as a proliferation marker. *J Nucl Med*, **39**, 1273-9.

BERNIER, J., DENEKAMP, J., ROJAS, A., MINATEL, E., HORIOT, J., HAMERS, H., ANTOGNONI, P., DAHL, O., RICHAUD, P., VAN GLABBEKE, M. & PIERART, M. (2000). ARCON: accelerated radiotherapy with carbogen and nicotinamide in head and neck squamous cell carcinomas. The experience of the Co-operative group of radiotherapy of the european organization for research and treatment of cancer (EORTC). *Radiother Oncol*, **55**, 111-9.

BLANKENBERG, F.G., KATSIKIS, P.D., TAIT, J.F., DAVIS, R.E., NAUMOVSKI, L., OHTSUKI, K., KOPIWODA, S., ABRAMS, M.J., DARKES, M., ROBBINS, R.C., MAECKER, H.T. & STRAUSS, H.W. (1998). In vivo detection and imaging of phosphatidylserine expression during programmed cell death. *Proc Natl Acad Sci U S A*, **95**, 6349-6354.

BLANKENBERG, F.G., KATSIKIS, P.D., TAIT, J.F., DAVIS, R.E., NAUMOVSKI, L., OHTSUKI, K., KOPIWODA, S., ABRAMS, M.J. & STRAUSS, H.W. (1999). Imaging of apoptosis (programmed cell death) with 99mTc annexin V. *J Nucl Med*, **40**, 184-91.

BLANKENBERG, F.G., TAIT, J., OHTSUKI, K. & STRAUSS, H.W. (2000). Apoptosis: the importance of nuclear medicine. *Nucl Med Commun*, **21**, 241-50.

BLASBERG, R.G. (2002). PET imaging of gene expression
Eur J Cancer, **38**, 2137-2146.

BLASBERG, R.G., ROELCKE, U., WEINREICH, R., BEATTIE, B., VON AMMON, K., YONEKAWA, Y., LANDOLT, H., GUENTHER, I., CROMPTON, N.E., VONTOBEL, P., MISSIMER, J., MAGUIRE, R.P., KOZIOROWSKI, J., KNUST, E.J., FINN, R.D. & LEENDERS, K.L. (2000). Imaging brain tumor proliferative activity with [124I]iododeoxyuridine. *Cancer Res*, **60**, 624-35.

BONASERA, T.A., O'NEIL, J.P., XU, M., DOBKIN, J.A., CUTLER, P.D., LICH, L.L., CHOE, Y.S., KATZENELLENBOGEN, J.A. & WELCH, M.J. (1996). Preclinical evaluation of fluorine-18-labeled androgen receptor ligands in baboons. *J Nucl Med*, **37**, 1009-15.

BONI, R., BLAUENSTEIN, P., DUMMER, R., VON SCHULTHESS, G.K., SCHUBIGER, P.A. & STEINERT, H.C. (1999). Non-invasive assessment of tumour cell

proliferation with positron emission tomography and [76Br]bromodeoxyuridine. *Melanoma Res*, **9**, 569-73.

BRADY, F., LUTHRA, S.K., BROWN, G.D., OSMAN, S., ABOAGYE, E., SALEEM, A. & PRICE, P.M. (2001). Radiolabelled tracers and anticancer drugs for assessment of therapeutic efficacy using PET. *Curr Pharm Des*, **7**, 1863-92.

BRAUN R., LANZEN J., TURNAGE J., ROSNER G. & DEWHIRST M. (2001). Effects of the interaction of carbogen and nocotinamide on R3230 Ac tumour blood flow in Fischer 344 rats. *Radiation Research*, **5**, 724-33.

BRAYBROOKE J., PROPPER D., O'BYRNE K., KOUKOURAKIS M., PATTERSON A., HOULBROOK S., LOVE S., VARCOE S., TAYLOR M., GANESON T., TALBOT D. & HARRIS A. (2000). Induction of thymidine phosphorylase as a pharmacodynamic endpoint in patients with advanced carcinoma treated with 5-fluorouracil, folinic acid and interferon alpha. *British Journal of Cancer*, **83**, 219-24.

BRIX G., BELLEMAN M., GERLACH L. & HABERKORN U. (1998). Intra and extracellular fluorouracil uptake: assessment with contrast-enhanced metabolic F-19 MR imaging. *Radiology*, **209**, 259-67.

BRIZEL, D.M., DODGE, R.K., CLOUGH, R.W. & DEWHIRST, M.W. (1999). Oxygenation of head and neck cancer: changes during radiotherapy and impact on treatment outcome. *Radiother Oncol*, **53**, 113-7.

BRIZEL, D.M., LIN, S., JOHNSON, J.L., BROOKS, J., DEWHIRST, M.W. & PIANTADOSI, C.A. (1995). The mechanisms by which hyperbaric oxygen and carbogen improve tumour oxygenation. *British Journal of Cancer*, **75**, 1120-4.

BROOKS, D.J., PLAYFORD, E.D., IBANEZ, V., SAWLE, G.V., THOMPSON, P.D., FINDLEY, L.J. & MARSDEN, C.D. (1992). Isolated tremor and disruption of the nigrostriatal dopaminergic system: an 18F-dopa PET study. *Neurology*, **42**, 1554-60.

BROOKS, P.C., STROMBLAD, S., KLEMKE, R., VISSCHER, D., SARKAR, F.H. & CHERESH, D.A. (1995). Antiintegrin alpha v beta 3 blocks human breast cancer growth and angiogenesis in human skin. *J Clin Invest*, **96**, 1815-22.

BROWN G., BRADY F. & STEEL C. (1993). A practical synthesis of 5-[^{18}F]Fluorouracil using HLPC and a study of its metabolic profile in rats. *J Label Compd Radiopharm.*, **32**, 521-22.

BUCK, A.K., SCHIRRMEISTER, H., HETZEL, M., VON DER HEIDE, M., HALTER, G., GLATTING, G., MATTFELDT, T., LIEWALD, F., RESKE, S.N. & NEUMAIER, B. (2002). 3-deoxy-3-[(18)F]fluorothymidine-positron emission tomography for noninvasive assessment of proliferation in pulmonary nodules. *Cancer Res*, **62**, 3331-4.

CANCER, A.C., META-ANALYSIS & PROJECT (1992). Modulation of Fluouracil in patients with advanced colorectal cancer: Evidence in terms of response rates. *Jornal of Clinical Oncology*, **10**, 896-903.

CANCER, M.-A.G.I. (2001). Alpha-interferon does not increase the efficacy of 5-fluorouracil in advanved colorectal cancer. *British Journal of Cancer*, **84**, 611-20.

CARSON, R.E., YAN, Y., DAUBE-WITHERSPOON, M., FREEDMAN, N. & BACHARACH, S.L. (1993). An approximation formula for the variance of PET region-of-interest values.

. *IEEE Trans Med Imaging*, **12**, 240-250.

CHANG, J., POWLES, T.J., ALLRED, D.C., ASHLEY, S.E., CLARK, G.M., MAKRIS, A., ASSERSOHN, L., GREGORY, R.K., OSBORNE, C.K. & DOWSETT, M. (1999). Biologic markers as predictors of clinical outcome from systemic therapy for primary operable breast cancer. *J Clin Oncol*, **17**, 3058-63.

CHAO, K.S., BOSCH, W.R., MUTIC, S., LEWIS, J.S., DEHDASHTI, F., MINTUN, M.A., DEMPSEY, J.F., PEREZ, C.A., PURDY, J.A. & WELCH, M.J. (2001). A novel approach to overcome hypoxic tumor resistance: Cu-ATSM-guided intensity-modulated radiation therapy. *Int J Radiat Oncol Biol Phys*, **49**, 1171-82.

CHAPLIN D., HORSMAN M., AND & MJ., T. (1990). Effect of the microregional heterogeneity of oxygen delivery within a murine tumour. *J Natl Cancer Inst*, **82**, 672-676.

CHAPLIN, D.J. & HILL, S.A. (2002). The development of combretastatin A4 phosphate as a vascular targeting agent. *Int J Radiat Oncol Biol Phys*, **54**, 1491-6.

CHAPLIN, D.J. & HILL, S.A. (1995). Temporal heterogeneity in microregional erythrocyte flux in experimental solid tumours. *Br J Cancer*, **71**, 1210-3.

CHEN J., WEI L., BERECZKI D., HANS F., OTSUKAT T., FINNEGAN W., PATRAK C. & J., A.F. (1994). Slightly altered permeability-surface area products imply some cerebral capillary recruitment during hypercapnia. *Microvascular Research*, **48**, 190-211.

CHO, Z.H., CHAN, J.K., ERICKSSON, L., SINGH, M., GRAHAM, S., MACDONALD, N.S. & YANO, Y. (1975). Positron Ranges Obtained from Biomedically Important Positron-Emitting Radionuclides. *J Nucl Med*, **16**, 1174-1176.

CHU, E., ZINN, S., BOARMAN, D. & ALLEGRA, C.J. (1990). Interaction of gamma interferon and 5-fluorouracil in the H630 human colon carcinoma cell line. *Cancer Res*, **50**, 5834-40.

CLEAVER JE. (1967). Thymidine metabolism and cell kinetics. *Frontiers of Biology*, **6**, 43-100.

COLLINGRIDGE, D.R., CARROLL, V.A., GLASER, M., ABOAGYE, E.O., OSMAN, S., HUTCHINSON, O.C., BARTHEL, H., LUTHRA, S.K., BRADY, F., BICKNELL, R., PRICE, P. & HARRIS, A.L. (2002). The development of [(124)I]iodinated-VG76e: a novel tracer for imaging vascular endothelial growth factor in vivo using positron emission tomography. *Cancer Res*, **62**, 5912-9.

COLLINS, V.P., LOEFFLER, R.K. & TIVEY, H. (1956). Observations on growth rates of human tumors. *Am J Roentgenol Radium Ther Nucl Med*, **76**, 988-1000.

CONTI, P.S., ALAUDDIN, M.M., FISSEKIS, J.R., SCHMALL, B. & WATANABE, K.A. (1995). Synthesis of 2'-fluoro-5-[11C]-methyl-1-beta-D-arabinofuranosyluracil ([11C]-FMAU): a potential nucleoside analog for in vivo study of cellular proliferation with PET. *Nucl Med Biol*, **22**, 783-9.

CRONE, C. (1963). The Permeability of Capillaries in Various Organs as Determined by Use of the 'Indicator Diffusion' Method. *Acta Physiol Scand*, **58**, 292-305.

CUNNINGHAM VJ. & JONES T. (1993). Spectral Analysis of Dynamic PET Studies. *J Cereb Blood Flow Metab*, **13**, 15-23.

CUNNINGHAM VJ. & LAMMERTSA AA. (1994). Radioligand Studies in Brain: Kinetic Analysis of PET Data. *Med Chem Res*, **5**, 79-96.

DAHLBOM, M. & HOFFMAN, E.J. (1988). An evaluation of a two-dimensional array detector for high resolution PET. *IEEE Trans Med Imaging*, **7**, 264-72.

DANENBERG, P.V. (1977). Thymidylate synthetase - a target enzyme in cancer chemotherapy. *Biochim Biophys Acta*, **473**, 73-92.

DARK, G.G., HILL, S.A., PRISE, V.E., TOZER, G.M., PETTIT, G.R. & CHAPLIN, D.J. (1997). Combretastatin A-4, an agent that displays potent and selective toxicity toward tumor vasculature. *Cancer Res*, **57**, 1829-34.

DAUBE-WITHERSPOON, M. (1995). Operational Guidelines. In *Principles of Nuclear Medicine*. ed Wagner, B. pp. 343-354: Saunders, WB.

DE GRAMONT, A., FIGER, A., SEYMOUR, M., HOMERIN, M., HMISSI, A., CASSIDY, J., BONI, C., CORTES-FUNES, H., CERVANTES, A., FREYER, G., PAPAMICHAEL, D., LE BAIL, N., LOUVET, C., HENDLER, D., DE BRAUD, F., WILSON, C., MORVAN, F. & BONETTI, A. (2000). Leucovorin and fluorouracil with or without oxaliplatin as first-line treatment in advanced colorectal cancer. *J Clin Oncol*, **18**, 2938-47.

DE JONG, I.J., PRUIM, J., ELSINGA, P.H., JONGEN, M.M., MENSINK, H.J. & VAALBURG, W. (2002a). Visualisation of bladder cancer using (11)C-choline PET: first clinical experience. *Eur J Nucl Med Mol Imaging*, **29**, 1283-8.

DE JONG, I.J., PRUIM, J., ELSINGA, P.H., VAALBURG, W. & MENSINK, H.J. (2002b). Visualization of prostate cancer with 11C-choline positron emission tomography. *Eur Urol*, **42**, 18-23.

DEHDASHTI, F., MINTUN, M.A., LEWIS, J.S., BRADLEY, J., GOVINDAN, R., LAFOREST, R., WELCH, M.J. & SIEGEL, B.A. (2003). In vivo assessment of tumor hypoxia in lung cancer with 60Cu-ATSM. *Eur J Nucl Med Mol Imaging*, **30**, 844-50.

DEHDASHTI, F., MORTIMER, J.E., SIEGEL, B.A., GRIFFETH, L.K., BONASERA, T.J., FUSSELMAN, M.J., DETERT, D.D., CUTLER, P.D., KATZENELLENBOGEN, J.A. & WELCH, M.J. (1995). Positron tomographic assessment of estrogen receptors in breast cancer: comparison with FDG-PET and in vitro receptor assays. *J Nucl Med*, **36**, 1766-74.

DI CHIRO, G. (1985). Brain imaging of glucose utilization in cerebral tumors. *Res Publ Assoc Res Nerv Ment Dis*, **63**, 185-97.

DI CHIRO, G., DELAPAZ, R.L., BROOKS, R.A., SOKOLOFF, L., KORNBLITH, P.L., SMITH, B.H., PATRONAS, N.J., KUFTA, C.V., KESSLER, R.M., JOHNSTON, G.S., MANNING, R.G. & WOLF, A.P. (1982). Glucose utilization of cerebral gliomas measured by [18F] fluorodeoxyglucose and positron emission tomography. *Neurology*, **32**, 1323-9.

DIMITRAKOPOULO-STRAUSS A., STRAUSS L., SCHLAG P., HOHENBERDER P., MOHLER M. & COBERDORFER F. (1998). Fluorine-18-Fluorouracil to Predict Therapy Response in Liver Metastases from Colorectal Cancer. *Journal Nuclear Medicine*, **39**, 1197-1202.

DIMITRAKOPOULOU, A., STRAUSS, L.G., CLORIUS, J.H., OSTERTAG, H., SCHLAG, P., HEIM, M., OBERDORFER, F., HELUS, F., HABERKORN, U. & VAN KAICK, G. (1993). Studies with positron emission tomography after systemic administration of fluorine-18-uracil in patients with liver metastases from colorectal carcinoma. *J Nucl Med*, **34**, 1075-81.

DIRAC, P. (1930). A theory of electrons and protons. *Proc Roy Soc A*, **126**, 360-365.

DOUILLARD, J.Y., CUNNINGHAM, D., ROTH, A.D., NAVARRO, M., JAMES, R.D., KARASEK, P., JANDIK, P., IVESON, T., CARMICHAEL, J., ALAKL, M., GRUIA, G., AWAD, L. & ROUGIER, P. (2000). Irinotecan combined with fluorouracil compared with fluorouracil alone as first-line treatment for metastatic colorectal cancer: a multicentre randomised trial. *Lancet*, **355**, 1041-7.

DUNN, T.J., BRAUN, R.D. & RHEUMS, W.E. (1999). The effects of hyperoxic and hypercarbic gases on tumour blood flow. *British Journal of Cancer.*, **80**, 117-26.

EARY, J.F., MANKOFF, D.A., SPENCE, A.M., BERGER, M.S., OLSHEN, A., LINK, J.M., O'SULLIVAN, F. & KROHN, K.A. (1999). 2-[C-11]thymidine imaging of malignant brain tumors. *Cancer Res*, **59**, 615-21.

ELIAS, L. & CRISSMAN, H.A. (1988). Interferon effects upon the adenocarcinoma 38 and HL-60 cell lines: antiproliferative responses and synergistic interactions with halogenated pyrimidine antimetabolites. *Cancer Res*, **48**, 4868-73.

ELIAS, L. & SANDOVAL, J.M. (1989). Interferon effects upon fluorouracil metabolism by HL-60 cells. *Biochem Biophys Res Commun*, **163**, 867-74.

ELSINGA, P.H., FRANSSEN, E.J., HENDRIKSE, N.H., FLUKS, L., WEEMAES, A.M., VAN DER GRAAF, W.T., DE VRIES, E.G., VISSER, G.M. & VAALBURG, W. (1996). Carbon-11-labeled daunorubicin and verapamil for probing P-glycoprotein in tumors with PET. *J Nucl Med*, **37**, 1571-5.

ERLICHMAN, C., FINE, S. & ELHAKIM, T. (1986). Plasma pharmacokinetics of 5-FU given by continuous infusion with allopurinol. *Cancer Treat Rep*, **70**, 903-4.

EVAN, G.I. & VOUSDEN, K.H. (2001). Proliferation, cell cycle and apoptosis in cancer. *Nature*, **411**, 342-8.

FALK S., WARD R. & BLEEMAN N. (1995). The influence of carbogen breathing on tumour tissue oxygenation in man evaluated by computerised $P0_2$ histography. *Br J Cancer*, **66**, 912-24.

FELDMAN, L.D., HORTOBAGYI, G.N., BUZDAR, A.U., AMES, F.C. & BLUMENSCHEIN, G.R. (1986). Pathological assessment of response to induction chemotherapy in breast cancer. *Cancer Res*, **46**, 2578-81.

FERRARA, N. (2002). VEGF and the quest for tumour angiogenesis factors. *Nat Rev Cancer*, **2**, 795-803.

FLANAGAN, F.L., DEHDASHTI, F. & SIEGEL, B.A. (1998). PET in breast cancer. *Semin Nucl Med*, **28**, 290-302.

FOCHER, F. & SPADARI, S. (2001). Thymidine phosphorylase: a two-face Janus in anticancer chemotherapy. *Curr Cancer Drug Targets*, **1**, 141-53.

FOLKMAN, J. (1971). Tumor angiogenesis: therapeutic implications. *N Engl J Med*, **285**, 1182-6.

FOLKMAN, J. (1990). What is the evidence that tumors are angiogenesis dependent? *J Natl Cancer Inst*, **82**, 4-6.

FOLKMAN, J. & INGBER, D. (1992). Inhibition of angiogenesis. *Semin Cancer Biol*, **3**, 89-96.

FOX, S.B., MOGHADDAM, A., WESTWOOD, M., TURLEY, H., BICKNELL, R., GATTER, K.C. & HARRIS, A.L. (1995). Platelet-derived endothelial cell growth factor/thymidine phosphorylase expression in normal tissues: an immunohistochemical study. *J Pathol*, **176**, 183-90.

FRACKOWIAK, R.S., LENZI, G.L., JONES, T. & HEATHER, J.D. (1980). Quantitative measurement of regional cerebral blood flow and oxygen metabolism in man using 15O and positron emission tomography: theory, procedure, and normal values. *J Comput Assist Tomogr*, **4**, 727-36.

GAMBHIR, S.S. (2002). Molecular imaging of cancer with positron emission tomography. *Nat Rev Cancer*, **2**, 683-93.

GAMBHIR, S.S., HERSCHMAN, H.R., CHERRY, S.R., BARRIO, J.R., SATYAMURTHY, N., TOYOKUNI, T., PHELPS, M.E., LARSON, S.M., BALATONI, J., FINN, R., SADELAIN, M., TJUVAJEV, J. & BLASBERG, R. (2000). Imaging transgene expression with radionuclide imaging technologies. *Neoplasia*, **2**, 118-38.

GANONG WF. (2001). Chapter 29: The heart as a pump. In *Review of Medical Physiology*. ed Ganong WF.: Lange Medical Books/McGraw-Hill Medical Publishing Division.

GERMANN, U.A., PASTAN, I. & GOTTESMAN, M.M. (1993). P-glycoproteins: mediators of multidrug resistance. *Semin Cell Biol*, **4**, 63-76.

GILLIES, R.J. (2002). In vivo molecular imaging. *J Cell Biochem Suppl*, **39**, 231-8.

GLASER, M., COLLINGRIDGE, D.R., ABOAGYE, E.O., BOUCHIER-HAYES, L., HUTCHINSON, O.C., MARTIN, S.J., PRICE, P., BRADY, F. & LUTHRA, S.K. (2003). Iodine-124 labelled annexin-V as a potential radiotracer to study apoptosis using positron emission tomography. *Appl Radiat Isot*, **58**, 55-62.

GOETHALS, P., VAN EIJKEREN, M. & LEMAHIEU, I. (1999). In vivo distribution and identification of ^{11}C-activity after injection of [methyl-^{11}C]thymidine in Wistar rats. *J Nucl Med*, **40**, 491-6.

GOTTESMAN, M.M. & PASTAN, I. (1993). Biochemistry of multidrug resistance mediated by the multidrug transporter. *Annu Rev Biochem*, **62**, 385-427.

GRAU, C., HORSMAN, M.R. & OVERGAARD, J. (1992). Improving the radiation response in a C3H mouse mammary carcinoma by normobaric oxygen or carbogen breathing. *Int J Radiat Oncol Biol Phys*, **22**, 415-9.

GRAY, L.H., CONGER, A.D., EBERT, M., HORNSEY, S. & SCOTT, O.C. (1953). The concentration of oxygen dissolved in tissues at the time of irradiation as a factor in radiotherapy. *Br J Radiol*, **26**, 638-48.

GREINWALD, J.H., JR., BURKE, D.K., BONTHIUS, D.J., BAUMAN, N.M. & SMITH, R.J. (1999). An update on the treatment of hemangiomas in children with interferon alfa-2a. *Arch Otolaryngol Head Neck Surg*, **125**, 21-7.

GREM, J.L., VAN GROENINGEN, C.J., ISMAIL, A.A., JOHNSTON, P.G., ALEXANDER, H.R. & ALLEGRA, C.J. (1995). The role of interferon-alpha as a modulator of fluorouracil and leucovorin. *Eur J Cancer*, **31A**, 1316-20.

GRIFFITHS, J.R., TAYLOR, N.J., HOWE, F.A., SAUNDERS, M.I., ROBINSON, S.P., HOSKIN, P.J., POWELL, M.E., THOUMINE, M., CAINE, L.A. & BADDELEY, H. (1997). The response of human tumors to carbogen breathing, monitored by Gradient-Recalled Echo Magnetic Resonance Imaging. *Int J Radiat Oncol Biol Phys*, **39**, 697-701.

GRIFFITHS JR., MCINTYRE D., HOWE FA., MCSHEEHY PM., OJUGO A., RODRIGUES LM., WADSWORT P., PRICE NP., LOFTS F., NICHOLSON G., SMID K., NOORDHIUS P., PETERS JP. & STUBBS M. (2001). Issues of Normal Tissue Toxicity in Patients and Animal Studies

Effect of Carbogen Breathing after 5-Fluorouracil Treatment. *Acta Oncologica*, **40**, 609-614.

GRIGGS, J., METCALFE, J.C. & HESKETH, R. (2001). Targeting tumour vasculature: the development of combretastatin A4. *Lancet Oncol*, **2**, 82-87.

GROOT-WASSINK, T., ABOAGYE, E.O., GLASER, M., LEMOINE, N.R. & VASSAUX, G. (2002). Adenovirus biodistribution and noninvasive imaging of gene expression in vivo by positron emission tomography using human sodium/iodide symporter as reporter gene. *Hum Gene Ther*, **13**, 1723-35.

GROOTOONK, S., SPINKS, T., T., J., MICHEL, C. & BOL, A. (1992). Correction for Scatter Using a Dual Energy WindowTechnique with a Tomograph Operating Without Septa. *IEEE 1991 Mediacl Imaging Conference Record*, 1569-1573.

GUDJONSSONA, O., BERGSTROM, M., KRISTJANSSON, S., WU, F., NYBERG, G., FASTH, K.J. & LANGSTROM, B. (2001). Analysis of 76Br-BrdU in DNA of brain tumors after a PET study does not support its use as a proliferation marker. *Nucl Med Biol*, **28**, 59-65.

GUENTHER, I., WYER, L., KNUST, E.J., FINN, R.D., KOZIOROWSKI, J. & WEINREICH, R. (1998). Radiosynthesis and quality assurance of 5-[124I]Iodo-2'-deoxyuridine for functional PET imaging of cell proliferation. *Nucl Med Biol*, **25**, 359-65.

GUNN R., YAPP J., WELLS P., OSMAN S., PRICE P., JONES V. & CUNNINGHAM VJ. (2000). A General Method to Correct PET Data for Tissue Metabolutes Using a Dual-Scan Approach. *J Nucl Med*, **41**, 706-11.

GUNN, R.N., SARGENT, P.A., BENCH, C.J., RABINER, E.A., OSMAN, S., PIKE, V.W., HUME, S.P., GRASBY, P.M. & LAMMERTSMA, A.A. (1998). Tracer kinetic modeling of the 5-HT1A receptor ligand [carbonyl-11C]WAY-100635 for PET. *Neuroimage*, **8**, 426-40.

GUYTON, A.C. & HALL, J.E. (1996). Local control of blood flow by the tissues, and humoral regulations. In *Textbook of medical physiology*. Philadelphia:
:
WB Saunders Company.

HARRIS BE., SONG R., SOONG SJ. & DIASIO RB. (1988). Relationship between dihdrpyrimidine dehydrogenase activity and plasma 5-fluorouracil levels with evidence for circadian variation of enzyme activity and plasma drug levels in cancer patients receiving 5-fluorouracil by protracted continuous infusion. *Cancer Research*, **50**, 197-201.

HARTE R., MATHEWS J., O'REILLY S. & PRICE P. (1998). Sources of Error in the Tissue and Tumor Measurements of 5-[^{18}F]Fluorouracil. *The Journal of Nuclear Medicine*, **39**, 1370-76.

HARTE R., MATHEWS J., O'REILLY., TILSEY O., OSMAN S., BROWN G., LUTHRA S., BRADY F., JONES T. & PRICE P. (1999). Tumour, Normal Tissue and Plasma Pharmacokinetic Studies of Fluorouracil Biomodulation With N-Phosphonoacetyl-L-aspartate, Folnic Acid and Inerferon Alpha. *Journal of Clinical Oncology*, **17**, 1580-89.

HAUBNER, R., WESTER, H.J., WEBER, W.A., MANG, C., ZIEGLER, S.I., GOODMAN, S.L., SENEKOWITSCH-SCHMIDTKE, R., KESSLER, H. & SCHWAIGER, M. (2001). Noninvasive imaging of alpha(v)beta3 integrin expression using 18F-labeled RGD-containing glycopeptide and positron emission tomography. *Cancer Res*, **61**, 1781-5.

HEGGIE G., SOMMADOSSI J., CROSS D., HUSTER W. & R., D. (1987). Clinical Pharmacokinetics of 5-fluorouracil and its metabolites in plasma, urine and bile. *Cancer Research*, **47**, 2203-06.

HENDRIKSE, N.H., FRANSSEN, E.J., VAN DER GRAAF, W.T., VAALBURG, W. & DE VRIES, E.G. (1999). Visualization of multidrug resistance in vivo. *Eur J Nucl Med*, **26**, 283-93.

HENZE, M., SCHUHMACHER, J., HIPP, P., KOWALSKI, J., BECKER, D.W., DOLL, J., MACKE, H.R., HOFMANN, M., DEBUS, J. & HABERKORN, U. (2001). PET imaging of somatostatin receptors using [68GA]DOTA-D-Phe1-Tyr3-octreotide: first results in patients with meningiomas. *J Nucl Med*, **42**, 1053-6.

HERSCOVITCH, P. & RAICHLE, M.E. (1983). Effect of tissue heterogeneity on the measurement of cerebral blood flow with the equilibrium C15O2 inhalation technique. *J Cereb Blood Flow Metab*, **3**, 407-15.

HIRST, D.G., KENNOVIN, G.D. & FLITNEY, F.W. (1994). The radiosensitizer nicotinamide inhibits arterial vasoconstriction. *Br J Radiol*, **67**, 795-9.

HOCKEL, M., SCHLENGER, K., ARAL, B., MITZE, M., SCHAFFER, U. & VAUPEL, P. (1996). Association between tumor hypoxia and malignant progression in advanced cancer of the uterine cervix. *Cancer Res*, **56**, 4509-15.

HONESS, D.J. & BLEEHEN, N.M. (1995). Perfusion changes in the RIF-1 tumour and normal tissues after carbogen and nicotinamide, individually and combined. *British Journal of Cancer*, **71**, 1175-80.

HOSKIN, P.J., SAUNDERS, M.I. & DISCHE, S. (1999). Hypoxic radiosensitizers in radical radiotherapy for patients with bladder carcinoma: hyperbaric oxygen, misonidazole, and accelerated radiotherapy, carbogen, and nicotinamide. *Cancer*, **86**, 1322-8.

HOUGHTON, J.A., MORTON, C.L., ADKINS, D.A. & RAHMAN, A. (1993). Locus of the interaction among 5-fluorouracil, leucovorin, and interferon-alpha 2a in colon carcinoma cells. *Cancer Res*, **53**, 4243-50.

HOUGHTON, J.A., TILLMAN, D.M. & HARWOOD, F.G. (1995). Ratio of 2'-deoxyadenosine-5'-triphosphate/thymidine-5'-triphosphate influences the commitment of human colon carcinoma cells to thymineless death. *Clin Cancer Res*, **1**, 723-30.

INOUE, T., KIM, E.E., WALLACE, S., YANG, D.J., WONG, F.C., BASSA, P., BUZDAR, A.U. & PODOLOFF, D.A. (1997). Preliminary study of cardiac accumulation of F-18 fluorotamoxifen in patients with breast cancer. *Clin Imaging*, **21**, 332-6.

ISAACS, A. & LINDENMAN, J. (1957). Virus Interference 1: The interferon. *Proc R Soc*, **147**, 258-267.

JACOBS, A., VOGES, J., RESZKA, R., LERCHER, M., GOSSMANN, A., KRACHT, L., KAESTLE, C., WAGNER, R., WIENHARD, K. & HEISS, W.D. (2001). Positron-emission tomography of vector-mediated gene expression in gene therapy for gliomas. *Lancet*, **358**, 727-9.

JAMAR F., LENERS N., LABAR D. & A., F. (1992). (2-11C)-Thymidine PET can in non-Hodgkins lymphoma. *Eur J Nucl Med*, **8**, 693.

JIRTLE, R.L. (1988). Chemical modification of tumour blood flow. *Int J Hyperthermia*, **4**, 355-71.

JONASCH, E. & HALUSKA, F.G. (2001). Interferon in oncological practice: review of interferon biology, clinical applications, and toxicities. *Oncologist*, **6**, 34-55.

KAANDERS, J.H., BUSSINK, J. & VAN DER KOGEL, A.J. (2002). ARCON: a novel biology-based approach in radiotherapy. *Lancet Oncol*, **3**, 728-37.

KAK, A.C. & SLANCY, M. (1988). *Principles of Computerised Tomographic Imaging*. New York.

KENNY, L., COOMBES, R.C., VIGUSHIN, D.M., AL-NAHHAS, A., SHOUSHA, S. & ABOAGYE, E.O. (2007). Imaging early changes in proliferation at 1 week post chemotherapy: a pilot study in breast cancer patients with 3'-deoxy-3'-[18F]fluorothymidine positron emission tomography. *Eur J Nucl Med Mol Imaging*, **34**, 1339-47.

KENNY, L.M., VIGUSHIN, D.M., AL-NAHHAS, A., OSMAN, S., LUTHRA, S.K., SHOUSHA, S., COOMBES, R.C. & ABOAGYE, E.O. (2005). Quantification of cellular proliferation in tumor and normal tissues of patients with breast cancer by [18F]fluorothymidine-positron emission tomography imaging: evaluation of analytical methods. *Cancer Res*, **65**, 10104-12.

KETY S. & SCHMIDT C. (1948). The effects of altered tensions of carbon dioxide and oxygen on cerebral blood flow and cerebral oxygen consumption of normal young men. *J Clinical Investigation*, **27**, 484-492.

KETY, S.S. (1965). Measurement of local contribution within the brain by means of inert, diffusible tracers; examination of the theory, assumptions and possible sources of error. *Acta Neurol Scand Suppl*, **14**, 20-3.

KETY, S.S. & SCHMIDT, C.F. (1948). The Nitrous Oxide Method for the Quantitative Determination of Cerebral Blood Flow in Man: Theory, Procedure and Normal Values. *J Clin Invest*, **27**, 476-83.

KHALIL, A.A., HORSMAN, M.R. & OVERGAARD, J. (1995). The importance of determining necrotic fraction when studying the effect of tumour volume on tissue oxygenation. *Acta Oncol*, **34**, 297-300.

KIMURA, H., BRAUN, R.D., ONG, E.T., HSU, R., SECOMB, T.W., PAPAHADJOPOULOS, D., HONG, K. & DEWHIRST, M.W. (1996). Fluctuations in red cell flux in tumor microvessels can lead to transient hypoxia and reoxygenation in tumor parenchyma. *Cancer Res*, **56**, 5522-8.

KISSEL, J., G. BRIX, M. BELLMAN, L. STRAUSS, A. DIMITRAKOPOULO-STRAUSS, R.PORT, U.HABERKORN & J.LORENZ. (1997). Pharmacokinetic Analysis of 5-[^{18}F]Fluorouracil Tissue Concentarions Measured with Positron Emission Tomogragphy in Patients with Liver Metastasis from Colorectal Adenoma. *Cancer Research*, **57**, 3415-423.

KROHN, K.A. (2001). Evaluation of alternative approaches for imaging cellular growth. *Q J Nucl Med*, **45**, 174-8.

KRUUV, J.A., INCH, W.R. & MCCREDIE, J.A. (1967). Blood flow and oxygenation of tumors in mice. I. Effects of breathing gases containing carbon dioxide at atmospheric pressure. *Cancer*, **20**, 51-9.

KUBOTA, R., YAMADA, S., KUBOTA, K., ISHIWATA, K., TAMAHASHI, N. & IDO, T. (1992). Intratumoral distribution of fluorine-18-fluorodeoxyglucose in vivo: high accumulation in macrophages and granulation tissues studied by microautoradiography. *J Nucl Med*, **33**, 1972-80.

LAMMERTSMA, A.A. (1987). Positron emission tomography and in vivo measurements of tumour perfusion and oxygen utilisation. *Cancer Metastasis Rev*, **6**, 521-39.

LAMMERTSMA, A.A. & JONES, T. (1992). Low oxygen extraction fraction in tumours measured with the oxygen-15 steady state technique: effect of tissue heterogeneity. *Br J Radiol*, **65**, 697-700.

LAMMERTSMA, A.A., JONES, T., FRACKOWIAK, R.S. & LENZI, G.L. (1981). A theoretical study of the steady-state model for measuring regional cerebral

blood flow and oxygen utilisation using oxygen-15. *J Comput Assist Tomogr*, **5**, 544-50.

LANDAU, W.M., FREYGANG, W.H., JR., ROLAND, L.P., SOKOLOFF, L. & KETY, S.S. (1955). The local circulation of the living brain; values in the unanesthetized and anesthetized cat. *Trans Am Neurol Assoc*, 125-9.

LARSON, S.M. (2002). Measuring Response to Treatment with Molecular Imaging. *Eur J Cancer*, **Spplement 7**, S12.

LARSON SM., GRUNBAUM Z., AND & JS., R. (1980). Positron imaging feasability studies: selective tumour concentration of ^{3}H-thymidine, ^{3}H-uridine and ^{14}C-2-deoxyglucose. *Radiology*, **134**, 771-3.

LARSON SM., WEIDEN PL. & ET AL. (1981). Characteristics of [^{3}H]thymidine uptake in rodent and canine neoplasms; Concise Communication. *J Nucl Med*, **22**, 869-74.

LEICHMAN, C.G. (1999). Schedule dependency of 5-fluorouracil. *Oncology (Williston Park)*, **13**, 26-32.

LEVCHENKO, A., MEHTA, B.M., LEE, J.B., HUMM, J.L., AUGENSEN, F., SQUIRE, O., KOTHARI, P.J., FINN, R.D., LEONARD, E.F. & LARSON, S.M. (2000). Evaluation of 11C-colchicine for PET imaging of multiple drug resistance. *J Nucl Med*, **41**, 493-501.

LEVI, F., GIACCHETTI, S., ADAM, R., ZIDANI, R., METZGER, G. & MISSET, J.L. (1995). Chronomodulation of chemotherapy against metastatic colorectal cancer. International Organization for Cancer Chronotherapy. *Eur J Cancer*, **31A**, 1264-70.

LEWIS, J.S., MCCARTHY, D.W., MCCARTHY, T.J., FUJIBAYASHI, Y. & WELCH, M.J. (1999). Evaluation of 64Cu-ATSM in vitro and in vivo in a hypoxic tumor model. *J Nucl Med*, **40**, 177-83.

LEWIS, J.S., SHARP, T.L., LAFOREST, R., FUJIBAYASHI, Y. & WELCH, M.J. (2001a). Tumor uptake of copper-diacetyl-bis(N(4)-methylthiosemicarbazone): effect of changes in tissue oxygenation. *J Nucl Med*, **42**, 655-61.

LEWIS, J.S. & WELCH, M.J. (2001b). PET imaging of hypoxia. *Q J Nucl Med*, **45**, 183-8.

LIU, A., CARLSON, K.E. & KATZENELLENBOGEN, J.A. (1992). Synthesis of high affinity fluorine-substituted ligands for the androgen receptor. Potential agents for imaging prostatic cancer by positron emission tomography. *J Med Chem*, **35**, 2113-29.

LOKICH, J.J., AHLGREN, J.D., GULLO, J.J., PHILIPS, J.A. & FRYER, J.G. (1989). A prospective randomized comparison of continuous infusion fluorouracil with a conventional bolus schedule in metastatic colorectal carcinoma: a Mid-Atlantic Oncology Program Study. *J Clin Oncol*, **7**, 425-32.

LONGLEY, D.B., LATIF, T., BOYER, J., ALLEN, W.L., MAXWELL, P.J. & JOHNSTON, P.G. (2003). The interaction of thymidylate synthase expression with p53-regulated signaling pathways in tumor cells. *Semin Oncol*, **30**, 3-9.

LONNEUX M., LABAR D., BOL A., JAMAR F. & S., P. (1996). Uptake of 2-11-C thymdine in colonic and bronchial tumors. In *Proc Eur Con Res Appl PET in Onc*. Groningen, Netherlands: PET Centrum AZG.

LOVQVIST, A., SUNDIN, A., AHLSTROM, H., CARLSSON, J. & LUNDQVIST, H. (1995). 76Br-labeled monoclonal anti-CEA antibodies for radioimmuno positron emission tomography. *Nucl Med Biol*, **22**, 125-31.

LOVQVIST, A., SUNDIN, A., AHLSTROM, H., CARLSSON, J. & LUNDQVIST, H. (1997). Pharmacokinetics and experimental PET imaging of a bromine-76-labeled monoclonal anti-CEA antibody. *J Nucl Med*, **38**, 395-401.

LUCIGNANI, G., LOSA, M., MORESCO, R.M., DEL SOLE, A., MATARRESE, M., BETTINARDI, V., MORTINI, P., GIOVANELLI, M. & FAZIO, F. (1997). Differentiation of clinically non-functioning pituitary adenomas from meningiomas and craniopharyngiomas by positron emission tomography with [18F]fluoro-ethyl-spiperone. *Eur J Nucl Med*, **24**, 1149-55.

MACLAREN, D.C., GAMBHIR, S.S., SATYAMURTHY, N., BARRIO, J.R., SHARFSTEIN, S., TOYOKUNI, T., WU, L., BERK, A.J., CHERRY, S.R., PHELPS, M.E. & HERSCHMAN, H.R. (1999). Repetitive, non-invasive imaging of the dopamine D2 receptor as a reporter gene in living animals. *Gene Ther*, **6**, 785-91.

MAKOWER, D., WADLER, S., HAYNES, H. & SCHWARTZ, E.L. (1997). Interferon induces thymidine phosphorylase/platelet-derived endothelial cell growth factor expression in vivo. *Clin Cancer Res*, **3**, 923-9.

MANKOFF, D.A., DEHDASHTI, F. & SHIELDS, A.F. (2000). Characterizing tumors using metabolic imaging: PET imaging of cellular proliferation and steroid receptors. *Neoplasia*, **2**, 71-88.

MANKOFF, D.A., SHIELDS, A.F., GRAHAM, M.M., LINK, J.M., EARY, J.F. & KROHN, K.A. (1998). Kinetic analysis of 2-[carbon-11]thymidine PET imaging studies: compartmental model and mathematical analysis. *J Nucl Med*, **39**, 1043-55.

MANKOFF, D.A., SHIELDS, A.F., GRAHAM, M.M., LINK, J.M. & KROHN, K.A. (1996). A graphical analysis method to estimate blood-to-tissue transfer constants for tracers with labeled metabolites. *J Nucl Med*, **37**, 2049-57.

MANKOFF, D.A., SHIELDS, A.F., LINK, J.M., GRAHAM, M.M., MUZI, M., PETERSON, L.M., EARY, J.F. & KROHN, K.A. (1999). Kinetic analysis of 2-[11C]thymidine PET imaging studies: validation studies. *J Nucl Med*, **40**, 614-24.

MARCHETTI, S., CHAZAL, M., DUBREUIL, A., FISCHEL, J.L., ETIENNE, M.C. & MILANO, G. (2001). Impact of thymidine phosphorylase surexpression on fluoropyrimidine activity and on tumour angiogenesis. *Br J Cancer*, **85**, 439-45.

MARTIAT, P., FERRANT, A., LABAR, D., COGNEAU, M., BOL, A., MICHEL, C., MICHAUX, J.L. & SOKAL, G. (1988). In vivo measurement of carbon-11 thymidine uptake in non-Hodgkin's lymphoma using positron emission tomography. *J Nucl Med*, **29**, 1633-7.

MCGUIRE, W.L., CHAMNESS, G.C. & FUQUA, S.A. (1991). Estrogen receptor variants in clinical breast cancer. *Mol Endocrinol*, **5**, 1571-7.

MCSHEEHY, P.M., ROBINSON, S.P., OJUGO, A.S., ABOAGYE, E.O., CANNELL, M.B., LEACH, M.O., JUDSON, I.R. & GRIFFITHS, J.R. (1998). Carbogen breathing increases 5-fluorouracil uptake and cytotoxicity in hypoxic murine RIF-1 tumors: a magnetic resonance study in vivo. *Cancer Res*, **58**, 1185-94.

MCSHEEHY, P.M., STUBBS, M. & GRIFFITHS, J.R. (2000). Role of pH in tumor-trapping of the anticancer drug 5-fluorouracil. *Advances in Enzyme Regulation.*, **40**, 63-80.

MEIKLE SR., MATHEWS JC., BROCK CS., WELLS PP., HARTE RAJ., CUNNINGHAM VJ., JONES T. & PRICE P. (1998). Pharmacokinetic assessment of novel

anti-cancer drugs using spectral analysis and positron emission tomography: A feasability study. *Cancer Chemother Pharmacol*, **42**, 183-93.

META-ANALYSIS & CANCER, G.I. (1998). Efficacy of Intravenous Continous Infusion of Fluorouracil Compared with Bolus Administration in Advanced Colorectal Cancer. *Journal of Clinical Oncology*, **16**, 301-8.

METZGER, R., DANENBERG, K., LEICHMAN, C.G., SALONGA, D., SCHWARTZ, E.L., WADLER, S., LENZ, H.J., GROSHEN, S., LEICHMAN, L. & DANENBERG, P.V. (1998). High basal level gene expression of thymidine phosphorylase (platelet-derived endothelial cell growth factor) in colorectal tumors is associated with nonresponse to 5-fluorouracil. *Clin Cancer Res*, **4**, 2371-6.

MILANO, G., FISCHEL, J.L., ETIENNE, M.C., RENEE, N., FORMENTO, P., THYSS, A., GASPARD, M.H., THILL, L. & CUPISSOL, D. (1994). Inhibition of dihydropyrimidine dehydrogenase by alpha-interferon: experimental data on human tumor cell lines. *Cancer Chemother Pharmacol*, **34**, 147-52.

MILLER, K.D., SWEENEY, C.J. & SLEDGE, G.W., JR. (2001). Redefining the target: chemotherapeutics as antiangiogenics. *J Clin Oncol*, **19**, 1195-206.

MIYADERA, K., SUMIZAWA, T., HARAGUCHI, M., YOSHIDA, H., KONSTANTY, W., YAMADA, Y. & AKIYAMA, S. (1995). Role of thymidine phosphorylase activity in the angiogenic effect of platelet derived endothelial cell growth factor/thymidine phosphorylase. *Cancer Res*, **55**, 1687-90.

MOGHADDAM, A. & BICKNELL, R. (1992). Expression of platelet-derived endothelial cell growth factor in Escherichia coli and confirmation of its thymidine phosphorylase activity. *Biochemistry*, **31**, 12141-6.

MOOLTEN, F.L. (1994). Drug sensitivity ("suicide") genes for selective cancer chemotherapy. *Cancer Gene Ther*, **1**, 279-87.

MORESCO, R.M., SCHEITHAUER, B.W., LUCIGNANI, G., LOMBARDI, D., ROCCA, A., LOSA, M., CASATI, R., GIOVANELLI, M. & FAZIO, F. (1997). Oestrogen receptors in meningiomas: a correlative PET and immunohistochemical study. *Nucl Med Commun*, **18**, 606-15.

MORTIMER, J.E., DEHDASHTI, F., SIEGEL, B.A., KATZENELLENBOGEN, J.A., FRACASSO, P. & WELCH, M.J. (1996). Positron emission tomography with 2-[18F]Fluoro-2-deoxy-D-glucose and 16alpha-[18F]fluoro-17beta-estradiol in breast cancer: correlation with estrogen receptor status and response to systemic therapy. *Clin Cancer Res*, **2**, 933-9.

MOTTRAM, J.C. (1936). A factor of importance in the radiotherapy of tumours. *Bri J Radiol*, **9**, 606-614.

MUNCH-PETERSEN, B., CLOOS, L., TYRSTED, G. & ERIKSSON, S. (1991). Diverging substrate specificity of pure human thymidine kinases 1 and 2 against antiviral dideoxynucleosides. *J Biol Chem*, **266**, 9032-8.

NAGUIB, F.N., EL KOUNI, M.H. & CHA, S. (1985). Enzymes of uracil catabolism in normal and neoplastic human tissues. *Cancer Res*, **45**, 5405-12.

NELSON, C.A., WANG, J.Q., LEAV, I. & CRANE, P.D. (1996). The interaction among glucose transport, hexokinase, and glucose-6-phosphatase with respect to 3H-2-deoxyglucose retention in murine tumor models. *Nucl Med Biol*, **23**, 533-41.

O'BRIEN, T.S., FOX, S.B., DICKINSON, A.J., TURLEY, H., WESTWOOD, M., MOGHADDAM, A., GATTER, K.C., BICKNELL, R. & HARRIS, A.L. (1996). Expression of the angiogenic factor thymidine phosphorylase/platelet-

derived endothelial cell growth factor in primary bladder cancers. *Cancer Res*, **56**, 4799-804.

OHTANI, T., KURIHARA, H., ISHIUCHI, S., SAITO, N., ORIUCHI, N., INOUE, T. & SASAKI, T. (2001). Brain tumour imaging with carbon-11 choline: comparison with FDG PET and gadolinium-enhanced MR imaging. *Eur J Nucl Med*, **28**, 1664-70.

OJUGO ASE., MCSHEEHY PM., STUBBS M., ALDER G., BASHFORD CL., MAXWELL RJ., LEACH MO., JUDSON IR. & JR., G. (1998). Influence of pH on the uptake of 5-fluorouracil into isolated tumour cells. *British Journal of Cancer*, **77**, 873-79.

OLLINGER, J. & FESSLER, J. (1997). Positron-Emission Tomography. *IEEE Signal Processing Magazine*, 43-55.

PATLAK CS., BLASBERG RG. & FENSTERMACHER JD. (1983). Graphical evaluation of blood to brain transfer constants from multiple time uptake data. *J Cereb Blood Flow Metab*, **3**, 1-7.

PATT, Y.Z., HOQUE, A., LOZANO, R., POZDUR, R., CHASE, J., CARRASCO, H., CHUANG, V., DELPASSAND, E.S., ELLIS, L., CURLEY, S., ROH, M. & JONES, D.V., JR. (1997). Phase II trial of hepatic arterial infusion of fluorouracil and recombinant human interferon alfa-2b for liver metastases of colorectal cancer refractory to systemic fluorouracil and leucovorin. *J Clin Oncol*, **15**, 1432-8.

PAZDUR, R., AJANI, J.A., PATT, Y.Z., WINN, R., JACKSON, D., SHEPARD, B., DUBROW, R., CAMPOS, L., QUARAISHI, M., FAINTUCH, J. & ET AL. (1990). Phase II study of fluorouracil and recombinant interferon alfa-2a in previously untreated advanced colorectal carcinoma. *J Clin Oncol*, **8**, 2027-31.

PELLAT-DECEUNYNCK, C., WIETZERBIN, J. & DRAPIER, J.C. (1994). Nicotinamide inhibits nitric oxide synthase mRNA induction in activated macrophages. *Biochem J*, **297 (Pt 1)**, 53-8.

PELLETIER, J. & SONENBERG, N. (1988). Internal initiation of translation of eukaryotic mRNA directed by a sequence derived from poliovirus RNA. *Nature*, **334**, 320-5.

PETERS CE., CHAPLIN D. & HIRST DG. (1997). Nicotinamide reduces interstitial fluid pressure in a dose- and time-dependant manner. *British Journal of Radiology*, **70**, 160-7.

PETERS, G.J., LANKELMA, J., KOK, R.M., NOORDHUIS, P., VAN GROENINGEN, C.J., VAN DER WILT, C.L., MEYER, S. & PINEDO, H.M. (1993). Prolonged retention of high concentrations of 5-fluorouracil in human and murine tumors as compared with plasma. *Cancer Chemother Pharmacol*, **31**, 269-76.

PHELPS, M.E., HOFFMAN, E.J., HUANG, S.-C. & TER-POGOSSIAN, M.M. (1975). Effect of Positron Range on Spatial Resolution. pp. 649-652.

PHILIPS, F.S., FEINBERG, A., CHOU, T.C., VIDAL, P.M., SU, T.L., WATANABE, K.A. & FOX, J.J. (1983). Distribution, metabolism, and excretion of 1-(2-fluoro-2-deoxy-beta-D- arabinofuranosyl)thymine and 1-(2-fluoro-2-deoxy-beta-D-arabinofuranosyl)-5- iodocytosine. *Cancer Res*, **43**, 3619-27.

PICCHIO, M., LANDONI, C., MESSA, C., GIANOLLI, L., MATARRESE, M., DE COBELLI, F., MASCHIO, A.D. & FAZIO, F. (2002). Positive [11C]choline and negative [18F]FDG with positron emission tomography in recurrence of prostate cancer. *AJR Am J Roentgenol*, **179**, 482-4.

PINEDO, H., PETERS, GF. (1988). Fluorouracil: Biochemistry and Pharmacology. *Journal of Clinical Oncology*, **6**, 1653-1664.

POMPER, M.G., CONSTANTINIDES, C.D., BARKER, P.B., BIZZI, A., DOBGAN, A.S., YOKOI, F., MCARTHUR, J.C. & WONG, D.F. (2002). Quantitative MR spectroscopic imaging of brain lesions in patients with AIDS: correlation with [11C-methyl]thymidine PET and thallium-201 SPECT. *Acad Radiol*, **9**, 398-409.

POWELL, M.E., COLLINGRIDGE, D.R., SAUNDERS, M.I., HOSKIN, P.J., HILL, S.A. & CHAPLIN, D.J. (1999). Improvement in human tumour oxygenation with carbogen of varying carbon dioxide concentrations. *Radiother Oncol*, **50**, 167-71.

POWELL MEB., HILL SA., SAUNDERS MI., HOSKIN PJ. & CHALIN DJ. (1996). Effect of carbogen breathing on tumour microregional blood flow in humans. *Radiotherapy & Oncology.*, **41**, 225-231.

POWELL MEB., HILL SA., SAUNDERS MI., HOSKIN PJ. & CHAPLIN DJ. (1997). Human Tumour Blood Flow is Enhanced by Nicotinamide and Carbogen Breathing. *Cancer Research*, **57**, 5261-4.

PRESANT C., WOLF W., ALBRIGHT M., SERVIS K., RING R., ATKINSON D. & AL., E. (1990). Human tumor fluorouracil trapping: clinical correlations of in vivo 19F nuclear magnetic resonance spectroscopy pharmacokinetics. *Journal of Clinical Oncology*, **8**, 1868-73.

PRESANT C., WOLF W., WALUCH V., WISEMAN C., KENNEDY P., BLAYNEY D. & AL., E. (1994). Association of intratumoural pharmacokinetics of fluorouracil with clinical response. *The Lancet*, **343**, 1184-87.

PRESANT, C.A., WOLF, W., WALUCH, V., WISEMAN, C.L., WEITZ, I. & SHANI, J. (2000). Enhancement of fluorouracil uptake in human colorectal and gastric cancers by interferon or by high-dose methotrexate: An in vivo human study using noninvasive (19)F-magnetic resonance spectroscopy. *J Clin Oncol*, **18**, 255-61.

PRISE, V.E., HONESS, D.J., STRATFORD, M.R., WILSON, J. & TOZER, G.M. (2002). The vascular response of tumor and normal tissues in the rat to the vascular targeting agent, combretastatin A-4-phosphate, at clinically relevant doses. *Int J Oncol*, **21**, 717-26.

RAICHLE, M.E., MARTIN, W.R., HERSCOVITCH, P., MINTUN, M.A. & MARKHAM, J. (1983). Brain blood flow measured with intravenous H2(15)O. II. Implementation and validation. *J Nucl Med*, **24**, 790-8.

RAMIREZ DE MOLINA, A., RODRIGUEZ-GONZALEZ, A., GUTIERREZ, R., MARTINEZ-PINEIRO, L., SANCHEZ, J., BONILLA, F., ROSELL, R. & LACAL, J. (2002). Overexpression of choline kinase is a frequent feature in human tumor-derived cell lines and in lung, prostate, and colorectal human cancers. *Biochem Biophys Res Commun*, **296**, 580-3.

RANICAR ASO., WILLIAMS CW., SCHNORR L. & ET AL. (1991). The on-line monitoring of continuously withdrawn arterial blood during PET studies using a single BGO/photomutiplier assembly and non-stick tubing. *Med Prog Tech*, **17**, 259-64.

RASEY, J.S., GRIERSON, J.R., WIENS, L.W., KOLB, P.D. & SCHWARTZ, J.L. (2002). Validation of FLT Uptake as a Measure of Thymidine Kinase-1 Activity in A549 Carcinoma Cells. *J Nucl Med*, **43**, 1210-1217.

RASEY, J.S., HOFSTRAND, P.D., CHIN, L.K. & TEWSON, T.J. (1999). Characterization of [18F]fluoroetanidazole, a new radiopharmaceutical for detecting tumor hypoxia. *J Nucl Med*, **40**, 1072-9.

RASEY, J.S., KOH, W.J., EVANS, M.L., PETERSON, L.M., LEWELLEN, T.K., GRAHAM, M.M. & KROHN, K.A. (1996). Quantifying regional hypoxia in human tumors with positron emission tomography of [18F]fluoromisonidazole: a pretherapy study of 37 patients. *Int J Radiat Oncol Biol Phys*, **36**, 417-28.

RASEY, J.S., KOH, W.J., GRIERSON, J.R., GRUNBAUM, Z. & KROHN, K.A. (1989). Radiolabelled fluoromisonidazole as an imaging agent for tumor hypoxia. *Int J Radiat Oncol Biol Phys*, **17**, 985-91.

ROBINSON, S.P., HOWE, F.A. & GRIFFITHS, J.R. (1995). Noninvasive monitoring of carbogen-induced changes in tumor blood flow and oxygenation by functional magnetic resonance imaging. *Int J Radiat Oncol Biol Phys*, **33**, 855-9.

ROBINSON, S.P., HOWE, F.A., STUBBS, M. & GRIFFITHS, J.R. (2000). Effects of nicotinamide and carbogen on tumour oxygenation, blood flow, energetics and blood glucose levels. *Br J Cancer*, **82**, 2007-14.

ROBINSON, S.P., RODRIGUES, L.M., GRIFFITHS, J.R. & STUBBS, M. (1999). Response of hepatoma 9618a and normal liver to host carbogen and carbon monoxide breathing. *Neoplasia*, **1**, 537-43.

ROBINSON, S.P., RODRIGUES, L.M., OJUGO, A.S., MCSHEEHY, P.M., HOWE, F.A. & GRIFFITHS, J.R. (1997). The response to carbogen breathing in experimental tumour models monitored by gradient-recalled echo magnetic resonance imaging. *Br J Cancer*, **75**, 1000-6.

RODRIGUES, L.M., MAXWELL, R.J., MCSHEEHY, P.M., PINKERTON, C.R., ROBINSON, S.P., STUBBS, M. & GRIFFITHS, J.R. (1997). In vivo detection of ifosfamide by 31P-MRS in rat tumours: increased uptake and cytotoxicity induced by carbogen breathing in GH3 prolactinomas. *Br J Cancer*, **75**, 62-8.

RODRIGUES, L.M., ROBINSON, S.P., MCSHEEHY, P.M., STUBBS, M. & GRIFFITHS, J.R. (2002). Enhanced uptake of ifosfamide into GH3 prolactinomas with hypercapnic hyperoxic gases monitored in vivo by (31)P MRS. *Neoplasia*, **4**, 539-43.

ROGERS, B.E., MCLEAN, S.F., KIRKMAN, R.L., DELLA MANNA, D., BRIGHT, S.J., OLSEN, C.C., MYRACLE, A.D., MAYO, M.S., CURIEL, D.T. & BUCHSBAUM, D.J. (1999). In vivo localization of [(111)In]-DTPA-D-Phe1-octreotide to human ovarian tumor xenografts induced to express the somatostatin receptor subtype 2 using an adenoviral vector. *Clin Cancer Res*, **5**, 383-93.

ROJAS A., HIRST VK., CALVERT A. & JOHNS H. (1996). Carbogen and nocotinamide as radiosensitisers in a murine mammary carcinoma using conventional and accelerated radiotherapy. *Int J Rad Oncol Biol Phys*, **5**, 357-65.

RUBIN, P., HANLEY, J., KEYS, H.M., MARCIAL, V. & BRADY, L. (1979). Carbogen breathing during radiation therapy-the Radiation Therapy Oncology Group Study. *Int J Radiat Oncol Biol Phys*, **5**, 1963-70.

RUTMAN, R.J., CANTAROW, A. & PASCHKIS, K.E. (1954). The catabolism of uracil in vivo and in vitro. *J Biol Chem*, **210**, 321-9.

SALEEM A., YAP J., OSMAN O., BRADY F. & B.., S. (2000). Modulation of fluorouracil tissue pharmacokinetics by eniluracil: in-vivo imaging of drug action. *The Lancet*, **355**, 2125-131.

SALONGA, D., DANENBERG, K.D., JOHNSON, M., METZGER, R., GROSHEN, S., TSAO-WEI, D.D., LENZ, H.J., LEICHMAN, C.G., LEICHMAN, L., DIASIO, R.B. & DANENBERG, P.V. (2000). Colorectal tumors responding to 5-fluorouracil have low gene expression levels of dihydropyrimidine dehydrogenase, thymidylate synthase, and thymidine phosphorylase. *Clin Cancer Res*, **6**, 1322-7.

SALTZ, L.B., COX, J.V., BLANKE, C., ROSEN, L.S., FEHRENBACHER, L., MOORE, M.J., MAROUN, J.A., ACKLAND, S.P., LOCKER, P.K., PIROTTA, N., ELFRING, G.L. & MILLER, L.L. (2000). Irinotecan plus fluorouracil and leucovorin for metastatic colorectal cancer. Irinotecan Study Group. *N Engl J Med*, **343**, 905-14.

SANTI, D.V., MCHENRY, C.S. & SOMMER, H. (1974). Mechanism of interaction of thymidylate synthetase with 5-fluorodeoxyuridylate. *Biochemistry*, **13**, 471-81.

SCHILSKY RL., LEVIN J., WEST WH., WONG A., COLWELL B., THIRWELL MP., ANSARI RH. & AL., E. (2002). Randomised, Open-Label, Phase III Study of a 28-Day Oral Regimen of Eniluracil Plus Fluorouracil Versus Intravenous Fluorouracil Plus Leucovorin as First-Line Thaerpy in Patients with Metasatis/Advanced Colorectal Cacer. *Journal of Clinical Oncology*, **20**, 1519-26.

SCHWARTZ, E.L., BAPTISTE, N., O'CONNOR, C.J., WADLER, S. & OTTER, B.A. (1994). Potentiation of the antitumor activity of 5-fluorouracil in colon carcinoma cells by the combination of interferon and deoxyribonucleosides results from complementary effects on thymidine phosphorylase. *Cancer Res*, **54**, 1472-8.

SCHWARTZ, E.L., BAPTISTE, N., WADLER, S. & MAKOWER, D. (1995). Thymidine phosphorylase mediates the sensitivity of human colon carcinoma cells to 5-fluorouracil. *J Biol Chem*, **270**, 19073-7.

SCHWARTZ, E.L., HOFFMAN, M., O'CONNOR, C.J. & WADLER, S. (1992). Stimulation of 5-fluorouracil metabolic activation by interferon-alpha in human colon carcinoma cells. *Biochem Biophys Res Commun*, **182**, 1232-9.

SHANI, J. & DANENBERG, P.V. (1984). Evidence that intracellular synthesis of 5-fluorouridine-5'-phosphate from 5-fluorouracil and 5-fluorouridine is compartmentalized. *Biochem Biophys Res Commun*, **122**, 439-45.

SHANI J. & WOLF W. (1977). A model for prediction of of chemotherapy response to 5-fluorouracil based on the differential distribution of 5-[^{18}F]fluorouracil in sensitive versus resistant lymphocytic leukemia in mice. *Cancer Research*, **37**, 2306-2308.

SHANI J., YOUNG D. & SCLESINGER T. (1982). Dosimetry and preliminary human studies of ^{18}F-5-fluorouracil. *Int J Nucl Med Biol*, **9**, 25-35.

SHIELDS, A.F., LARSON, S.M., GRUNBAUM, Z. & GRAHAM, M.M. (1984). Short-term thymidine uptake in normal and neoplastic tissues: studies for PET. *J Nucl Med*, **25**, 759-64.

SHIELDS, A.F., LIM, K., GRIERSON, J., LINK, J. & KROHN, K.A. (1990). Utilization of labeled thymidine in DNA synthesis: studies for PET. *J Nucl Med*, **31**, 337-42.

SHIELDS AF., GRAMAM MM., KOZAWA SM., KOZELL LB. & LINK JM. (1992). Contribution of labeled carbon dioxide to PET imaging of carbon-11-labeled compounds. *J Nucl Med*, **33**, 1334-6.

SHIELDS AF., GRIERSON JR., DOHMEN BM., MACHULLA HJ., STAYANOFF JC., LAWHORN-CREWS JM., OBRADOVICH JE., MUZIK O. & MANGNER TJ. (1998a). Imaging proliferation in vivo with [F-18]FLT and positron emission tomography. *Nat.Med*, **4**, 1334-6.

SHIELDS AF., MANKOFF DA., LINK JM., GRAHAM MM., EARY J., KOZAWA S M., ZHENG M., LEWELLEN B., LEWELLEN TK., GRIERSON JR. & KROHN KA. (1998b). Carbon-11-Thymidine and FDG to Measure Therapy Response. *J Nucl Med*, **39**, 1757-61.

SHWEIKI, D., ITIN, A., SOFFER, D. & KESHET, E. (1992). Vascular endothelial growth factor induced by hypoxia may mediate hypoxia-initiated angiogenesis. *Nature*, **359**, 843-5.

SIBTAIN, A., HILL, S., GOODCHILD, K., SHAH, N., SAUNDERS, M. & HOSKIN, P.J. (2002). The modification of human tumour blood flow using pentoxifylline, nicotinamide and carbogen. *Radiotherapy and Oncology*, **62**, 69-76.

SIEMANN, D.W. (1998). The tumor microenvironment: a double-edged sword. *Int J Radiat Oncol Biol Phys*, **42**, 697-9.

SMYCZEK-GARGYA, B., FERSIS, N., DITTMANN, H., VOGEL, U., REISCHL, G., MACHULLA, H.J., WALLWIENER, D., BARES, R. & DOHMEN, B.M. (2004). PET with [18F]fluorothymidine for imaging of primary breast cancer: a pilot study. *Eur J Nucl Med Mol Imaging*, **31**, 720-4.

SOONG, R., SHAH, N., SALTO-TELLEZ, M., TAI, B.C., SOO, R.A., HAN, H.C., NG, S.S., TAN, W.L., ZEPS, N., JOSEPH, D., DIASIO, R.B. & IACOPETTA, B. (2008). Prognostic significance of thymidylate synthase, dihydropyrimidine dehydrogenase and thymidine phosphorylase protein expression in colorectal cancer patients treated with or without 5-fluorouracil-based chemotherapy. *Ann Oncol*, **19**, 915-919.

SPINKS, T., T., J., BAILEY, D.L., TOWNSEND, D.W., GROOTOONK, S. & AL., E. (1992). Physical performance of a positron tomograph for brain imaging with retractable septa. *Phys. Med. Biol*, **37**, 1637-1655

STEEL, C., BRADY, F., SAJINDER, L., BROWN, G., KHAN, I., POOLE, K., SERGIS, A., JONES, T. & PRICE, P. (1999). An automated radiosynthesis of 2-[11C]thymidine using anhydrous [11C]urea derived from [11C]phosgene *Appl Radiat Isot*, **51**, 377-388.

STRATFORD, M.R., ROJAS, A., HALL, D.W., DENNIS, M.F., DISCHE, S., JOINER, M.C. & HODGKISS, R.J. (1992). Pharmacokinetics of nicotinamide and its effect on blood pressure, pulse and body temperature in normal human volunteers. *Radiother Oncol*, **25**, 37-42.

STROMBLAD, S. & CHERESH, D.A. (1996). Integrins, angiogenesis and vascular cell survival. *Chem Biol*, **3**, 881-5.

STROTHER, S.C., CASEY, M.E. & HOFFMAN, E.J. (1990). Measuring PET scanner sensitivity: relating countrates to image signal-to-noise ratios using noise equivalents counts. *IEEE Trans Nucl Sci*, **37**, 783-788.

STUBBS, M., ROBINSON, S.P., RODRIGUES, L.M., PARKINS, C.S., COLLINGRIDGE, D.R. & GRIFFITHS, J.R. (1998). The effects of host carbogen (95% oxygen/5% carbon dioxide) breathing on metabolic characteristics of Morris hepatoma 9618a. *Br J Cancer*, **78**, 1449-56.

SUN, H., SLOAN, A., MANGNER, T.J., VAISHAMPAYAN, U., MUZIK, O., COLLINS, J.M., DOUGLAS, K. & SHIELDS, A.F. (2005). Imaging DNA synthesis with [18F]FMAU and positron emission tomography in patients with cancer. *Eur J Nucl Med Mol Imaging*, **32**, 15-22.

SUNDORO-WU, B.M., SCHMALL, B., CONTI, P.S., DAHL, J.R., DRUMM, P. & JACOBSEN, J.K. (1984). Selective alkylation of pyrimidyldianions: synthesis and purification of 11C labeled thymidine for tumor visualization using positron emission tomography. *Int J Appl Radiat Isot*, **35**, 705-8.

TAHERI, M.R., WICKREMASINGHE, R.G. & HOFFBRAND, A.V. (1982). Functional compartmentation of DNA precursors in human leukaemoblastoid cell lines. *Br J Haematol*, **52**, 401-9.

TAKEBAYASHI, Y., AKIYAMA, S., AKIBA, S., YAMADA, K., MIYADERA, K., SUMIZAWA, T., YAMADA, Y., MURATA, F. & AIKOU, T. (1996). Clinicopathologic and prognostic significance of an angiogenic factor, thymidine phosphorylase, in human colorectal carcinoma. *J Natl Cancer Inst*, **88**, 1110-7.

TANNOCK, I. (1992). Cell Proliferation. In *The Basic Science of Oncology*. eds Tannock, I.F. & Hill, R.P. pp. 154-177. New York: McGraw-Hill.

TAVITIAN, B. (2000). In vivo antisense imaging. *Q J Nucl Med*, **44**, 236-55.

TAVITIAN, B., TERRAZZINO, S., KUHNAST, B., MARZABAL, S., STETTLER, O., DOLLE, F., DEVERRE, J.R., JOBERT, A., HINNEN, F., BENDRIEM, B., CROUZEL, C. & DI GIAMBERARDINO, L. (1998). In vivo imaging of oligonucleotides with positron emission tomography. *Nat Med*, **4**, 467-71.

THEWS, O., KELLEHER, D. & VAUPEL, P. (2002). Dynamics of tumor oxygenation and red blood cell flux in response to inspiratory hyperoxia combined with different levels of inspiratory hypercapnia. *Radiotherapy and Oncology*, **62**.

THOMLINSON, R.H. & GRAY, L.H. (1955). The histological structure of some human lung cancers and the possible implications for radiotherapy. *Br J Cancer*, **9**, 539-49.

TJUVAJEV, J.G., STOCKHAMMER, G., DESAI, R., UEHARA, H., WATANABE, K., GANSBACHER, B. & BLASBERG, R.G. (1995). Imaging the expression of transfected genes in vivo. *Cancer Res*, **55**, 6126-32.

TOZER, G.M., PRISE, V.E., WILSON, J., LOCKE, R.J., VOJNOVIC, B., STRATFORD, M.R., DENNIS, M.F. & CHAPLIN, D.J. (1999). Combretastatin A-4 phosphate as a tumor vascular-targeting agent: early effects in tumors and normal tissues. *Cancer Res*, **59**, 1626-34.

UGUR, O., KOTHARI, P.J., FINN, R.D., ZANZONICO, P., RUAN, S., GUENTHER, I., MAECKE, H.R. & LARSON, S.M. (2002). Ga-66 labeled somatostatin analogue DOTA-DPhe1-Tyr3-octreotide as a potential agent for positron emission tomography imaging and receptor mediated internal radiotherapy of somatostatin receptor positive tumors. *Nucl Med Biol*, **29**, 147-57.

VAN DE WIELE, C., LAHORTE, C., OYEN, W., BOERMAN, O., GOETHALS, I., SLEGERS, G. & DIERCKX, R.A. (2003a). Nuclear medicine imaging to predict response to radiotherapy: a review. *Int J Radiat Oncol Biol Phys*, **55**, 5-15.

VAN DE WIELE, C., LAHORTE, C., VERMEERSCH, H., LOOSE, D., MERVILLIE, K., STEINMETZ, N.D., VANDERHEYDEN, J.L., CUVELIER, C.A., SLEGERS, G. & DIERCK, R.A. (2003b). Quantitative tumor apoptosis imaging using

technetium-99m-HYNIC annexin V single photon emission computed tomography. *J Clin Oncol*, **21**, 3483-7.

VAN DER WILT, C.L., SMID, K., AHERNE, G.W., NOORDHUIS, P. & PETERS, G.J. (1997). Biochemical mechanisms of interferon modulation of 5-fluorouracil activity in colon cancer cells. *Eur J Cancer*, **33**, 471-8.

VAN HEERDE, W.L., DE GROOT, P.G. & REUTELINGSPERGER, C.P. (1995). The complexity of the phospholipid binding protein Annexin V. *Thromb Haemost*, **73**, 172-9.

VANDER BORGHT, T., LABAR, D., PAUWELS, S. & LAMBOTTE, L. (1991). Production of [2-11C]thymidine for quantification of cellular proliferation with PET. *Int J Rad Appl Instrum [A]*, **42**, 103-4.

VANDER BORGHT, T., PAUWELS, S., LAMBOTTE, L., LABAR, D., DE MAEGHT, S., STROOBANDT, G. & LATERRE, C. (1994). Brain tumor imaging with PET and 2-[carbon-11]thymidine. *J Nucl Med*, **35**, 974-82.

VANDER BORGHT, T.M., LAMBOTTE, L.E., PAUWELS, S.A. & DIVE, C.C. (1990). Uptake of thymidine labeled on carbon 2: a potential index of liver regeneration by positron emission tomography. *Hepatology*, **12**, 113-8.

VARAGNOLO, L., STOKKEL, M.P., MAZZI, U. & PAUWELS, E.K. (2000). 18F-labeled radiopharmaceuticals for PET in oncology, excluding FDG. *Nucl Med Biol*, **27**, 103-12.

VAUPEL, P., THEWS, O. & HOECKEL, M. (2001). Treatment resistance of solid tumors: role of hypoxia and anemia. *Med Oncol*, **18**, 243-59.

VAUPEL P., KALLINOWSKI F. & OKUNIEFF P. (1989). Blood flow and Nutrient Supply, and Metabolic Microenvironment of Human Tumours: A Review. *Cancer Research*, **49**, 6449-65.

VERHOVEN, B., KRAHLING, S., SCHLEGEL, R.A. & WILLIAMSON, P. (1999). Regulation of phosphatidylserine exposure and phagocytosis of apoptotic T lymphocytes. *Cell Death Differ*, **6**, 262-70.

VESSELLE, H., GRIERSON, J., MUZI, M., PUGSLEY, J.M., SCHMIDT, R.A., RABINOWITZ, P., PETERSON, L.M., VALLIERES, E. & WOOD, D.E. (2002). In vivo validation of 3'deoxy-3'-[(18)F]fluorothymidine ([(18)F]FLT) as a proliferation imaging tracer in humans: correlation of [(18)F]FLT uptake by positron emission tomography with Ki-67 immunohistochemistry and flow cytometry in human lung tumors. *Clin Cancer Res*, **8**, 3315-23.

WADLER, S., HOROWITZ, R., MAO, X. & SCHWARTZ, E.L. (1996). Effect of interferon on 5-fluorouracil-induced perturbations in pools of deoxynucleotide triphosphates and DNA strand breaks. *Cancer Chemother Pharmacol*, **38**, 529-35.

WADLER, S. & SCHWARTZ, E.L. (1997a). New Advances in Interferon Therapy of Cancer. *Oncologist*, **2**, 254-267.

WADLER, S. & SCHWARTZ, E.L. (1997b). Role of interferon as a modulator of fluoropyrimidines: reply to a recent editorial. *Ann Oncol*, **8**, 139-40; discussion 141.

WADLER, S., SCHWARTZ, E.L., GOLDMAN, M., LYVER, A., RADER, M., ZIMMERMAN, M., ITRI, L., WEINBERG, V. & WIERNIK, P.H. (1989). Fluorouracil and recombinant alfa-2a-interferon: an active regimen against advanced colorectal carcinoma. *J Clin Oncol*, **7**, 1769-75.

WANG, L., WU, W.Z., SUN, H.C., WU, X.F., QIN, L.X., LIU, Y.K., LIU, K.D. & TANG, Z.Y. (2003). Mechanism of interferon alpha on inhibition of

metastasis and angiogenesis of hepatocellular carcinoma after curative resection in nude mice. *J Gastrointest Surg*, **7**, 587-94.

WARBURG, O. (1956). On the origin of cancer cells. *Science*, **123**, 309-14.

WEISSLEDER, R. & MAHMOOD, U. (2001). Molecular imaging. *Radiology*, **219**, 316-33.

WELLS, J.M., MANKOFF, D.A., MUZI, M., O'SULLIVAN, F., EARY, J.F., SPENCE, A.M. & KROHN, K.A. (2002a). Kinetic analysis of 2-[11C]thymidine PET imaging studies of malignant brain tumors: compartmental model investigation and mathematical analysis. *Mol Imaging*, **1**, 151-9.

WELLS, P., ABOAGYE, E., GUNN, R.N., OSMAN, S., BODDY, A.V., TAYLOR, G.A., RAFI, I., HUGHES, A.N., CALVERT, A.H., PRICE, P.M. & NEWELL, D.R. (2003). 2-[11C]thymidine positron emission tomography as an indicator of thymidylate synthase inhibition in patients treated with AG337. *J Natl Cancer Inst*, **95**, 675-82.

WELLS, P., GUNN, R.N., ALISON, M., STEEL, C., GOLDING, M., RANICAR, A.S., BRADY, F., OSMAN, S., JONES, T. & PRICE, P. (2002b). Assessment of proliferation in vivo using 2-[(11)C]thymidine positron emission tomography in advanced intra-abdominal malignancies. *Cancer Res*, **62**, 5698-702.

WELLS, P., GUNN, R.N., STEEL, C., RANICAR, A.S., BRADY, F., OSMAN, S., JONES, T. & PRICE, P. (2005). 2-[11C]Thymidine Positron Emission Tomography Reproducibility in Humans. *Clinical Cancer Research*, **11**, 4341-4347.

WESTLIN, W.F. (2001). Integrins as targets of angiogenesis inhibition. *Cancer J*, **7 Suppl 3**, S139-43.

WILSON, C.B., LAMMERTSMA, A.A., MCKENZIE, C.G., SIKORA, K. & JONES, T. (1992). Measurements of blood flow and exchanging water space in breast tumors using positron emission tomography: a rapid and noninvasive dynamic method. *Cancer Res*, **52**, 1592-7.

WOHLHUETER, R.M., MARZ, R. & PLAGEMANN, P.G. (1979). Thymidine transport in cultured mammalian cells. Kinetic analysis, temperature dependence and specificity of the transport system. *Biochim Biophys Acta*, **553**, 262-83.

WU, A.M., YAZAKI, P.J., TSAI, S.-W., NGUYEN, K., ANDERSON, A.-L., MCCARTHY, D.W., WELCH, M.J., SHIVELY, J.E., WILLIAMS, L.E., RAUBITSCHEK, A.A., WONG, J.Y.C., TOYOKUNI, T., PHELPS, M.E. & GAMBHIR, S.S. (2000). High-resolution microPET imaging of carcinoembryonic antigen-positive xenografts by using a copper-64-labeled engineered antibody fragment. *PNAS*, **97**, 8495-8500.

YAP JT., RHODES CG., CUNNINGMAM VJ., JONES T., ANDERSON H. & P., P. (2000). Measurement of cardiac output in PET tumour blood flow studies. *J Nucl Med*, **41**, p 182 poster 827.

YEH, S.H., LIU, R.S., WU, L.C., YANG, D.J., YEN, S.H., CHANG, C.W., YU, T.W., CHOU, K.L. & CHEN, K.Y. (1996). Fluorine-18 fluoromisonidazole tumour to muscle retention ratio for the detection of hypoxia in nasopharyngeal carcinoma. *Eur J Nucl Med*, **23**, 1378-83.

YOSHIMOTO, S., ISHIZAKI, Y., SASAKI, T. & MUROTA, S. (1991). Effect of carbon dioxide and oxygen on endothelin production by cultured porcine cerebral endothelial cells. *Stroke*, **22**, 378-83.

YOUNES, C.K., BOISGARD, R. & TAVITIAN, B. (2002). Labelled oligonucleotides as radiopharmaceuticals: pitfalls, problems and perspectives. *Curr Pharm Des*, **8**, 1451-66.

YOUNG, H., BAUM, R., CREMERIUS, U., HERHOLZ, K., HOEKSTRA, O., LAMMERTSMA, A.A., PRUIM, J. & PRICE, P. (1999). Measurement of clinical and subclinical tumour response using [18F]-fluorodeoxyglucose and positron emission tomography: review and 1999 EORTC recommendations. European Organization for Research and Treatment of Cancer (EORTC) PET Study Group. *Eur J Cancer*, **35**, 1773-82.

ZASADNY, K.R. & WAHL, R.L. (1993). Standardized uptake values of normal tissues at PET with 2-[fluorine-18]-fluoro-2-deoxy-D-glucose: variations with body weight and a method for correction. *Radiology*, **189**, 847-50.

ZIEGLER, S.I., HABERKORN, U., BYRNE, H., TONG, C., KAJA, S., RICHOLT, J.A., BYRNE, H., TONG, C., SCHOSSER, R., KRIETER, H., KAJA, S., RICHOLT, J.A., LAMMERTSMA, A.A. & PRICE, P. (1996). Measurement of liver blood flow using oxygen-15 labelled water and dynamic positron emission tomography: limitations of model description. *Eur J Nucl Med*, **23**, 169-77.

ZIEMER, L.S., EVANS, S.M., KACHUR, A.V., SHUMAN, A.L., CARDI, C.A., JENKINS, W.T., KARP, J.S., ALAVI, A., DOLBIER, W.R., JR. & KOCH, C.J. (2003). Noninvasive imaging of tumor hypoxia in rats using the 2-nitroimidazole 18F-EF5. *Eur J Nucl Med Mol Imaging*, **30**, 259-66.

ZIJLSTRA, J.G., DE VRIES, E.G. & MULDER, N.H. (1987). Drug resistance in medical oncology. *Neth J Med*, **30**, 85-93.

ZIJLSTRA, S., GUNAWAN, J. & BURCHERT, W. (2003). Synthesis and evaluation of a 18F-labelled recombinant annexin-V derivative, for identification and quantification of apoptotic cells with PET. *Appl Radiat Isot*, **58**, 201-7.

ZLOTECKI, R.A., BAXTER, L.T., BOUCHER, Y. & JAIN, R.K. (1995). Pharmacologic modification of tumor blood flow and interstitial fluid pressure in a human tumor xenograft: network analysis and mechanistic interpretation. *Microvasc Res*, **50**, 429-43.